

MICROGEOMETRY INDUCED NON-UNIQUENESS
IN THE ELASTIC AND ELECTRICAL PROPERTIES OF ROCKS

A DISSERTATION
SUBMITTED TO THE DEPARTMENT OF GEOPHYSICS
AND THE COMMITTEE ON GRADUATE STUDIES
OF STANFORD UNIVERSITY
IN PARTIAL FULFILLMENT OF THE REQUIREMENTS
FOR THE DEGREE OF
DOCTOR OF PHILOSOPHY

Priyanka Dutta

July 2018

Abstract

Most naturally occurring rocks are complex, heterogeneous composites and the exact micro-geometry of a rock sample is seldom known in its entirety. This lack of information about the unknown, exact micro-geometry of a rock translates into uncertainty or non-uniqueness in the effective rock properties that are micro-geometry dependent, such as elastic moduli, electrical conductivity, dielectric permittivity and fluid permeability among others. In this dissertation we explore important areas of rock-physics where micro-geometry induced non-uniqueness is not commonly or adequately addressed, estimating the practical impact of the unaccounted non-uniqueness and suggesting schemes to remedy that.

We study the elastic properties of randomly oriented single-phase poly-crystals, noting the often ignored fact that most isotropic mineral elastic moduli reported in published literature usually and arbitrarily correspond to the mid-point of existing poly-crystal property bounds, developed to account for micro-geometry induced non-uniqueness. The magnitude of the usually unaccounted non-uniqueness or uncertainty in effective elastic moduli, given by the width of the bounds, increases with increasing elastic anisotropy of the constituent mineral crystals. Using a self-consistent scheme, we develop a model to study the impact of crystal shape and relative lattice orientation on moving the effective poly-crystal elastic moduli within the bounds. For aggregates of crystals with transverse isotropy, we use Monte-Carlo simulations and a regression tree based sensitivity analysis to demonstrate the relationship between

fractional bound widths of effective elastic moduli and single crystal elastic parameters. Additionally, we show that aggregates of layered laminates represent an example of poly-crystal micro-geometry that may violate the embedded bounds for elastic solid substitution.

We also study elastic properties of preferentially oriented single-phase polycrystals. For a given orientation distribution function (ODF) of the constituent crystals, effective elastic properties are most commonly computed as ODF weighted averages of the single crystal elastic stiffness tensor (Voigt scheme, corresponding to uniform strain) or the single crystal elastic compliance tensor (Reuss scheme, corresponding to uniform stress). In previously published literature authors mostly use one scheme or another without systematically evaluating the impact of this choice on the estimated poly-crystal properties. Focusing on composites with rotational symmetry, we demonstrate that elastic moduli and anisotropy parameters estimated using Voigt and Reuss schemes can be considerably different from each other, the difference representing micro-geometric non-uniqueness and generally increasing with increasing elastic anisotropy of the constituent crystals. Using Monte-Carlo simulations and a regression tree based sensitivity analysis we demonstrate the impact of single-crystal elastic properties on the difference between the Voigt and Reuss estimates of the effective Thomsen's anisotropy parameters in a poly-crystal of rotational symmetry.

We study cross-property relations between the electrical conductivity and the bulk modulus of rocks, demonstrating some inadequacies in popular one-to-one conductivity-modulus relationships and the importance of factoring in porosity when using or interpreting cross-property relations. We propose the use of the narrowest rigorous cross-property bounds due to Gibiansky and Torquato as an alternative, wherein the range of effective bulk modulus predicted for a given value of rock conductivity (and vice versa) captures the inherent micro-geometric non-uniqueness

of a composite. Based on digital and laboratory data we obtain empirical constraints on Gibiansky and Torquato's rigorous cross-bounds to make them narrower for some common reservoir rocks, such as brine filled sandstones and carbonates. Finally, we demonstrate the use of the constrained cross-bounds to estimate the range of the Archie cementation factor of a formation when presented with large-scale elastic (e.g., seismic) and electrical (e.g., CSEM) surveys.

Finally, we study the problem of electrical fluid substitution - predicting the change in the effective electrical conductivity of a composite when one constituent conducting phase is substituted with another while the micro-geometry remains fixed. We demonstrate that the substitution problem is inherently non-unique due to variations in micro-geometry. We extend the concept of the embedded bounds, developed initially for elastic solid substitution, to obtain rigorous equations for substitution bounds on the electrical conductivity of two-phase, three-dimensional isotropic composites. We prove that when the conductivity contrast between composite phases is high, estimates from the popular Archie's law correspond approximately to the upper bound on the change of conductivity due to substitution. Inclusion modeling suggests that vuggy or poorly-connected pore space could account for conductivity changes smaller than predicted by Archie's law. Comparison of the conductivity substitution bounds with brine-saturated sandstone data of varying clay content reveals that the position of measured data within the conductivity substitution bounds can be indicative of the effective clay content in shaly sand samples.

Acknowledgments

This dissertation was funded by the Stanford Rock Physics and Borehole Geophysics Project. My final years at Stanford were also partly financed by the Anadarko/SEG and the Earl D. & Reba C. Griffin Memorial Scholarships.

I want to start by thanking my reading committee members: Prof. Gerald M. Mavko, Prof. Tapan Mukerji, and Dr. Jack P. Dvorkin. Thanks to Prof. Dustin M. Schroeder for serving on my defense committee, and to Prof. Roland N. Horne for serving as my defense chair. I also want to thank Prof. Mark D. Zoback for being part of my annual review committee. I am grateful to each of you for your encouragement, advice and constructive feedback.

My time at Stanford accorded me the privilege of knowing and working closely with my advisor, Gerald ‘Gary’ Mavko. I have learned so much from him: the importance of asking the right questions, of striving to rise above jargon to truly understand the physics behind phenomena, and of always keeping my mind open to alternate points of view. True to his style, he has selflessly shared with me his time, knowledge, wisdom, books and codes. Even curious brain-strengthening red-and-gold sachets of ginseng syrup! Gary, thank you for teaching me all I know about rock physics, and so much about being a good scientist and a good human being.

Any mention of my fondness for Gary is incomplete without mentioning his wife, Barbara. Thank you, Barbara, for your love and generosity, for the bagels and the amazing chocolate chip cookies, and the fun excursions to the shopping center. I

can never thank you and Gary enough for standing by me when times were tough, together you represent one of the best parts of my Stanford experience.

Many thanks to Tapan Mukerji, for always having a solution to getting unstuck in research. We say ‘Tapan knows everything’ - I am genuinely amazed by the vastness of your knowledge and your humility. Thank you, Tapan, for continually inspiring us how to analyze, work and communicate better. Many thanks to Jack Dvorkin, for showing us applications of rock physics to real-world problems. Jack, thank you for the constant support, advice, and encouragement, it meant a lot. And thanks to Prof. Amos Nur, for creating, guiding and standing by our beloved SRB community for all these years. I am also grateful to Dr. James Spencer and Dr. Stewart Levin, for many insightful, actionable suggestions. Many thanks to Prof. Satyen Sengupta, Prof. David Kohlstedt, Prof. Saibal Gupta and Prof. Santanu Bhowmik for believing in me and encouraging me to come to graduate school.

I am grateful to the Geophysics staff members for their constant help and support, especially Fuad, Nancy, Rachael, Elena, and Cory. And Jared of course, for patiently helping us with a smile and generously sharing his impressive candy collection! I am also indebted to Stanford University for its gift of the endless opportunities and resources to help us know and develop ourselves beyond being academics. And for steadfastly holding our hands as we navigate the delicate juncture of life that is graduate school for so many of us.

I feel very fortunate to be part of a group as diverse, talented and friendly as SRB. I will always look back at our memories with great fondness, from the picnics and group lunches to the extended discussions on every topic ranging from rock physics to travel experiences to questioning ‘the nature of our reality’! Thank you all: Tiziana, Nishank, Humberto, Uri, Sabrina, Natt, Abdulla, Vishal, Osama, Iris, Yuki, Chen, Pinar, Chisato, Ammar, Abrar, Salma, Helene, Wei, Obi, Rayan, Amrita, Adam, Mashael, Monirah, Juan Pablo, Zhishuai, Danica, Yu, Piyapa, Dulcie, Krongrath,

Dario, Stephanie and Fabian. A special shout-out to Nishank for helping me settle into Stanford, for lots of yummy mutton and many useful discussions around the material presented in this dissertation. I am also profoundly grateful for my first-year office-mates: Fatemeh, Alex, Humberto, Lei, TJ, and Badr, and for the beautiful friendship that we have forged over the years. I will cherish memories of our good times together forever! Thanks also to Fatimah, Ankush, Elizabeth, Noha, Kevin, Gader and Robert for making even the basement seem like a fun place to be!

Finally, and most importantly, a big thank you to my amazing family. My grandparents for their affection, and Mamma especially, for putting a little fighter inside me. My parents-in-law, Dada and Boudi for loving and supporting me as their own. Didi and Aman da for showing me how to ace life with a smile and good food, irrespective of circumstances. My nephews Sayan and Arin, for bringing unimaginable joy to our lives. My loving husband Arka, for being my anchor, my best friend and a true partner through the highs and lows of this fabulous adventure. And Ma and Baba, for everything: all that I am and ever hope to be, I owe to you. Having you as family is my greatest privilege and all sincere effort in my life, including this dissertation, is dedicated to you.

Contents

Abstract	iv
Acknowledgments	vii
1 Introduction	2
1.1 Motivation	2
1.2 Chapter descriptions	5
2 Elastic properties of isotropic poly-crystals	9
2.1 Abstract	9
2.2 Introduction	11
2.3 Statistical homogenization of crystal properties	13
2.3.1 Poly-crystal Voigt-Reuss (VR) bounds	13
2.3.2 Poly-crystal Voigt-Reuss-Hill (VRH) estimate	17
2.3.3 Poly-crystal Hashin-Shtrikman (HS) bounds	18
2.3.4 Voigt-Reuss & Hashin-Shtrikman bounds and Hill estimates for some common minerals	19
2.3.5 Tensor isotropic projections and poly-crystal Voigt-Reuss estimates	21
2.4 Physical significance of bounds and measures of universal anisotropy .	24

2.5	Relationship between isotropic bound-widths and crystal parameters	25
2.5.1	Characterizing domains with transverse isotropic symmetry	26
2.5.2	Monte-Carlo simulations	28
2.5.2.1	General constraints	29
2.5.2.2	Constraints based on TI projections of common minerals	29
2.5.2.3	Final simulation inputs	30
2.5.3	Analysis using cross plots	32
2.5.4	Analysis using Gradient Boosting Machines (GBM)	36
2.5.4.1	Primer on Gradient Boosting Machines (GBM)	36
2.5.4.2	Inferences using Gradient Boosting Machines	37
2.5.5	Trends for some common minerals	42
2.5.6	Analysis of poly-crystal Hashin-Shtrikman bounds	43
2.6	What moves us between the bounds	48
2.6.1	Derivation of a self-consistent framework	48
2.6.2	Implementation of the self-consistent model	50
2.6.3	Modeling results for some common minerals	53
2.7	Solid substitution in composites with micro-anisotropy	60
2.7.1	The embedded bounds	60
2.7.2	Isotropic aggregates of Backus laminates	61
2.7.3	Narrowing of bounds with additional geometric information .	62
2.7.4	Substituted Backus aggregate, case 1: softer pore-fill	64
2.7.5	Substituted Backus aggregate, case 2: stiffer pore-fill	67
2.7.6	Similarity with Milton's bounds	69
2.8	Clay elastic moduli	70
2.9	Conclusions	71
2.10	Appendix A: TI projection of minerals	73
2.11	Appendix B: Backus Average	74

3 Elastic properties of anisotropic poly-crystals	77
3.1 Abstract	77
3.2 Anisotropic poly-crystal Voigt-Reuss estimates	79
3.2.1 General Theory	79
3.2.2 Approximate formulations using Legendre Polynomials	81
3.2.2.1 Approximate Voigt formulations	82
3.2.2.2 Approximate Reuss formulations	84
3.2.3 Discretized formulations	86
3.2.4 The VRH or Average Tensor	87
3.3 Voigt-Reuss modeling results	87
3.3.1 Chosen micro-domains and their elastic parameters	87
3.3.2 Chosen Orientation Distribution Functions	88
3.3.3 Voigt-Reuss modeling for compaction ODF	91
3.3.4 Voigt-Reuss modeling for Fisher ODF	94
3.3.5 Thomsen parameter delta	96
3.3.6 Monte-Carlo analysis of anisotropic poly-crystals	97
3.3.7 Impact on Vp/Vs ratio	106
3.3.8 Impact on AVO	107
3.4 Conclusions	111
4 Electrical-elastic cross-relations in rocks	114
4.1 Abstract	114
4.2 Background and motivation	115
4.3 Hashin-Shtrikman cross-plot lines in the σ^* - K^* plane	118
4.4 Gibiansky and Torquato cross-bounds	123
4.4.1 GT bounds for known phase volume fractions	123
4.4.2 Realizability of the GT bounds	126

4.4.3	GT bounds for arbitrary phase volume fractions	127
4.5	GT cross-bounds vs. effective medium modeling: Oblate and prolate pore-spaces	129
4.6	GT bounds vs. cross-property data	134
4.6.1	Comparison with digital data	134
4.6.1.1	Sandstone data	134
4.6.1.2	Carbonate data	140
4.6.2	Comparison with laboratory data	143
4.7	GT bounds for determining Archie cementation factor	149
4.8	Conclusions	154
4.9	Appendix	155
5	Conductivity substitution	157
5.1	Abstract	157
5.2	Introduction	158
5.3	Theory	159
5.3.1	Previous work	159
5.3.2	The embedded bounds	161
5.3.2.1	Derivation of the embedded bounds	162
5.3.2.2	Equations describing the embedded bounds	167
5.4	Geometric interpretation of the embedded bounds	170
5.4.1	Mineral and fluid coated embedded bounds	170
5.4.2	Interpretation using effective medium theories	171
5.5	Comparison of the embedded bounds with Archie's Law	174
5.5.1	Conditional equivalence between Archie's Law and the fluid- coated embedded bound	175
5.6	Comparison of the embedded bounds with measured data	180

5.6.1	The Waxman-Smits dataset	180
5.6.2	Comparison using constant and variable mineral conductivity	181
5.7	Conclusions	187

List of Tables

2.1	Estimates of isotropic poly-crystal bulk ('K') and shear ('G') moduli for some common minerals, expressed in units of GPa. 'HS+' and 'HS-' represent the upper and lower poly-crystal HS bounds respectively. For reference, the phase bulk moduli are also reported in g/cc.	20
2.2	TI elastic parameters and corresponding values of dfk , dfg and dfp for some minerals/domains of interest in earth science applications. Domains less symmetric than TI originally have been projected onto the TI space.	30
2.3	Properties of phases used in the solid substitution exercise	62
4.1	Properties of digital sandstone samples, sorted by porosity. The computed bulk modulus of the last sample, marked by '**', violates the HS bounds (Saxena & Mavko, 2016).	134
4.2	Properties of digital carbonate samples, sorted by porosity (Saxena and Mavko, 2016).	140
4.3	Laboratory measurements on selected low clay samples (Han et al., 2010).	144
4.4	Porosity and mineralogy of selected low clay samples (Han et al., 2010).	145
4.5	Physical properties of components used in modeling Han's (2010) data.	145

List of Figures

1.1	SC models M1 and M2, equivalent w.r.t. effective conductivity for the state of ‘initial σ ’, but not equivalent w.r.t. effective conductivity for the state of ‘final σ ’, and not equivalent w.r.t. effective bulk modulus ‘K’. 2 different properties (effective conductivity ‘ σ ’ and bulk modulus ‘K’) are plotted on this figure, each normalized by the corresponding property value for model M2.	4
2.1	Poly-crystalline structure of (top-left) a metal alloy, (top-right) ice, (bottom-left) a multimineralic rock and (bottom-right) a clay sample.	11
2.2	Normalized bulk and shear modulus values for each phase in Table 2.1, scaled such that in each case, the Voigt and Reuss moduli range between 0 and 1, and all other moduli estimates are scaled accordingly.	21
2.3	Schematic showing three poly-crystals with approximately the same lattice orientations but significantly different microgeometries that could lead to significantly different elastic properties.	25
2.4	Schematic representation of layered/fractured TI media, the arrows representing the axes of symmetry and the corresponding transverse planes being isotropic. The material on the left has a vertical symmetry axis (VTI).	27

2.5	Histograms and pair-wise cross-plots of the 5 distinct, but not orthogonal VTI micro-domain parameters from Monte-Carlo simulations, subject to constraints given by Equations 2.34 to 2.36.	31
2.6	Variation of fractional difference between the Voigt and Reuss estimates of the effective shear modulus (dfg) with the VTI micro-domain constants. Monte-Carlo simulations reveal that Thomsen parameter γ dominates the shear modulus spread, which in general, increases with increasing γ	33
2.7	Variation of fractional difference between the Voigt and Reuss estimates of the effective bulk modulus (dfk) with the VTI micro-domain constants. Monte-Carlo simulations reveal that Thomsen parameter ϵ dominates the bulk modulus spread, which in general, increases with increasing ϵ . The control of ϵ on the bulk-modulus spread is not as strong as that of γ on the shear modulus spread.	34
2.8	Variation of fractional difference between the Voigt and Reuss estimates of the effective P-wave modulus (dfp) with the VTI micro-domain constants. Monte-Carlo simulations reveal that Thomsen parameter ϵ dominates the P-wave modulus spread, which in general, increases with increasing ϵ . The minimum fractional difference in the P-wave modulus estimates scales almost linearly with ϵ	35

2.9 Top, left: ‘Relative influence’ values from a gradient boosted meta-model for the shear modulus spread (dfg), indicating that the micro-domain γ (labeled ‘gam’) is the elastic parameter with biggest influence on dfg ; Top, right: dfg predicted by the GBM meta-model against the true dfg in a blind test-set data, showing good match between the modeled and true data, with a mean-absolute-error (MAE) of 0.025; Bottom: Two-way partial dependence plot of ‘ dfg ’ (plot color) with γ (x-axis, labeled as ‘gam’) and δ (y-axis, labeled as ‘del’).	38
2.10 Top, left: ‘Relative influence’ values from a gradient boosted meta-model for the bulk modulus spread (dfk), indicating that the micro-domain γ is the elastic parameter with the biggest influence on dfk ; Top, right: dfk predicted by the GBM meta-model against the true dfk in a blind test-set data, showing good match between the modeled and true data, with a mean-absolute-error (MAE) of 0.034. Bottom: Two-way partial dependence plot of ‘ dfk ’ (plot color) with ϵ (x-axis, labeled as ‘eps’) and γ (y-axis, labeled as ‘gam’).	39
2.11 Left: ‘Relative influence’ values from a gradient boosted meta-model for the P-wave modulus spread (dfp), indicating that the micro-domain ϵ is the elastic parameter with biggest influence on dfp ; Right: dfp predicted by the GBM meta-model against the true dfp in a blind test-set data, showing good match between the modeled and true data, with a mean-absolute-error (MAE) of 0.025. Bottom: Two-way partial dependence plot of ‘ dfp ’ (plot color) with ϵ (x-axis, labeled as ‘eps’) and γ (y-axis, labeled as ‘gam’).	41

2.12 Composite dfg , dfk and dfp against domain parameters ($C_{33}, C_{44}, \epsilon, \gamma, \delta$) for the eleven transverse isotropic phases listed in Table 2.2. The consistent positive correlation between composite parameters dfg , dfk and dfp and domain parameters ϵ and γ contrasts strongly against the more random variations between the composite and domain parameters in the other three cases.	43
2.13 Variation of fractional difference between the HS estimates of the effective shear modulus of macro-composite (dfg) with the VTI micro-domain constants. Monte-Carlo simulations reveal that domain parameter γ dominates the composite HS shear modulus spread, which in general, increases with increasing γ	45
2.14 Left: ‘Relative influence’ values from a gradient boosted meta-model of the composite HS shear modulus spread ($dfg2$), indicating that the micro-domain γ (labeled ‘gam’) is the elastic parameter with biggest influence on $dfg2$; Right: Two-way partial dependence plot of composite ‘ $dfg2$ ’ (plot color) with domain parameters γ (x-axis, labeled as ‘gam’) and δ (y-axis, labeled as ‘del’).	46
2.15 Left: ‘Relative influence’ values from a gradient boosted meta-model of the composite HS bulk modulus spread ($dfk2$), indicating that the micro-domain ϵ (labeled ‘eps’) is the elastic parameter with biggest influence on $dfk2$; Right: Two-way partial dependence plot of composite ‘ $dfk2$ ’ (plot color) with domain parameters ϵ (x-axis, labeled as ‘eps’) and C_{44} (y-axis, labeled as ‘c44’).	47

2.16 Left: ‘Relative influence’ values from a gradient boosted meta-model of the composite HS P-wave modulus spread ($dfp2$), indicating that the micro-domain γ (labeled ‘gam’) is the elastic parameter with biggest influence on $dfp2$, closely followed by micro-domain ϵ (labeled ‘eps’); Right: Two-way partial dependence plot of composite ‘ $dfp2$ ’ (plot color) with domain parameters γ (x-axis) and ϵ (y-axis).	47
2.17 Norm error ($\ T_{iso}\ - \ I\ $) in the self-consistent model of poly-crystal illite, with hexagonal crystal symmetry, for aspect ratios ranging from $\exp(-4)$ [oblate grain shapes] to $\exp(4)$ [prolate grain shapes]. The norm error is 0 for spherical grains (aspect ratio = 1) and non-zero elsewhere.	53
2.18 Self-consistent model for poly-crystal illite, with hexagonal crystal symmetry, for aspect ratios ranging from $\exp(-3)$ [oblate grain shapes] to $\exp(3)$ [prolate grain shapes].	54
2.19 Self-consistent model for poly-crystal illite, with hexagonal crystal symmetry, for aspect ratios ranging from $\exp(-3)$ [oblate grain shapes] to $\exp(3)$ [prolate grain shapes], and relative angle between the grain symmetry axis and crystal lattice varying between $0-\pi$, in steps of $\pi/10$.	55
2.20 Self-consistent model for poly-crystal α -quartz, with trigonal crystal symmetry, for aspect ratios ranging from $\exp(-3)$ [oblate grain shapes] to $\exp(3)$ [prolate grain shapes], and relative angle between the grain symmetry axis and crystal lattice varying between $0-\pi$, in steps of $\pi/10$.	57
2.21 Self-consistent model for poly-crystal muscovite, with monoclinic crystal symmetry, for aspect ratios ranging from $\exp(-3)$ [oblate grain shapes] to $\exp(3)$ [prolate grain shapes], and relative angle between the grain symmetry axis and crystal lattice varying between $0-\pi$, in steps of $\pi/10$	58

2.22 For the general case of spheroidal grain shapes, elastic modulus estimates from our self-consistent model are in excellent agreement with the results of Qiu & Weng (1991); the example here is of hexagonal zinc crystals.	59
2.23 Schematic representation of a doubly coated-sphere realization of the embedded bounds by Mavko and Saxena (2013), implicitly assuming isotropy at all scales.	61
2.24 Schematic representation of an isotropic composite of two isotropic phases, with micro-scale anisotropy. (a) shows the layering of the two phases to form an anisotropic micro-domain, and (b) shows several micro-domains oriented randomly to form the isotropic macro-composite.	61
2.25 Narrowing of bounds with additional geometric information: Poly-crystal Voigt-Reuss bounds (labeled ‘angular Voigt-Reuss’) for the Backus laminates are narrower than the isotropic Hashin-Shtrikman bounds with no micro-geometric information	63
2.26 Solid substitution in composite with micro-scale anisotropy: substituting clay in a quartz-clay composite with heavy oil, only the poly-crystal/angular Reuss estimate of bulk modulus falls within the predicted embedded bounds though the errors in general are not significant (< 0.1%).	65
2.27 Solid substitution in composite with micro-scale anisotropy: substituting clay in a quartz-clay composite with heavy oil, only the poly-crystal/angular Reuss estimate of bulk modulus falls within the predicted embedded bounds though the errors in general are not significant (< 0.1%).	66

2.28 Solid substitution in composite with micro-scale anisotropy: substituting clay in a quartz-clay composite with pyrite, both polycrystal/angular Voigt and Reuss estimates of bulk and shear moduli fall outside the predicted embedded bounds with errors of the order of 3%).	68
3.1 Euler angles (θ, ψ, ϕ) specifying tilt of the local ‘crystal’ axes relative to the global coordinate axes.	80
3.2 (L-R) Compaction ODF polar plots (projection of the 3D ODF on a vertical plane) for compaction factors $a = 1, 3$ and 9 . As compaction factor increases, more micro-domains become horizontal, and their TI symmetry axes have larger probability density in the vertical directions, close to $\theta = 0$ or π	90
3.3 (L-R) Fisher ODF polar plots (projection of the 3D ODF on a vertical plane) for concentration factors $c = 1, 3$ and 9 . As concentration factor increases, more micro-domains become horizontal, and their TI symmetry axes have larger probability density in the vertical directions, close to $\theta = 0$ or π	91
3.4 Difference between Voigt and Reuss estimates of various macrocomposite elastic properties as they vary with increasing domain alignment (for the compaction ODF) for mica-muscovite micro-domains. The figure also shows comparison between Voigt and Reuss estimates using Legendre polynomial approximations (labeled ‘Voigt-poly’ and ‘Reuss-poly’) and discretized summations (labeled ‘Voigt-num’ and ‘Reuss-num’). It is evident that the two methods lead nearly identical results.	92

3.5	Difference between Voigt and Reuss estimates of various macro-composite elastic properties as they vary with increasing domain alignment (for the compaction ODF) for Ulm's shale micro-domains.	94
3.6	Difference between Voigt and Reuss estimates of various macro-composite elastic properties as they vary with increasing domain alignment (for the Fisher ODF) for mica-muscovite micro-domains.	95
3.7	Difference between Voigt and Reuss estimates of various macro-composite elastic properties as they vary with increasing domain alignment (for the Fisher ODF) for Ulm's shale micro-domains.	96
3.8	Difference (<i>deps</i>) between Voigt and Reuss estimates of macro-composite elastic parameter ϵ with micro-domain parameters C_{33} , C_{44} , ϵ , γ and δ for a compaction ODF with a compaction factor of 3.	98
3.9	Clockwise from left: Relative influence of various micro-domain parameters on the Voigt-Reuss difference ' <i>deps</i> ' in the estimated composite parameter ϵ using GBM on Monte-Carlo samples (for compaction ODF with compaction factor 3); Goodness of GBM fit, demonstrated by comparing true <i>deps</i> ('test.data\$deps') and GBM predicted <i>deps</i> ('pred.gbm') on a blind test dataset; 2-way partial dependence plot showing the variation in composite <i>deps</i> with joint variation in domain parameters δ ('del') and ϵ ('eps').	100
3.10	Difference (<i>dgam</i>) between Voigt and Reuss estimates of macro-composite elastic parameter γ with micro-domain parameters C_{33} , C_{44} , ϵ , γ and δ for a compaction ODF with a compaction factor of 3. The largest positive value of composite ' <i>dgam</i> ' increases monotonically with domain γ	101

3.11 Clockwise from left: Relative influence of various micro-domain parameters on the Voigt-Reuss difference ‘ <i>dgam</i> ’ in the estimated composite parameter γ using GBM on Monte-Carlo samples (for compaction ODF with compaction factor 3); Goodness of GBM fit, demonstrated by comparing true <i>dgam</i> (‘ <i>test.data\$dgam</i> ’) and GBM predicted <i>dgam</i> (‘ <i>pred.gbm</i> ’) on a blind test dataset; 2-way partial dependence plot showing the variation in composite <i>dgam</i> with joint variation in domain parameters C_{44} and γ (‘ <i>gam</i> ’).	102
3.12 Difference (<i>ddel</i>) between Voigt and Reuss estimates of macro-composite elastic parameter δ with micro-domain parameters C_{33} , C_{44} , ϵ , γ and δ for a compaction ODF with a compaction factor of 3.	104
3.13 Clockwise from left: Relative influence of various micro-domain parameters on the Voigt-Reuss difference ‘ <i>ddel</i> ’ in the estimated composite parameter δ using GBM on Monte-Carlo samples (for compaction ODF with compaction factor 3); Goodness of GBM fit, demonstrated by comparing true <i>ddel</i> (‘ <i>test.data\$ddel</i> ’) and GBM predicted <i>ddel</i> (‘ <i>pred.gbm</i> ’) on a blind test dataset; 2-way partial dependence plot showing the variation in composite <i>ddel</i> with joint variation in domain parameters γ (‘ <i>gam</i> ’) and δ (‘ <i>del</i> ’).	105
3.14 Difference between Voigt and Reuss estimates of Vp-Vs ratio with increasing domain alignment (using the compaction ODF) in (left): aggregates of mica-muscovite domains, and (right): aggregates of Ulm’s shale unit domains.	107
3.15 Difference between Voigt and Reuss AVO responses for an isotropic sandstone layer overlain by anisotropic mica-muscovite, at various degrees of mechanical compaction.	110

3.16 Difference between Voigt and Reuss AVO responses for an isotropic sandstone layer overlain by anisotropic Ulm's shale unit, at various degrees of mechanical compaction.	111
4.1 Cross-property relations by Carcione et. al. (2007) for [left] digital bulk modulus-conductivity computations on brine filled sandstone samples, and [right] laboratory measurements on brine filled clean sandstone samples.	116
4.2 Foam and suspension micro-geometries and their mapping to Hashin-Shtrikman (HS) bounds. Foams correspond to upper HS bounds for bulk modulus and lower HS bounds for conductivity. Suspensions correspond to the opposite HS bound combination.	118
4.3 The mapping of HS-foam (black line) and HS-suspension (blue line) micro-geometries in the σ^* - K^* plane. Micro-geometry inconsistent and physically non-realizable ‘foam-suspension’ and ‘suspension-foam’ lines are also plotted as dashed red lines. The sub-figure on the right plots conductivity on a log scale, the kink in the ‘HS-suspension’ line is an artifact of sampling, accentuated by the large conductivity contrast between the constituent phases.	119
4.4 The importance of porosity in cross-property relations: points X_1 , X_2 and X_3 have the same values of bulk modulus and conductivity but at different values of porosity. Only X_1 is a true suspension, but in the σ^* - K^* plane all three points plot on the HS-suspension cross-plot line, and can potentially cause misinterpretations.	121
4.5 Data-points that lie well within the individual HS bounds for bulk modulus or conductivity don't necessarily lie within the micro-geometry consistent HS-lines in the σ^* - K^* plane.	122

4.6	GT cross-bounds (given by outermost pair of 5 hyperbolae segments GT1, GT2, GT3, GT4, GT5) for a solid-brine isotropic composite with a porosity of 0.35.	126
4.7	GT bounds at multiple porosities, stacked in the conductivity-bulk modulus space (σ^* - K^* plane). Porosity decreases as we move up and left. The top sub-figure plots conductivity in a linear scale while the bottom one plots conductivity in a log scale to show the low conductivity/porosity features better.	128
4.8	Estimates of effective medium models against the GT cross-bounds for a sandstone-brine composite with 10% porosity. Top panel of the figure shows results of self-consistent modeling (labeled ‘SCA’ on the left and DEM modeling (labeled ‘DEM’) with two critical porosity (PHIC) values (1 and 0.4) on the right. The bottom panel shows the same plots with conductivity on a log-scale instead of linear.	131
4.9	Estimates of effective medium models against the GT cross-bounds for a sandstone-brine composite with 10% porosity. Top panel of the figure shows results of self-consistent modeling (labeled ‘SCA’ on the left and DEM modeling (labeled ‘DEM’) with two critical porosity (PHIC) values (1 and 0.4) on the right. The bottom panel shows the same plots with conductivity on a log-scale instead of linear.	132
4.10	Digitally computed bulk modulus and conductivity (black stars) for four brine filled sandstone samples with different porosities, along with the 5 GT curves (labeled ‘GT1’, ‘GT2’, ‘GT3’, ‘GT4’ & ‘GT5’) and modeled self-consistent points for a range of aspect ratios (labeled ‘SCA’) corresponding to each sample. The self-consistent points are color coded by the aspect ratio of the brine-filled pore-space, the quartz phase modeled as spherical grains with aspect ratio 1.	135

4.11 Digital data points against the corresponding GT bounds for all 24 sandstone samples, plotted in order of increasing sample porosity. The GT curves are estimated using the digital estimate of electrical conductivity combined with information on porosity and phase property end-points. The digital sandstone samples, spanning a wide range of porosity values, lie within a narrow bulk modulus band around the embedded curve ‘GT3’, shaded and labeled as ‘reduced range’.	137
4.12 Digital data points against the corresponding GT bounds for all 24 sandstone samples, plotted in order of increasing sample porosity. The GT curves are estimated using the digital estimate of bulk modulus combined with information on porosity and phase property end-points. The digital sandstone samples, spanning a wide range of porosity values, lie within a narrow conductivity band around the embedded curve ‘GT3’, shaded and labeled as ‘reduced range’.	139
4.13 Digitally computed bulk modulus and conductivity (black stars) for two brine filled carbonate samples with different porosities, along with the 5 GT curves (labeled ‘GT1’,‘GT2’,‘GT3’,‘GT4’ & ‘GT5’) and modeled self-consistent points for a range of aspect ratios (labeled ‘SCA’) corresponding to each sample. The self-consistent points are color coded by the aspect ratio of the brine-filled pore-space, the calcite phase modeled as spherical grains with aspect ratio 1.	141

4.14 Digital data points against the corresponding GT bounds for all 5 carbonate samples, plotted in order of increasing sample porosity. The GT curves are estimated using the digital estimate of conductivity combined with information on porosity and phase property end-points. The digital carbonate samples, spanning a wide range of porosity values, lie within a narrow bulk modulus band around the embedded curve ‘GT3’, shaded and labeled as ‘reduced range’.	142
4.15 Digital data points against the corresponding GT bounds for all 5 carbonate samples, plotted in order of increasing sample porosity. The GT curves are estimated using the digital estimate of bulk modulus combined with information on porosity and phase property end-points. The digital carbonate samples, spanning a wide range of porosity values, lie within a narrow conductivity band around the embedded curve ‘GT3’, shaded and labeled as ‘reduced range’.	143
4.16 Laboratory measured conductivity and bulk modulus estimates (black stars [60 MPa] and circles [8MPa]) for four brine filled sandstone samples with different porosities, along with the 5 GT curves (labeled ‘GT1’,‘GT2’,‘GT3’,‘GT4’ & ‘GT5’, for bulk modulus computed from 60 MPa conductivity) and modeled self-consistent points for a range of aspect ratios (labeled ‘SCA’) corresponding to each sample. The self-consistent points are color coded by the aspect ratio of the brine-filled pore-space, the quartz phase modeled as spherical grains with aspect ratio 1.	146

4.17 Laboratory measured data points against the corresponding GT bounds for the 17 selected sandstone samples (clay component < 5%) from Han's (2010) dataset, plotted in order of increasing sample porosity. The GT curves are estimated using the laboratory measurement of sample conductivities combined with information on porosity and phase property end-points. The sandstone samples, spanning a wide range of porosity values, lie within a narrow conductivity band around the embedded curve 'GT3', shaded and labeled as 'reduced range'.	147
4.18 Laboratory measured data points against the corresponding GT bounds for the 17 selected sandstone samples (clay component < 5%) from Han's (2010) dataset, plotted in order of increasing sample porosity. The GT curves are estimated using estimates of sample bulk moduli from laboratory measurements, combined with information on porosity and phase property end-points. The sandstone samples, spanning a wide range of porosity values, lie within a narrow conductivity band around the embedded curve 'GT3', shaded and labeled as 'reduced range'.	149
4.19 Variation of 'm' in the σ^* - K^* cross-property space for a brine saturated sandstone of porosity 0.3. For a constant value of formation conductivity, we get a range of possible values of formation bulk modulus (computed as per the 'reduced range' GT bounds) and a constant value of 'm'. The color-bar on left sub-figure shows the entire range of 'm' for this example, while on the right sub-figure the color-bar has a maximum of 'm' = 2.5, to better reveal the variation of 'm' at higher values of formation conductivity.	151

4.20 Variation in ‘m’ in the σ^*-K^* plane, using the ‘reduced range’ GT bounds. The top left sub-figure shows the variation in the maximum possible value of ‘m’, the top right sub-figure shows variations in the minimum values of ‘m’. The bottom panel shows the variation in the range of ‘m’ (= the difference between the maximum and minimum values of ‘m’ for any given σ^*-K^* pair). While the theoretical maximum value of ‘m’ can be as high as 5.5, the range of ‘m’ for any allowable σ^*-K^* pair is only about 1.75.	152
5.1 HS bounds for a 2-phase, 3-dimensional, isotropic mineral-fluid composite with mineral conductivity $\sigma_{min} = 0.01S/m$, and fluid conductivity $\sigma_{fluid} = 10S/m$	162
5.2 Points P1 and Q1 on the lower and upper HS bounds of the initial composite (shown as solid HS lines) map exactly and uniquely to points P2 and Q2, respectively on the lower and upper bounds of the final/substituted composite (shown as dashed HS lines).	163
5.3 For a point R1 in between the HS bounds of the initial composite (solid lines), we can find points P1 and Q1 such that an upper (or lower) HS line connecting points P1 and Q1 also passes through R1. With this construct, points P1, Q1 and R1 in the initial composite map exactly and uniquely to the points P2, Q2, and R2 in the final/substituted composite.	163
5.4 Infinite number of possible HS constructs between intermediate endpoints that pass through the point R1 (lying within the HS bounds) in the initial composite, shown by gray lines.	164

5.5	The single point R1 in the initial composite maps over a range of conductivity values in the final/substituted composite, showing that the problem of conductivity substitution is inherently non-unique due to the unknown exact micro-geometry of a composite.	165
5.6	Micro-geometry induced non-uniqueness in conductivity substitution enhanced for larger contrast between conductivity of the initial ($\sigma_{fluid}^{(1)} = 5S/m$) and final fluids ($\sigma_{fluid}^{(2)} = 15S/m$).	166
5.7	Embedded constructs corresponding to conductivity substitution limits in the final/substituted composite: HS_{min+} , HS_{min-} , HS_{fluid+} and HS_{fluid-}	167
5.8	Embedded bound curves for electrical conductivity substitution. Top: Fluid substitution, increase of fluid conductivity by a factor of 10; mineral conductivity constant. Bottom: Mineral substitution, increase of mineral conductivity by a factor of 10; fluid conductivity constant. Porosity = 0.3.	169
5.9	Schematic representation of the doubly-coated sphere geometries that realize the embedded bounds for conductivity substitution.	171
5.10	SC model predictions (black dots) compared with embedded bound predictions (red and blue curves) for conductivity substitution. Porosity=0.3. The fluid conductivity increases by a factor of 10; mineral conductivity remains constant. Aspect ratios (labeled ‘ar’ in the figure) close to 1 represent shapes that are spherical, less than 1 are oblate/crack-like and greater than 1 are prolate/tube-like.	172

5.11 DEM predictions compared with embedded bound predictions (red and blue curves) for conductivity substitution. Porosity=0.3. The fluid conductivity increases by a factor of 10; mineral conductivity remains constant. Blue dots show low conductivity grains added to a high conductivity background. Red dots show high conductivity pores added to a low conductivity background.	173
5.12 Embedded bound curves for fluid substitution of conductivity, labeled ‘mineral coated’ and ‘fluid coated’. Fluid conductivity increases by factor of 5; porosity = 0.05; initial fluid conductivity is 10,000 times larger than the mineral conductivity. The blue curve shows the embedded bound which is almost equal to Archie's law (black stars) predictions except at very low conductivities. Dashed lines show the HS bounds for initial and final compositions.	176
5.13 Embedded bound curves for fluid substitution of conductivity, labeled ‘mineral coated’ and ‘fluid coated’. Fluid conductivity increased by factor of 5; porosity = 0.3; initial fluid conductivity is only 10 times larger than the mineral conductivity. Archie's law (black stars) significantly over predicts the change due to substitution for this reduced conductivity contrast between the constituent phases.	177
5.14 Embedded bounds, Archie's Law predictions and measured data for fluid substitution in sandstones with variable clay content, going from an initial brine conductivity of 228 to a final of 21.3 mS/cm using (top) a constant matrix conductivity of 0.0001 mS/cm, and (bottom) Bussian's inverted grain conductivity, accounting for the variable clay content.	182
5.15 Histogram of Bussian's estimates of the matrix/grain conductivity, varying between 0-1.23 mS/cm.	183

5.16 Embedded bounds, Archie's Law predictions and measured data for fluid substitution in sandstones with variable clay content, going from an initial brine conductivity of 228 to a final of 37.3 mS/cm using (top) a constant matrix conductivity of 0.0001 mS/cm, and (bottom) Bussian's inverted grain conductivity, accounting for the variable clay content.	185
5.17 Embedded bounds, Archie's Law predictions and measured data for fluid substitution in sandstones with variable clay content, going from an initial brine conductivity of 228 to a final of 81.9 mS/cm using (top) a constant matrix conductivity of 0.0001 mS/cm, and (bottom) Bussian's inverted grain conductivity, accounting for the variable clay content.	186

...

Chapter 1

Introduction

1.1 Motivation

Most rocks on earth are heterogeneous, multi-phase composites with complex internal micro-geometries. These complex micro-geometries are often difficult to characterize completely, despite the existence of a significant volume of research in this area, from spatial correlation functions to micro-tomography and image analysis to laboratory and petrophysical methods and more (Berryman & Milton, 1988 [1], Blair et al., 1996 [2], Schild et al., 2001 [3], Radlinski et al., 2002 [4], Youssef et al., 2007 [5], Anovitz & Cole, 2015 [6]). In practice, however, rock micro-geometries mostly remain poorly or incompletely characterized.

This lack of information about the unknown exact micro-geometry of a rock translates into uncertainty or non-uniqueness in rock properties that are micro-geometry or micro-structure dependent, such as elastic moduli, electrical conductivity, dielectric permittivity and fluid permeability among others. The primary motivation of this dissertation is to understand the nature and implications of micro-geometry induced non-uniqueness in the elastic and electrical properties of naturally occurring rocks. In addition to studying non-uniqueness or uncertainty in individual properties, we also

research non-uniqueness in the cross-relation between two different properties and the expected change in an effective property due to change in a composite phase.

In this dissertation, we quantify non-uniqueness or uncertainty in rock properties primarily by using rigorous ‘bounds’ that use various physics-based schemes (e.g., variational principles, translation, and embedding, among others) to define a range of property values encompassing all possible rock micro-geometries (Hashin & Shtrikman, 1962 [7], 1963 [8], Gibiansky & Torquato, 1996 [9], 1998 [10], Mavko & Saxena, 2013 [11]). In some instances, we use empirical evidence to define ‘narrower’ bounds, corresponding to reduced property uncertainty associated with a subset of composite micro-geometries that we are more likely to encounter in real earth materials. We also use stochastic simulations to study the relationship between rock properties at the micro-scale (\ll scale of measurement/interest) and the magnitude of uncertainty in effective properties at macro-scale (\approx scale of measurement/interest). The composites discussed in this dissertation are assumed to have welded contacts between constituent grains/crystals.

A vast majority of rock physics models produce unique estimates of effective rock properties, of cross-property relations and expected property changes due to phase substitution. The uniqueness of such estimates stems from specific implicit or explicit micro-geometry assumptions made by a given model. For a multi-phase composite with known end member properties and volume fractions, a given effective property can be realized by many different micro-geometries or models. It is important to note that micro-geometries or models that yield the same effective property under a given set of conditions might yield different effective properties when the conditions change.

We demonstrate this using a simple example, in Figure 1.1, using a self-consistent (SC) modeling scheme (Berryman, 1995 [12]). We consider a two-phase composite in its initial state, with the first phase having a conductivity (σ) of 0.1 S/m and a volume fraction of 0.7, the second phase having a conductivity of 5 S/m and a

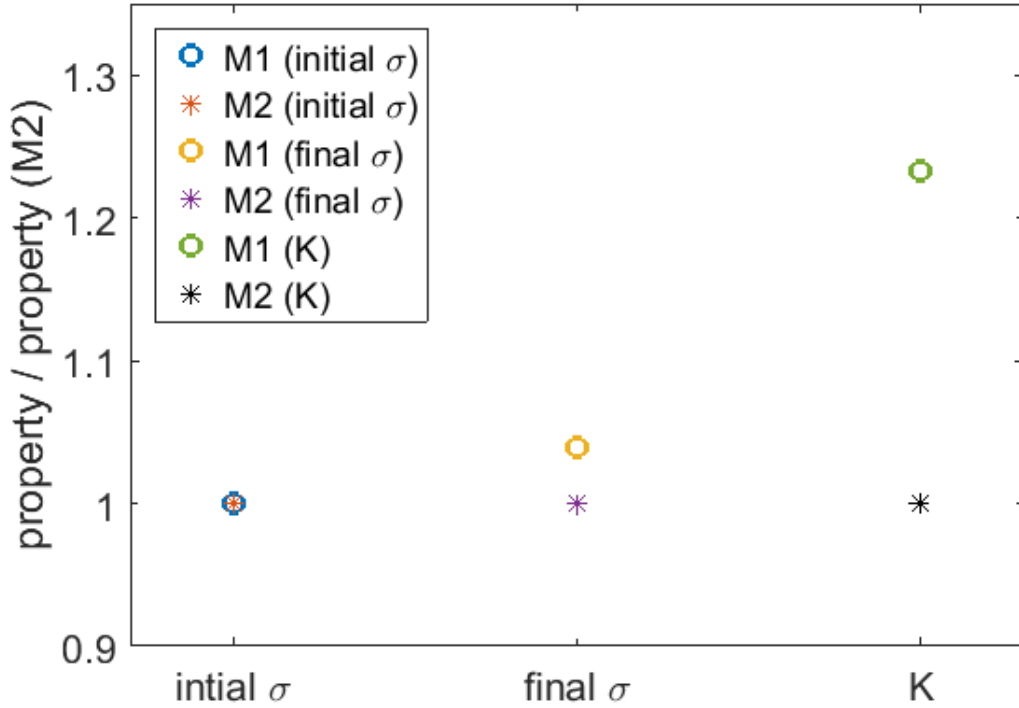


Figure 1.1: SC models M1 and M2, equivalent w.r.t. effective conductivity for the state of ‘initial σ ’, but not equivalent w.r.t. effective conductivity for the state of ‘final σ ’, and not equivalent w.r.t. effective bulk modulus ‘K’. 2 different properties (effective conductivity ‘ σ ’ and bulk modulus ‘K’) are plotted on this figure, each normalized by the corresponding property value for model M2.

volume fraction of 0.3. Further, we consider two SC microgeometries: M1, with the first phase having spherical geometry (aspect ratio ‘AR’ = 1) and the second phase having prolate/needle-like geometry (‘AR’ = 5), and, M2, with the first phase having spherical geometry (aspect ratio ‘AR’ = 1) and the second phase having oblate/crack-like geometry (‘AR’ = 0.2275). In the initial state, and with respect to the property of effective conductivity, M1 and M2 are equivalent, with conductivity = 0.6356 S/m, shown by coincident points corresponding to ‘initial σ ’ in the Figure 1.1. However, if we change the conductivity of the second phase to 15 S/m, while holding the first

phase constant, M1 and M2 have effective conductivity values of 1.484 S/m and 1.427 S/m respectively, shown by non-coincident points corresponding to ‘final σ ’ in the figure. This shows that microgeometries that were equivalent for a given set of end member properties might no longer remain equivalent when one of the end member properties change. Also, if the first phase has bulk and shear moduli of 36 and 45 GPa, and the second phase has bulk (K) and shear moduli of 2.5 and 0 GPa, then the effective bulk moduli of M1 and M2 are 18.13 GPa and 14.70 GPa respectively, shown by non-coincident points corresponding to ‘K’ in the figure. This shows that microgeometries that are equivalent with respect to one physical property (conductivity) can be very different with respect to another (bulk modulus).

1.2 Chapter descriptions

In the second chapter of the dissertation, we study the effect of micro-geometry induced non-uniqueness on the elastic bulk and shear moduli of single phase composites of anisotropic crystals/domains with randomly oriented crystal axes. We reiterate the important and often disregarded fact that a vast majority of the isotropic elastic moduli of minerals reported in the literature are simply some mean of the polycrystal Voigt and Reuss bounds (Voigt, 1908 [13], Reuss 1929 [14]) representing the two extreme boundary conditions of uniform strain and uniform stress, respectively. The true elastic modulus of a poly-crystal is, in fact, non-unique and can lie anywhere between these bounds. The width of the bounds represents uncertainty due to the unknown exact micro-geometry of a composite and increases with increasing anisotropy of the constituent crystals/domains. We explore the relationship between the fractional difference of the poly-crystal elastic bounds at a macro scale and the elastic parameters characterizing the constituent crystals/domains at a micro scale using stochastic simulations on crystal/domains with transverse isotropic symmetry.

We also investigate the impact of grain-shapes in moving the effective elastic moduli between the poly-crystal bounds by developing and using a self-consistent model idealized spheroidal grains.

In the third chapter, we study micro-geometry induced non-uniqueness in the elastic moduli and anisotropy parameters of single phase composites of anisotropic crystals/domains with rotationally symmetric crystal axis alignment. We reiterate the fact that the two most commonly used schemes for determining the effective elastic properties of these composites are in fact the Voigt and Reuss schemes of rotational summation, corresponding to the extreme boundary conditions of uniform strain and uniform stress, respectively. In general, the Voigt and Reuss schemes do not produce equivalent results and the difference represents uncertainty due to the unknown exact micro-geometry of a composite. We use stochastic simulations to study the relationship between macro-scale property uncertainties and micro-scale crystal elastic parameters. We show the impact of the property uncertainty on important formation evaluation parameters such as Vp-Vs ratios and AVO intercepts and gradients. We also show that Thomsen parameter ‘ δ ’ (Thomsen, 1986 [15]) in rotationally symmetric poly-crystal composites attain their highest positive values for states of low (but not completely random) crystal alignment.

In the fourth chapter, we discuss cross-property bounds between the electrical conductivity and bulk modulus of a rock - predicting the range of effective bulk modulus for a known effective conductivity (and vice-versa) and known constituent phase properties, for three dimensional, isotropic, two-phase composites. Rigorous cross-property bounds due to the pioneering work of Gibiansky and Torquato (1996 [9], 1998 [10]) are discussed, wherein a range of effective bulk modulus values can be predicted for a given value of rock conductivity (and vice versa), the inherent non-uniqueness in prediction capturing the uncertainty due to the unknown exact

micro-geometry of a composite. Using digital and laboratory data we propose empirical constraints on Gibiansky and Torquato's rigorous cross-bounds to make them narrower and therefore more useful when dealing with some common reservoir rocks, specifically brine filled sandstones and carbonates. We also discuss the importance of factoring in porosity when using or interpreting cross-property bounds or relations. Finally, we demonstrate the use of constrained cross-bounds to estimate the Archie cementation factor (Archie, 1942 [16]) of a rock when presented with large-scale elastic (e.g., seismic) and electrical (e.g. CSEM) surveys.

The fifth and final chapter discusses the problem of electrical fluid substitution - predicting the change in effective conductivity or dielectric constant of a three dimensional, two-phase, isotropic composite that occurs when one conducting phase is substituted with another while the microgeometry remains fixed. The substitution problem is non-unique. For a given composite, knowing the initial effective conductivity, the phase conductivities, and the porosity permits prediction of only the range of possible effective conductivity values upon change of one or more phase (fluid or solid) conductivities. The precise change depends on details of the composite microstructure, which, as discussed previously, are seldom completely known. Rigorous equations for substitution bounds for two-phase isotropic composites are presented, based on the concept of embedding developed by Mavko and Saxena (2013, [11]). When the conductivity contrast between the composite phases is high, Archie's law (Archie, 1942 [16]) corresponds approximately to the upper bound on the change of conductivity upon substitution. Inclusion modeling suggests that vuggy or poorly-connected pore space could account for conductivity changes smaller than predicted by Archie's law. Comparison of the conductivity substitution bounds with brine-saturated sandstone data with varying clay content reveals that the position of measured data with respect to the conductivity substitution bounds can be indicative of the effective clay content in shaly sand samples.

...

Chapter 2

Elastic properties of isotropic poly-crystals

2.1 Abstract

Single phase composites, also known as poly-crystals, are ubiquitous in nature and amongst engineered materials. Understanding the elastic properties of poly-crystals is, therefore, a problem of fundamental importance in physical sciences. In this chapter, we focus our attention on the elastic properties of randomly oriented crystals or micro-domains that result in isotropic macro-composites or aggregates.

We re-iterate the important and often neglected fact that a vast majority of the isotropic elastic moduli of various minerals reported in the literature are simply some mean of the poly-crystal Voigt and Reuss bounds, representing the two extreme boundary conditions of uniform strain and uniform stress, respectively. The true elastic modulus of a poly-crystal lies somewhere between these bounds. The width of the bounds represent uncertainty due to the unknown exact micro-geometry of a composite and usually increase with increasing anisotropy of the constituent crystals or domains. A tighter set of poly-crystal ‘Hashin-Shtrikman’ bounds can be derived

using variational principles.

We explore the relationship between the fractional difference of the poly-crystal elastic bounds and the elastic parameters characterizing the constituent crystals or domains. Our analyses are based on Monte-Carlo simulations and are applied to domains with transverse isotropic symmetry. We conclude that Thomsen parameter γ of the micro-domains dominates the fractional bound-width for the macro-composite shear modulus. Fractional bound-widths for the bulk modulus and the P-wave modulus of the macro-composite are dominated by micro-domain Thomsen parameters ϵ and γ .

We investigate the impact of grain-shapes in moving us between the poly-crystal bounds on elastic moduli using a self-consistent modeling scheme. Considering spheroidal grains of varying aspect ratios, we conclude that self-consistent estimates of elastic moduli for spherical grain shapes are unique and unaffected by changes in the relative crystal orientation. For non-spherical grain shapes, the exact self-consistent moduli span a range of values depending on the relative angle between the grain axis and crystal lattice, with the range increases with increasing non-sphericity.

Using our understanding of poly-crystal elastic bounds we demonstrate that adding geometric information can help us narrow the bounds on effective elastic moduli. We also test the ‘embedded’ solid substitution bounds on isotropic aggregates of layered laminates and show that laminar aggregates represent an example of poly-crystal microgeometry that can violate the embedded bounds.

Finally, by comparing isotropic elastic moduli of clays from their single-crystal stiffness tensors to some reported experimental values in popular literature, we hypothesize the possibility of unaccounted micro-pores in experimental clay samples.

2.2 Introduction

Single phase composites or poly-crystals, are ubiquitous in nature and amongst engineered materials. Common examples include most commercial metals, alloys, ceramics and ice. In the earth, almost all rocks are poly-crystals, aggregates of a large number of anisotropic crystals/grains. Shales, accounting for more than 75% of sedimentary basins (Hornby et. al., 1994 [17]), are aggregates of a large number of anisotropic clay domains (Bandyopadhyay, 2009 [18]), small regions of locally oriented clay platelets and bound water, representing a poly-domain system analogous to poly-crystals. Understanding the elastic properties of poly-crystals is therefore fundamental in physical sciences. Figure 2.1 shows images of the poly-crystalline nature of some of some common materials.

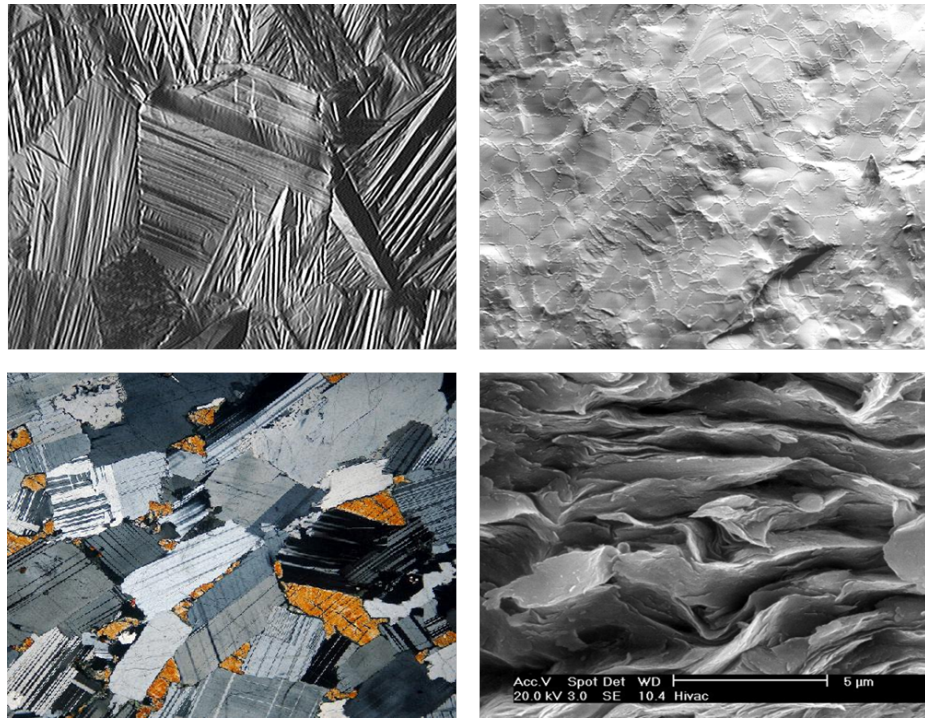


Figure 2.1: Poly-crystalline structure of (top-left) a metal alloy, (top-right) ice, (bottom-left) a multimineralic rock and (bottom-right) a clay sample.

Not unsurprisingly then, elastic properties of poly-crystals have been studied in great detail for a very long time. In this chapter, we focus our attention on the elastic properties of randomly oriented poly-crystals/domains that result in isotropic composites/aggregates. The term ‘isotropic’ implies that the physical properties of the composite do not vary in magnitude based on the direction of measurement. For ‘anisotropic’ crystals on the other hand, physical properties change with measurement direction.

The spatial scales of the crystals/domains are obviously smaller than those of the composites/aggregates. As a reminder of this relative difference in spatial scale, the crystals/domains are often prefixed with the word ‘micro’ while the composites/aggregates are prefixed with the word ‘macro’. The words ‘crystal’ and ‘domain’ are used interchangeably, as are the words ‘composite’ and ‘aggregate’.

Properties of a poly-crystal are dependent on but notably different from those of its constituent crystallites/grains. The initial motivation for the research presented in this chapter was to understand how the isotropic elastic moduli of poly-crystals are related to their constituent single-crystal elastic stiffness tensors, which are most often anisotropic. As a specific example, we wanted to understand how we derived the commonly used 36 GPa bulk modulus and 45 GPa shear modulus values to completely define isotropic quartz when the single quartz crystal is highly anisotropic (trigonal), requiring 6 independent elastic moduli for complete characterization.

A closer look at popular published values for the isotropic moduli of quartz (Mavko et. al., 2009 [19]) revealed two main methods of estimating these values. The first method involves determining the anisotropic stiffness tensor of a single quartz crystal and performing some form of statistical homogenization (detailed in Section 2.3) on it, most popularly, the Hill average (Mason, 1943 [20], Koga et al., 1958 [21], Mc. Skimin, 1965 [22], Anderson and Liebermann, 1966 [23]). The second method involves making measurements on real sandstone samples and backing out the moduli

of isotropic quartz by empirically removing the effect of porosity and/or clay (Han et al., 1986 [24], Blangy, 1992 [25]). Interestingly, the moduli determined from the two approaches are in reasonable agreement, not just in case of quartz, but in case of most poly-crystal aggregates (Hendrix, 1998 [26]). One of our most significant realizations from this preliminary investigation was the well established yet often neglected fact that even single phase isotropic composites have non-unique properties due to the lack of complete information about their complex micro-geometries. This motivated us to further investigate the nature and practical implications of this non-uniqueness, especially in the context of seismic geophysics, representing the main results derived in this chapter.

2.3 Statistical homogenization of crystal properties

2.3.1 Poly-crystal Voigt-Reuss (VR) bounds

One of the most commonly employed methods for determining effective properties of poly-crystals is based on statistically homogenizing the constituent crystal properties (Kube, 2016 [27]), dating back to Voigt, who considered the effective elastic stiffness tensor of a poly-crystal to be equal to the volume average the single-crystal elastic tensor over all possible crystal orientations (Voigt, 1928 [13]). Implicit to Voigt's approach is the assumption of uniform strain throughout the poly-crystal aggregate, satisfying kinematic compatibility at grain boundaries, at the cost of losing static/traction compatibility. This can be understood as follows: suppose a poly-crystal aggregate of a linear elastic material of effective stiffness tensor C^* experiences an overall strain ε^* when subjected to an overall stress σ^* (Note that the generic notation for strains used in this thesis is ' ε ', not to be confused with the

Thomsen parameter with generic notation ‘ ϵ ’). Also suppose a single crystal within the aggregate has stiffness tensor C , experiencing a local strain ε and a local stress σ . According to Hooke’s Law, we can write:

$$\sigma_{ij}^* = C_{ijkl}^* : \varepsilon_{kl}^* \quad (2.1)$$

$$\sigma_{ij} = C_{ijkl} : \varepsilon_{kl} \quad (2.2)$$

Taking a volume average on both sides of Equation 2.2 (denoted by $\langle \rangle$) and considering the fact that the volume average of stresses and strains over individual crystals equal the overall stress and strain in the aggregate, for a case of uniform strain we get:

$$\langle \sigma_{ij} \rangle = \langle C_{ijkl} : \varepsilon_{kl} \rangle \Rightarrow \sigma_{ij}^* = \langle C_{ijkl} : \varepsilon_{kl} \rangle = \langle C_{ijkl} \rangle : \varepsilon_{kl}^* \quad (2.3)$$

Equating Equations 2.1 and 2.3 we can see that the effective elastic stiffness tensor of a poly-crystal equals the volume average of the single-crystal elastic tensor (over all spatial orientations) under the assumption of uniform strain:

$$C_{Voigt}^* = \langle C_{ijkl} \rangle \quad (2.4)$$

Converse to Voigt’s homogenization scheme, Reuss showed that under the assumption of uniform stress within a poly-crystal aggregate the effective elastic compliance tensor ($S^* = [C^*]^{-1}$) of a poly-crystal is equal to the volume average of the single-crystal compliance tensor S over all possible crystal orientations (Reuss, 1929 [14]). This approach satisfies static/traction compatibility at the cost of kinematic compatibility at grain boundaries. As in case of the Voigt approach, this can be understood as follows:

$$\varepsilon_{ij} = S_{ijkl} : \sigma_{kl} \Rightarrow \langle \varepsilon_{ij} \rangle = \langle S_{ijkl} : \sigma_{kl} \rangle \Rightarrow \varepsilon_{ij}^* = \langle S_{ijkl} : \sigma_{kl}^* \rangle \quad (2.5)$$

Equation 2.5 implies:

$$C_{Reuss}^* = [S_{Reuss}^*]^{-1} = \langle S_{ijkl} \rangle^{-1} \quad (2.6)$$

The true effective stiffness of a poly-crystal (C_{True}^*) obviously satisfies both static and kinematic compatibility conditions. Hill showed that the Voigt and Reuss estimates of the effective stiffness formed bounds on this true value (Hill, 1952 [28]):

$$C_{Voigt}^* \geq C_{True}^* \geq C_{Reuss}^* \quad (2.7)$$

Equation 2.7 implies that the eigenvalues of the true effective stiffness tensor are always less than or equal to the corresponding eigenvalues of the Voigt effective tensor and greater than or equal to those of the Reuss effective tensor. An isotropic material has two independent eigenvalues: $3K$ and $2G$, where K and G represent the bulk and shear modulus of the material respectively. Hence, for isotropic poly-crystals, Equation 2.7 can be restated as:

$$K_{Voigt}^* \geq K_{True}^* \geq K_{Reuss}^* \quad (2.8)$$

$$G_{Voigt}^* \geq G_{True}^* \geq G_{Reuss}^* \quad (2.9)$$

Corresponding estimates of Young's modulus E and Poisson's ratio ν can be determined by substituting the appropriate value of K and G into Equations 2.11 and 2.10. Note that while the inequality $E_{Voigt}^* \geq E_{True}^* \geq E_{Reuss}^*$ holds, the same is not true of the Poisson's ratio.

$$\frac{1}{E} = \frac{1}{3G} + \frac{1}{9K} \quad (2.10)$$

$$\nu = \frac{1}{2} \left[1 - \frac{3G}{3K + G} \right] \quad (2.11)$$

For the special case when lattice-orientations within a poly-crystal are completely random, resulting in an isotropic composite, the Voigt and Reuss estimates of the poly-crystal bulk and shear moduli are given by the closed form expressions, as in Equations 2.12 - 2.15. The poly-crystal Voigt and Reuss bounds are also sometimes referred to as the angular Voigt and Reuss bounds in this thesis.

$$9K_{Voigt} = (C_{11} + C_{22} + C_{33}) + 2(C_{12} + C_{23} + C_{31}) \quad (2.12)$$

$$15G_{Voigt} = (C_{11} + C_{22} + C_{33}) - (C_{12} + C_{23} + C_{31}) + 3(C_{44} + C_{55} + C_{66}) \quad (2.13)$$

$$\frac{1}{K_{Reuss}} = (S_{11} + S_{22} + S_{33}) + 2(S_{12} + S_{23} + S_{31}) \quad (2.14)$$

$$\frac{15}{G_{Reuss}} = 4(S_{11} + S_{22} + S_{33}) - 4(S_{12} + S_{23} + S_{31}) + 3(S_{44} + S_{55} + S_{66}) \quad (2.15)$$

In Equations 2.12 - 2.15 C_{ij} 's and S_{ij} 's are the 2-subscript Voigt notation representation (not to be confused with the Voigt tensor) of the original 4-subscript crystal stiffness and compliance tensors respectively. It is interesting to note that of the 21 possible independent stiffness tensor components (in case of the most general crystal structure), only 9 appear in the expressions for isotropic Voigt moduli. Similarly, only

9 of 21 possible compliance tensor components appear in the expressions for isotropic Reuss moduli. The Voigt and Reuss moduli considered together, however, encompass all 21 tensor components.

2.3.2 Poly-crystal Voigt-Reuss-Hill (VRH) estimate

While the true poly-crystal moduli may lie anywhere between the Voigt-Reuss bounds, Hill observed that measured values of elastic moduli fall almost mid-way between the Voigt and Reuss estimates, and suggested that empirically, an arithmetic or geometric average of the two extreme values would be a good approximation to the true poly-crystal moduli (Hill, 1952 [28]). This gave rise to what is popularly known as the poly-crystal Voigt-Reuss-Hill (VRH) average (Chung, 1963 [29]), expressed simply as the arithmetic mean of the Voigt and Reuss estimates of moduli, as in Equations 2.16 and 2.17.

$$K_{Hill} = \frac{K_{Voigt} + K_{Reuss}}{2} \quad (2.16)$$

$$G_{Hill} = \frac{G_{Voigt} + G_{Reuss}}{2} \quad (2.17)$$

Since all elements in an isotropic stiffness tensor are linear combinations of the bulk and shear moduli, the stiffness tensor corresponding to the Hill moduli is actually the arithmetic mean of the Voigt and Reuss poly-crystal stiffness tensors, often known as the VRH average tensor, and also referred to as the ‘Average Tensor’ in Chapter 3 of this thesis. The concept of the VRH tensor becomes more relevant when we move on to the case of poly-crystals that are not oriented randomly, giving rise to anisotropic composites, as we shall see in the Chapter 3.

2.3.3 Poly-crystal Hashin-Shtrikman (HS) bounds

When no geometrical or statistical details are known about the micro-geometry of a poly-crystal, the best possible bounds are ones on the average elastic behavior, expressed solely in terms of the single crystal elastic stiffnesses, as in the case of Voigt-Reuss bounds (Watt, 1979 [30]). Using variational principles, Hashin and Shtrikman developed tighter bounds for isotropic poly-crystal aggregates, originally applied to poly-crystals of cubic symmetry (Hashin and Shtrikman, 1962, [31], [7]).

The poly-crystal Hashin-Shtrikman (HS) bounds are based on limits of elastic energy deviations from a reference isotropic state, and the optimal bounds are extremal values in regimes where the residual elastic tensor, defined as the difference between the actual anisotropic moduli and moduli of a reference isotropic material, is either positive definite or negative definite (Brown, 2015 [32]). The HS optimal bounds always lie within the Voigt-Reuss (VR) bounds, and are often significantly tighter than them (Watt, 1979 [30]).

Empirical evidence suggests that measurements of elastic properties of composites with randomly oriented crystals lie within HS bounds (Watt et al., 1976 [33], Brown et al., 2016 [34]). According to Watt, the HashinShtrikman optimal bounds are the tightest possible constraints for a poly-crystal aggregate without microstructural details such as the shape and size distributions of the constituent crystals. Isotropic HS bounds for low symmetry crystals do not lend themselves to closed form analytical expressions, necessitating iterative numerical solutions (Watt, 1980 [35], Brown, 2015 [32], Kube, 2016 [27]). The HS bound calculations used in this chapter primarily follow Brown's method.

2.3.4 Voigt-Reuss & Hashin-Shtrikman bounds and Hill estimates for some common minerals

As mentioned in the previous section, the HS bounds lie within and are often significantly tighter than the VR bounds. Although the actual moduli may lie anywhere between the bounds, in practice, VRH averages have been widely used as approximations of the unknown exact poly-crystal moduli. The VRH averages frequently lie within the tighter HS bounds, as is evident from Table 2.1, showing calculations for some common minerals encountered in earth sciences, with mineral properties as per the Rock Physics Handbook (Mavko et al., 2009 [19]).

Watt (Watt et al., 1976 [33]) presented examples of a number of poly-crystals for which this is not true. According to Watt, ideally, the mean of the HS bounds is a more appropriate approximation than the VRH average. However, due to the significantly simpler computation of the VRH averages, and their accuracy being sufficient for many practical cases (Hendrix, 1998 [26]) even when compared with many theoretically complex models, the VRH averages remain the most common approximation to isotropic poly-crystal moduli.

Table 2.1 shows that for the minerals considered, in each case, the HS bounds are tighter than the VR bounds and contain the Hill estimate. The ‘reported’ values from various journal publications are in close agreement with the VRH values, and upon closer examination, are often VRH estimates from single crystal stiffness tensors. It is useful to note that for domains exhibiting cubic symmetry, the isotropic bulk moduli from the two bounding techniques are the same, but the shear moduli are different. In other words, poly-crystals of cubic symmetry have a unique bulk modulus, but the same does not hold true for their shear modulus values.

Figure 2.2 shows the normalized bulk and shear modulus values for each phase in Table 2.1, scaled such that in each case, the Voigt and Reuss moduli range between

Table 2.1: Estimates of isotropic poly-crystal bulk ('K') and shear ('G') moduli for some common minerals, expressed in units of GPa. 'HS+' and 'HS-' represent the upper and lower poly-crystal HS bounds respectively. For reference, the phase bulk moduli are also reported in g/cc.

Phase	Voigt	Reuss	HS+	HS-	Hill	Reported	Density
Pyrite (Cubic)	K: 142.73 G: 128.6	142.73 122.74	142.7 126.2	142.7 124.9	142.7 125.7	142.7 125.7	4.93
Halite (Cubic)	K: 24.9 G: 14.94	24.9 14.51	24.89 14.76	24.9 14.69	24.9 14.72	24.9 14.7	2.16
Ice (Hexagonal)	K: 8.72 G: 3.44	8.72 3.36	8.72 3.4	8.72 3.4	8.72 3.4	8.73 3.4	0.92
Ulms shale (Hexagonal)	K: 25.53 G: 7.54	22.45 5.72	24.45 6.83	23.67 6.38	23.99 6.63	** **	
Calcite (Trigonal)	K: 76.02 G: 36.8	70.59 27.13	74.35 32.84	72.99 30.38	73.3 31.96	73.3 32	2.71
-quartz (Trigonal)	K: 38.12 G: 47.6	37.56 40.98	37.88 44.6	37.78 43.44	37.84 44.29	37.8 44.3	2.65
Dolomite (Trigonal)	K: 99.4 G: 51.8	90.3 39.67	96.14 46.9	93.94 43.97	94.85 45.73	94.9 45.7	2.84
Aragonite (Orthorhombic)	K: 49.04 G: 40.48	44.78 36.76	47.02 38.94	46.08 38.11	46.91 38.62	46.9 38.5	2.93
Albite (Monoclinic)	K: 60.55 G: 30.93	52.83 27.19	57.52 29.47	55.6 28.64	56.69 29.06	56.9 28.6	2.6
Anorthite (Monoclinic)	K: 89 G: 43	79.24 37.24	85.68 40.76	83.24 39.33	84.12 40.12	84.2 39.9	2.75

0 and 10, and all other moduli estimates are scaled accordingly. The sub-figure for bulk modulus does not show the first three phases as these phases have a unique bulk modulus value. The figure once again reveals that the HS bounds are significantly narrower than the VR bounds, and that the Hill estimates, though within the HS bounds in these examples, are variably positioned inside the HS bounds. It is interesting to note that in case of the normalized shear modulus values, the Hill estimate is, in general, closer to the upper HS bound.

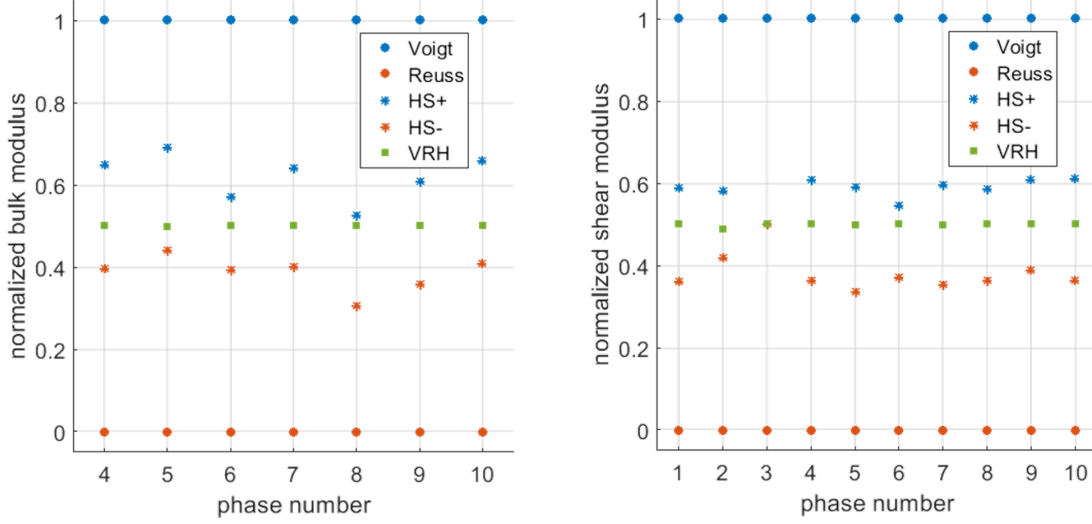


Figure 2.2: Normalized bulk and shear modulus values for each phase in Table 2.1, scaled such that in each case, the Voigt and Reuss moduli range between 0 and 1, and all other moduli estimates are scaled accordingly.

2.3.5 Tensor isotropic projections and poly-crystal Voigt-Reuss estimates

Finding the elastic stiffness tensor of a specific symmetry closest to that of a lower symmetry is a problem of interest in many fields and has been well studied (Fedorov, 1968 [36], Helbig, 1996 [37], Browaeys and Chevrot, 2004 [38], Dellinger, 2005 [39], Moakher and Norris, 2006 [40], Norris, 2006 [41]; Caro, 2014 [42]). The closest tensor of greater symmetry can provide a simpler approximation to the original tensor as demonstrated in Section 2.5.2.2, or can be useful in filtering out lower symmetry tensor components introduced by measurement errors/computational approximations. The basic process of tensor projection involves minimizing some metric of distance between the original tensor and its higher symmetry projection. A commonly used distance metric is the Euclidean distance ' d_E ', given by Equation 2.18, and a convenient implementation of the corresponding projection system was developed by Caro

(Caro, 2014 [42]), involving a simple matrix multiplication, as in equation 2.19.

$$d_E(C_1, C_2) = \|C_1 - C_2\| \quad (2.18)$$

$$X_{sym} = PX \quad (2.19)$$

In equation 2.19, X_{sym} and X are elastic stiffness/compliance tensors expressed as a vector of length 21, related to their Kelvin notation tensor components as given by Equation 2.20 ('T' superscript representing transpose) and P is a 21x21 matrix projector (Browaeys and Chevrot, 2004 [38]). For isotropic or rotation invariant projections, $P = P_{iso}$ is given by Equations 2.21 & 2.22.

$$\begin{aligned} X = (c_{11}, c_{22}, c_{33}, \sqrt{2}c_{23}, \sqrt{2}c_{13}, \sqrt{2}c_{12}, c_{44}, c_{55}, c_{66}, \sqrt{2}c_{14}, \sqrt{2}c_{25}, \sqrt{2}c_{36}, \sqrt{2}c_{34}, \sqrt{2}c_{15}, \\ \sqrt{2}c_{26}, \sqrt{2}c_{24}, \sqrt{2}c_{35}, \sqrt{2}c_{16}, \sqrt{2}c_{56}, \sqrt{2}c_{46}, \sqrt{2}c_{45})^T \end{aligned} \quad (2.20)$$

$$P_{iso} = \begin{bmatrix} M_{iso} & 0_{9 \times 12} \\ 0_{12 \times 9} & 0_{12 \times 12} \end{bmatrix} \quad (2.21)$$

$$M_{iso} = \begin{bmatrix} 3/15 & 3/15 & 3/15 & \sqrt{2}/15 & \sqrt{2}/15 & \sqrt{2}/15 & 2/15 & 2/15 & 2/15 \\ 3/15 & 3/15 & 3/15 & \sqrt{2}/15 & \sqrt{2}/15 & \sqrt{2}/15 & 2/15 & 2/15 & 2/15 \\ 3/15 & 3/15 & 3/15 & \sqrt{2}/15 & \sqrt{2}/15 & \sqrt{2}/15 & 2/15 & 2/15 & 2/15 \\ \sqrt{2}/15 & \sqrt{2}/15 & \sqrt{2}/15 & 4/15 & 4/15 & 4/15 & -\sqrt{2}/15 & -\sqrt{2}/15 & -\sqrt{2}/15 \\ \sqrt{2}/15 & \sqrt{2}/15 & \sqrt{2}/15 & 4/15 & 4/15 & 4/15 & -\sqrt{2}/15 & -\sqrt{2}/15 & -\sqrt{2}/15 \\ \sqrt{2}/15 & \sqrt{2}/15 & \sqrt{2}/15 & 4/15 & 4/15 & 4/15 & -\sqrt{2}/15 & -\sqrt{2}/15 & -\sqrt{2}/15 \\ 2/15 & 2/15 & 2/15 & -\sqrt{2}/15 & -\sqrt{2}/15 & -\sqrt{2}/15 & 1/15 & 1/15 & 1/15 \\ 2/15 & 2/15 & 2/15 & -\sqrt{2}/15 & -\sqrt{2}/15 & -\sqrt{2}/15 & 1/15 & 1/15 & 1/15 \\ 2/15 & 2/15 & 2/15 & -\sqrt{2}/15 & -\sqrt{2}/15 & -\sqrt{2}/15 & 1/15 & 1/15 & 1/15 \end{bmatrix} \quad (2.22)$$

The isotropic tensor projections resulting from minimizing the Euclidean distance relative to the original tensor of lower symmetry as described above are equivalent to those using Torquato's (Torquato, 2002 [43]) projection tensors. According to Torquato, the isotropic part of any stiffness/compliance tensor (C_{iso}) can be expressed in terms of projection tensors Λ_h and Λ_s , as given by Equations 2.23 - 2.25.

$$C_{iso} = 3K\Lambda_h + 2\mu\Lambda_s \quad (2.23)$$

$$\begin{aligned} (\Lambda_h)_{ijkl} &= \frac{1}{3}\delta_{ij}\delta_{kl} \\ (\Lambda_s)_{ijkl} &= \frac{1}{2}[\delta_{ik}\delta_{jl} + \delta_{il}\delta_{jk}] - \frac{1}{3}\delta_{ij}\delta_{kl} \end{aligned} \quad (2.24)$$

$$\begin{aligned} 3K &= (C : \Lambda_h) / ||\Lambda_h||^2 = \frac{1}{3}C_{iijj} \\ 2\mu &= (C : \Lambda_s) / ||\Lambda_s||^2 = C_{ijij} - \frac{2}{3}C_{iijj} \end{aligned} \quad (2.25)$$

We found that tensor isotropic projections starting with the stiffness tensor are exactly equal to the poly-crystal isotropic Voigt estimate. Conversely, projections starting with the compliance tensor are exactly equal to the poly-crystal Reuss estimate. Hence $C_{iso} \neq (S_{iso})^{-1}$, where $S = C^{-1}$. This is in line with the fact that the Euclidean distance between two tensors is not necessarily equal to that between their inverses (Mavko, new book). Extending this to general Euclidean tensor projections would mean that projections done using the stiffness tensor are ‘Voigt’-like, while projections done using compliance tensors are ‘Reuss’-like.

2.4 Physical significance of bounds and measures of universal anisotropy

The difference between the Voigt-Reuss estimates or the Hashin-Shtrikman bounds represent the uncertainty due to the unknown exact micro-geometry of a composite as demonstrated in Figure 2.3 . The figure shows schematically three poly-crystals with the same (approximately) lattice orientations but significantly different micro-geometries that could lead to significantly different elastic properties. Obviously, when the micro-scale domains are isotropic, the VR/HS estimates of both the bulk and shear moduli of the composite are equivalent irrespective of micro-geometry. As the anisotropy of the micro-domains increase, the VR/HS estimates of the poly-crystal elastic moduli move progressively apart.

In fact the difference between the Voigt and Reuss estimates of elastic moduli of poly-crystals is often used as a crystal symmetry-independent measure of anisotropy. This is different from the traditional measure of anisotropy used in seismic geophysics as proposed by Thomsen (Thomsen, 1986 [15]) for weak anisotropy in VTI materials, extended to orthotropic materials by Tsvankin (Tsvankin, 1997 [44]). A popular

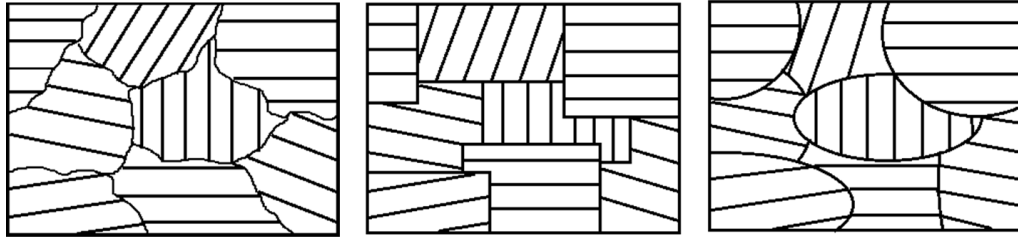


Figure 2.3: Schematic showing three poly-crystals with approximately the same lattice orientations but significantly different microgeometries that could lead to significantly different elastic properties.

measure of universal anisotropy is the Chung-Buessem anisotropy index (Chung and Buessem, 1967 [45]) which uses the difference in the Voigt-Reuss shear moduli estimates to quantify a crystal symmetry independent measure of elastic anisotropy, as shown in Equation 2.26, where G^V and G^R are the Voigt and Reuss estimates of the shear modulus, respectively.

$$A^C = \frac{G^V - G^R}{G^V + G^R} \quad (2.26)$$

A recent, more generalized measure of universal elastic anisotropy defines the anisotropy index as given in Equation 2.27 (Ranganathan and Ostoja-Starzewski, 2008 [46]). Both the measures are identically zero for isotropic materials, as expected.

$$A^U = 5\frac{G^V}{G^R} + \frac{K^V}{K^R} - 6 \quad (2.27)$$

2.5 Relationship between isotropic bound-widths and crystal parameters

In previous sections of this chapter we have seen that the elastic moduli of isotropic aggregates of anisotropic crystals/domains are non-unique due to lack of our knowledge

of the exact aggregate micro-geometry. In this section we explore how the fractional bound-widths (representing the magnitude of non-uniqueness) for the elastic moduli of an isotropic aggregate are impacted by the elastic parameters characterizing the constituent micro-domains/crystals, focusing on domains with transverse isotropic symmetry. The Voigt-Reuss fractional bound widths for bulk, shear and P-wave moduli of poly-crystals have been termed ‘ dfk ’, ‘ dfg ’ and ‘ dfp ’ respectively, and are defined as per the system of equations given by 2.28.

$$\begin{aligned} dfk &= \frac{(K^V - K^R)}{K^R}; \quad dfg = \frac{(G^V - G^R)}{G^R} \\ dfp &= \frac{(P^V - P^R)}{P^R} = \frac{(K^V + \frac{4}{3}G^V) - (K^R + \frac{4}{3}G^R)}{K^R + \frac{4}{3}G^R} \end{aligned} \quad (2.28)$$

2.5.1 Characterizing domains with transverse isotropic symmetry

Materials exhibiting transverse isotropy (TI) are of special interest in geophysics. Layered and fractured rocks are common examples of TI media, depicted schematically in Figure 2.4. The physical properties of a transversely isotropic material are symmetric about an axis that is normal to the plane of isotropy. Within this transverse plane the material properties are isotropic, that is they are the same in all directions. TI materials require 5 distinct elastic parameters to be specified for complete characterization.

For the exercises in this chapter we consider a TI domain with a vertical symmetry axis (VTI) and based on physical relevance choose the following 5 distinct (but not orthogonal) elastic parameters to characterize it: stiffness moduli C_{33} and C_{44} , and Thomsen parameters epsilon (ϵ), gamma (γ) and delta (δ). C_{33} and C_{44} are related

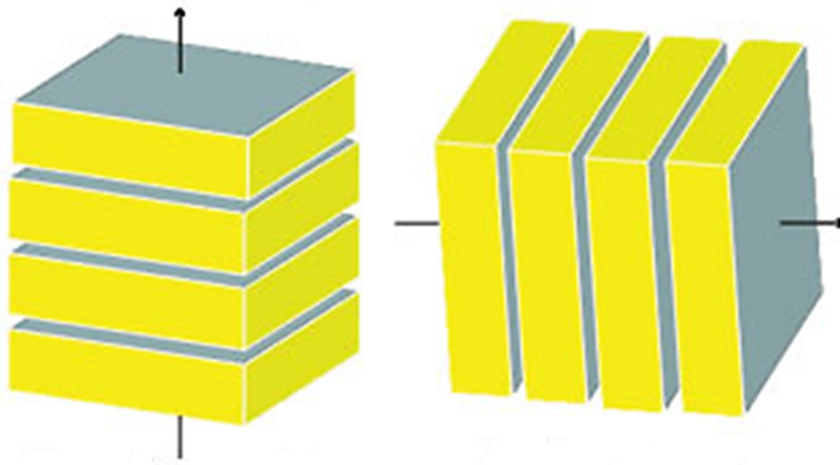


Figure 2.4: Schematic representation of layered/fractured TI media, the arrows representing the axes of symmetry and the corresponding transverse planes being isotropic. The material on the left has a vertical symmetry axis (VTI).

to the vertical P-wave (V_p) and S-wave (V_s) velocities, the most commonly measured elastic logs in geophysics, as per Equations 2.29 and 2.30, where ρ is the bulk density of the composite.

$$V_p = \sqrt{\frac{C_{33}}{\rho}} \quad (2.29)$$

$$V_s = \sqrt{\frac{C_{44}}{\rho}} \quad (2.30)$$

The dimensionless Thomsen parameters ϵ , γ and δ quantify weak anisotropy in transverse isotropic (TI) materials (Thomsen, 1986 [15]). For a TI material with a vertical symmetry axis (X3) the Thomsen parameters are given by Equations 2.31 - 2.33. ϵ is the P-wave anisotropy parameter, representing fractional difference between vertical and horizontal P-wave velocities. γ is the S-wave anisotropy parameter, representing fractional difference between the vertical S-wave velocity and the horizontally polarized horizontal S-wave velocity. δ represents a short offset effect, capturing

the relationship between the NMO velocity and the zero-offset velocity recorded by check-shots (Rajput and Thakur, 2016 [47]).

$$\epsilon = \frac{C_{11} - C_{33}}{2C_{33}} \quad (2.31)$$

$$\gamma = \frac{C_{66} - C_{44}}{2C_{44}} \quad (2.32)$$

$$\delta = \frac{(C_{13} + C_{44})^2 - (C_{33} - C_{44})^2}{2C_{33}(C_{33} - C_{44})} \quad (2.33)$$

2.5.2 Monte-Carlo simulations

Analytical expressions for differences in Voigt-Reuss estimates of composites with VTI micro-domains are intricate, coupled and highly non-linear functions of all 5 elastic constants of the constituent domains. In addition, the relative impact of the domain parameters on the fractional bound-widths depend on the parameters themselves. Hence, to understand the general impact of the domain elastic parameters on the fractional bound-widths of the composite, we use numerical Monte-Carlo simulations.

This means that we randomly generate many samples of the five domain parameters (subject to constraints mentioned in 2.5.2.1 and 2.5.2.2), run them through the forward model (Equations 2.12-2.15 & 2.28) to generate the fractional bound-widths dfg , dfk and dfp as outputs, and then compare all of the outputs and inputs simultaneously to understand the global nature of their inter-relationship.

We start by uniformly sampling the 5 domain elastic constants within ranges seen in commonly encountered earth materials. Accordingly, we vary C_{33} and C_{44} between 0 and 150 GPa, ϵ and γ between -0.2 and 3 and δ between -0.5 and 1. However, not every combination of the 5 elastic constants can represent realistic micro-domains, and they need to be vetted based on appropriate constraints.

2.5.2.1 General constraints

Energy considerations mandate that a linear isotropic material with transverse isotropic symmetry satisfy the conditions in Equation 2.34 (Mavko et al., 2009 [19]). These are the first two constrains on the Monte-Carlo samples.

$$C_{11} > |C_{12}|; \quad (C_{11} + C_{12})C_{33} > 2C_{13}^2 \quad (2.34)$$

Ruling out cases where C_{13} is imaginary and considering the fact that the vertical P-wave velocity is usually always greater than the vertical S-wave velocity, we add two additional constraints (Equation 2.35) to our simulation samples.

$$\text{imaginary}(C_{13}) = 0; \quad C_{33} > C_{44} \quad (2.35)$$

2.5.2.2 Constraints based on TI projections of common minerals

Table 2.2 lists the 5 TI elastic parameters and the corresponding values of dfk , dfg and dfp for some minerals/domains of interest in earth science applications. Note that not all minerals/domains listed here are originally of transverse isotropic symmetry. Those that are less symmetric than TI have been projected onto the TI space using the methods outlined by Browaeys and Chevrot (Browaeys and Chevrot, 2004 [38]), discussed in an appendix at the end of the chapter. The original mineral symmetries are listed in Table 2.2. The original mineral/domain properties for the hexagonal phases in the table or those used for TI projection for phases of lower symmetry are from the handbook (Mavko et al., 2009 [19]), except for Ulm's shale (Ortega et al., 2007 [48]). As is evident from the table, our chosen range for the domain parameters hold well for these common minerals, except for the extreme C_{33} value of graphite.

Table 2.2 lists out the TI constants for a variety of minerals/domains from various

Table 2.2: TI elastic parameters and corresponding values of dfk , dfg and dfp for some minerals/domains of interest in earth science applications. Domains less symmetric than TI originally have been projected onto the TI space.

Phase name	Original symmetry	C33	C44	eps	gam	del	dfk	dfg	dfp
α -quartz	trigonal	106.10	57.80	-0.09	-0.15	0.26	0.01	0.03	0.03
muscovite	monoclinic	59.00	17.00	1.06	1.54	-0.03	0.39	0.54	0.45
illite	hexagonal	55.00	11.70	1.14	2.49	-0.25	0.43	0.93	0.63
dolomite	trigonal	113.00	39.80	0.41	0.34	0.25	0.10	0.08	0.09
Ulm's shale	hexagonal	24.20	3.70	0.43	1.07	0.06	0.14	0.32	0.18
calcite	trigonal	84.00	33.50	0.36	0.17	0.54	0.08	0.06	0.07
aragonite	orthogonal	85.00	33.50	0.23	0.14	-0.10	0.07	0.04	0.05
albite	monoclinic	128.00	23.50	-0.10	0.19	-0.28	0.01	0.05	0.03
anorthite	monoclinic	156.00	32.00	0.02	0.21	-0.24	0.01	0.06	0.03
graphite	hexagonal	283.40	66.10	1.37	3.02	-0.11	0.45	1.11	0.71
ice (270K)	hexagonal	14.70	2.96	-0.03	0.07	-0.19	0.00	0.03	0.01

symmetry classes, including ones that are known to be extremely anisotropic, such as graphite. Yet the fractional difference between the Voigt-Reuss moduli of the domains never attain very extreme values, usually being less than 1. Accordingly, we impose three additional constraints on the Monte-Carlo simulations as per Equation 2.36.

$$dfk \leq 1; \quad dfg \leq 1.5; \quad dfp \leq 1 \quad (2.36)$$

2.5.2.3 Final simulation inputs

Figure 2.5 shows the histograms and pair-wise cross-plots of the final VTI parameters from one realization of about 42,500 Monte-Carlo samples, subject to the seven constraints discussed above. We use these simulated samples to forward model the corresponding fractional differences between the predicted Voigt and Reuss moduli of the macro-aggregate and study their relationship with the micro-domain VTI parameters. The mineral/domains reported in Table 2.2 show some degree of positive

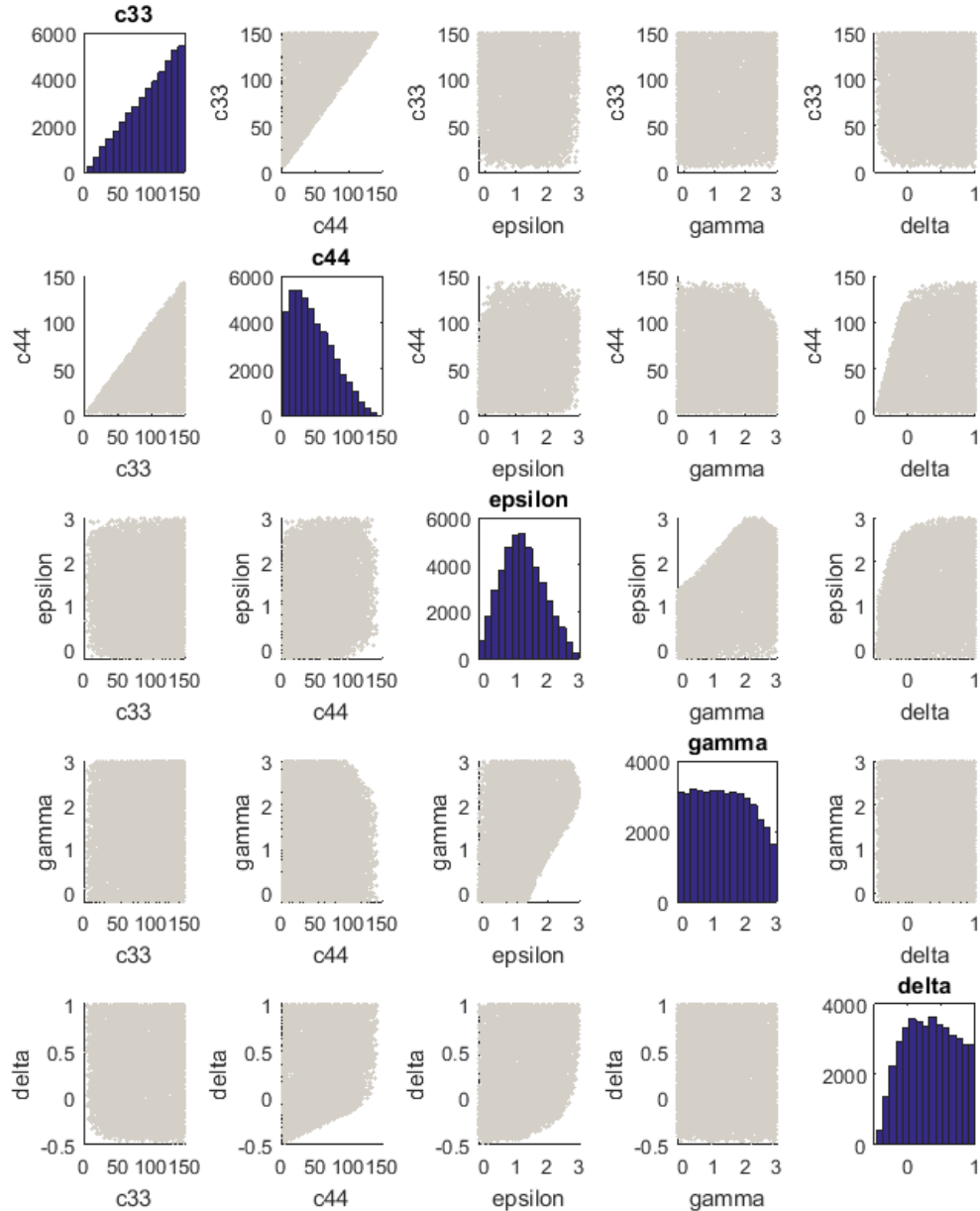


Figure 2.5: Histograms and pair-wise cross-plots of the 5 distinct, but not orthogonal VTI micro-domain parameters from Monte-Carlo simulations, subject to constraints given by Equations 2.34 to 2.36.

correlation between the Thomsen parameters ϵ and γ , not been explicitly modeled in our simulations.

2.5.3 Analysis using cross plots

Figure 2.6 shows the variation of fractional difference between the Voigt and Reuss estimates of the effective shear modulus (from Monte-Carlo simulations) with the VTI domain constants using 2D cross-plots. On each sub-figure, the median line and the 10th, 25th, 75th and 90th percentile lines are drawn. It is obvious from the figure that even though all 5 domain constants vary randomly in the simulations (subject to the constraints stated above), the fractional difference between the Voigt and Reuss estimates of the effective shear modulus (dfg) shows the tightest correlation with domain Thomsen parameter γ and that correlation is positive. Hence we can say that, γ dominates the shear modulus spread which, in general, increases with increasing γ . The simulations also reveal that, for the range of inputs considered, the minimum fractional difference in the shear estimates scales almost linearly with γ and somewhat non-linearly with ϵ , as is evident from Figure 2.6.

Figure 2.7 shows the variation of fractional difference between Voigt and Reuss estimates of the effective bulk modulus (dfk) with VTI domain constants. It is evident from the figure that the bulk modulus spread is most correlated with domain Thomsen parameter ϵ though the correlation is not nearly as strong as that between dfg and γ . This correlation is also positive on an average, meaning the bulk modulus spread generally which increases with increasing ϵ . At the higher end of their ranges, C_{44} and γ also seem to have increased impact over dfk , demonstrated by the narrowing of the percentile lines.

Figure 2.8 shows the variation of fractional difference between Voigt and Reuss estimates of the effective P-wave modulus (dfp), from Monte-Carlo simulations, with

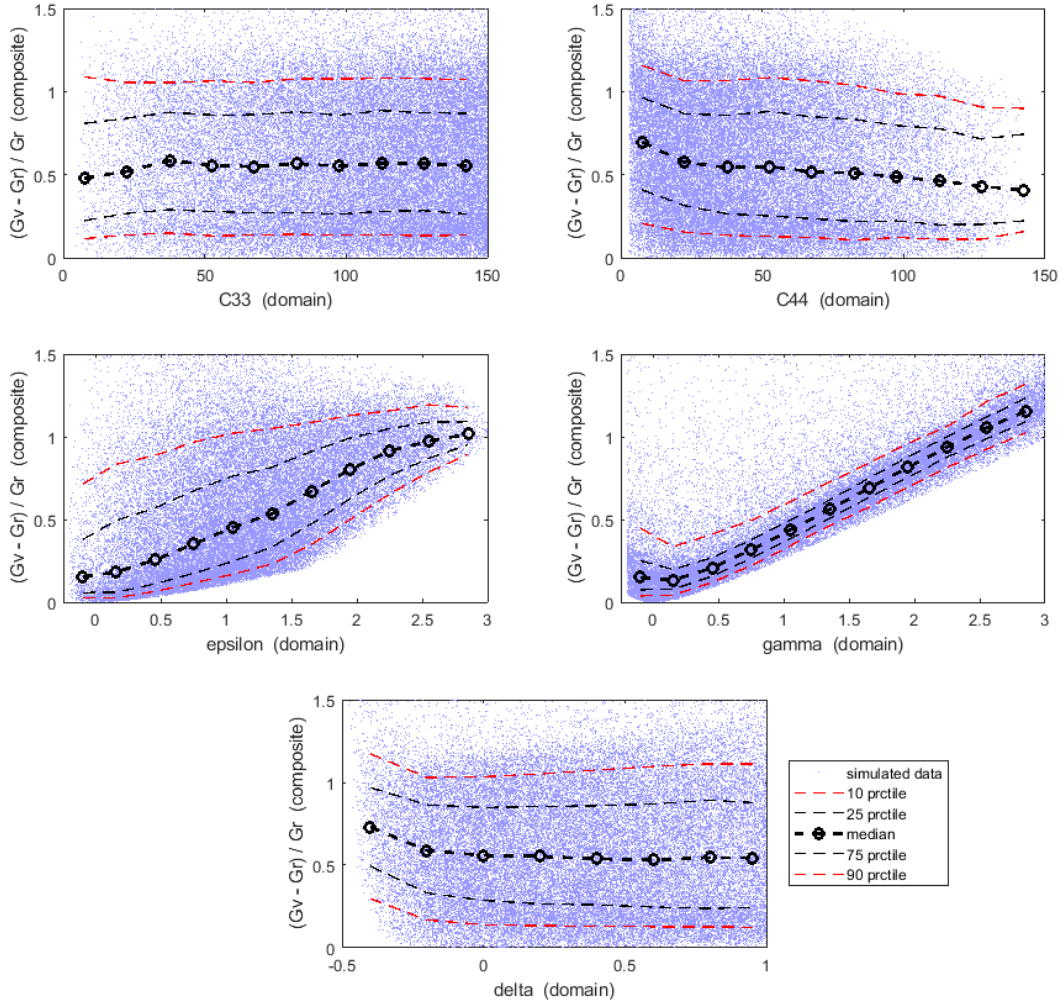


Figure 2.6: Variation of fractional difference between the Voigt and Reuss estimates of the effective shear modulus (G_{dfg}) with the VTI micro-domain constants. Monte-Carlo simulations reveal that Thomsen parameter γ dominates the shear modulus spread, which in general, increases with increasing γ .

VTI domain constants. The figure shows that domain Thomsen parameter ϵ dominates the P-wave modulus spread, which, on an average, increases with increasing ϵ . The control of ϵ on the P-modulus spread seems stronger than that over bulk

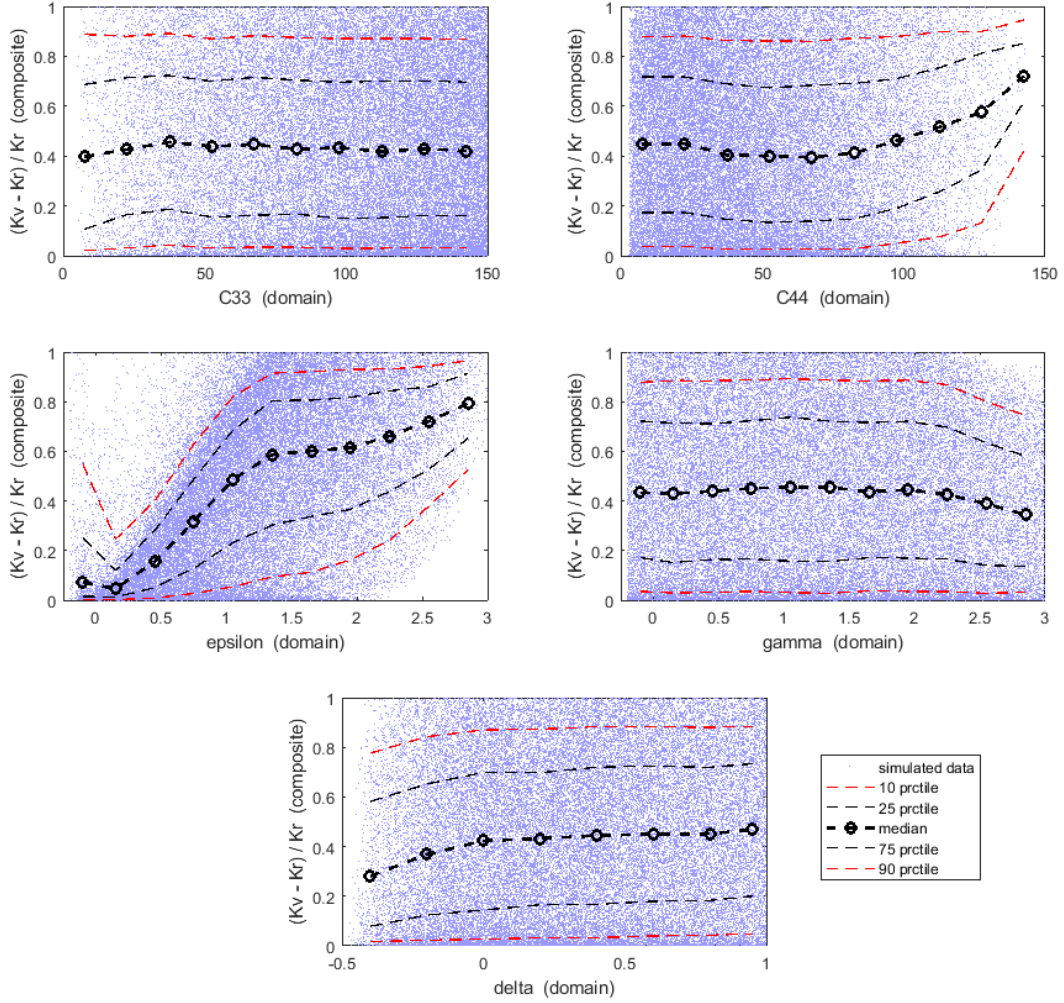


Figure 2.7: Variation of fractional difference between the Voigt and Reuss estimates of the effective bulk modulus (dfk) with the VTI micro-domain constants. Monte-Carlo simulations reveal that Thomsen parameter ϵ dominates the bulk modulus spread, which in general, increases with increasing ϵ . The control of ϵ on the bulk-modulus spread is not as strong as that of γ on the shear modulus spread.

modulus, but not as strong as that of γ over dfg . Of the other domain parameters, γ seems to also have some influence on dfp . The simulations reveal that for the

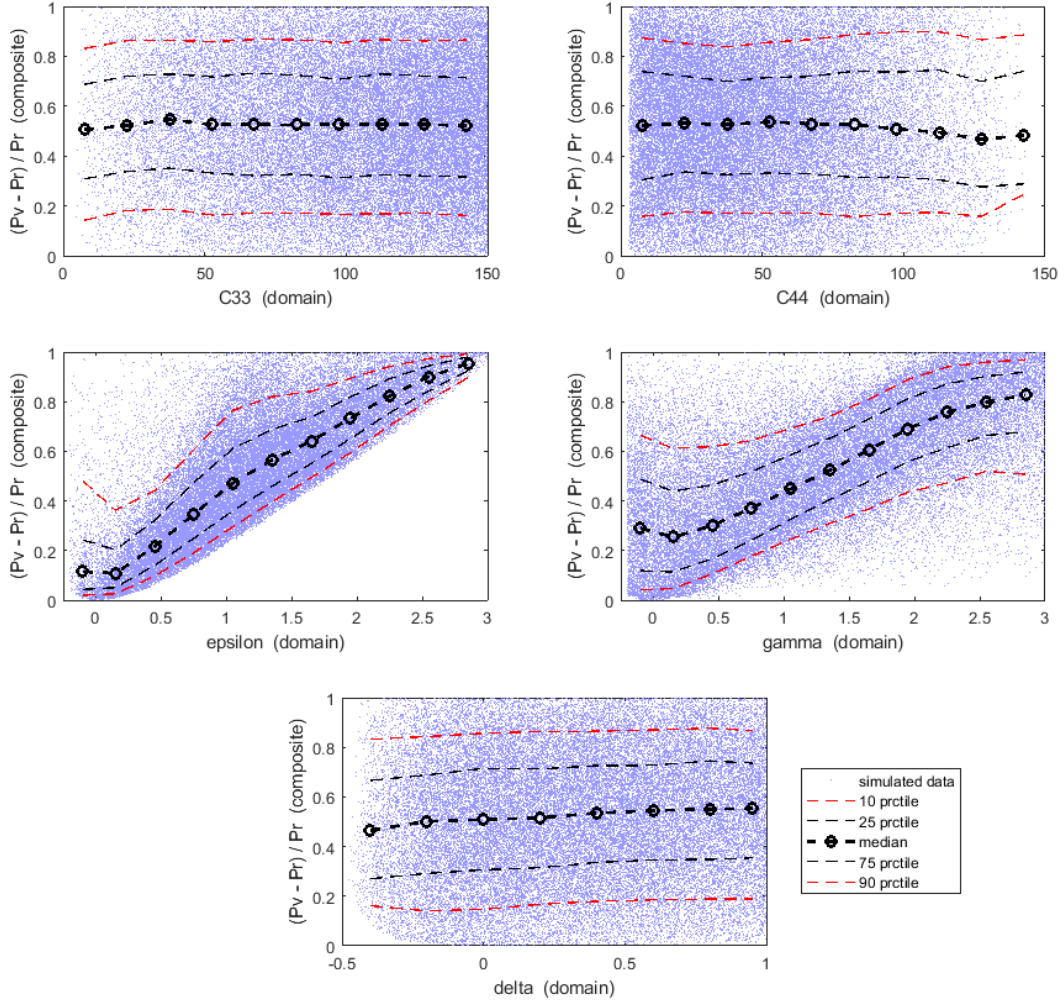


Figure 2.8: Variation of fractional difference between the Voigt and Reuss estimates of the effective P-wave modulus (dfp) with the VTI micro-domain constants. Monte-Carlo simulations reveal that Thomsen parameter ϵ dominates the P-wave modulus spread, which in general, increases with increasing ϵ . The minimum fractional difference in the P-wave modulus estimates scales almost linearly with ϵ

range of inputs considered, the minimum fractional difference in the P-wave modulus estimates scales almost linearly with ϵ (Figure 2.8).

2.5.4 Analysis using Gradient Boosting Machines (GBM)

In the previous sub-section we investigated how fractional VR bound-widths of isotropic aggregates are impacted by elastic parameters of the constituent micro-domains by qualitatively exploring our Monte-Carlo simulations using at cross-plots and quantile lines. In this sub-section we attempt to quantify our understanding by exploring our simulations with a powerful statistical learning tool called Gradient Boosting Machines, or more popularly, GBM. The basic idea here is to build a statistical meta-model that is a good fit to our simulation data and extract measures of variable importance from the meta-model using sophisticated open-source tools.

2.5.4.1 Primer on Gradient Boosting Machines (GBM)

Gradient Boosting Machines (Breiman, 1997 [49], Freidman, 1999 [50] [51], Mason et al., 2000 [52]) represent a powerful machine learning technique wherein a robust statistical meta-model or surrogate model is built to fit the training data, which in our case is the output from the constrained Monte-Carlo simulations. The term meta-model means model of a model, signifying that the statistical model is an approximation of the poly-crystal VR model that we have set out to study. The GBM model is built iteratively; at each iteration the focus is building a model (usually a ‘tree’) that fits the error (squared error with the true model in our specific case) from the previous iteration, until some convergence criterion is satisfied (Friedman et al., 2001 [53]). The final model is the sum of all the iterative models. GBM is especially good at handling highly coupled, non-linear data efficiently, which makes it a good choice for our current investigation.

‘Trees’ (Brieman, 1984 [54]) are learning models that, very simply put, optimally partition the training input space (simulations C_{33} , C_{44} , ϵ , γ and δ in our case) and within each partition, assign a constant output (dfg or dfk or dfp in our case) equal

to the average of the output samples within the partition, such that the overall error with the true model is minimized. For gradient boosted trees, we can conveniently compute the ‘relative influence’ of each input variable in predicting an output based on the maximum improvement in squared error due to a partition along that input variable, averaged over all partitions in a tree, and further averaged over all trees in a boosted ensemble (Friedman et al., 2001 [53]). The relative influence measures are conveniently scaled to add up to 100, and we use these values to quantify the relative impact/influence of the domain elastic parameters on the fractional VR bound-widths.

2.5.4.2 Inferences using Gradient Boosting Machines

To quantify the importance of each of the 5 micro-domain elastic parameters on the composite shear modulus spread, we use the ‘relative influence’ values from a gradient boosted (GBM) meta-model of the shear modulus spread (dfg), as shown in Figure 2.9 (top, left). The sub-figure shows the ‘relative influence’ values (of the micro-domain elastic parameters) from the GBM meta-model (adding up to a total of 100%) for the shear modulus spread (dfg), indicating that the micro-domain γ (abbreviated as ‘*gam*’ in the sub-figure) is the elastic parameter with the biggest influence on dfg , as was qualitatively observed with Figure 2.6. The top right sub-figure is a QC for the GBM meta-model, with the dfg predicted by the meta-model (labeled ‘pred.gbm’) plotted against the true dfg (labeled ‘test\$dfg’) in a blind test-set data, showing relatively good match between the modeled and true data, with a mean-absolute-error (MAE) of 0.025. The black line shows the ideal ‘predicted = observed’ trend.

To further understand the nature of variation of composite ‘ dfg ’ with variation in values of the two domain parameters of maximum relative influence, the bottom panel of Figure 2.9 shows a two-way partial dependence plot of ‘ dfg ’ (plot color) with γ (x-axis, labeled as ‘*gam*’) and δ (y-axis, labeled as ‘*del*’). Partial dependence plots show the dependence between a target response (dfg in this case) and a set of target

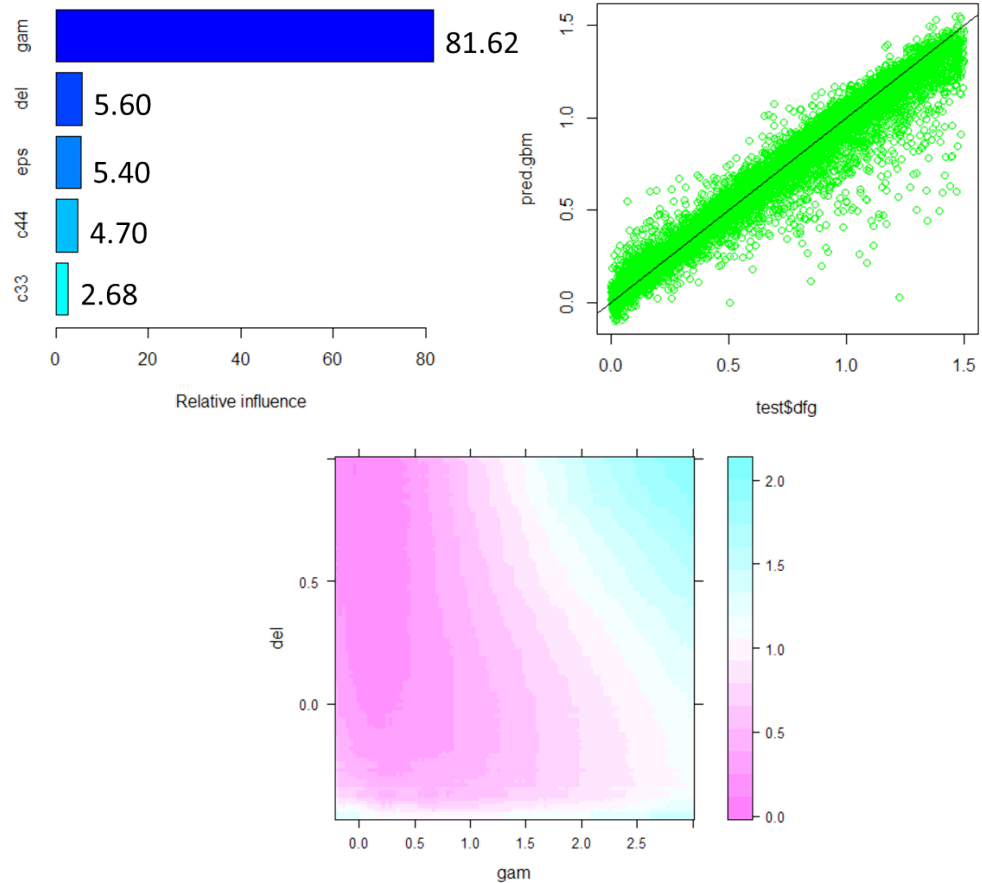


Figure 2.9: Top, left: ‘Relative influence’ values from a gradient boosted meta-model for the shear modulus spread (dfg), indicating that the micro-domain γ (labeled ‘ gam ’) is the elastic parameter with biggest influence on dfg ; Top, right: dfg predicted by the GBM meta-model against the true dfg in a blind test-set data, showing good match between the modeled and true data, with a mean-absolute-error (MAE) of 0.025; Bottom: Two-way partial dependence plot of ‘ dfg ’ (plot color) with γ (x-axis, labeled as ‘ gam ’) and δ (y-axis, labeled as ‘ del ’).

variables (γ and δ in this case), marginalizing over the values of all other variables (the ‘complement’ variables). It shows that the largest positive values of composite ‘ dfg ’ occur for high values of domain parameter γ (> 2.5) combined with high values of δ (> 0.75). For relatively low values of domain γ , composite dfg remains consistently

low (< 0.3) except at highly negative values of domain δ (< -0.4).

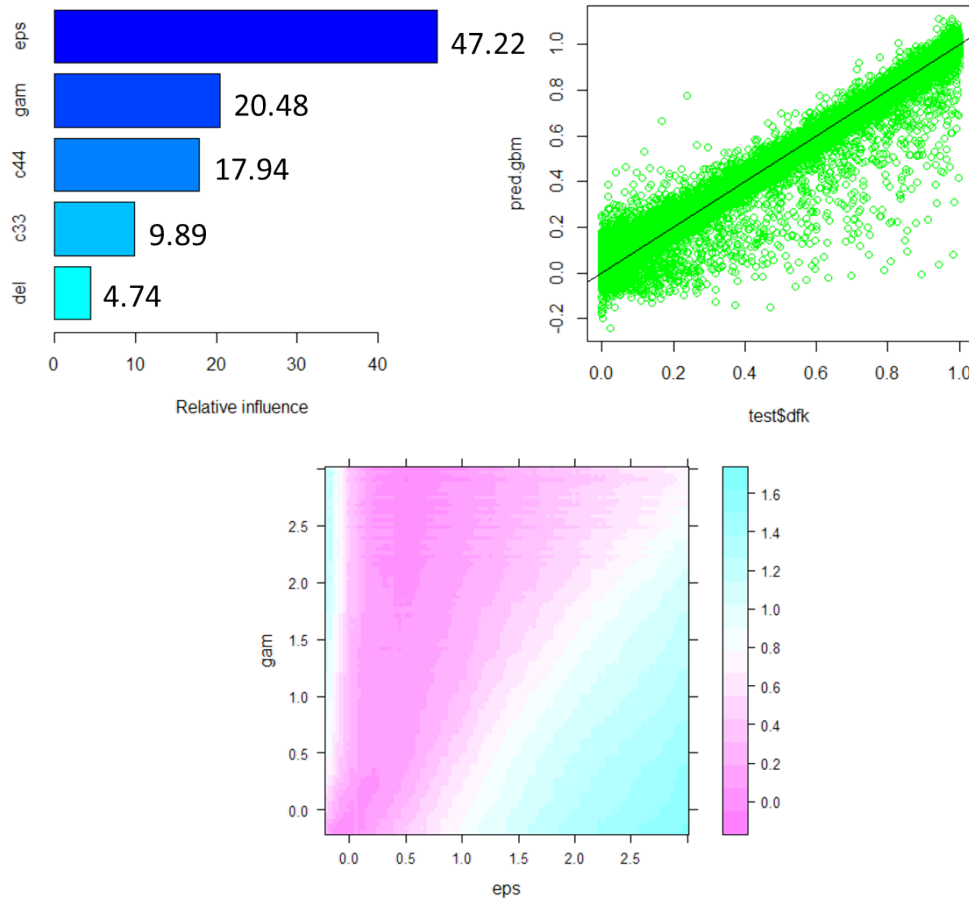


Figure 2.10: Top, left: ‘Relative influence’ values from a gradient boosted meta-model for the bulk modulus spread (dfg), indicating that the micro-domain γ is the elastic parameter with the biggest influence on dfg ; Top, right: dfk predicted by the GBM meta-model against the true dfk in a blind test-set data, showing good match between the modeled and true data, with a mean-absolute-error (MAE) of 0.034. Bottom: Two-way partial dependence plot of ‘ dfk ’ (plot color) with ϵ (x-axis, labeled as ‘ eps ’) and γ (y-axis, labeled as ‘ gam ’).

Figure 2.10 (top, left) shows the relative influence values of the domain elastic

parameters on the composite fractional bulk modulus spread ‘ dfk ’ from a GBM meta-model. The sub-figure shows that the domain parameter with the highest relative influence on dfk is ϵ though its influence value is only about 4/7 that of γ on dfg . γ and C_{44} are the domain parameters with second and third highest relative influences on dfk . The top right sub-figure is a QC for the GBM meta-model for dfk showing relatively good match between the predicted and true test-set dfk values, with a mean-absolute error of 0.034. The bottom panel of Figure 2.10 shows a two-way partial dependence plot of ‘ dfk ’ (plot color) with ϵ (x-axis, labeled as ‘eps’) and γ (y-axis, labeled as ‘gam’). It shows that the largest positive values of composite ‘ dfk ’ occur for high values of domain parameter ϵ (> 2.5) combined with low values of γ (< 0.25). For low positive values of domain ϵ (0 - 0.5), composite dfk remains consistently low (< 0.2).

Figure 2.11 (top, left) shows the relative influence values of the domain elastic parameters on the composite fractional bulk modulus spread ‘ dfp ’ from a GBM meta-model. The sub-figure shows that the domain parameter with the highest relative influence on dfp is ϵ with an influence value of 61.75, lying in-between that of γ on dfg and ϵ on dfk . γ is the other domain parameter with some influences on dfp . The top right sub-figure is a QC for the GBM meta-model for dfp showing relatively good match between the predicted and true test-set dfp values, with a mean-absolute error of 0.025. The bottom panel of Figure 2.11 shows a two-way partial dependence plot of ‘ dfp ’ (plot color) with ϵ (x-axis, labeled as ‘eps’) and γ (y-axis, labeled as ‘gam’). It shows that the largest positive values of composite ‘ dfp ’ occur for negative values of domain parameter ϵ (> 2.5) combined with high values of γ (> 2.5). The lowest values of composite dfp occur for low values of domain ϵ (< 0.5) combined with low values of γ (< 0.5).

It is important to note that in our case, the GBM relative influence values correspond to the reduction of squared error attributable to each variable (Friedman,

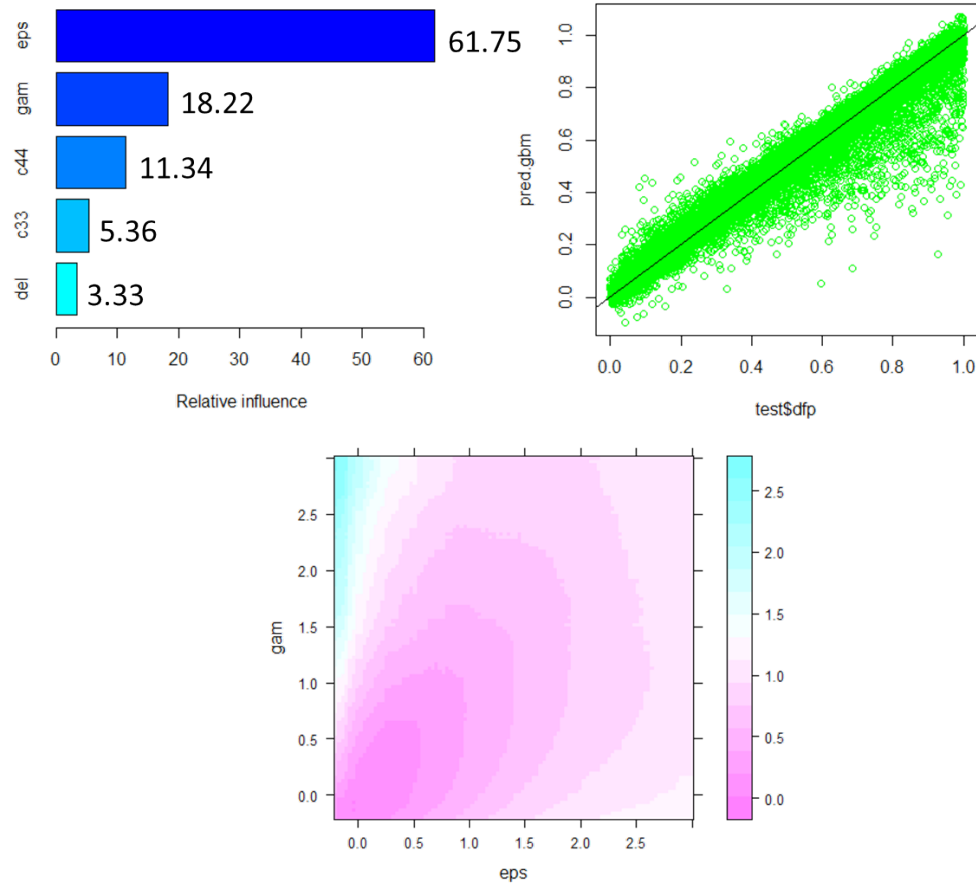


Figure 2.11: Left: ‘Relative influence’ values from a gradient boosted meta-model for the P-wave modulus spread (dfp), indicating that the micro-domain ϵ is the elastic parameter with biggest influence on dfp ; Right: dfp predicted by the GBM meta-model against the true dfp in a blind test-set data, showing good match between the modeled and true data, with a mean-absolute-error (MAE) of 0.025. Bottom: Two-way partial dependence plot of ‘ dfp ’ (plot color) with ϵ (x-axis, labeled as ‘ ϵ ’) and γ (y-axis, labeled as ‘ γ ’).

2001 [50]), normalized to sum up to 100. The values reported here correspond to one specific realization of the training and test datasets, and are likely to vary slightly for a different realization, without altering any of our primary inferences. In addition, expressing the impact of a specific micro-domain elastic parameter on the macro-scale

elastic modulus spread in terms of GBM relative influence values is one of many ways of quantifying what we qualitatively observe from the cross-plots in sub-section 2.5.3. Relative influence values from our analysis align well with our observations in 2.5.3. The simple method outlined in this sub-section is convenient and effective due to free and easy access to sophisticated statistical learning packages in recent times, and can be a useful first-pass analysis on measured/synthetic datasets.

2.5.5 Trends for some common minerals

Figure 2.12 shows plots of composite dfg , dfk and dfp against domain parameters ($C_{33}, C_{44}, \epsilon, \gamma, \delta$) for the transverse isotropic phases listed in Table 2.2.

The general inferences made earlier in the earlier section about the relationships between the mciro-domain elastic parameters and the macro-composite fractional Voigt-Reuss differences hold well for these eleven domains. The consistent positive correlation between composite parameters dfg , dfk and dfp and domain parameters ϵ and γ contrasts strongly against the more random variations between the composite and domain parameters in the other three cases.

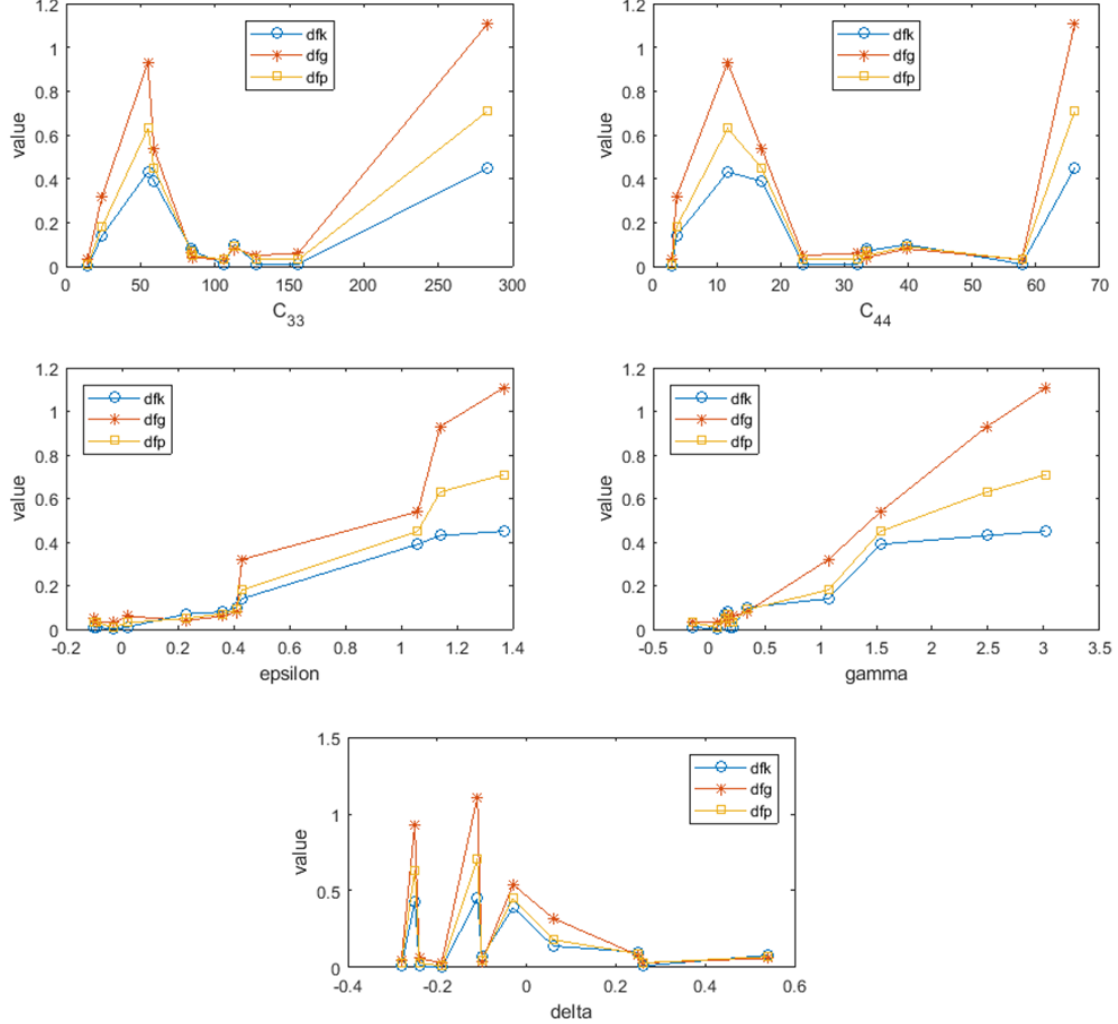


Figure 2.12: Composite dfg , dfk and dfp against domain parameters ($C_{33}, C_{44}, \epsilon, \gamma, \delta$) for the eleven transverse isotropic phases listed in Table 2.2. The consistent positive correlation between composite parameters dfg , dfk and dfp and domain parameters ϵ and γ contrasts strongly against the more random variations between the composite and domain parameters in the other three cases.

2.5.6 Analysis of poly-crystal Hashin-Shtrikman bounds

In the absence of generalized analytical expressions, to understand how poly-crystal Hashin-Shtrikman bounds are affected by the micro-domain/crystal properties, we

once again use Monte-Carlo simulations, with inputs already vetted from the VR analysis. Not unexpectedly, the correlations of the fractional difference of the upper and lower HS bounds with the micro-domain properties are quite similar to those in case of the Voigt-Reuss bounds discussed in the previous sections.

As an example, Figure 2.13 shows the variation of fractional difference between the upper and lower H-S bounds of the effective shear modulus (from Monte-Carlo simulations) with the VTI domain constants. On each sub-figure, the median line and the 10th, 25th, 75th and 90th percentile lines are drawn. It is obvious from the figure that even though all 5 domain constants vary randomly in the simulations, the fractional difference between the upper and lower H-S bounds of the effective shear modulus shows the tightest correlation with domain Thomsen parameter γ ; that correlation is positive. Hence, as in the VR case, domain parameter γ dominates the composite shear modulus spread which, in general, increases with increasing γ . The simulations also reveal that, for the range of inputs considered, the minimum fractional difference in the shear estimates scales almost linearly with γ and non-linearly with ϵ .

Figures 2.14 - 2.16 show results of GBM analysis on Monte-Carlo samples for fractional difference in poly-crystal HS bounds for shear modulus ($dfg2 = (G_{HS+} - G_{HS-})/G_{HS-}$), bulk modulus ($dfk2 = (K_{HS+} - K_{HS-})/K_{HS-}$), and P-wave modulus ($dfp2 = (P_{HS+} - P_{HS-})/P_{HS-}$) respectively.

In Figure 2.14, the left sub-figure shows the GBM-derived relative influence of domain parameters ($C_{33}, C_{44}, \epsilon, \gamma, \delta$ labeled as ‘c33’, ‘c44’, ‘eps’, ‘gam’, ‘del’ respectively) in predicting the composite HS shear modulus spread ‘ $dfg2$ ’. Similar to the VR analysis results, domain parameter γ dominates the composite $dfg2$. The right sub-figure shows a two-way partial dependence plot of ‘ $dfg2$ ’ (plot color) with γ (x-axis) and δ (y-axis). It shows that the largest positive values of composite ‘ $dfg2$ ’ occur for high values of domain parameter γ (> 2.5) combined with high values of δ

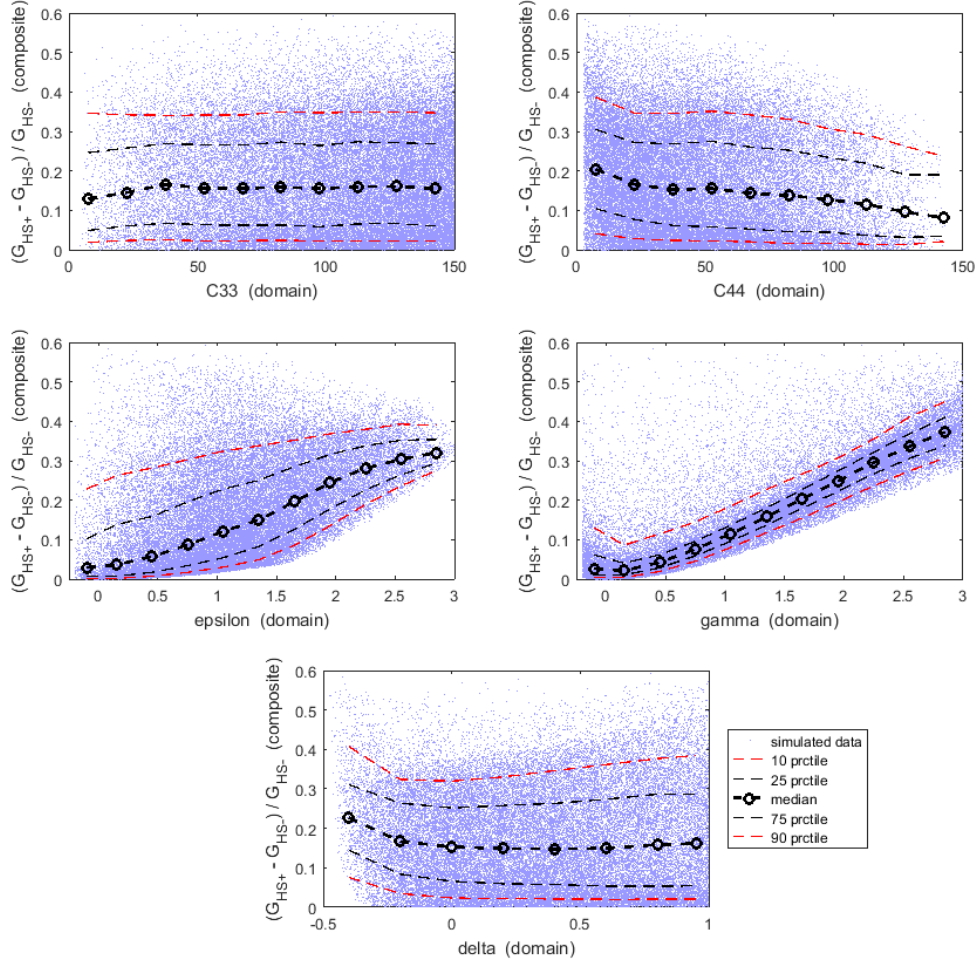


Figure 2.13: Variation of fractional difference between the HS estimates of the effective shear modulus of macro-composite (dfg) with the VTI micro-domain constants. Monte-Carlo simulations reveal that domain parameter γ dominates the composite HS shear modulus spread, which in general, increases with increasing γ .

(> 0.75). For low values of domain parameter γ (< 0.5) composite $dfg2$ is consistently low (< 0.2) except at highly negative values of δ (< -0.4).

Similarly, in Figure 2.15, the left sub-figure shows that domain parameter ϵ dominates the composite HS bulk modulus spread ‘ $dfk2$ ’. The right sub-figure shows a

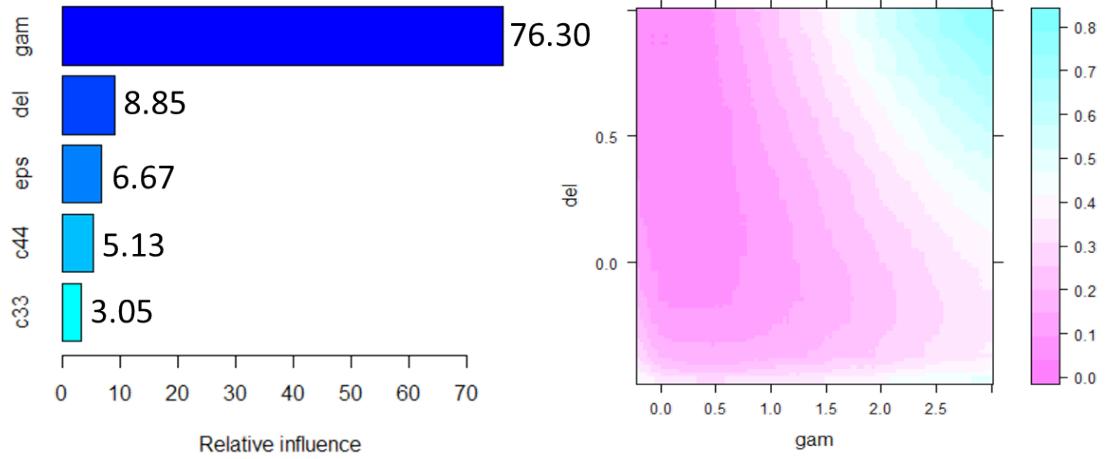


Figure 2.14: Left: ‘Relative influence’ values from a gradient boosted meta-model of the composite HS shear modulus spread ($dfg2$), indicating that the micro-domain γ (labeled ‘gam’) is the elastic parameter with biggest influence on $dfg2$; Right: Two-way partial dependence plot of composite ‘ $dfg2$ ’ (plot color) with domain parameters γ (x-axis, labeled as ‘gam’) and δ (y-axis, labeled as ‘del’).

two-way partial dependence plot of $dfk2$ (plot color) with ϵ (x-axis) and C_{44} (y-axis). It shows that the largest positive values of composite ‘ $dfk2$ ’ occur for high values of domain parameter ϵ (> 2.5) combined with low values of C_{44} (< 15 GPa). Low values of domain parameter ϵ (< 0.5) combined with low values of C_{44} (< 25 GPa) lead to low values of composite $dfk2$.

Finally, in Figure 2.16, the left sub-figure shows that domain parameter γ dominates the composite HS P-wave modulus spread ‘ $dfp2$ ’, closely followed by domain parameter ϵ . The right sub-figure shows a two-way partial dependence plot of $dfp2$ (plot color) with γ (x-axis) and ϵ (y-axis). It shows that the largest positive values of composite ‘ $dfp2$ ’ occur for high values of domain parameter γ (> 2.5) combined with low/negative values of ϵ (< 0). Low values of domain parameter γ ($< .25$) combined with low values of ϵ ($< .5$) lead to low values of composite $dfp2$ (< 0.1).

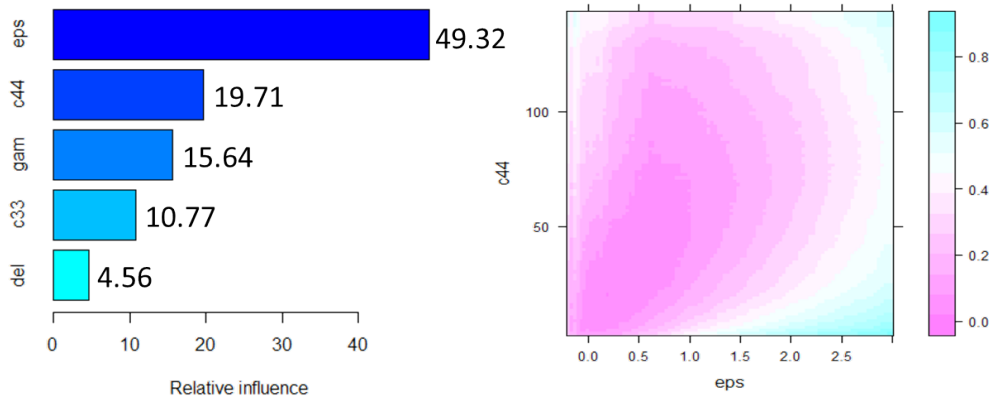


Figure 2.15: Left: ‘Relative influence’ values from a gradient boosted meta-model of the composite HS bulk modulus spread ($dfk2$), indicating that the micro-domain ϵ (labeled ‘eps’) is the elastic parameter with biggest influence on $dfk2$; Right: Two-way partial dependence plot of composite ‘ $dfk2$ ’ (plot color) with domain parameters ϵ (x-axis, labeled as ‘eps’) and C_{44} (y-axis, labeled as ‘ $c44$ ’).

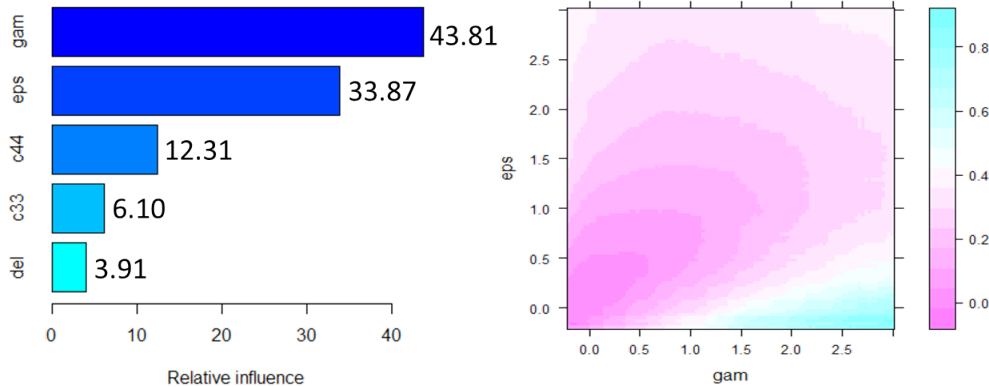


Figure 2.16: Left: ‘Relative influence’ values from a gradient boosted meta-model of the composite HS P-wave modulus spread ($dfp2$), indicating that the micro-domain γ (labeled ‘gam’) is the elastic parameter with biggest influence on $dfp2$, closely followed by micro-domain ϵ (labeled ‘eps’); Right: Two-way partial dependence plot of composite ‘ $dfp2$ ’ (plot color) with domain parameters γ (x-axis) and ϵ (y-axis).

2.6 What moves us between the bounds

We move between the poly-crystal elastic bounds based on the micro-structure of the poly-crystal, i.e., the distribution of crystal orientations and crystal grain shapes. To study the impact of crystal grain shapes on the isotropic moduli of a poly-crystal aggregate, we have developed a self-consistent model, based on Kröner's (Kröner, 1958 [55]) method of modeling each crystal in the aggregate as an inclusion embedded in a uniform isotropic matrix. The most general version of this problem is mathematically complex, so for the purpose of our analysis we make the simplifying assumption of holding the relative angle between a crystal grain and its lattice orientation constant.

2.6.1 Derivation of a self-consistent framework

Suppose $\bar{\sigma}$ and $\bar{\epsilon}$ represent the average stress and the average strain in a poly-crystal aggregate. Then, by definition, the effective elastic stiffness tensor of the aggregate C^* is given by Equation 2.37 as:

$$\bar{\sigma} = C^* : \bar{\epsilon} \implies \bar{\sigma}_{ij} = C_{ijkl}^* : \bar{\epsilon}_{kl} \quad (2.37)$$

Suppose each inclusion phase in this problem is represented by crystals having the same orientation ' Ω ' (relative to a reference orientation) in space, and suppose $\bar{\sigma}^\Omega$ and $\bar{\epsilon}^\Omega$ represent the average stress and the average strain in a given inclusion phase of fractional volume x^Ω such that $\sum_\Omega x^\Omega = 1$. Suppose in the global co-ordinate system, the stiffness tensor of this phase is C^Ω . Then we can say that:

$$\bar{\sigma} = \sum_\Omega x^\Omega \bar{\sigma}^\Omega = \sum_\Omega x^\Omega C^\Omega \bar{\epsilon}^\Omega = \sum_\Omega x^\Omega C^\Omega T^{(\Omega)} \bar{\epsilon} \quad (2.38)$$

In Equation 2.38 $T^{(\Omega)}$ is the strain concentration tensor associated with crystals having orientation (Ω) in space, and is related to the corresponding Eshelby tensor

S^Ω (Eshelby, 1957 [56]) as per Equation 2.39. The strain concentration tensor for a given phase (orientation, in this case) in a composite relates the average strain in that phase ($\bar{\epsilon}^\Omega$) to the overall strain in the composite ($\bar{\epsilon}$). while C^Ω and S^Ω are simply the rotated versions of reference tensors C and S , $T^{(\Omega)}$ at this point is not simply a rotation of the reference tensor T , indicated by the additional brackets around its superscript.

$$T^{(\Omega)} = [I + S^\Omega : C*^{-1} : (C^\Omega - C*)]^{-1} \quad (2.39)$$

In Equation 2.38, C^Ω related to the stiffness tensor C in the lattice/local co-ordinate system by Equation 2.40:

$$C_{ijkl}^\Omega = Q_{pi}Q_{qj}Q_{rk}Q_{sl}C_{pqrs} \quad (2.40)$$

In Equation 2.40 Q_{pi} represent elements of the rotation matrix given by Equation 2.41. (ψ, θ, ϕ) are the Euler angles associated with the solid angle Ω defined so that they map the global co-ordinate system to the local crystallographic axes. As per usual convention, θ varies between 0 & π while ψ and ϕ vary between 0 & 2π .

$$Q = \begin{bmatrix} \cos(\psi)\cos\phi - \sin(\psi)\sin(\phi)\cos(\theta) & \sin(\psi)\cos\phi + \cos(\psi)\sin(\phi)\cos(\theta) & \sin(\phi)\sin(\theta) \\ -\cos(\psi)\sin\phi - \sin(\psi)\cos(\phi)\cos(\theta) & -\sin(\psi)\sin(\phi) + \cos(\psi)\cos(\phi)\cos(\theta) & \cos(\phi)\sin(\theta) \\ \sin(\psi)\sin(\theta) & -\cos(\psi)\sin(\theta) & \cos(\theta) \end{bmatrix} \quad (2.41)$$

By comparing Equations 2.37 and 2.38 we can derive our primary self consistent formulation as:

$$\sum_\Omega x^\Omega (C* - C^\Omega) T^{(\Omega)} = 0 \implies C* = \frac{\sum_\Omega x^\Omega C^\Omega T^{(\Omega)}}{\sum_\Omega x^\Omega T^{(\Omega)}} \quad (2.42)$$

Since T^Q is a function of the unknown effective stiffness C^* in Equation 2.42, the equation is solved iteratively, with an initial guess for C^* given by the poly-crystal Hill average, as given by Equations 2.16 and 2.17.

2.6.2 Implementation of the self-consistent model

A convenient and computationally efficient way to rotate fourth order tensors (instead of the more computation heavy Equation 2.40) is through simple matrix multiplication in the 6-dimensional, 2^{nd} order Kelvin notation domain (Mehrabadi and Cowin, 1990 [57], Moesen, 2012 [58]). Any fourth order tensor ‘ A ’ satisfying minor symmetry, that is $A_{ijkl} = A_{jikl} = A_{ijlk}$ can be rotated to A' in matrix notation as given by equation 2.43, where N is an orthogonal transformation matrix given by Equation 2.44, such that $N^T = N^{(-1)}$ or $NN^T = N^TN = I$, where N^T and $N^{(-1)}$ are the transpose and inverse of the original tensor N respectively and ‘ I ’ is the identity matrix. q_{ij} ’s in Equation 2.44 are elements of the rotation matrix given by Equation 2.41. N with suitable multipliers to transform to Voigt notation domain gives two slightly different transformation matrices for stiffness and compliance tensors, forming the basis of ‘Bond rotation’ (Mavko et al., 2009 [19], Auld, 1973,[59]).

$$A' = NAN^T \quad (2.43)$$

$$N = \begin{bmatrix} q_{11}^2 & q_{12}^2 & q_{13}^2 & \sqrt{2}q_{12}q_{13} & \sqrt{2}q_{11}q_{13} & \sqrt{2}q_{11}q_{12} \\ q_{21}^2 & q_{22}^2 & q_{23}^2 & \sqrt{2}q_{22}q_{23} & \sqrt{2}q_{21}q_{23} & \sqrt{2}q_{21}q_{22} \\ q_{31}^2 & q_{32}^2 & q_{33}^2 & \sqrt{2}q_{32}q_{33} & \sqrt{2}q_{31}q_{33} & \sqrt{2}q_{31}q_{32} \\ \sqrt{2}q_{21}q_{31} & \sqrt{2}q_{22}q_{32} & \sqrt{2}q_{23}q_{33} & q_{22}q_{33} + q_{23}q_{32} & q_{23}q_{31} + q_{21}q_{33} & q_{21}q_{32} + q_{22}q_{31} \\ \sqrt{2}q_{31}q_{11} & \sqrt{2}q_{32}q_{12} & \sqrt{2}q_{33}q_{13} & q_{32}q_{13} + q_{33}q_{12} & q_{33}q_{11} + q_{31}q_{13} & q_{31}q_{12} + q_{32}q_{11} \\ \sqrt{2}q_{11}q_{21} & \sqrt{2}q_{12}q_{22} & \sqrt{2}q_{13}q_{23} & q_{12}q_{23} + q_{13}q_{22} & q_{13}q_{21} + q_{11}q_{23} & q_{11}q_{22} + q_{12}q_{21} \end{bmatrix} \quad (2.44)$$

Since C , S and T satisfy minor symmetry, each of these tensors can be rotated using Equation 2.43. We can now rewrite Equation 2.39 as 2.45. Note that I and $C*$ (and hence $C*^{-1}$) are isotropic and hence invariant to rotation, and that inner pairs of consecutive N^T and N in the tensor products result in I and hence disappear from the final expression. Also it can be easily demonstrated that a rotation followed by an inverse is equivalent to an inverse followed by a rotation.

$$\begin{aligned} T^{(\Omega)} &= [I + S^\Omega : C*^{-1} : (C^\Omega - C*)]^{-1} \\ &= [NIN^T + (NSN^T) : (NC*^{-1}N^T) : (NCN^T - NC*N^T)]^{-1} \\ &= [N(I + S : C*^{-1} : (C - C*))N^T]^{-1} \\ &= N([I + S : C*^{-1} : (C - C*)]^{-1})N^T = T^\Omega \end{aligned} \quad (2.45)$$

Equation 2.45 shows that the strain concentration tensor $T^{(\Omega)}$ associated with the rotated C and S is equivalent to the rotated reference strain concentration tensor T^Ω . Hence Equation 2.42 can be rewritten as Equation 2.46, where $(CT)_{iso}$ and $(T)_{iso}$ are simply the isotropic projections of tensors CT and T using any of the methods described in Section 2.3.5. This simplifies the self consistent computation

greatly, as multiple discretized summations over Ω can simply be replaced by a matrix multiplication.

$$\begin{aligned} C* &= \frac{\sum_{\Omega} x^{\Omega} C^{\Omega} T^{\Omega}}{\sum_{\Omega} x^{\Omega} T^{\Omega}} = \frac{\sum_{\Omega} x^{\Omega} (NCN^T)(NTN^T)}{\sum_{\Omega} x^{\Omega} NTN^T} \\ &= \frac{\sum_{\Omega} x^{\Omega} N(CT)N^T}{\sum_{\Omega} x^{\Omega} NTN^T} = \frac{(CT)_{iso}}{T_{iso}} \end{aligned} \quad (2.46)$$

The equivalence of Equations 2.42 and 2.46 was numerically verified by comparing the match between self-consistent modeling results using isotropic projection and results using summation of discretized Euler angles. They match very well, as demonstrated in Section 2.6.3, and one of the reasons for the slight mismatch at non-spherical aspect ratios could be insufficient discretization. In addition, ideally, when the self-consistent iterations converge $\sum_{\Omega} x^{\Omega} T^{\Omega} = T_{iso} = I$, but we do not always observe this in our implementations. In general, the farther we deviate from spherical grain shapes, the larger the deviation of T_{iso} from I , especially for oblate grain shapes, as demonstrated by Figure 2.17. This figure is generated for illite grains, with the x-axis representing grain aspect ratios (< 1 oblate, > 1 prolate), y-axis representing the ‘norm error’, difference between the norm of T_{iso} and its ideal estimate I ($\|T_{iso}\| - \|I\|$). The norm error is 0 for spherical grains.

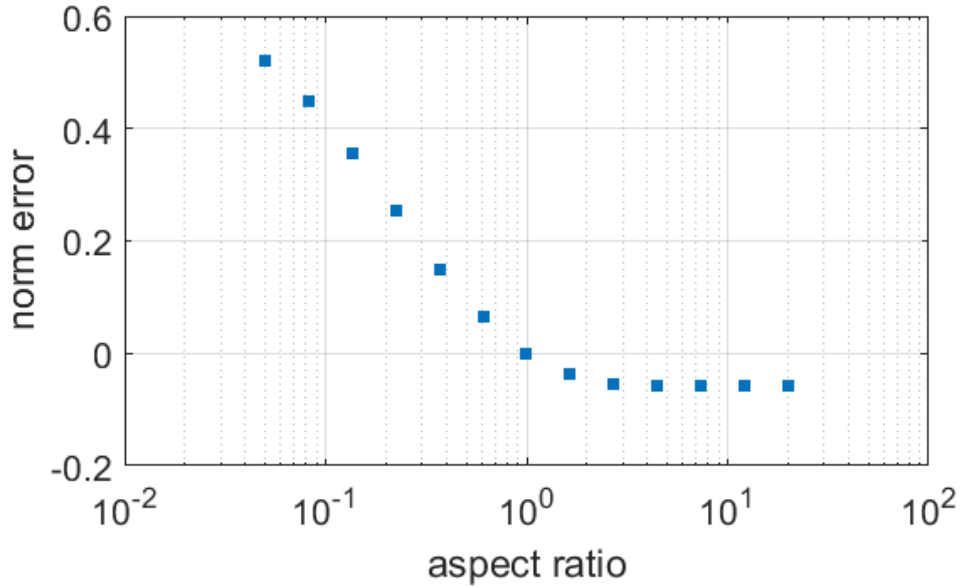


Figure 2.17: Norm error ($\|T_{iso}\| - \|I\|\)$) in the self-consistent model of poly-crystal illite, with hexagonal crystal symmetry, for aspect ratios ranging from $\exp(-4)$ [oblate grain shapes] to $\exp(4)$ [prolate grain shapes]. The norm error is 0 for spherical grains (aspect ratio = 1) and non-zero elsewhere.

2.6.3 Modeling results for some common minerals

Figure 2.18, shows results of self-consistent modeling for a range of grain aspect ratios on poly-crystal aggregates illite, with hexagonal/transverse isotropic symmetry (Katahara, 1996 [60]), the Voigt-notation stiffness matrix of a single crystal given by 2.47 in units of GPa. Grain aspect ratios less than one represent oblate grain geometries, equal to one represents spherical grains and greater than one represents prolate grain geometries.

$$C_{ij}^{\text{illite}} = \begin{bmatrix} 179.9 & 39.9 & 14.5 & 0 & 0 & 0 \\ 39.9 & 179.9 & 14.5 & 0 & 0 & 0 \\ 14.5 & 14.5 & 55 & 0 & 0 & 0 \\ 0 & 0 & 0 & 11.7 & 0 & 0 \\ 0 & 0 & 0 & 0 & 11.7 & 0 \\ 0 & 0 & 0 & 0 & 0 & 70 \end{bmatrix} \quad (2.47)$$

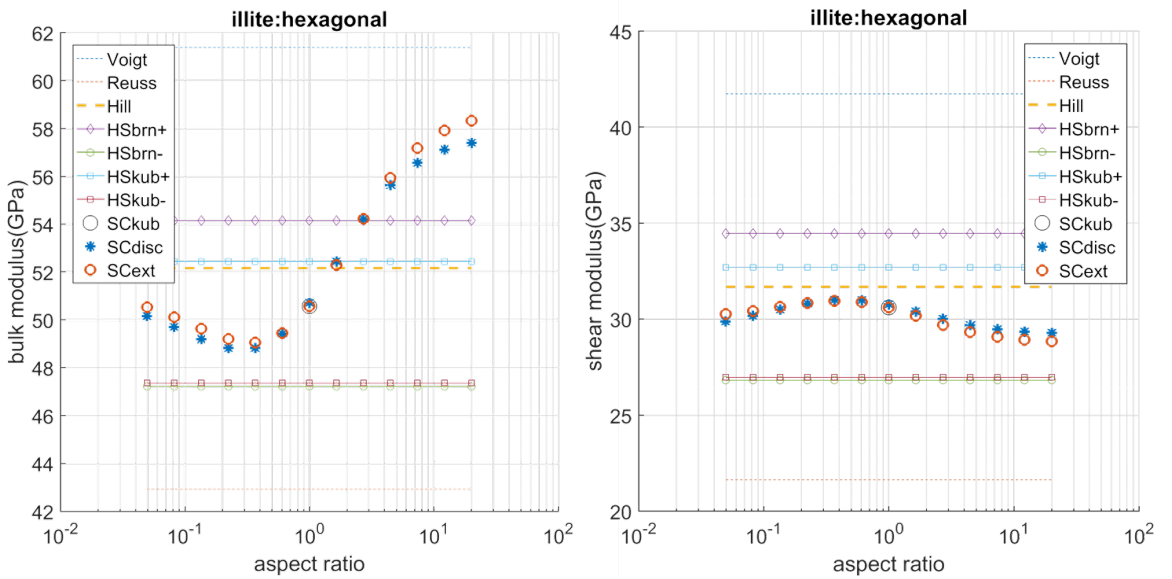


Figure 2.18: Self-consistent model for poly-crystal illite, with hexagonal crystal symmetry, for aspect ratios ranging from $\exp(-3)$ [oblate grain shapes] to $\exp(3)$ [prolate grain shapes].

In Figure 2.18, in addition to the poly-crystal Voigt, Reuss and Hill estimates two sets of Hashin-Shtrikman bounds have been plotted. ‘HSbrn+’ and ‘HSbrn-’ are the upper and lower Hashin-Shtrikman bounds using Brown’s implementation (Brown, 2016 [34]), while ‘HSkub+’ and ‘HSkub-’ are due to Kube (Kube, 2016 [27]). In the absence of closed form expressions, especially for crystals of lower symmetry,

the Hashin-Shtrikman bounds have to be approximated numerically, and can hence converge to different values based on the nature of numerical approximation, as is evident from the difference between estimates due to Brown and Kube.

Figure 2.18 also shows self-consistent estimates using both isotropic projections ('SCext') and summation over discretized Euler angles ('SCdisc'). The two outputs are ideally equivalent, as proven in sub-section 3.7, and match fairly well in the figure with the slight mismatch at highly non-spherical grain shapes being potentially attributable to insufficient discretization in 'SCdisc'. The points labeled 'SCkub' in the sub-figures correspond to poly-crystal self-consistent estimates for spherical grain shapes due to Kube (2016 [27]), and match our results very closely.

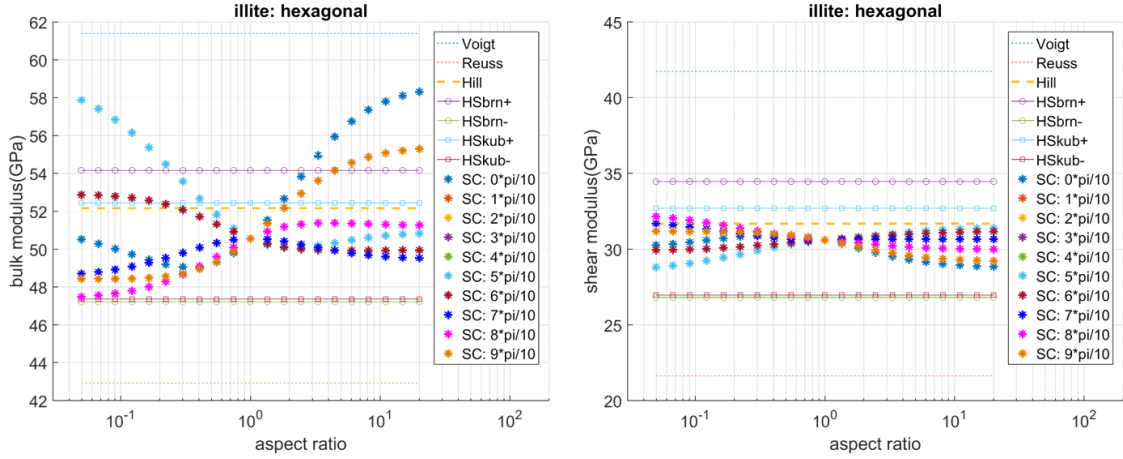


Figure 2.19: Self-consistent model for poly-crystal illite, with hexagonal crystal symmetry, for aspect ratios ranging from $\exp(-3)$ [oblate grain shapes] to $\exp(3)$ [prolate grain shapes], and relative angle between the grain symmetry axis and crystal lattice varying between $0-\pi$, in steps of $\pi/10$.

It is to be noted here that Figure 2.18 shows the variation in the elastic moduli of a randomly oriented aggregate of illite crystals for a specific and fixed orientation between the grain shape and crystal lattice. When the orientation between the grain shape and crystal lattice is held fixed at a different value, the pattern of moduli variation with aspect ratio changes. This is demonstrated in Figure 2.19, where we

look aggregate moduli variation with grain shape for various relative angles between the grain symmetry axis and crystal lattice, from $0-\pi$, in increments of $\pi/10$, labeled as ‘SC: $x\pi/10$ ’ in the figure.

Similarly, we perform self-consistent modeling for a range of grain aspect ratios on poly-crystal aggregates α -quartz, with trigonal symmetry (Hearmon, 1984 [61], Mavko et al., 2009, [19]), and muscovite, with monoclinic symmetry (Vaughan and Guggenheim, 1986 [62], Mavko et al., 2009 [19]), the Voigt-notation stiffness matrices of single crystals given by 2.48 and 2.49, respectively, in units of GPa. Figure 2.20 shows modeling results for α -quartz and Figure 2.21 shows modeling results for muscovite, with the relative angles between the grain symmetry axis and crystal lattice varying from $0-\pi$ in both cases, in increments of $\pi/10$, labeled as ‘SC: $x\pi/10$ ’ in the figures.

$$C_{ij}^{\alpha-quartz} = \begin{bmatrix} 86.60 & 6.70 & 12.60 & -17.80 & 0 & 0 \\ 6.70 & 86.60 & 12.60 & 17.80 & 0 & 0 \\ 12.60 & 12.60 & 106.10 & 0 & 0 & 0 \\ -17.80 & 17.80 & 0 & 57.80 & 0 & 0 \\ 0 & 0 & 0 & 0 & 57.80 & -17.80 \\ 0 & 0 & 0 & 0 & -17.80 & 39.95 \end{bmatrix} \quad (2.48)$$

$$C_{ij}^{muscovite} = \begin{bmatrix} 184.0 & 48.0 & 24.0 & 0 & -2.0 & 0 \\ 48.0 & 178.0 & 22.0 & 0 & 3.9 & 0 \\ 24.0 & 22.0 & 59.0 & 0 & 1.2 & 0 \\ 0 & 0 & 0 & 16.0 & 0 & 0.5 \\ -2.0 & 3.9 & 1.2 & 0 & 18.0 & 0 \\ 0 & 0 & 0 & 0.5 & 0 & 72.0 \end{bmatrix} \quad (2.49)$$

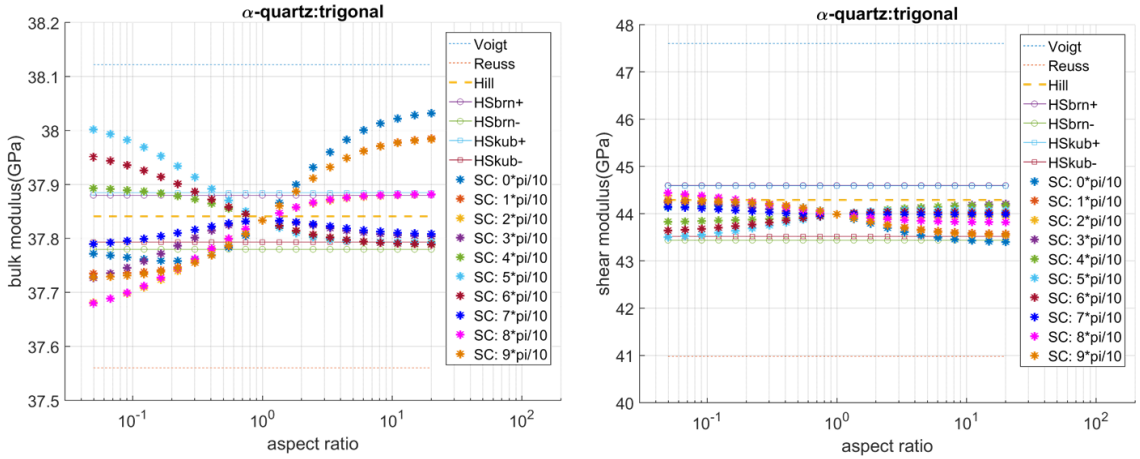


Figure 2.20: Self-consistent model for poly-crystal α -quartz, with trigonal crystal symmetry, for aspect ratios ranging from $\exp(-3)$ [oblate grain shapes] to $\exp(3)$ [prolate grain shapes], and relative angle between the grain symmetry axis and crystal lattice varying between $0-\pi$, in steps of $\pi/10$.

Despite the difference in their underlying crystal symmetries, the variations in isotropic poly-crystal moduli with grain shapes are very similar in the three cases. In each case, all of the modeled self-consistent points lie within the Voigt-Reuss limits, as expected. The self-consistent moduli estimates at aspect ratio 1, agree exactly with previous estimates by Kube (Kube, 2016 [27]) and by extension, Berryman (Berryman, 2005 [63], 2011 [64]). For the general case of spheroidal grain shapes,

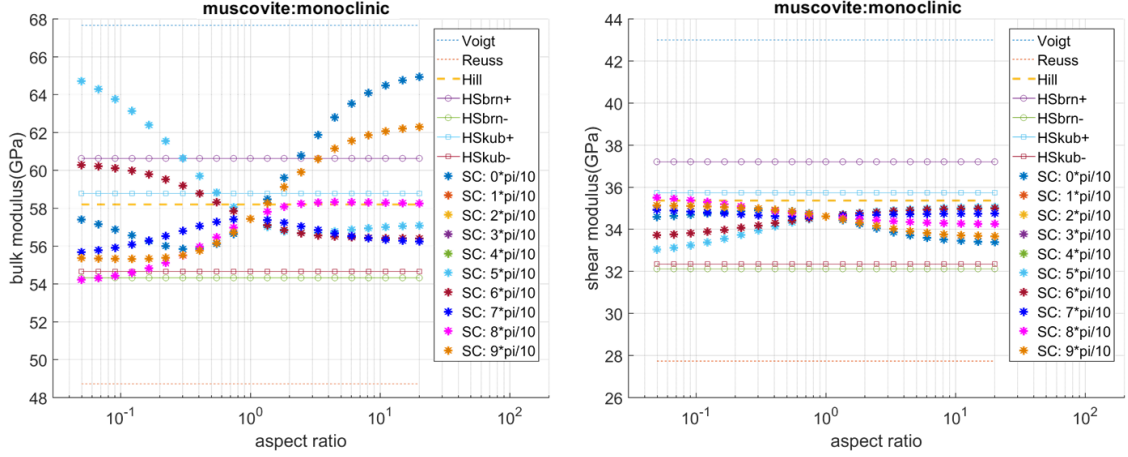


Figure 2.21: Self-consistent model for poly-crystal muscovite, with monoclinic crystal symmetry, for aspect ratios ranging from $\exp(-3)$ [oblate grain shapes] to $\exp(3)$ [prolate grain shapes], and relative angle between the grain symmetry axis and crystal lattice varying between $0-\pi$, in steps of $\pi/10$.

elastic modulus estimates from our self-consistent model are in excellent agreement with the results of Qiu & Weng (1991 [65]), as demonstrated by Figure 2.22 for the case of hexagonal zinc crystals. The modeled shear moduli also lie inside the much narrower HS bounds. In some instances, the modeled bulk moduli lie outside the HS bounds for increasingly non-spherical grain shapes. Self-consistent estimates for spherical grain shapes are unaffected by the change in the crystal orientation, as expected. For non-spherical grain shapes, the exact SC moduli span a range of values depending on the relative angle between the grain axis and crystal lattice, with the range increasing with increasing non-sphericity.

It is important to note that the HS bounds for poly-crystals are numerically estimated, often with significant difference between one implementation and another based of specific assumptions made by an author. For example, in Brown's implementation (Brown, 2015, [32]) the HS bounds on poly-crystal elastic moduli are found by first defining a residual elasticity tensor as the difference between the crystal stiffness tensor and the stiffness tensor of a reference isotropic material. The optimal moduli

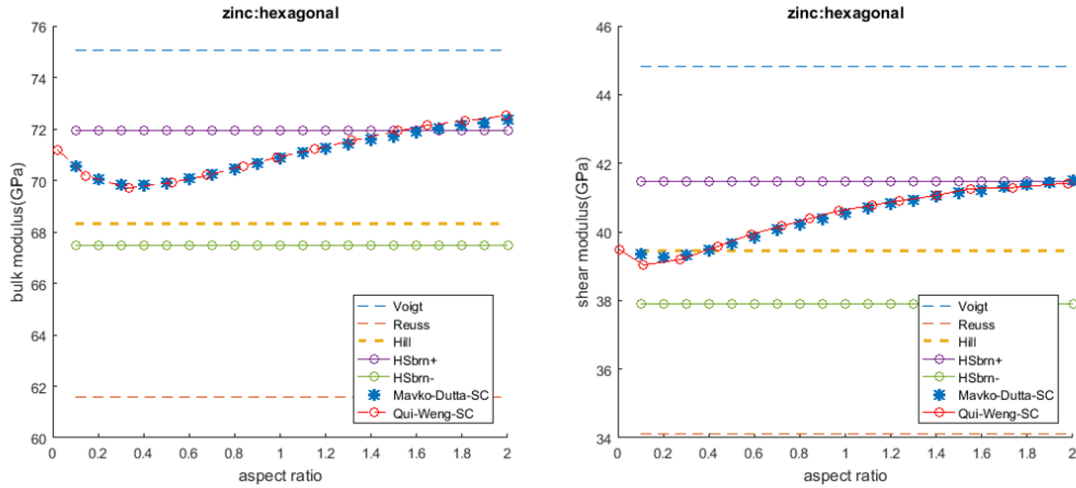


Figure 2.22: For the general case of spheroidal grain shapes, elastic modulus estimates from our self-consistent model are in excellent agreement with the results of Qiu & Weng (1991); the example here is of hexagonal zinc crystals.

are then determined by searching along the boundary of the positive/negative definite regimes of this residual tensor. On the other hand, in Kube's implementation (Kube, 2016 [27]), the poly-crystal HS bounds are determined as part of iteratively solving the expression for self-consistent estimates assuming the average grain shape of the medium to be spherical. The specific assumption of average spherical grain shapes are a likely explanation for why the HS bounds due to Kube are almost always narrower than those due to Brown.

Despite the occasional variational bound violation in bulk modulus, the reason for which we do not completely understand, this SC model gives us a sense of how the isotropic moduli of a poly-crystal aggregate vary with changing grain shape and relative grain-crystal lattice orientation to move within the Voigt-Reuss bounds. It is also important to note that in this study we do not explicitly address the issue of possible correlation between the grain shape and lattice orientation of naturally occurring poly-crystals.

2.7 Solid substitution in composites with micro-anisotropy

Predicting the change in the elastic moduli of a rock due to change in its pore-fill is a problem of fundamental importance in geophysics. Gassmann (Gassmann, 1951 [66]) derived expressions for the change in effective elastic moduli of a mono-mineralic, isotropic rock for the case of pore-fills that are ideal fluids with homogeneous pore-pressure. Since then, there has been a large body of work to generalize Gassmann's results for heterogeneous mineralogies (Brown and Korringa, 1975 [67]), inhomogeneous pore-pressure (Gibiansky and Torquato, 1998 [10]), solid pore-fill (Ciz and Shapiro, 2007 [68]), Mavko and Saxena, 2013 [11]), etc. In this section we test the embedded bounds due to Mavko and Saxena ([11]) for an isotropic composite of two isotropic phases, constructed such that the composite is anisotropic at a micro-scale.

2.7.1 The embedded bounds

Mavko and Saxena ([11]) presented a technique for computing the change in the effective bulk modulus of a rock when substituting solid, fluid or visco-elastic pore-fills. This technique uses the Hashin-Shtrikman (Hashin and Shtrikman, 1963 [8]) bounds recursively such that the results are always physically realizable, resulting in 'embedded bounds'. The embedded bounds are realized by 'doubly coated-sphere' geometries, as shown in Figure 2.23, implicitly assuming isotropy at all scales. For fluid substitution, the embedded bounds reduce to the bounds by Gibiansky and Torquato ([10]), illustrating that those bounds are optimum.

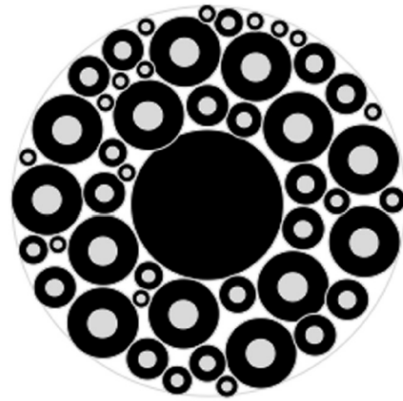


Figure 2.23: Schematic representation of a doubly coated-sphere realization of the embedded bounds by Mavko and Saxena (2013), implicitly assuming isotropy at all scales.

2.7.2 Isotropic aggregates of Backus laminates

To construct an isotropic composite that is anisotropic at a micro-scale, we first creating layered micro-domains of the two constituent isotropic phases, and then orienting the domains randomly to create an isotropic macro-composite, shown schematically in Figure 2.24.

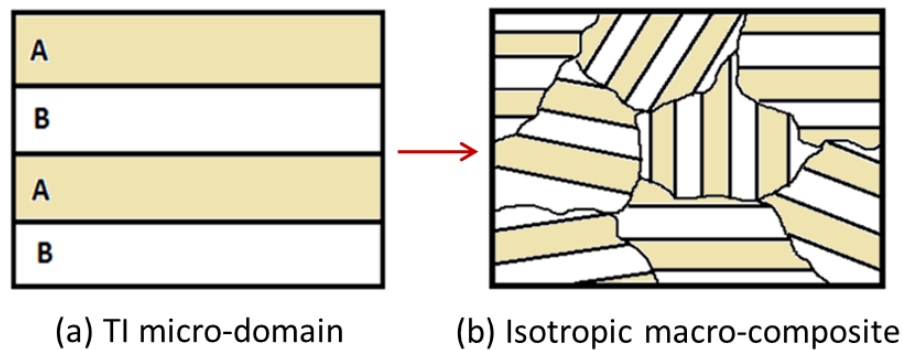


Figure 2.24: Schematic representation of an isotropic composite of two isotropic phases, with micro-scale anisotropy. (a) shows the layering of the two phases to form an anisotropic micro-domain, and (b) shows several micro-domains oriented randomly to form the isotropic macro-composite.

We construct the initial composite with isotropic quartz and clay, with isotropic clay moduli as per Han (Han, 1986 [24]). The transverse isotropic (TI) properties of the layered micro-domains are computed using Backus' (Backus, 1962 [69]) theory, discussed in greater details in the Appendix. The range of moduli for the macro-composite is computed by combining the TI micro-domains with equations 2.12–2.15. From the initial composite we construct two substituted composites, one by substituting the initial clay phase with a softer pore-fill and another by substituting the initial clay phase with a stiffer pore-fill. Elastic properties of the various phases used in this section have been tabulated in Table 2.3.

Table 2.3: Properties of phases used in the solid substitution exercise

Phase name	Bulk modulus (GPa)	Shear modulus (GPa)
Quartz	36	45
Clay	25	9
Softer pore-fill (heavy oil)	4	3
Stiffer pore-fill (pyrite)	147	132

2.7.3 Narrowing of bounds with additional geometric information

In creating isotropic aggregates of Backus laminates we can demonstrate how adding geometric information helps us progressively narrow bounds on effective elastic properties. Let us consider the case of the composite of quartz and heavy oil, as shown in Figure 2.25, with pore-fill fraction (ϕ) referring to the volume fraction of heavy oil in the composite.

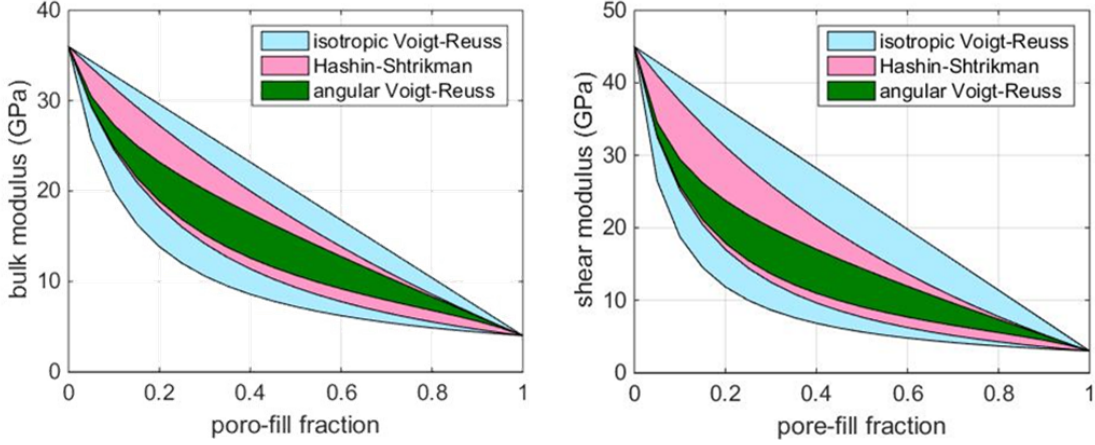


Figure 2.25: Narrowing of bounds with additional geometric information: Poly-crystal Voigt-Reuss bounds (labeled ‘angular Voigt-Reuss’) for the Backus laminates are narrower than the isotropic Hashin-Shtrikman bounds with no micro-geometric information .

When we know nothing about the micro-geometry of a two phase composite of isotropic quartz and heavy oil (properties as in Table 2.3) the bulk and shear moduli of the composite can lie anywhere within the isotropic Voigt-Reuss bounds, given by Equations 2.50 - 2.51, as shown in Figure 2.25 by the blue shaded lenses. If to this most general case we add the information that the overall composite is isotropic, we get a narrower set of bounds, the Hashin-Shtrikman bounds, as indicated by the pink shaded lenses in the figure. The Hashin-Shtrikman bounds lie within and are significantly narrower than the isotropic Voigt-Reuss bounds.

$$K_V^{comp} = (1 - \phi)K^{qtz} + \phi K^{HO}; \quad G_V^{comp} = (1 - \phi)G^{qtz} + \phi G^{HO} \quad (2.50)$$

$$\frac{1}{K_R^{comp}} = \frac{(1 - \phi)}{K^{qtz}} + \frac{\phi}{K^{HO}}; \quad \frac{1}{G_R^{comp}} = \frac{(1 - \phi)}{G^{qtz}} + \frac{\phi}{G^{HO}} \quad (2.51)$$

Further information about the micro-geometry of the composite in the form of

randomly oriented Backus laminates of quartz and heavy oil lead us to the polycrystal/angular Voigt-Reuss bounds, represented by the green shaded regions in Figure 2.25, lying within the Hashin-Shtrikman bounds, and significantly narrower than them. In general we think of bounds on rock properties to be representative of the uncertainty due to their unknown exact micro-geometry. This exercise demonstrates how adding geometric information reduces uncertainty and results in progressively narrower bounds.

2.7.4 Substituted Backus aggregate, case 1: softer pore-fill

To test the embedded bounds on isotropic aggregates of Backus laminates the first substituted composite is constructed by substituting the clay pore-fill in the initial composite with a significantly softer pore-fill, corresponding approximately to heavy oil (HO). The bulk modulus of the substituted composite is estimated in two ways. First, the Voigt and Reuss elastic moduli of the substituted isotropic composite are computed in terms of the elastic properties of the substituted Backus micro-domains using Equations 2.12-2.15. Second, four sets of embedded bounds are predicted for the substituted composite: 2 sets corresponding to the bulk and shear moduli change starting with the Voigt stiffness of the initial composite, and 2 sets corresponding to the bulk and shear moduli change starting with the Reuss stiffness of the initial composite.

Figure 2.26 shows the change in bulk modulus for the first substituted composite when the pore-fill volume fraction is 0.5. The x-axis of the figure corresponds to the possible bulk moduli of the initial composite, labeled ‘A+B’, extending from the quartz-clay lower Hashin-Shtrikman bound of 29.79GPa to the upper Hashin-Shtrikman bound of 30.16GPa. The y-axis corresponds to possible bulk moduli of the substituted composite, labeled ‘A+C’, extending from the quartz-HO lower Hashin-Shtrikman bound of 9.4GPa to the upper Hashin-Shtrikman bound of 16.9GPa.

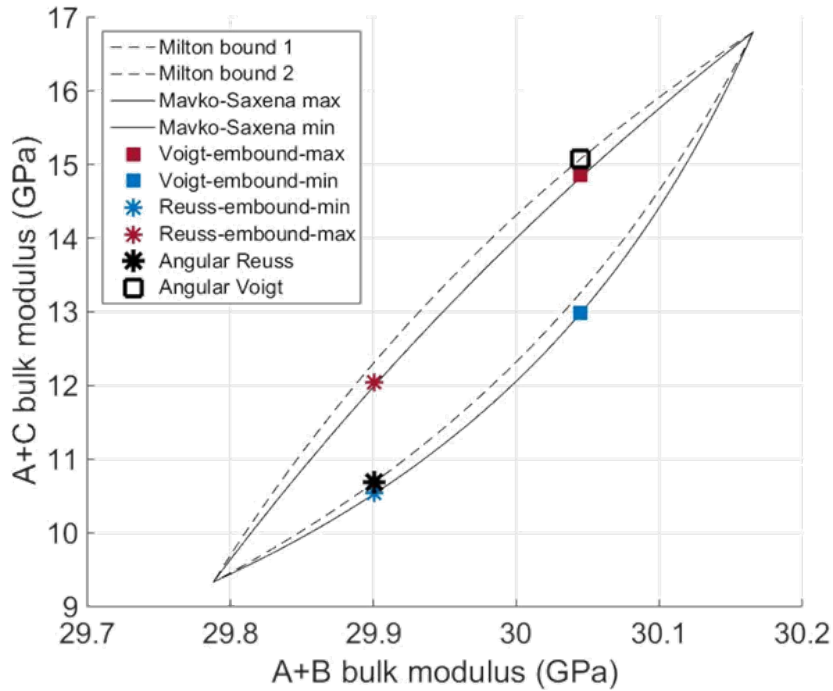


Figure 2.26: Solid substitution in composite with micro-scale anisotropy: substituting clay in a quartz-clay composite with heavy oil, only the poly-crystal/angular Reuss estimate of bulk modulus falls within the predicted embedded bounds though the errors in general are not significant (< 0.1%).

The solid lines enclosing a lenticular space in figure 2.26 are the embedded bounds. The bounds are unique at Hashin-Shtrikman points, such that if the initial composite lies on the lower(upper) Hashin-Shtrikman bound, the substituted composite also lies on the corresponding lower(upper) Hashin-Shtrikman bound. Accordingly the lower(upper) end of the lens enclosed by the embedded bounds correspond to the lower(upper) HS bounds of the initial and substituted composites. If the initial composite lies in between the Hashin-Shtrikman bounds, the modulus of the substituted composite is non-unique, depending on the unknown exact micro-geometry of the composite in question, indicated by the opening up of the area between the embedded bounds in the wide part of the lens.

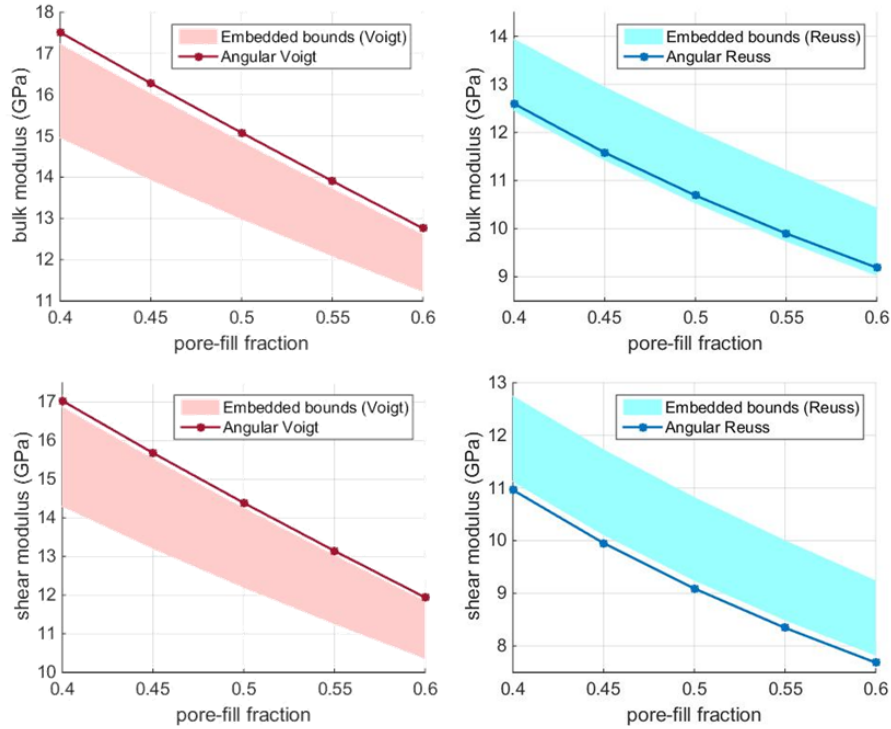


Figure 2.27: Solid substitution in composite with micro-scale anisotropy: substituting clay in a quartz-clay composite with heavy oil, only the poly-crystal/angular Reuss estimate of bulk modulus falls within the predicted embedded bounds though the errors in general are not significant (< 0.1%).

The poly-crystal Voigt and Reuss estimates of bulk modulus for the initial composite are 29.9GPa and 30.04GPa respectively. The embedded bounds corresponding to the initial Voigt estimate are 13 GPa and 14.9Gpa, plotted against the initial Voigt estimate as red and blue filled squares, labeled ‘Voigt-embound-max’ and ‘Voigt-embound-min’ respectively. The embedded bounds corresponding to the initial Reuss estimate are 10.6 GPa and 12.05Gpa, plotted against the initial Reuss estimate as red and blue stars, labeled ‘Reuss-embound-max’ and ‘Reuss-embound-min’ respectively. The angular/poly-crystal Voigt estimate of bulk modulus for the substituted Backus domain aggregate is 15.1GPa, plotted against the initial Voigt estimate as a black square. The angular Reuss estimate of bulk modulus for the substituted Backus

domain aggregate is 10.75GPa, plotted against the initial Reuss estimate as a black star.

As is evident from Figure 2.26, the poly-crystal Reuss estimate of bulk modulus of the substituted composite lies within the embedded bounds but the poly-crystal Voigt estimate of bulk modulus does not. Figure 2.27 shows the angular/poly-crystal Voigt-Reuss estimates and the corresponding embedded bounds for both bulk and shear moduli of the substituted composite, for pore-fill fractions ranging from 0.4 to 0.6. Though the deviation from the embedded bounds is not significant (<0.1%), of the four cases, only the angular Reuss estimate of bulk modulus lies within the embedded bounds, showing that isotropic composites made of TI layered domains, are an example of rocks that do not necessarily obey the embedded bounds.

2.7.5 Substituted Backus aggregate, case 2: stiffer pore-fill

This effect is demonstrated further in the second substituted composite, constructed by substituting the clay pore-fill in the initial composite with a significantly stiffer pore-fill, corresponding approximately to pyrite. Figure 2.28 compares the computed moduli for the second substituted composite with the corresponding predicted range of substituted moduli using the embedded bounds. In this case, both the Voigt and Reuss bulk and shear moduli lie outside the embedded bounds. Interestingly, the absolute values of the embedded bounds predicted starting with the Reuss moduli of the initial composite are actually higher than those predicted starting with the Voigt moduli of the initial composite.

The examples of the two substituted composites show that the change in elastic moduli upon substitution of pore-fill that falls outside the range predicted by the embedded bounds, built recursively from the Hashin-Shtrikman constructs. However, for each of the three (initial, first and second substituted) macro-scale isotropic composites, the computed Voigt and Reuss poly-crystal elastic moduli fall within the

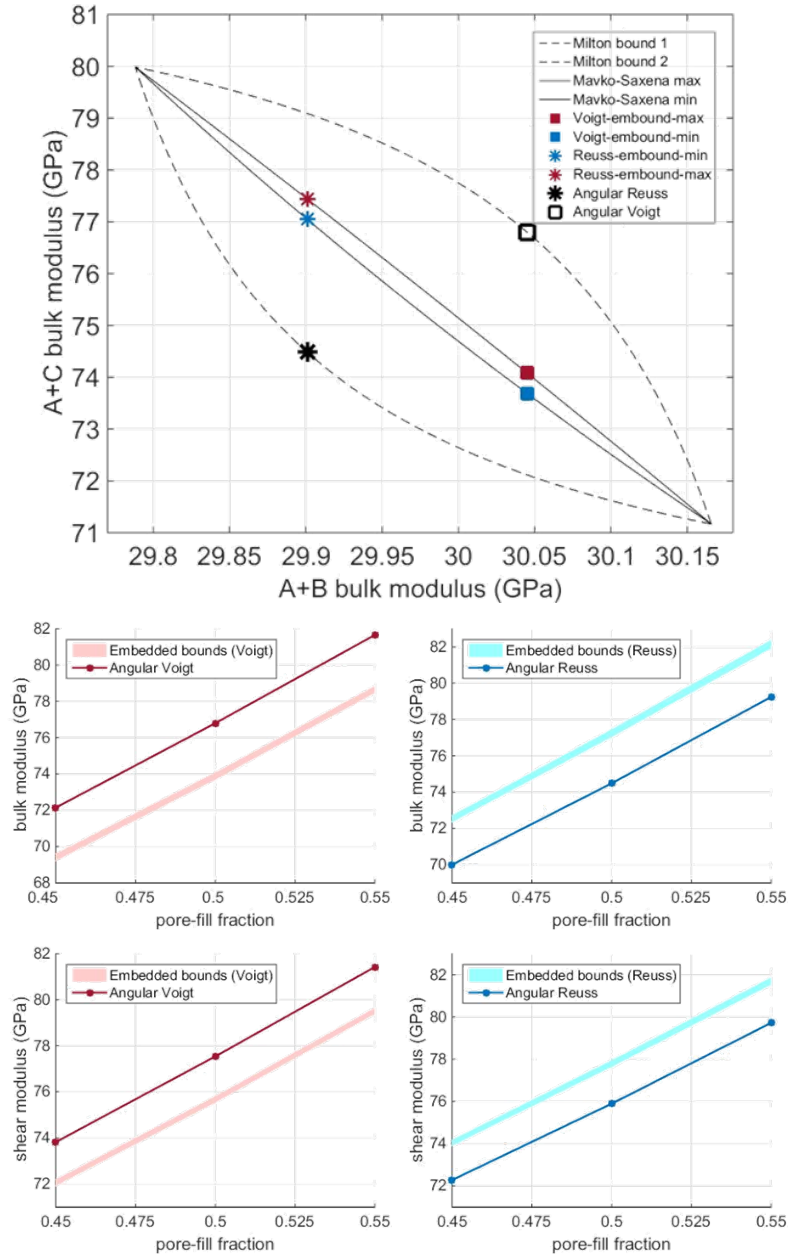


Figure 2.28: Solid substitution in composite with micro-scale anisotropy: substituting clay in a quartz-clay composite with pyrite, both poly-crystal/angular Voigt and Reuss estimates of bulk and shear moduli fall outside the predicted embedded bounds with errors of the order of 3%).

Hashin-Shtrikman bounds. This phenomenon is due to the specification of layered geometry of the micro-domains constituting the composite, and is discussed in greater details in the following section.

2.7.6 Similarity with Milton's bounds

It is worth noting that for both the substituted composites, bulk and shear moduli post substitution lie on bounds derived by Vinogradov and Milton (Vinogradov and Milton, 2005 [70]) for anisotropic micro-geometries while studying the total creep in visco-elastic composite materials under hydrostatic or antiplane loading. These are labeled as ‘Milton-bound 1’ and ‘Milton-bound 2’ in Figures 2.26 and 2.28.

Vinogradov and Milton’s work described the problem of correlating the immediate and relaxed bulk moduli of a visco-elastic composite. This is equivalent to coupling two pure elastic states characterized by changing the elastic moduli of the constituent phases from their immediate (initial) to relaxed (substituted) states, and is hence analogous to the problem of solid substitution.

For the most general case, Vinogradov and Milton introduced four curves, the outermost pair of which formed bounds on the change in elastic moduli of a substituted composite. This is true of what the authors define as the ‘well-ordered case’, defined by relations amongst the shear moduli of the phases in the initial (G_2^{init}, G_1^{init}) and substituted (G_2^{sub}, G_1^{sub}) composites, defined by Equation 2.52, with our first substituted composite (softer pore-fill) as example. Two of these four curves correspond to the doubly-coated sphere geometry of the embedded bounds.

$$(G_2^{init} - G_1^{init})(G_2^{sub} - G_1^{sub}) \geq 0 \quad (2.52)$$

For the ‘badly-ordered case’, defined by Equation 2.53, with our second substituted composite (stiffer pore-fill) as example, the bounds are given by the two curves that

do not correspond to the embedded bounds. Some isolated points on these bounds correspond to known micro-geometries, such as randomly oriented Backus laminates and composite layered cylinders.

$$(G_2^{init} - G_1^{init})(G_2^{sub} - G_1^{sub}) \leq 0 \quad (2.53)$$

This section thus shows an example of rock micro-geometry that does not always obey the embedded bounds for solid substitution, drawing parallels with the work of Vinogradov and Milton, who were studying creep in viscoelastic composites.

2.8 Clay elastic moduli

We have seen that the Hill estimate of the isotropic moduli of poly-crystals, though heuristic, lies within both the Voigt-Reuss and the Hashin-Shtrikman bounds and is often considered a good approximation to the expected elastic moduli of an isotropic poly-crystal (Hendrix, 1998 [26]).

Let us consider the transversely isotropic elastic tensors for illite and chlorite (Katahara, 1996 [60]), two common clay minerals, shown in their Voigt-notation stiffness matrices in 2.54-2.55, in units of GPa:

$$C_{ij}^{\text{illite}} = \begin{bmatrix} 179.9 & 39.9 & 14.5 & 0 & 0 & 0 \\ 39.9 & 179.9 & 14.5 & 0 & 0 & 0 \\ 14.5 & 14.5 & 55 & 0 & 0 & 0 \\ 0 & 0 & 0 & 11.7 & 0 & 0 \\ 0 & 0 & 0 & 0 & 11.7 & 0 \\ 0 & 0 & 0 & 0 & 0 & 70 \end{bmatrix} \quad (2.54)$$

$$C_{ij}^{chlorite} = \begin{bmatrix} 181.6 & 16.8 & 20.3 & 0 & 0 & 0 \\ 16.8 & 181.69 & 20.3 & 0 & 0 & 0 \\ 20.3 & 20.3 & 106.8 & 0 & 0 & 0 \\ 0 & 0 & 0 & 11.4 & 0 & 0 \\ 0 & 0 & 0 & 0 & 11.4 & 0 \\ 0 & 0 & 0 & 0 & 0 & 82.4 \end{bmatrix} \quad (2.55)$$

The corresponding Hill estimates for the bulk and shear moduli of the isotropic illite poly-crystal are 52.17GPa and 31.69GPa respectively. For chlorite, the isotropic poly-crystal Hill estimates for the bulk and shear are 52.17GPa and 31.69GPa respectively.

In comparison, some of the experimental values isotropic bulk and shear moduli of clays reported in popular literature are as follows (Mavko, 2009 [19]): Gulf clays are reported to have K = 25GPa, G = 9GPa (Han, 1986 [24]), or K = 21GPa, G = 7GPa (Tosaya, 1982 [71]). It is evident that the reported experimental moduli of clay samples are far softer than their poly-crystal Hill estimates.

One simple way to explain this discrepancy in the measured and estimated elastic moduli of clays is considering micro-porosity in the clay samples, frequently observed in SEM images of clay. Hence, when using the reported values of clay in rock physics calculations it is important to define the total porosity of a rock by adding an appropriate amount of micro-porosity that is potentially associated with the clay phase.

2.9 Conclusions

In this chapter we have re-iterated the important and often neglected fact that a vast majority of the isotropic elastic moduli of various minerals reported in the literature

are simply some mean of the poly-crystal Voigt and Reuss bounds, representing the two extreme boundary conditions of uniform strain and uniform stress, respectively. A tighter set of poly-crystal ‘Hashin-Shtrikman’ bounds can be derived using variational principles.

The true elastic modulus of a poly-crystal can lie anywhere between these bounds, depending on the unknown exact microgeometry. The width of the bounds usually increase with increasing anisotropy of the constituent crystals or domains, and can be used as a symmetry-independent measure of crystal anisotropy. Remembering that the true moduli of an isotropic poly-crystal lie within a range instead of being fixed at an average value can potentially help us model poly-crystal properties better.

We explored the magnitude of the relative influence of elastic parameters characterizing VTI crystals/domains on the fractional bound widths of poly-crystal effective elastic moduli. Our analyses, based on constrained Monte-Carlo simulations and GBM meta-models revealed that on an average, domain Thomsen parameter γ controlled over 80% of the fractional shear bound-width dfg . Domain Thomsen parameter ϵ controlled about 47% of the fractional bulk bound-width dfk , followed by γ (20%) and vertical shear modulus C_{44} (18%). About 62% of the fractional P-wave bound-width was due to domain parameter ϵ , followed by γ (18%). In each case, the correlation between the dominant domain parameter and the corresponding fractional bound-width is positive. The minimum values of dfg and dfp scale almost linearly with domain parameters γ and ϵ respectively.

We developed a self-consistent model to understand the impact of grain-shapes in moving us between the poly-crystal bounds. The model demonstrated that self-consistent estimates for spherical grain shapes are unique and unaffected by the change in the crystal orientation. For non-spherical grain shapes such as oblates and prolates, the exact moduli span a range of values depending on the relative angle between the grain axis and crystal lattice, with the range increases with increasing

non-sphericity in the grain shape.

We demonstrated the narrowing of elastic bounds upon adding geometric information. We tested the embedded solid substitution bounds, which implicitly assume isotropy at all scales, on randomly oriented aggregates of layered laminates and found that laminar aggregates are an example of poly-crystal microgeometry that can violate the embedded bounds.

Finally, by comparing isotropic elastic moduli of clays from their single-crystal stiffness tensors to some reported experimental values in popular literature, we hypothesized the possibility of unaccounted micro-porosity in the experimental clay samples.

2.10 Appendix A: TI projection of minerals

We discussed some strategies to estimate the isotropic projection of elastic stiffness tensors of a specific symmetry in Section 2.3.5. These projections were based on minimizing the Euclidean distance between the original tensor and its projection. In this section we discuss the extension of those strategies to project stiffness tensors onto their nearest transversely isotropic forms (Caro, 2014 [42], Browaeys and Chevrot, 2004 [38]), as used in Section 2.5.2.2 to generate the values in Table 2.2. Once again the projections involve a simple matrix multiplication, as in equation 2.56, where X_{sym} and X are elastic stiffness/compliance tensors expressed as a vector of length 21, related to their Kelvin notation tensor components as given by Equation 2.20 and P is a 21x21 matrix projector. For hexagonal or transversely isotropic projections, $P = P_{hex}$ is given by Equations 2.57 & 2.58.

$$X_{sym} = PX \quad (2.56)$$

$$P_{hex} = \begin{bmatrix} M_{hex} & 0_{9x12} \\ 0_{12x9} & 0_{12x12} \end{bmatrix} \quad (2.57)$$

$$M_{hex} = \begin{bmatrix} 3/8 & 3/8 & 0 & 0 & 0 & 1/4\sqrt{2} & 0 & 0 & 1/4 \\ 3/8 & 3/8 & 0 & 0 & 0 & 1/4\sqrt{2} & 0 & 0 & 1/4 \\ 0 & 0 & 1 & 0 & 0 & 0 & 0 & 0 & 0 \\ 0 & 0 & 0 & 1/2 & 1/2 & 0 & 0 & 0 & 0 \\ 0 & 0 & 0 & 1/2 & 1/2 & 0 & 0 & 0 & 0 \\ 1/4\sqrt{2} & 1/4\sqrt{2} & 0 & 0 & 0 & 3/4 & 0 & 0 & -1/2\sqrt{2} \\ 0 & 0 & 0 & 0 & 0 & 0 & 1/2 & 1/2 & 0 \\ 0 & 0 & 0 & 0 & 0 & 0 & 1/2 & 1/2 & 0 \\ 1/4 & 1/4 & 0 & 0 & 0 & -1/2\sqrt{2} & 0 & 0 & 1/2 \end{bmatrix} \quad (2.58)$$

As in case of isotropic projections, TI projections of stiffness tensors are not equivalent to the inverse of the TI projections of the corresponding compliance tensors, the former being more ‘Voigt-like’ and the latter being more ‘Reuss-like’. Projection parameters listed in Table 2.2 are generated using stiffness tensors, in a ‘Voigt-like’ scheme.

2.11 Appendix B: Backus Average

The general form of a transversely isotropic stiffness tensor (in Voigt notation) with its axis of symmetry in the x_3 direction is given by matrix 2.59.

$$\begin{bmatrix} C_{11} & C_{12} & C_{13} & 0 & 0 & 0 \\ C_{12} & C_{11} & C_{13} & 0 & 0 & 0 \\ C_{13} & C_{13} & C_{33} & 0 & 0 & 0 \\ 0 & 0 & 0 & C_{44} & 0 & 0 \\ 0 & 0 & 0 & 0 & C_{44} & 0 \\ 0 & 0 & 0 & 0 & 0 & C_{66} = \frac{1}{2}(C_{11} - C_{12}) \end{bmatrix} \quad (2.59)$$

Backus (1962 [69]) showed that in the long-wavelength limit, the effective stiffness tensor components of a layered medium of transversely isotropic materials can be given by Equations 2.60 - 2.65. In these equations the uppercase tensor components correspond to the effective layered media while the lowercase tensor components correspond to the constituent layers. The brackets $\langle \cdot \rangle$ indicate weighted volumetric averages of the properties enclosed by them. The properties of the layered micro-domains discussed in Section 2.7 are generated using this scheme.

$$C_{11} = \frac{\langle c_{13}/c_{33} \rangle^2}{\langle 1/c_{33} \rangle} - \langle c_{13}^2/c_{33} \rangle + \langle c_{11} \rangle \quad (2.60)$$

$$C_{12} = C_{11} - \langle c_{11} \rangle + \langle c_{12} \rangle \quad (2.61)$$

$$C_{13} = \frac{\langle c_{13}/c_{33} \rangle}{\langle 1/c_{33} \rangle} \quad (2.62)$$

$$C_{33} = \langle 1/c_{33} \rangle^{-1} \quad (2.63)$$

$$C_{44} = \langle 1/c_{44} \rangle^{-1} \quad (2.64)$$

$$C_{66} = \langle c_{66} \rangle \quad (2.65)$$

...

Chapter 3

Elastic properties of anisotropic poly-crystals

3.1 Abstract

The Voigt and Reuss schemes of rotational summation are the most commonly used methods in geophysics for determining the effective elastic properties of oriented poly-crystals with micro-scale anisotropy. In general, the two schemes do not produce equivalent results, the difference representing uncertainty due to the unknown exact micro-geometry of a composite. In this chapter, we aim to understand the nature and impact of this difference, focussing on composites with rotational or transverse isotropic (TI) symmetry.

Unlike the case of isotropic poly-crystals, choosing Voigt over Reuss (or vice versa) for a TI composite does not systematically over/under-estimate all of the composite elastic parameters of interest (stiffness tensor components C33 & C44 and Thomsen's anisotropy parameters ϵ , γ and δ). With the Voigt and Reuss estimates forming tensorial bounds on the elastic stiffness of a composite, elastic parameters corresponding to a 'Hill' tensor, the average of the Voigt and Reuss stiffness tensors (analogous to

the case of isotropic poly-crystals) might offer a good working approximation to the true effective anisotropic composite properties.

Micro-domains with negative values of Thomsen parameter δ develop a positive-peaked bulge with increasing disorder or misalignment, before going to zero in a perfectly disordered, isotropic macro-composite. This is in line with the common observation that crystals of clay minerals often exhibit negative values of δ , but clay-rich shales, with some degree of crystal misalignment, almost always show positive δ values.

Monte-Carlo analyses of a TI orientation distribution function (ODF) related to mechanical compaction of sediments reveal that domain/crystal Thomsen parameters δ and ϵ are the strongest predictors for the Voigt-Reuss difference in the composite Thomsen parameter ϵ . Domain parameters C_{44} and γ have the strongest relative influence on composite parameter γ , the maximum value of which also scales monotonically with the domain γ . For composite parameter δ , domain parameters γ and δ are most predictive.

Important formation evaluation parameters such as Vp-Vs ratios and AVO intercepts and gradients can be significantly impacted by the choice of a Voigt scheme over a Reuss, leading to very different interpretations. Greater the elastic anisotropy of the constituent micro-domains, larger the difference between Voigt and Reuss interpretations.

3.2 Anisotropic poly-crystal Voigt-Reuss estimates

3.2.1 General Theory

The crystallographic texture of a poly-crystal aggregate refers to crystal orientations within the aggregate. Crystallographic texture is often estimated using X-Ray Diffraction (XRD) experiments and is quantified as an Orientation Distribution Function (ODF), expressed as $W(\Omega)$, where $\Omega = (\theta, \psi, \phi)$, symbolizing the three Euler angles that specify the tilt of the local ‘crystal’ axes relative to the global coordinate axes (Roe, 1965 [72], Sayers, 1987 [73]), as shown in Figure 3.1. $W(\theta, \psi, \phi)$ gives the probability density for a particular orientation (Johanson et al., 2004 [74]), i.e., volume fraction of grains with crystal-axes aligned along (θ, ψ, ϕ) . Since the grain volume fractions considering all orientations should add up to 1, $W(\theta, \psi, \phi)$ is subject to the normalization condition given by Equation 3.1. Accordingly, isotropic orientation distributions correspond to $W = 1/8\pi^2$.

$$\int_{\phi=0}^{2\pi} \int_{\psi=0}^{2\pi} \int_{\theta=0}^{\pi} W(\theta, \psi, \phi) \sin\theta d\theta d\psi d\phi = 1 \quad (3.1)$$

In Equation 3.1 integration over θ and ψ is an integration over the surface of a sphere with infinitesimal surface area $\sin\theta d\theta d\psi$, hence the $\sin\theta$ term in the integration. Often we substitute θ by $\xi = \cos\theta$, so that Equation 3.1 can be simplified to 3.2.

$$\int_{\phi=0}^{2\pi} \int_{\psi=0}^{2\pi} \int_{\xi=-1}^1 W(\xi, \psi, \phi) d\xi d\psi d\phi = 1 \quad (3.2)$$

We demonstrated in the previous chapter how under the assumption of uniform strain the effective elastic stiffness tensor of a poly-crystal equals the volume average

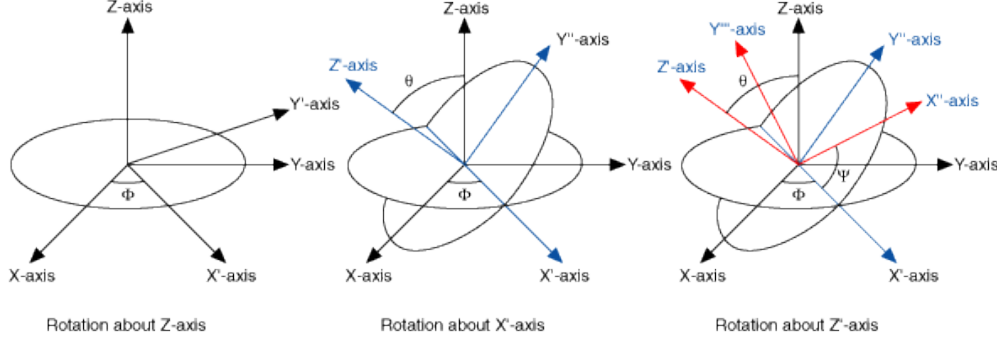


Figure 3.1: Euler angles (θ, ψ, ϕ) specifying tilt of the local ‘crystal’ axes relative to the global coordinate axes.

of the single-crystal elastic tensor (over all spatial orientations). Combining this with the definition of ODFs we can express the general poly-crystal Voigt average as in Equation 3.3. $C^{(\theta, \psi, \phi)}$ is the stiffness tensor (in the global coordinates) of the poly-crystal with Euler angles (θ, ψ, ϕ) , and is related to the crystal tensor in local co-ordinates by Equations 3.4 and 3.5.

$$C_{Voigt}^* = \int_{\phi=0}^{2\pi} \int_{\psi=0}^{2\pi} \int_{\xi=-1}^1 W(\xi, \psi, \phi) [C^{(\theta, \psi, \phi)}] d\xi d\psi d\phi \quad (3.3)$$

$$C_{ijkl}^{(\theta, \psi, \phi)} = Q_{pi} Q_{qj} Q_{rk} Q_{sl} C_{pqrs} \quad (3.4)$$

$$Q = \begin{bmatrix} \cos(\psi)\cos\phi - \sin(\psi)\sin(\phi)\cos(\theta) & \sin(\psi)\cos\phi + \cos(\psi)\sin(\phi)\cos(\theta) & \sin(\phi)\sin(\theta) \\ -\cos(\psi)\sin\phi - \sin(\psi)\cos(\phi)\cos(\theta) & -\sin(\psi)\sin(\phi) + \cos(\psi)\cos(\phi)\cos(\theta) & \cos(\phi)\sin(\theta) \\ \sin(\psi)\sin(\theta) & -\cos(\psi)\sin(\theta) & \cos(\theta) \end{bmatrix} \quad (3.5)$$

Similarly, we showed in the previous chapter how under the assumption of uniform stress the effective elastic compliance tensor of a poly-crystal is the volume average of the single-crystal compliance tensor over all spatial orientations. Hence, the general

poly-crystal Reuss average can be expressed as in Equation 3.6.

$$S_{Reuss}^* = \int_{\phi=0}^{2\pi} \int_{\psi=0}^{2\pi} \int_{\xi=-1}^1 W(\xi, \psi, \phi) [S^{(\theta, \psi, \phi)}] d\xi d\psi d\phi = [C_{Reuss}^*]^{-1} \quad (3.6)$$

The triple integrals in Equations 3.3 and 3.6 involve tensor rotations and are generally cumbersome to estimate numerically. A relatively easy way is to consider approximate formulations by expressing ODFs in terms of generalized spherical harmonics, as described in Section 3.2.2. In section 3.2.3 we compute the same integrals as discretized summations over the range of (θ, ψ, ϕ) and show that for the cases considered in this chapter, the results from the Legendre expansions are almost exactly equivalent to those from the more computation intensive discrete summations.

In previously published literature on the effective properties of poly-crystals with anisotropic ODFs, authors have either used the Voigt (Morris, 1969 [75], Sayers, 1995 [76], Johansen et al., 2004 [74], Bandopadhyay, 2009 [18]) or the Reuss (Sayers, 1987 [73], Sayers, 1995 [77]) scheme of rotational summation without specifically addressing the difference in results due to the choice of one scheme over the other. Important motivations for the research presented in this chapter include understanding the magnitude of difference between effective elastic properties estimated using the Voigt and Reuss schemes, the relationship of the macro-scale difference with the micro-scale crystal/domain properties, and, the impact of the difference on common formation evaluation parameters.

3.2.2 Approximate formulations using Legendre Polynomials

ODFs are often conveniently expressed in terms of generalized spherical harmonics (Roe, 1969, Sayers, 1994, Johanson et al., 2004), as given by Equation 3.7, where $Z_{lmn}(\xi)$ are the normalized Legendre functions (Roe, 1965 [72]).

$$W(\xi, \psi, \phi) = \sum_{l=0}^{\infty} \sum_{m=-l}^l \sum_{n=-l}^l W_{lmn} Z_{lmn}(\xi) e^{-im\psi} e^{-in\phi} \quad (3.7)$$

Using the orthogonality of spherical harmonics, coefficients W_{lmn} in Equation 3.7 can be expressed as per Equation 3.8. For fourth rank tensors, such as the elastic stiffness or compliance tensors, spatial averages only depend on W_{lmn} for $l \leq 4$ (Sayers, 1994 [78], Bandyopadhyay, 2009 [18]). For hexagonal crystals and orthorhombic aggregates this further simplifies to W_{lmn} being restricted to $n = 0$ and l and m having even values. For hexagonal crystals and hexagonal aggregates, the case of primary interest in this study, both n and m have to be zero valued, meaning the only coefficients of relevance are W_{000} , W_{200} and W_{400} . The corresponding expressions for Z_{lmn} are as given by Equation 3.9.

$$W_{lmn} = \frac{1}{4\pi^2} \int_{\phi=0}^{2\pi} \int_{\psi=0}^{2\pi} \int_{\xi=-1}^1 W(\xi, \psi, \phi) Z_{lmn}(\xi) e^{-im\psi} e^{-in\phi} d\xi d\psi d\phi \quad (3.8)$$

$$Z_{000}(\xi) = \sqrt{\frac{1}{2}}; \quad Z_{200}(\xi) = \sqrt{\frac{5}{2} \frac{(3\xi^2 - 1)}{2}}; \quad Z_{400}(\xi) = \sqrt{\frac{9}{2} \frac{(35\xi^4 - 30\xi^2 + 3)}{8}}; \quad (3.9)$$

3.2.2.1 Approximate Voigt formulations

Based on the ODFs expressed in terms of spherical harmonics, the general expression for the effective Voigt stiffness tensor of an aggregate is given by Equation 3.10, where C_{ijkl}^{iso} is Voigt estimate of the isotropic poly-crystal stiffness, and ΔC_{ijkl} is the corresponding anisotropic deviation. Explicitly, the non-zero elements of C_{ijkl}^{iso} are given by equations 3.11 - 3.13, where c_{ij} are the elements of the single crystal (hexagonal) stiffness tensor in Voigt notation.

$$C_{ijkl} = C_{ijkl}^{iso} + \Delta C_{ijkl} \quad (3.10)$$

$$C_{11}^{iso} = C_{22}^{iso} = C_{33}^{iso} = \frac{1}{15}(8c_{11} + 3c_{33} + 4c_{13} + 8c_{44}) \quad (3.11)$$

$$C_{12}^{iso} = C_{23}^{iso} = C_{31}^{iso} = \frac{1}{15}(c_{11} + c_{33} + 5c_{12} + 8c_{13} - 4c_{44}) \quad (3.12)$$

$$C_{44}^{iso} = C_{55}^{iso} = C_{66}^{iso} = \frac{1}{30}(7c_{11} + 2c_{33} - 5c_{12} - 4c_{13} + 12c_{44}) \quad (3.13)$$

Approximate closed form solutions for the components of ΔC_{ijkl} for the polycrystal Voigt averaged stiffness tensor of a hexagonal aggregate composed of hexagonal micro-domains is given as per Equations 3.14 - 3.19 (Morris, 1969 [75], Sayers, 1995 [77])

$$\Delta C_{11} = \frac{4\sqrt{2}}{105}\pi^2(2\sqrt{5}c_3W_{200} + 3c_1W_{400}) \quad (3.14)$$

$$\Delta C_{33} = -\frac{16\sqrt{2}}{105}\pi^2(\sqrt{5}c_3W_{200} - 2c_1W_{400}) \quad (3.15)$$

$$\Delta C_{12} = -\frac{4\sqrt{2}}{315}\pi^2(2\sqrt{5}(7c_2 - c_3)W_{200} - 3c_1W_{400}) \quad (3.16)$$

$$\Delta C_{13} = \frac{4\sqrt{2}}{315}\pi^2(\sqrt{5}(7c_2 - c_3)W_{200} - 12c_1W_{400}) \quad (3.17)$$

$$\Delta C_{44} = -\frac{2\sqrt{2}}{315}\pi^2(\sqrt{5}(7c_2 + c_3)W_{200} + 24c_1W_{400}) \quad (3.18)$$

$$\Delta C_{66} = \frac{4\sqrt{2}}{315}\pi^2(\sqrt{5}(7c_2 + c_3)W_{200} + 3c_1W_{400}) \quad (3.19)$$

In Equations 3.15 - 3.19, the c_i 's are expressed in terms of elements c_{ij} of the

single crystal elastic stiffness tensor as per Equations 3.20 - 3.22. For an isotropic crystal each of these estimates are identically zero.

$$c_1 = c_{11} + c_{33} - 2c_{13} - 4c_{44} \quad (3.20)$$

$$c_2 = c_{11} - 3c_{12} + 2c_{13} - 2c_{44} \quad (3.21)$$

$$c_3 = 4c_{11} - 3c_{33} - c_{13} - 2c_{44} \quad (3.22)$$

3.2.2.2 Approximate Reuss formulations

The general expression for the effective Reuss compliance tensor of an aggregate is given by Equation 3.23, where S_{ijkl}^{iso} is the Reuss estimate of the isotropic poly-crystal compliance, and ΔS_{ijkl} is the corresponding anisotropic deviation. The non-zero elements of S_{ijkl}^{iso} are given by equations 3.24 - 3.26, where s_{ij} are the elements of the single crystal (hexagonal) compliance tensor in Voigt notation.

$$S_{ijkl} = S_{ijkl}^{iso} + \Delta S_{ijkl} \quad (3.23)$$

$$S_{11}^{iso} = S_{22}^{iso} = S_{33}^{iso} = \frac{1}{15}(8s_{11} + 3s_{33} + 4s_{13} + 2s_{44}) \quad (3.24)$$

$$S_{12}^{iso} = S_{23}^{iso} = S_{31}^{iso} = \frac{1}{15}(s_{11} + s_{33} + 5s_{12} + 8s_{13} - s_{44}) \quad (3.25)$$

$$S_{44}^{iso} = S_{55}^{iso} = S_{66}^{iso} = \frac{2}{15}(7s_{11} + 2s_{33} - 5s_{12} - 4s_{13} + 3s_{44}) \quad (3.26)$$

Approximate closed form solutions for the components of ΔS_{ijkl} for the polycrystal Reuss averaged compliance tensor of a hexagonal aggregate composed of hexagonal micro-domains is given as per Equations 3.27 - 3.32 (Sayers, 1987 [79])

$$S_{11} = S_{44}^{iso} + \frac{4\sqrt{2}}{105}\pi^2(2\sqrt{5}s_3W_{200} + 3s_1W_{400}) \quad (3.27)$$

$$S_{33} = S_{33}^{iso} - \frac{16\sqrt{2}}{105}\pi^2(\sqrt{5}s_3W_{200} - 2s_1W_{400}) \quad (3.28)$$

$$S_{12} = S_{12}^{iso} - \frac{4\sqrt{2}}{315}\pi^2(2\sqrt{5}(7s_2 - s_3)W_{200} - 3s_1W_{400}) \quad (3.29)$$

$$S_{13} = S_{13}^{iso} + \frac{4\sqrt{2}}{315}\pi^2(\sqrt{5}(7s_2 - s_3)W_{200} - 12s_1W_{400}) \quad (3.30)$$

$$S_{44} = S_{44}^{iso} - \frac{8\sqrt{2}}{315}\pi^2(\sqrt{5}(7s_2 + s_3)W_{200} + 24s_1W_{400}) \quad (3.31)$$

$$S_{66} = 2(S_{11} - S_{12}) \quad (3.32)$$

In Equations 3.28 - 3.32, the s_i 's are expressed in terms of elements s_{ij} of the single crystal elastic compliance tensor as per Equations 3.33 - 3.35. For an isotropic crystal each of these estimates are identically zero.

$$s_1 = s_{11} + s_{33} - 2s_{13} - s_{44} \quad (3.33)$$

$$s_2 = s_{11} - 3s_{12} + 2s_{13} - s_{44}/2 \quad (3.34)$$

$$s_3 = 4s_{11} - 3s_{33} - s_{13} - s_{44}/2 \quad (3.35)$$

3.2.3 Discretized formulations

We computed the integrals in Equations 3.3 and 3.6 as discretized summations as given by Equations 3.36 and 3.37 to compare against the corresponding estimates from the Legendre polynomial approximations. We did this comparison for two different ODFs (compaction ODF and fisher ODF) and for each ODF, two different micro-domains (mica-muscovite and Ulm's shale), detailed in the subsequent sections. In each case, the results from the Legendre polynomial approximations were in excellent agreement with those from the discretized summations.

$$C_{Voigt}^* = \sum_{\phi=0}^{2\pi} \sum_{\psi=0}^{2\pi} \sum_{\theta=0}^{\pi} W(\theta, \psi, \phi) \sin\theta [C^{(\theta, \psi, \phi)}] d\theta d\psi d\phi \quad (3.36)$$

$$S_{Reuss}^* = \sum_{\phi=0}^{2\pi} \sum_{\psi=0}^{2\pi} \sum_{\theta=0}^{\pi} W(\theta, \psi, \phi) \sin\theta [S^{(\theta, \psi, \phi)}] d\theta d\psi d\phi = [C_{Reuss}^*]^{-1} \quad (3.37)$$

In our discretized implementation, we discretized the Euler angles adaptively, such when the probability density is less uniform, the discretization is finer to capture the ODF sufficiently. As an example, for the compaction ODF, we used $d\theta = d\psi = d\phi = \pi/(25 * a)$, ‘a’ indicating the level of compaction, and hence the non-uniformity in the ODF. As a check for sufficient discretization, for every C_{Voigt}^* and C_{Reuss}^* we also computed the sum $\sum_{\phi=0}^{2\pi} \sum_{\psi=0}^{2\pi} \sum_{\theta=0}^{\pi} W(\theta, \psi, \phi) \sin\theta d\theta d\psi d\phi$ to make sure it was sufficiently close to 1, hence satisfying the normalization condition given by Equation 3.1.

3.2.4 The VRH or Average Tensor

In the previous chapter we discussed the Voigt-Reuss-Hill (VRH) estimates of the bulk and shear moduli of isotropic poly-crystal aggregates (Hill, 1952 [28]). Generalizing the concept further for anisotropic aggregates, we can define a VRH tensor, as an average of the iso-strain Voigt and iso-stress Reuss stiffness tensors (Zuo et al., 1992 [80], Man and Huang, 2011 [81]), as shown in Equation 3.38.

$$C_{Hill} = [C_{Voigt} + (S_{Reuss})^{-1}]/2 \quad (3.38)$$

The Hill approximation generally gives good results but may fail in case of large grain-shape anisotropy (Zuo et al., 1992 [80]). This in line with our observations from self-consistent modeling in the previous chapter, where self-consistent estimates for spherical grain-shapes were often close to the Hill estimate while deviation from grain sphericity caused deviation from the Hill moduli values. Empirically, the VRH estimates had in most cases accuracies comparable to results obtained from more sophisticated modeling techniques such as self-consistent schemes, and were often adequate for several practical applications (Hu, 1980 [82], Hirao et al., 1987 [83], Hirsekorn, 1990 [84]).

3.3 Voigt-Reuss modeling results

3.3.1 Chosen micro-domains and their elastic parameters

For the purpose of this study we choose two different VTI micro-domains. The first is a ‘mica-muscovite’ representing single crystal properties of illite (Tosaya, 1982, [71]) might be seen in a pure, highly aligned and anisotropic clay-aggregate. The second is an ‘Ulm’s shale’ unit, representing a fundamental building block of shale elasticity behavior (Ortega et. al, 2007 [48]), with relatively lower anisotropy. The elastic

stiffness tensor for mica-muscovite crystals is given in units of GPa by 3.39 (Sayers, 2005 [85]; Tosaya 1982 [71]), and the corresponding Thomsen parameters are: $\epsilon = 1.12$, $\gamma = 2.28$, $\delta = -0.2368$. The stiffness tensor for Ulm's unit is given by 3.40 and has Thomsen parameters: $\epsilon = 0.43$, $\gamma = 1.07$, $\delta = 0.06$.

$$C_{musc} = \begin{bmatrix} 178 & 42.4 & 14.5 & 0 & 0 & 0 \\ 42.4 & 178 & 14.5 & 0 & 0 & 0 \\ 14.5 & 14.5 & 54.9 & 0 & 0 & 0 \\ 0 & 0 & 0 & 12.2 & 0 & 0 \\ 0 & 0 & 0 & 0 & 12.2 & 0 \\ 0 & 0 & 0 & 0 & 0 & 67.8 \end{bmatrix}, \quad \epsilon = 1.12, \gamma = 2.28, \delta = -0.2368 \quad (3.39)$$

$$C_{ulm} = \begin{bmatrix} 44.9 & 21.7 & 18.1 & 0 & 0 & 0 \\ 21.7 & 44.9 & 18.1 & 0 & 0 & 0 \\ 18.1 & 18.1 & 24.2 & 0 & 0 & 0 \\ 0 & 0 & 0 & 3.7 & 0 & 0 \\ 0 & 0 & 0 & 0 & 3.7 & 0 \\ 0 & 0 & 0 & 0 & 0 & 11.6 \end{bmatrix}, \quad \epsilon = 0.43, \gamma = 1.07, \delta = 0.06 \quad (3.40)$$

3.3.2 Chosen Orientation Distribution Functions

We discussed in the previous chapter how materials with vertical transverse isotropy (VTI) are of special interest in geophysical applications. In this chapter our analyses are based on VTI micro-domains aligned as per VTI orientation distribution functions (ODFs), result in aggregates with VTI symmetry. Since VTI ODFs are symmetric about vertical axes, they are functions of a single Euler angle, ' θ ', representing the tilt

of a domain symmetry axis w.r.t. the vertical axis in the global co-ordinate system. For our analyses in this chapter, we choose two different VTI ODFs.

The first chosen ODF is related to mechanical compaction of sediments. Initial deposition of clay platelets in a flocculated state followed by subsequent bioturbation (Bennet et al., 1991, [86]) results in fresh sea floor sediments having random/isotropic orientation of clay minerals. While the newly formed clay has porosity of the order of 70-80%, at larger depths this porosity reduces to about 10% (Kastube and Williamson, 1994, [87]). Attributing the loss in porosity primarily to mechanical compaction, yields compaction factors of 3-5. The corresponding change in the ODF of fresh sediments from isotropic to increasingly aligned due to mechanical compaction alone (Owens, 1973 [88], Baker et al., 1993 [89]) can be represented by a ‘compaction ODF’, given by Equation 3.41.

$$W_c(\theta, \psi, \phi) = \frac{1}{8\pi^2} \frac{a^2}{(\cos^2(\theta) + a^2 \sin^2(\theta))^{3/2}} \quad (3.41)$$

In this equation, the compaction factor $a \geq 1$ is the aspect ratio of the strain ellipse representing the ratio of the initial to the final thickness of the compacted layer. It is assumed that compaction occurs in the vertical direction only, with no shear strain, such that a layer with an initial unit thickness will have thickness $1/a$.

Figure 3.2 shows the projections of compaction ODFs for compaction factors $a = 1, 3$ and 9 on a vertical plane, the bold red numbers indicating the scale for the ODF magnitudes in the polar plots. At $a = 1$, or initial sediment state, the clay platelets are uniformly oriented, as indicated by the circular projection of the ODF. As compaction increases ($a > 1$) the platelet axes increasing line up with the vertical direction ($\theta = 0, \pi$).

The second ODF is a statistical model called Fisher distribution, originally introduced to analyze paleomagnetic data (Watson, 1966, [90]), given by Equation 3.42.

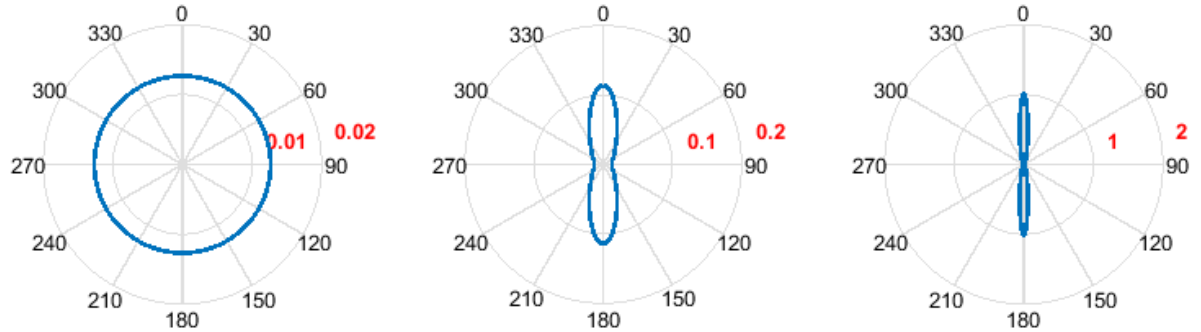


Figure 3.2: (L-R) Compaction ODF polar plots (projection of the 3D ODF on a vertical plane) for compaction factors $a = 1, 3$ and 9 . As compaction factor increases, more micro-domains become horizontal, and their TI symmetry axes have larger probability density in the vertical directions, close to $\theta = 0$ or π .

In the Fisher distribution, concentration factor c correlates directly with the degree of scattering in the ODF, and $k_F(c)$ is a constant chosen to satisfy the normalization condition given by Equation (odfnorm). As in case of the compaction ODF, as ‘ c ’ increases, micro-domains are more aligned, with their symmetry axes in the vertical direction ($\theta = 0, \pi$), as shown in Figure 3.3

$$f_F(\theta) = \frac{1}{2\pi} k_F(c) \exp(c \cos(\theta)) \quad (3.42)$$

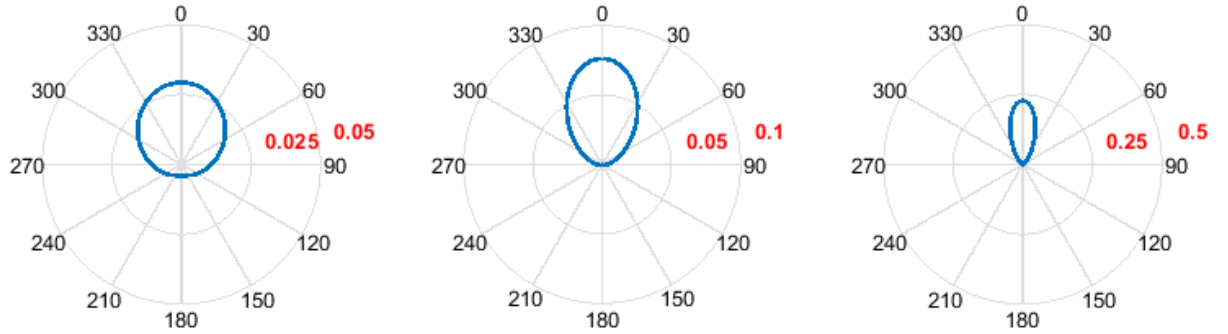


Figure 3.3: (L-R) Fisher ODF polar plots (projection of the 3D ODF on a vertical plane) for concentration factors $c = 1, 3$ and 9 . As concentration factor increases, more micro-domains become horizontal, and their TI symmetry axes have larger probability density in the vertical directions, close to $\theta = 0$ or π .

3.3.3 Voigt-Reuss modeling for compaction ODF

Figures 3.4 and 3.5 show the difference between Voigt and Reuss estimates of various macro-composite elastic properties with increasing domain alignment of the compaction ODF for the mica-muscovite and Ulm's shale micro-domains respectively. In addition to the two moduli (C_{33} and C_{44}) and three Thomsen parameters (ϵ , γ and δ), the figures also show the behavior of the normalized anellipticity parameter η (Alkhalifah and Tsvankin, 1995 [91]), important in seismic applications, given by Equation 3.43.

$$\eta = \frac{\epsilon - \delta}{1 + 2\delta} \quad (3.43)$$

The figures also show estimates of the 6 elastic parameters mentioned for the VRH tensor, average of the Voigt and Reuss stiffness tensors, labeled as ‘AT’ (for Average Tensor). Elastic parameters corresponding to the VRH tensor lie almost midway between those of the Voigt and Reuss tensors. Figure 3.4 also shows the comparison

between Voigt and Reuss estimates using Legendre polynomial approximations (labeled ‘Voigt-poly’ and ‘Reuss-poly’) and discretized summations (labeled ‘Voigt-num’ and ‘Reuss-num’). It is evident that the two methods lead to very similar results, and for future analyses we simply use the computationally efficient Legendre polynomial approximations.

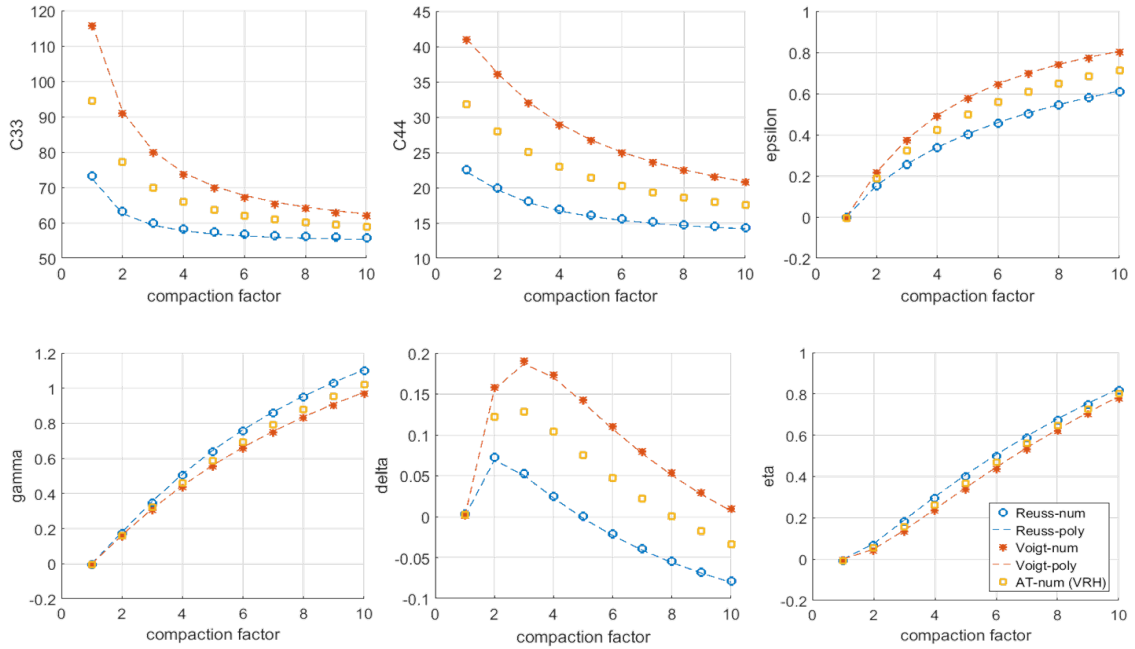


Figure 3.4: Difference between Voigt and Reuss estimates of various macro-composite elastic properties as they vary with increasing domain alignment (for the compaction ODF) for mica-muscovite micro-domains. The figure also shows comparison between Voigt and Reuss estimates using Legendre polynomial approximations (labeled ‘Voigt-poly’ and ‘Reuss-poly’) and discretized summations (labeled ‘Voigt-num’ and ‘Reuss-num’). It is evident that the two methods lead nearly identical results.

Both figures show that the moduli and anisotropy parameters calculated using the Voigt and Reuss schemes are systematically and often considerably different from each other. The anisotropy parameters are 0 for the perfectly disordered case ($a = 1$). With increasing alignment composite elastic parameters trend towards the single domain properties listed in Section 3.3.1. Unlike in the isotropic case, choosing

one scheme over the other for a VTI composite does not systematically over/underestimate all of the composite elastic parameters of interest. This is not unexpected, as only the eigenvalues of the Voigt tensor are guaranteed to be greater than or equal to the corresponding eigenvalues of the Reuss tensor. Eigenvalues for VTI stiffness tensors, expressed in their Voigt notation tensor components, are given by Equations 3.44 (Mehrabadi and Cowin, 1990 [57], Mavko et al., 2009 [19]).

$$\begin{aligned} eig1 &= c_{33} + \sqrt{2}c_{13}(\beta + \sqrt{\beta^2 + 1}), & \beta &= \frac{\sqrt{2}}{4c_{13}}(c_{11} + c_{12} - c_{33}) \\ eig2 &= c_{33} + \sqrt{2}c_{13}(\beta - \sqrt{\beta^2 + 1}) \\ eig3 &= c_{11} - c_{12} = 2c_{66} \\ eig4 &= 2c_{44} \end{aligned} \tag{3.44}$$

In both our examples, Voigt gives higher estimates of C_{33} , C_{44} , ϵ and δ , while Reuss gives higher estimates of γ and η . It is interesting to note that the parameters converge differently with increasing domain alignment, quantified by increasing values of the compaction factor ‘a’. As an example at a compaction factor of 10, for both micro-domains, the Voigt and Reuss estimates of C_{33} are very close to converging to the single crystal C_{33} value (54.9 GPa for mica-muscovite, 24.2 GPa for Ulm’s shale). On the other hand, at the same compaction factor, the Voigt and Reuss estimates of Thomsen parameter δ are quite different from each other, and in case of mica-muscovite, quite far from the single crystal δ value of -0.2368.

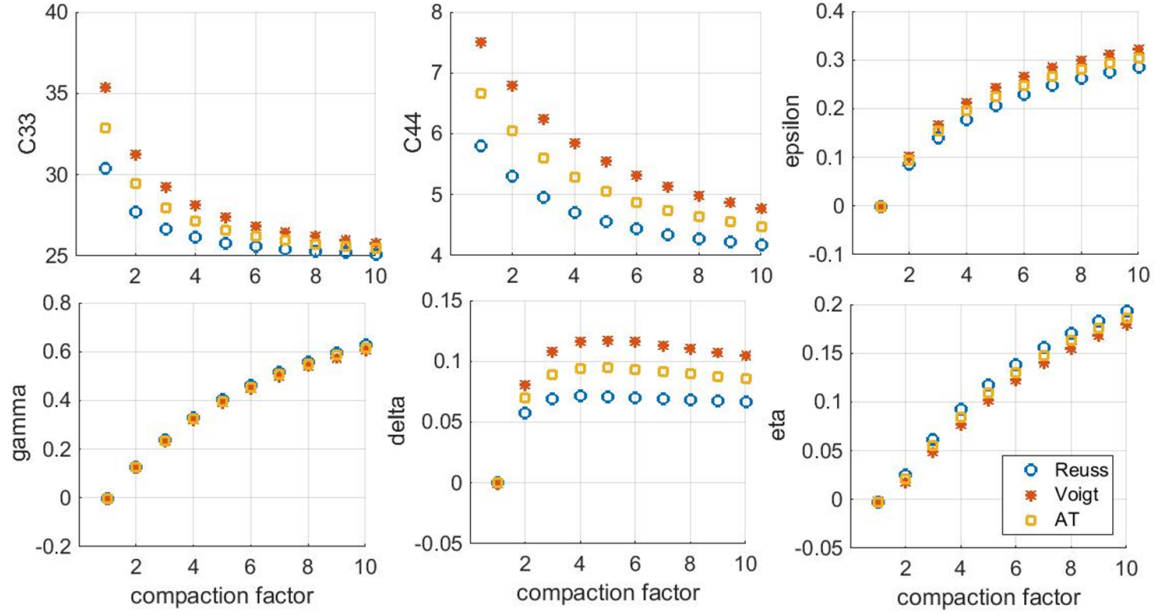


Figure 3.5: Difference between Voigt and Reuss estimates of various macro-composite elastic properties as they vary with increasing domain alignment (for the compaction ODF) for Ulm's shale micro-domains.

3.3.4 Voigt-Reuss modeling for Fisher ODF

Observations made by running the mica-muscovite and Ulm's shale micro-domains through the Fisher ODF are very similar to those made with the compaction ODF, shown in Figures 3.6 and 3.7. As with the compaction ODF, Voigt averaging gives higher estimates of C_{33} , C_{44} , ϵ and δ , while Reuss gives higher estimates of γ and η for both the micro-domains. With increasing domain alignment, represented by increasing values of the concentration factor ‘ c ’, both Voigt and Reuss estimates of the composite C_{33} converge rapidly to the micro-domain C_{33} value, while for Thomsen parameter δ , Voigt and Reuss estimates differ significantly.

Elastic parameters of the Average Tensor lie almost mid-way between the parameters from Voigt and Reuss tensors for both micro-domains. This combined with the

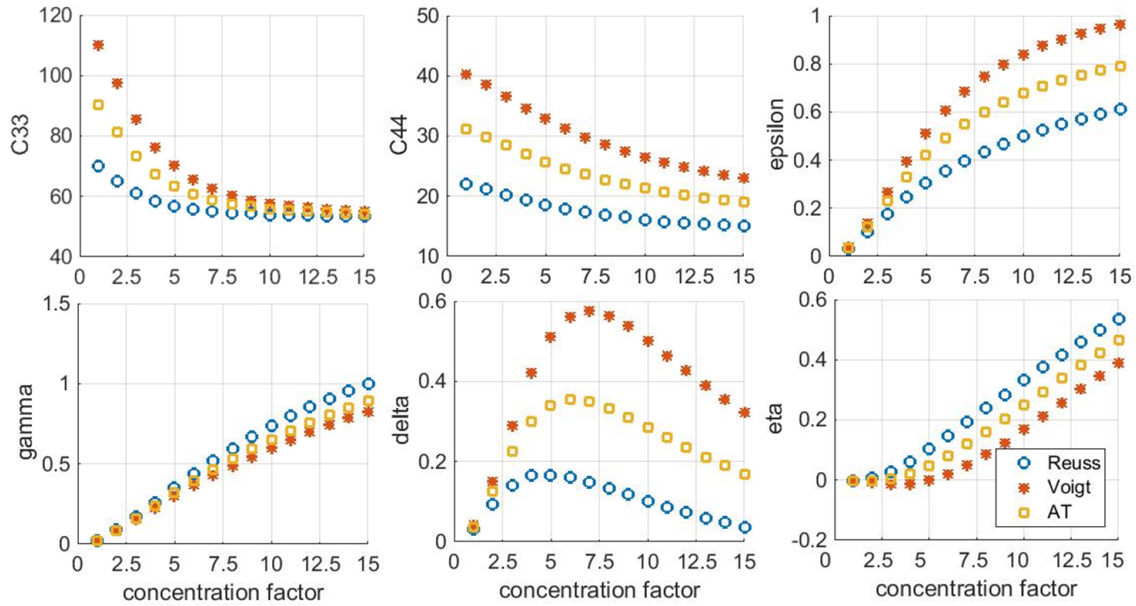


Figure 3.6: Difference between Voigt and Reuss estimates of various macro-composite elastic properties as they vary with increasing domain alignment (for the Fisher ODF) for mica-muscovite micro-domains.

discussion in Section 3.2.4, and the wide success of VRH estimates in isotropic polycrystals might indicate that the VRH tensor might be a good starting point to get a working approximation for the effective elastic properties of anisotropic poly-crystals.

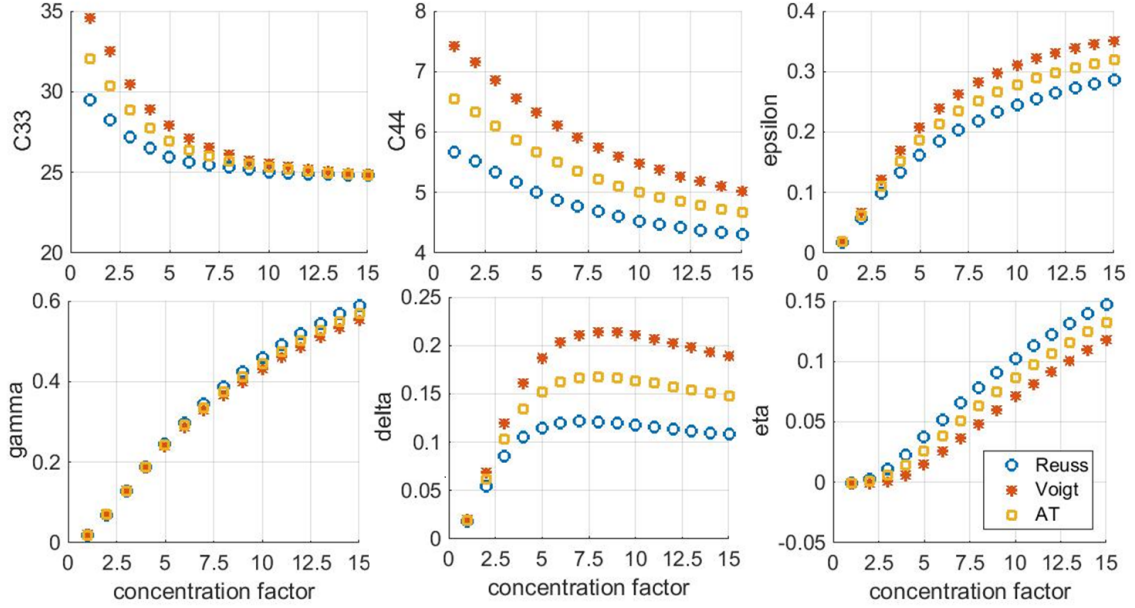


Figure 3.7: Difference between Voigt and Reuss estimates of various macro-composite elastic properties as they vary with increasing domain alignment (for the Fisher ODF) for Ulm's shale micro-domains.

3.3.5 Thomsen parameter delta

Thomsen parameter δ is key to understanding the difference between the small-offset normal move-out velocity and vertical velocity and it is also essential for small-offset AVO interpretation (Thomsen, 1986 [15], Sayers, 2005 [85]) making it very important in seismic geophysics. However, the sign of this parameter is not well understood, and it can assume both positive and negative values. As an example, single crystal elastic constants for clay minerals often involve negative values of δ (Alexander and Kyzhov, 1961 [92], Katahara, 1996 [60]) while measurements on clay-rich shale samples exhibit positive δ values (Jones and Wang, 1981 [93], Vernik and Nur, 1992 [94], Hornby, 1994 [17], Johnston and Christensen, 1995 [95], and Wang, 2002, [96]. Sayers (Sayers, 2005 [85]) conducted a detailed study on the sign of δ and one plausible explanation that he came up with for the change in sign in going from single clay crystals to clay-rich

shales was misalignment of clay particles.

This is exactly what we see in our mica-muscovite sample, used as a representative for illite, a common clay mineral, for both the compaction and Fisher ODFs. Single crystal mica-muscovite has a negative value of δ (-0.2368). Figures 3.4 and 3.6 show that the negative δ in the mica-muscovite domains develops a positive-peaked bulge with increasing disorder (lower compaction/concentration factors) before going to 0 in the perfectly disordered, isotropic composite. For both ODFs, the positive peaks occur close to but not quite at the point of isotropy, representing partial misalignment, consistent with Sayers' observation. A less pronounced but similar bulge is also present for the Ortega micro-domain.

It is worth noting that δ is the only composite elastic parameter that does not show a monotonic change with increasing alignment of the micro-domains (with increasing compaction/concentration factors). In addition, the peak of positive delta values coincide approximately with the largest difference between the Voigt and Reuss estimates of δ . This might mean that at the level of domain misalignment typical of naturally occurring shales, the choice of Voigt vs. Reuss averaging scheme makes the most difference in the estimate of the critical seismic anisotropy parameter δ .

3.3.6 Monte-Carlo analysis of anisotropic poly-crystals

In the previous subsections we studied the difference between Voigt and Reuss estimates of elastic parameters for anisotropic poly-crystals based on two specific micro-domains, mica-muscovite and Ulm's fundamental shale unit. In this section we attempt a more global understanding of VTI poly-crystals using Monte-Carlo simulations. We start with the 42,000 distinct VTI micro-domain samples vetted in Chapter 2, using various theoretical and practical constraints. For each of these micro-domains we compute the poly-crystal elastic parameters for the compaction ODF at a compaction factor of 3 (corresponding approximately to the largest different between

Voigt and Reuss estimates of Thomsen parameter δ).

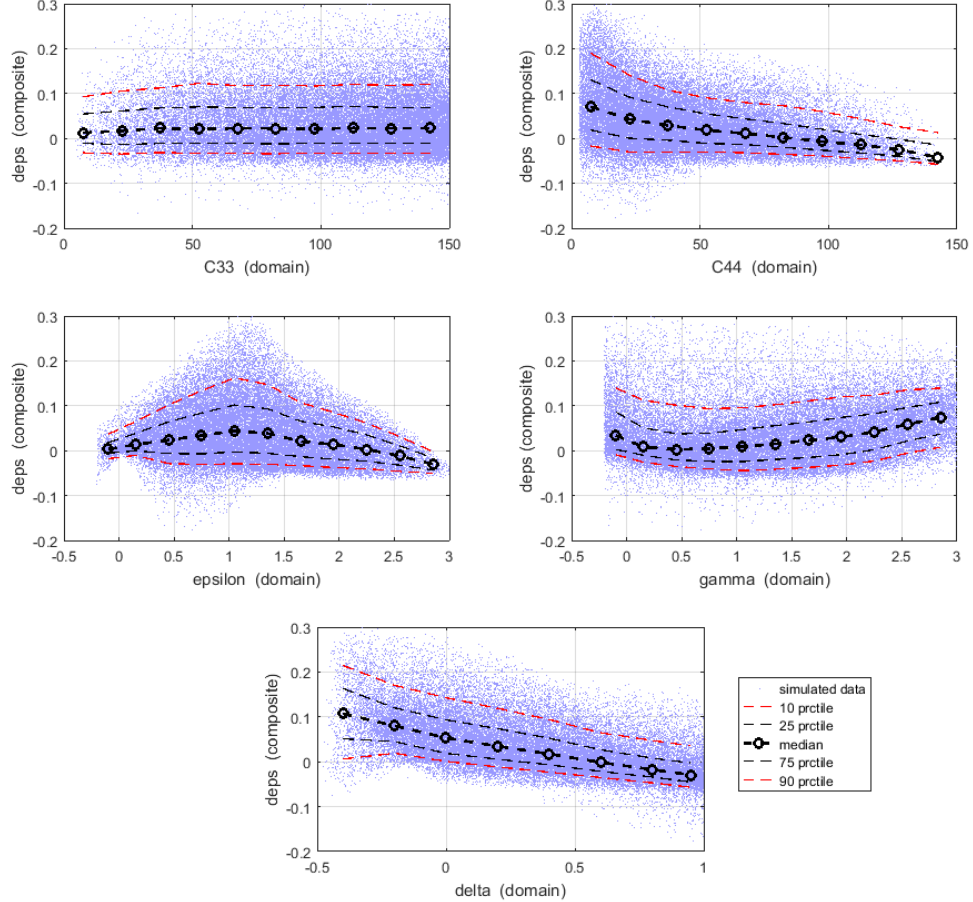


Figure 3.8: Difference ($deps$) between Voigt and Reuss estimates of macro-composite elastic parameter ϵ with micro-domain parameters C_{33} , C_{44} , ϵ , γ and δ for a compaction ODF with a compaction factor of 3.

Figure 3.8 shows the variation of the difference between Voigt and Reuss estimates of macro-composite Thomsen parameter ϵ , labeled ‘ $deps$ ’ ($= \epsilon_{Voigt} - \epsilon_{Reuss}$) with micro-domain parameters C_{33} , C_{44} , ϵ , γ and δ (labeled ‘c33’, ‘c44’, ‘eps’, ‘gam’ and ‘del’ respectively). The median and the 10th, 25th, 75th and 90th percentile lines

are plotted in each sub-figure. Immediately, we can see that while for of our specific examples in the previous subsections Voigt estimates of ϵ were greater than the corresponding Reuss estimates, this is not universally true, as proven by the negative values of ‘*deps*’, which seem to correlate well with large positive values of the domain Thomsen parameter δ .

The Monte-Carlo samples and results are also analyzed to better understand relative influence of the micro-domain elastic properties on the macro-composite ‘*deps*’ using gradient boosted tree meta-models (GBM) as outlined in the previous chapter. The top panel of Figure 3.9 shows the results of the the GBM analysis, with the percent relative influences on the left and the fit of the GBM meta-model to a blind test set (showing good match) on the right. We can see that on an average, micro-domain parameters δ and ϵ have the greatest relative influence on the difference between Voigt and Reuss estimates of macro-composite Thomsen parameter ϵ , for a factor 3 compaction ODF.

To further understand the nature of variation of composite ‘*deps*’ with variation in values of the two domain parameters of maximum relative influence, the bottom panel of Figure 3.9 shows a two-way partial dependence plot of ‘*deps*’ (plot color) with δ (x-axis) and ϵ (y-axis). Partial dependence plots show the dependence between a target response (*deps* in this case) and a set of target variables (δ and ϵ in this case), marginalizing over the values of all other variables (the ‘complement’ variables). In this case, our two-way partial dependence plot shows the dependence of median ‘*deps*’ on joint values of δ and ϵ . It shows that the largest positive values of composite ‘*deps*’ occur for two distinct combinations of domain parameters δ and ϵ : low δ (< -0.2) - high ϵ (> 0.75) and high δ (> 0.3) - low ϵ (< 0). Largest negative values of ‘*deps*’ occur primarily for high δ (> 0.5) - high ϵ (> 1.5) and to a small extent for low δ (< -0.25) - low ϵ (< 0).

Similarly, Figure 3.10 shows the variation of the difference between Voigt and

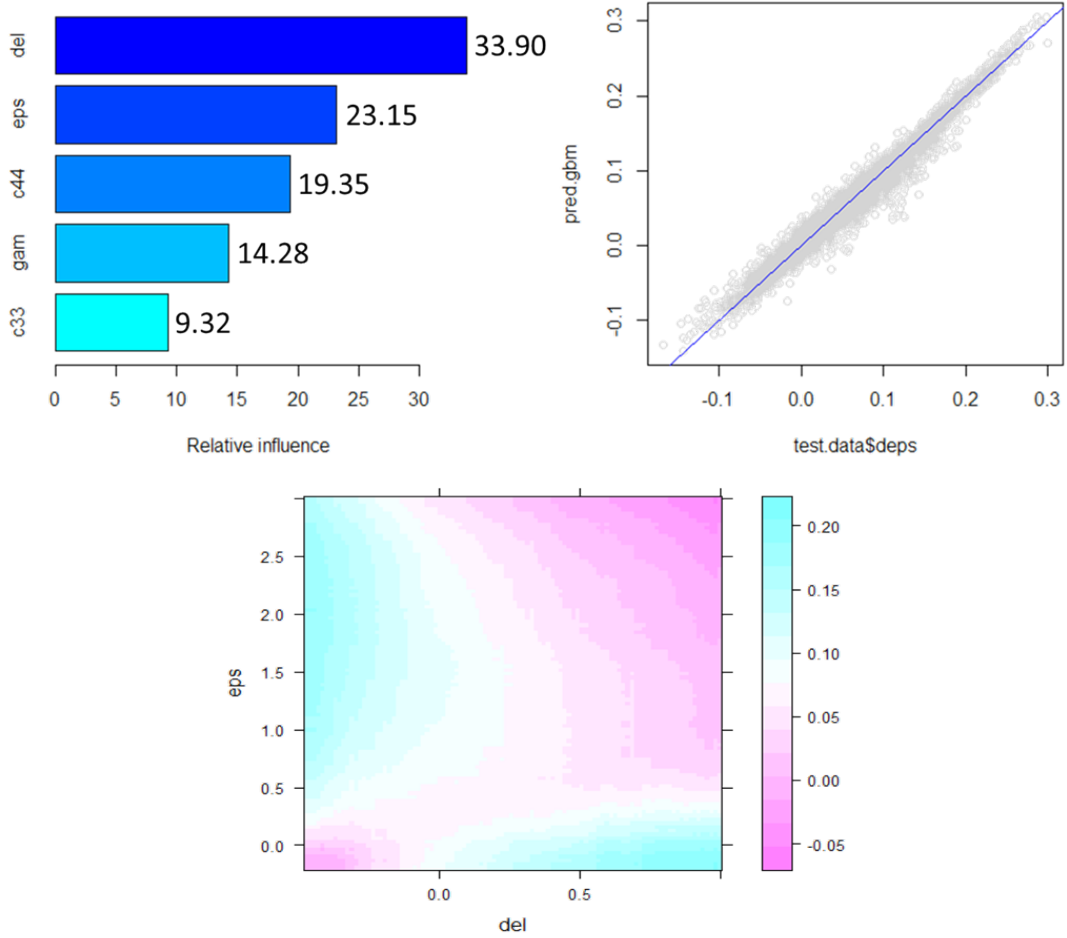


Figure 3.9: Clockwise from left: Relative influence of various micro-domain parameters on the Voigt-Reuss difference ‘*deps*’ in the estimated composite parameter ϵ using GBM on Monte-Carlo samples (for compaction ODF with compaction factor 3); Goodness of GBM fit, demonstrated by comparing true *deps* (‘*test.data\$deps*’) and GBM predicted *deps* (‘*pred.gbm*’) on a blind test dataset; 2-way partial dependence plot showing the variation in composite *deps* with joint variation in domain parameters δ (‘*del*’) and ϵ (‘*eps*’).

Reuss estimates of macro-composite Thomsen parameter γ , labeled ‘*dgam*’ ($= \gamma_{Voigt} - \gamma_{Reuss}$) with micro-domain parameters C_{33} , C_{44} , ϵ , γ and δ . In the figure, the median and the 10th, 25th, 75th and 90th percentile lines are plotted in each sub-figure. We can

see that while for our specific examples in the previous subsections Voigt estimates of γ were lesser than the corresponding Reuss estimates, this is not universally true, as proven by the positive values of ‘ $d\gamma$ ’, which seem to correlate well with large positive values of the domain Thomsen parameters γ and δ . In fact the largest positive value of composite ‘ $d\gamma$ ’ increases monotonically with domain γ .

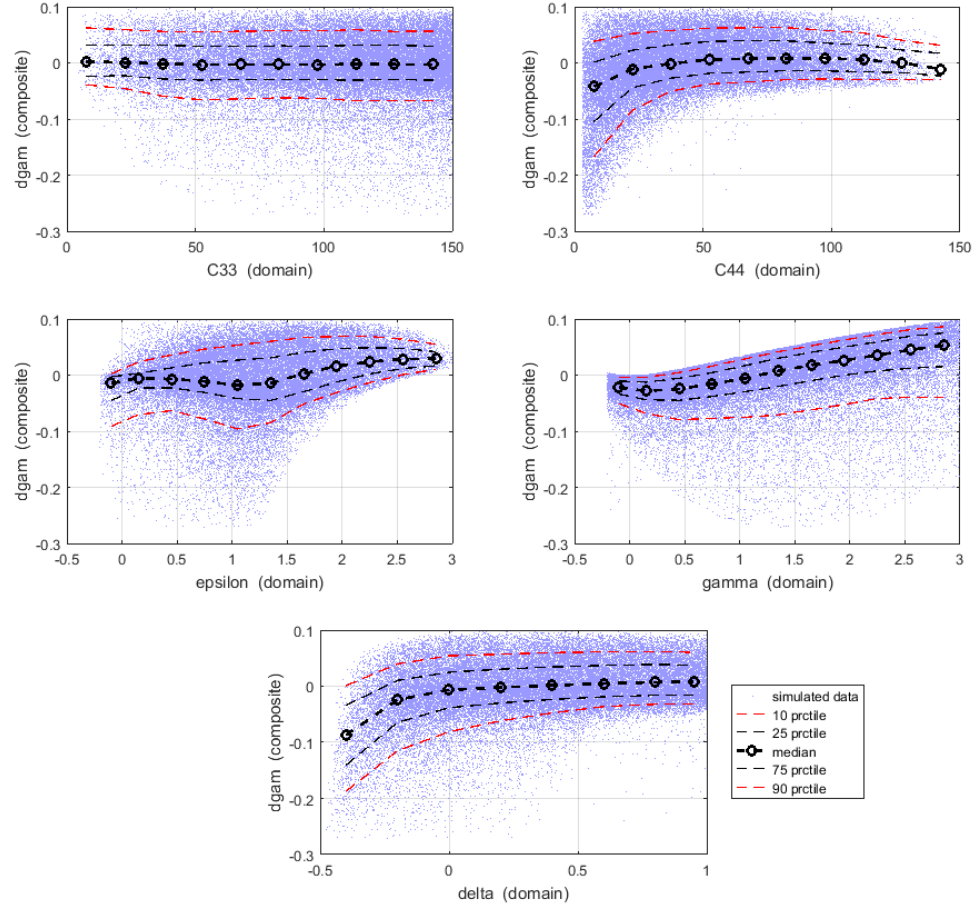


Figure 3.10: Difference ($d\gamma$) between Voigt and Reuss estimates of macro-composite elastic parameter γ with micro-domain parameters C_{33} , C_{44} , ϵ , γ and δ for a compaction ODF with a compaction factor of 3. The largest positive value of composite ‘ $d\gamma$ ’ increases monotonically with domain γ

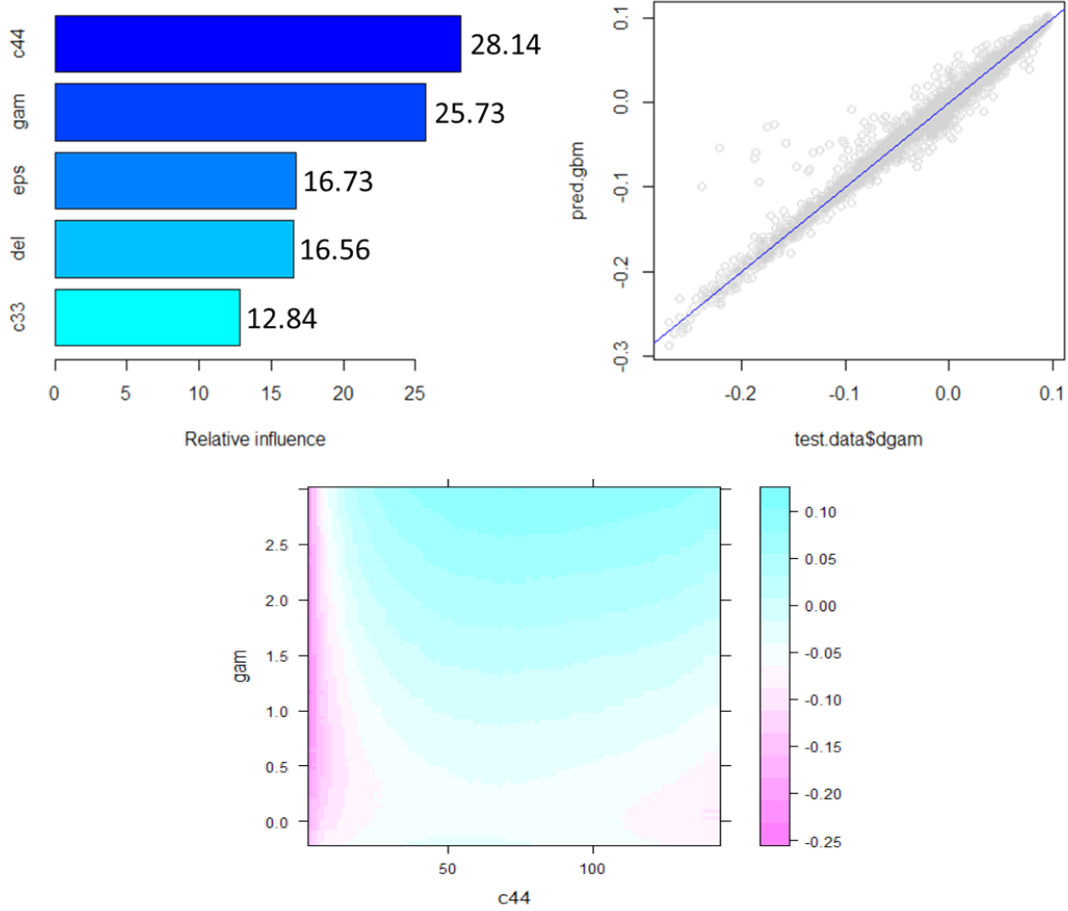


Figure 3.11: Clockwise from left: Relative influence of various micro-domain parameters on the Voigt-Reuss difference ‘ $dgam$ ’ in the estimated composite parameter γ using GBM on Monte-Carlo samples (for compaction ODF with compaction factor 3); Goodness of GBM fit, demonstrated by comparing true $dgam$ (‘`test.data$dgam`’) and GBM predicted $dgam$ (‘`pred.gbm`’) on a blind test dataset; 2-way partial dependence plot showing the variation in composite $dgam$ with joint variation in domain parameters C_{44} and γ (‘`gam`’).

The top panel of Figure 3.11 shows the results of GBM analysis on Monte-Carlo samples and results, to better understand relative influence of the micro-domain elastic properties on the macro-composite ‘ $dgam$ ’. The GBM meta-model shows good

match to the analytical model for a blind test set data (right sub-figure). We can see that on an average, micro-domain parameters c_{44} and γ have the greatest relative influence on the difference between Voigt and Reuss estimates of macro-composite Thomsen parameter γ , for a factor 3 compaction ODF. The bottom panel of the figure shows the two-way partial dependence plot for median ‘ $dgam$ ’ (plot color) on joint values of c_{44} (x-axis) and γ (y-axis), the domain parameters with maximum relative influence. The plot reveals that the largest negative values of ‘ $dgam$ ’ occur for very low values of c_{44} (<6 GPa) while the largest positive values correspond to high values of γ (>2.5).

Finally, Figure 3.12 shows the variation of the difference between Voigt and Reuss estimates of macro-composite Thomsen parameter δ , labeled ‘ $ddel$ ’ ($= \delta_{Voigt} - \delta_{Reuss}$) with micro-domain parameters C_{33} , C_{44} , ϵ , γ and δ . As usual, the median and the 10th, 25th, 75th and 90th percentile lines are plotted in each sub-figure. It is evident that while for of our specific examples in the previous subsections Voigt estimates of δ were greater than the corresponding Reuss estimates, this is not universally true, as proven by the negative values of ‘ $ddel$ ’, which correlate well with large positive values of the domain Thomsen parameter δ , and small values of parameter γ .

Figure 3.13 shows the results of GBM analysis on Monte-Carlo samples and results, to understand relative influence of the micro-domain elastic properties on the macro-composite ‘ $ddel$ ’. The GBM meta-model shows good match to the analytical model for a blind test set data (right sub-figure). We can see that on an average, micro-domain parameters γ and δ have the greatest relative influence on the difference between Voigt and Reuss estimates of macro-composite Thomsen parameter δ , for a factor 3 compaction ODF. The bottom panel of the figure shows the two-way partial dependence plot for median values of composite ‘ $ddel$ ’ (plot color) on joint values of γ (x-axis) and δ (y-axis), the domain parameters with maximum relative influence. The plot reveals that the largest positive values of ‘ $ddel$ ’ occur for high γ (2) - low

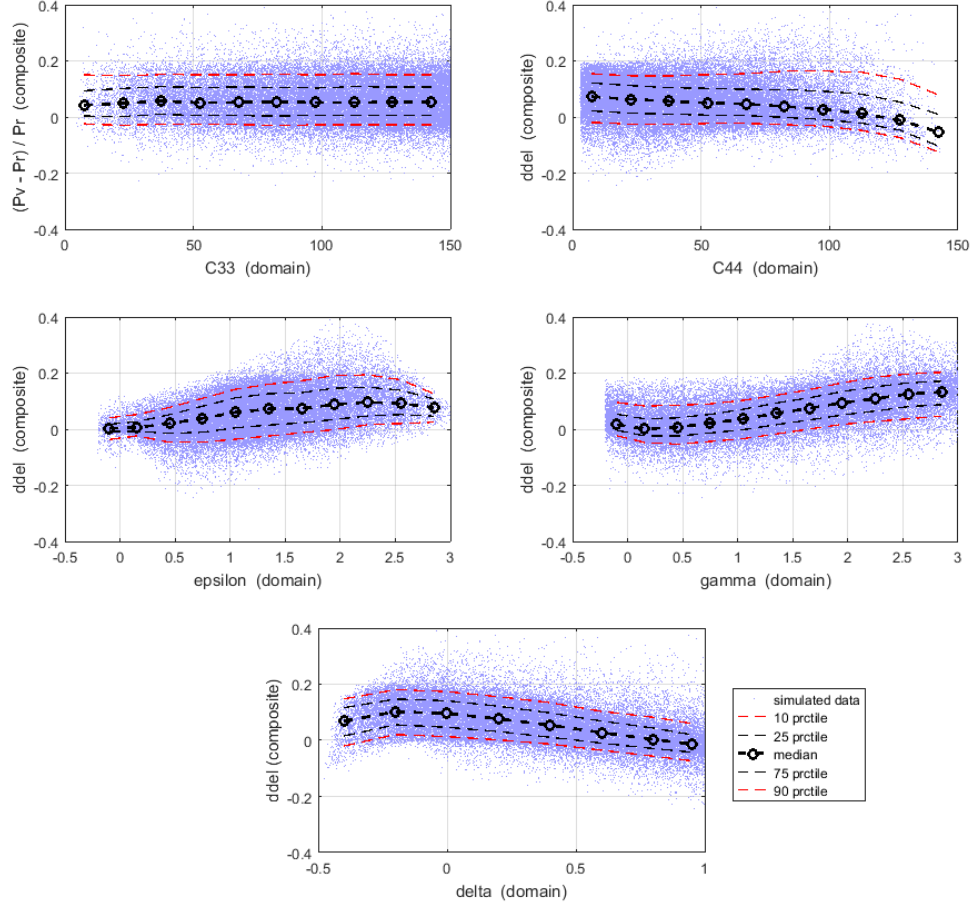


Figure 3.12: Difference ($ddel$) between Voigt and Reuss estimates of macro-composite elastic parameter δ with micro-domain parameters C_{33} , C_{44} , ϵ , γ and δ for a compaction ODF with a compaction factor of 3.

δ ($j0$) combinations. For γ values < 0.75 , the variation in $ddel$ is quite small.

As pointed out in Chapter 2, the relative influence values correspond to reduction of squared error attributable to each variable in optimizing a GBM model (Friedman, 2001 [50]), normalized to sum up to 100. The values reported here correspond to a specific realization of the training and test datasets, and are likely to vary slightly for a

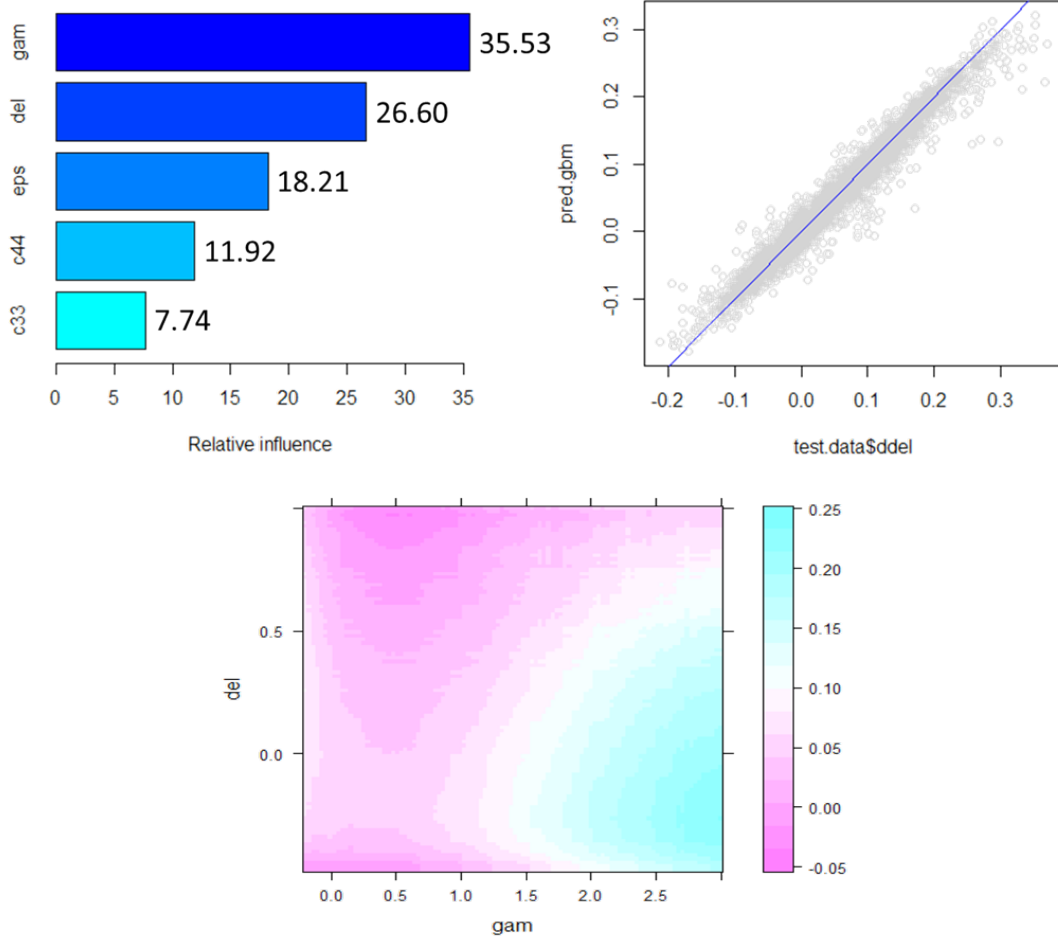


Figure 3.13: Clockwise from left: Relative influence of various micro-domain parameters on the Voigt-Reuss difference ‘*ddel*’ in the estimated composite parameter δ using GBM on Monte-Carlo samples (for compaction ODF with compaction factor 3); Goodness of GBM fit, demonstrated by comparing true *ddel* (‘*test.data\$ddel*’) and GBM predicted *ddel* (‘*pred.gbm*’) on a blind test dataset; 2-way partial dependence plot showing the variation in composite *ddel* with joint variation in domain parameters γ (‘*gam*’) and δ (‘*del*’).

different realization, without altering our primary inferences. In addition, expressing the impact of a specific micro-domain elastic parameter on the uncertainty in macro-scale elastic parameters in terms of GBM relative influence values is one of many ways

of quantifying what we qualitatively observe from the cross-plots. Relative influence values from our GBM analysis align well with our cross-plot observations. The simple method outlined in this sub-section is convenient and effective due to free and easy access to sophisticated statistical learning packages in recent times, and can be useful for first-pass analyses on measured/synthetic datasets.

3.3.7 Impact on Vp/Vs ratio

The ratio of the vertical P-wave wave velocity to the vertical S-wave velocity is an important parameter in formation evaluation, used for many purposes, such as a lithology indicator, determining porosity, saturation and degree of consolidation, identifying pore fluid, and predicting velocities (Pickett, 1963 [97], Gardner and Harris, 1968 [98], Gregory, 1976 [99], Tatham, 1982 [100], Hornby and Murphy, 1987 [101], Castagna et al., 1985 [102], Han et al., 1986 [24]) . The Vp/Vs ratio can depend on several factors like porosity, degree of consolidation, clay content, differential pressure, pore geometry, etc. For dry or gas-saturated rocks the velocity ratio is nearly constant irrespective of porosity and differential pressure, while for wet rocks it shows significant dependence on porosity and differential pressure (Lee, 2003 [103]). Mathematically, $V_p/V_s = \sqrt{c_{33}/\rho}/\sqrt{c_{44}/\rho} = \sqrt{c_{33}/c_{44}}$.

Figure 3.14 shows the difference between Voigt and Reuss estimates of the Vp/Vs ratio for the mica-muscovite (right) and Ulm's shale unit (left) domains, for the compaction ODF, with compaction factors varying from 1 (isotropic domain alignment) to 10 (strongly aligned domains). The figure shows that for our cases of interest, the Voigt estimate of the velocity ratio is lower than the Reuss estimate. As in case of the composite elastic parameter δ , the Vp/Vs ratio also does not change monotonically with increasing compaction factor, but has a negative crest for partially aligned domains, between compaction factors 2-3. It is interesting to note that while the relative differences between the Voigt and Reuss estimates of C_{33} and C_{44} decrease

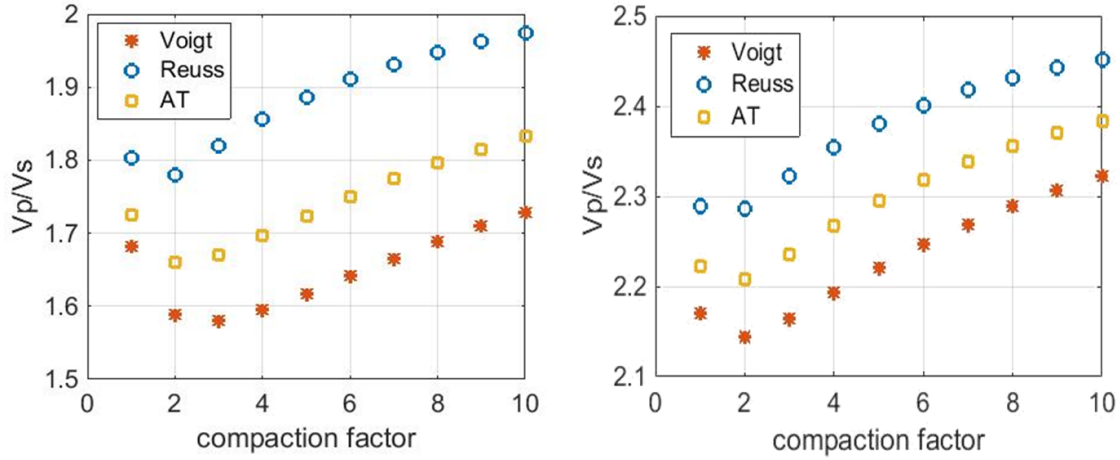


Figure 3.14: Difference between Voigt and Reuss estimates of V_p - V_s ratio with increasing domain alignment (using the compaction ODF) in (left): aggregates of mica-muscovite domains, and (right): aggregates of Ulm's shale unit domains.

steadily with increasing domain alignment (increasing values of compaction factor), their ratio does not show the same trend. In addition, the V_p / V_s ratio from the Average or VRH tensor (labeled ‘AT’), does not lie midway between the Voigt and Reuss estimates, but closer to the lower Voigt estimate, especially in case of mica-muscovite.

3.3.8 Impact on AVO

Amplitude variation with offset (AVO) refers to the variation in seismic reflection amplitude with change in shotpoint-receiver distance and is extensively used in seismic analysis as an indicator of lithology and fluid content changes in rocks above and below a reflector/formation interface. In this section we will study the difference in the Voigt-Reuss AVO signatures of a couple of interfaces mimicking a dry sandstone reservoir overlain by a shaly layer. The properties of the sandstone layer are taken from laboratory measurements on a Fontainebleau sample (David et al., 2013, [104]), with 12.8% porosity, bulk density of 2309 kg/m^3 , and P and S wave velocities of 3997 m/s and 2803 m/s respectively.

We consider two cases for the overlying shaly layer: in the first case the layer is composed of highly anisotropic illite needles/domains (elastic properties of mica muscovite, as per Tosaya, 1982, [71]) under mechanical compaction, while in the second case the layer is composed of mechanically compacted Ulm's shale units/domains (Ortega and Ulm, 2007 [48]) of relatively low elastic anisotropy. The elastic properties of the two domains are discussed in detail in Section 3.3.1 of the chapter. In each case we consider 4 levels of compaction, with the smallest compaction factor ‘1’ corresponding to a completely random/isotropic arrangement of the domains and the largest compaction factor ‘6’ corresponding to highly aligned domains.

AVO response of a seismic P-P wave in weakly anisotropic VTI medium with small impedance contrast is modeled as per the work of Thomsen et al. (1993 [105]), corrected by Rüger (1997 [106]), given by equations 3.45 - 3.48. In these equations Z is the acoustic impedance, α is the vertical P-wave velocity, β is the vertical S-wave velocity, μ is the corresponding shear modulus, and ϵ and δ are two of the three Thomsen parameters.

$$R_{PP}(\theta) \approx R_{PP-iso}(\theta) + R_{PP-aniso}(\theta) \quad (3.45)$$

$$R_{PP-iso}(\theta) \approx \frac{1}{2} \left(\frac{\Delta Z}{Z} \right) + \frac{1}{2} \left[\frac{\Delta \alpha}{\bar{\alpha}} - \left(\frac{2\beta}{\bar{\alpha}} \right)^2 \frac{\Delta \mu}{\bar{\mu}} \right] \sin^2 \theta + \frac{1}{2} \left(\frac{\Delta \alpha}{\bar{\alpha}} \right) \sin^2 \theta \tan^2 \theta \quad (3.46)$$

$$R_{PP-aniso}(\theta) \approx \frac{\Delta \delta}{2} \sin^2 \theta + \frac{\Delta \epsilon}{2} \sin^2 \theta \tan^2 \theta \quad (3.47)$$

$$\begin{aligned}
Z &= \rho\alpha, & \bar{Z} &= (Z_1 + Z_2)/2, & \Delta Z &= Z_2 - Z_1 \\
\alpha &= \sqrt{C_{33}/\rho}, & \bar{\alpha} &= (\alpha_1 + \alpha_2)/2, & \Delta\alpha &= \alpha_2 - \alpha_1 \\
\beta &= \sqrt{C_{44}/\rho}, & \bar{\beta} &= (\beta_1 + \beta_2)/2, & \Delta\beta &= \beta_2 - \beta_1 \\
\mu &= \rho\beta^2, & \bar{\mu} &= (\mu_1 + \mu_2)/2, & \Delta\mu &= \mu_2 - \mu_1 \\
\delta &= \frac{C_{11} - C_{33}}{2C_{33}(C_{33} - C_{44})}, & \bar{\delta} &= (\delta_1 + \delta_2)/2, & \Delta\delta &= \delta_2 - \delta_1 \\
\epsilon &= \frac{(C_{13} + C_{44})^2 - (C_{33} - C_{44})^2}{2C_{33}}, & \bar{\epsilon} &= (\epsilon_1 + \epsilon_2)/2, & \Delta\epsilon &= \epsilon_2 - \epsilon_1
\end{aligned} \tag{3.48}$$

Figure 3.15 shows the Voigt-Reuss AVO responses of the isotropic sandstone layer overlain by anisotropic illite/mica-muscovite at various degrees of mechanical compaction. The estimated effective elastic properties of the overlying layer differ based on the choice of Voigt/Reuss averaging scheme, resulting in different AVO responses of the interface. The figure shows that the Voigt and Reuss AVO responses are significantly different from each other but the differences reduce with increasing compaction, as both averaging schemes result in effective property estimates closer to the single crystal properties for the overlying illite layer.

Figure 3.16 shows the Voigt-Reuss AVO responses of the isotropic sandstone layer overlain by anisotropic Ulm's shale domains at various degrees of mechanical compaction. The figure shows that the Voigt and Reuss AVO responses are not as drastically different from each other as in the previous case, but the differences still reduce with increasing compaction. Comparing Figures 3.15 and 3.16 we can conclude that the Voigt-Reuss differences in AVO signatures of an interface can be significant if one of the layers is composed of micro-domains with strong elastic anisotropy. Lower the domain-anisotropy, lower the Voigt-Reuss differences.

The discussions in this chapter are valid for any composite with a spatially varying

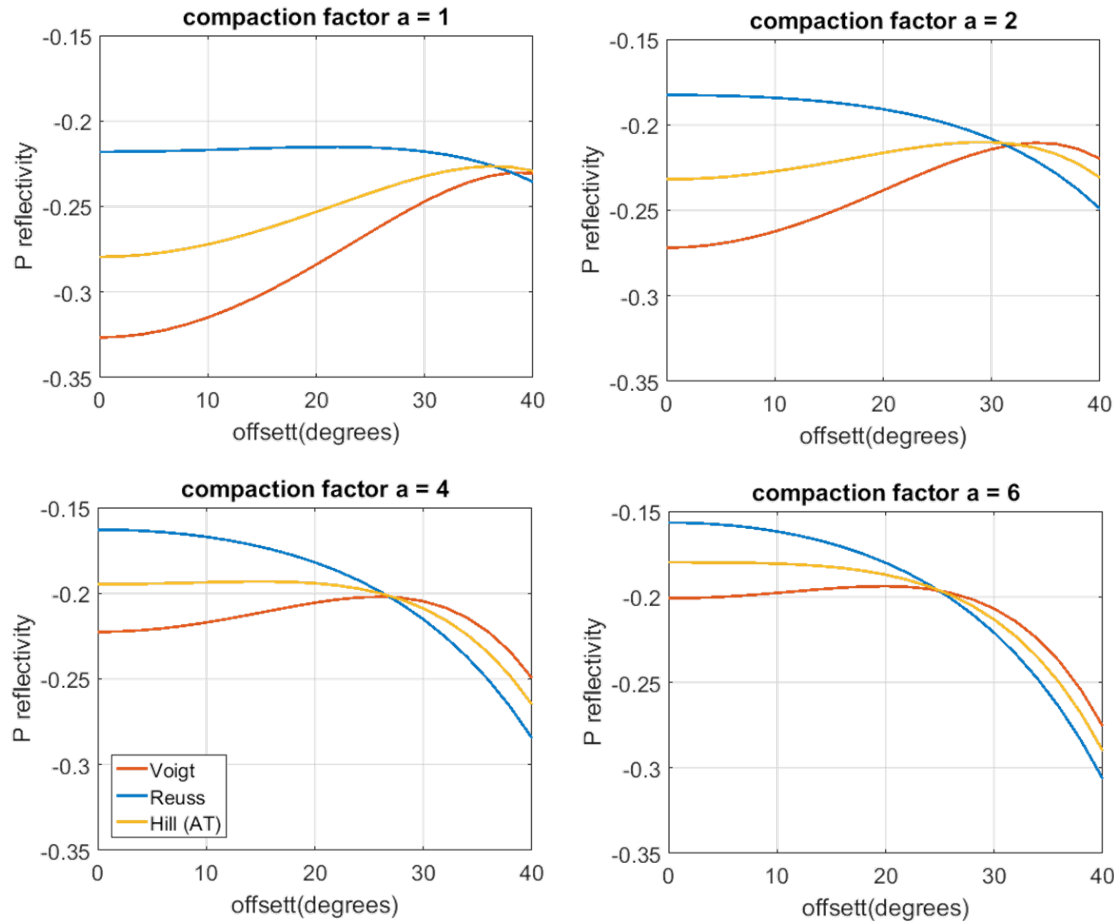


Figure 3.15: Difference between Voigt and Reuss AVO responses for an isotropic sandstone layer overlain by anisotropic mica-muscovite, at various degrees of mechanical compaction.

elastic stiffness/compliance tensor, and as such, can be readily generalized to the case to multi-phase poly-crystals.

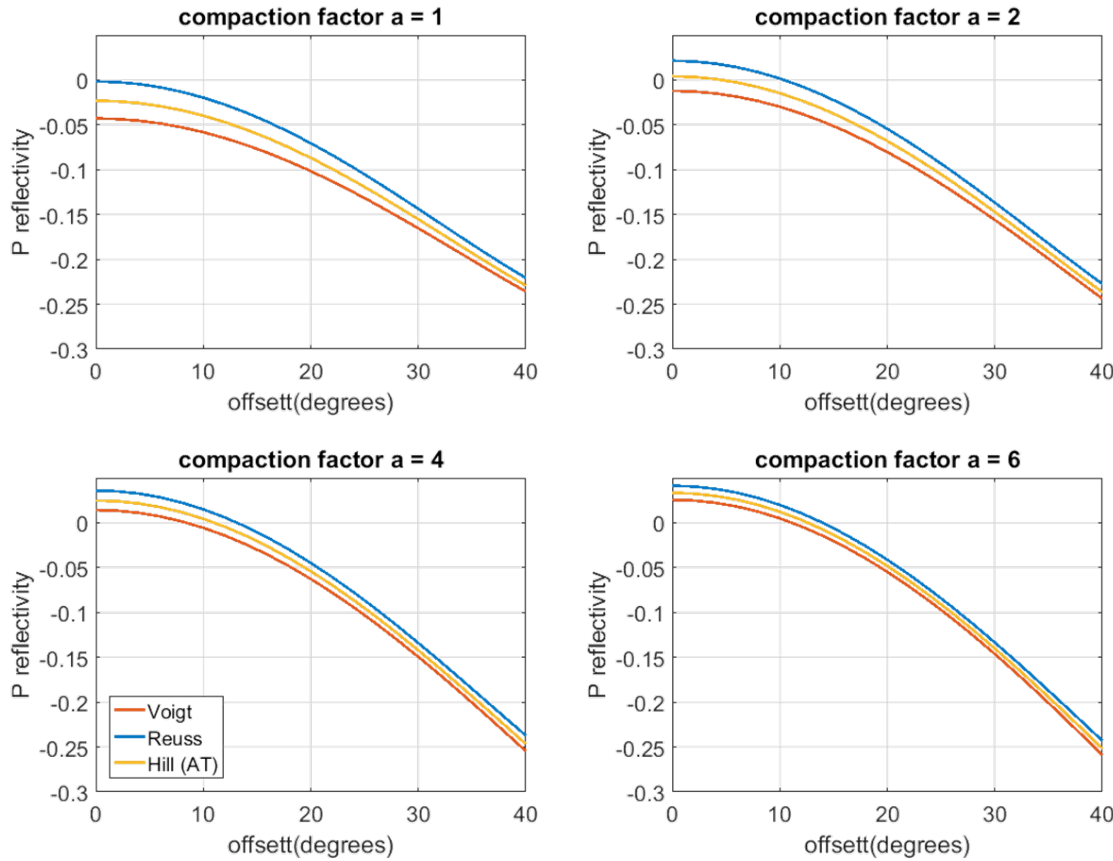


Figure 3.16: Difference between Voigt and Reuss AVO responses for an isotropic sandstone layer overlain by anisotropic Ulm's shale unit, at various degrees of mechanical compaction.

3.4 Conclusions

Composites exhibiting sub-measurement-scale anisotropy are often modeled as collections of variously aligned anisotropic micro-domains, and their effective elastic properties are usually computed using the Voigt or Reuss schemes of rotational summation. Results from the two schemes are not equivalent, and the difference depends on the magnitude of elastic anisotropy in the constituent micro-domains and represents uncertainty due to the unknown exact micro-geometry of the composite. For the isotropic case, composite bulk (K) and shear (G) moduli obtained by the Voigt and

Reuss schemes form the widest possible bounds (VR) on those moduli, as discussed in details in the previous chapter. In this chapter, we studied how the effective composite properties derived from the two schemes differ for anisotropic composites/aggregates.

Our studies focused on composites with rotational/transverse isotropic symmetry with a vertical axis (VTI) and demonstrated that the elastic moduli and anisotropy parameters calculated using Voigt and Reuss schemes are often considerably different from each other. We created four specific VTI composites by combining VTI crystals/micro-domains (mica-muscovite and Ulm's shale unit) with VTI orientation distribution functions (ODF) (compaction ODF and Fisher ODF). Unlike in the case of isotropic aggregates, choosing one scheme over the other for a VTI composite does not systematically over/under-estimate all of the composite elastic parameters of interest (stiffness tensor components C₃₃ and C₄₄ related to the vertical P-wave and S-wave velocities and Thomsen's anisotropy parameters ϵ , γ and δ). For our four specific cases, Voigt gives higher estimates of C₃₃, C₄₄, ϵ and δ , while Reuss gives higher estimates of γ and η .

With Voigt and Reuss forming tensorial bounds on the stiffness of a composite, we suggest that elastic parameters corresponding to a 'Hill' tensor, the arithmetic average of the Voigt and Reuss stiffness tensors (analogous to the case of isotropic aggregates) might offer good working approximations to the effective anisotropic composite properties, as demonstrated in previous studies in material sciences and engineering.

Micro-domains with negative values of Thomsen parameter δ develop a positive-peaked bulge with increasing disorder/misalignment (lower compaction/concentration factors), before going to zero in a perfectly disordered, isotropic macro-composite. This is in line with the common observation that crystals of clay minerals often exhibit negative values of δ , but laboratory/seismic measurements on clay-rich shales, with some degree of crystal misalignment, almost always show positive δ values.

Monte-Carlo analysis of a VTI ODF related to mechanical compaction of sediments reveal that domain/crystal Thomsen parameters δ and ϵ are the strongest predictors for the Voigt-Reuss difference in the composite Thomsen parameter ϵ . Domain parameters C_{44} and γ have the strongest relative influence on composite parameter γ , the maximum value of which also scales monotonically with domain parameter γ . For composite parameter δ , domain parameters γ and δ are most predictive. 2-way partial dependence plots using domain parameters of highest relative influence show that the largest positive values of composite ‘*deps*’ occur for two distinct combinations of domain parameters δ and ϵ : low δ (< -0.2) - high ϵ (> 0.75) and high δ (> 0.3) - low ϵ (< 0). Largest negative values of ‘*deps*’ occur primarily for high δ (> 0.5) - high ϵ (> 1.5) and to a small extent for low δ (< -0.25) - low ϵ (< 0). Similarly, largest negative values of ‘*dgam*’ occur for very low values of c_{44} (< 6 GPa) while the largest positive values correspond to high values of γ (> 2.5). Finally, largest positive values of ‘*ddel*’ occur for high γ ($i2$) - low δ ($j0$) combinations. For γ values < 0.75 , the variation in *ddel* is quite small.

Important formation evaluation parameters such as Vp-Vs ratios and AVO intercepts and gradients can also be significantly impacted by the choice of a Voigt scheme over a Reuss, leading to very different interpretations. Greater the anisotropy in the micro-domains, more significant the difference between Voigt-Reuss interpretations.

...

Chapter 4

Electrical-elastic cross-relations in rocks

4.1 Abstract

In this chapter we discuss cross-property bounds between the electrical conductivity and the elastic bulk modulus of a rock - predicting the range of effective bulk modulus for a known effective conductivity (and vice-versa) with known constituent phase properties, for three dimensional, isotropic, 2-phase composites. Rigorous cross-property bounds exist, and the narrowest of these are due to the pioneering work of Gibiansky and Torquato, wherein the range of effective bulk modulus for a given value of rock conductivity (and vice versa) predicted using these bounds is sharper than the bulk modulus range from the Hashin-Shtrikman bounds. The inherent non-uniqueness in cross-property relations captures the uncertainty due to the unknown exact micro-geometry of a composite. We discuss empirical constraints on Gibiansky and Torquato's rigorous cross-bounds to make them narrower and therefore more useful when dealing with some common reservoir rocks, specifically brine filled sandstones and carbonates. We also discuss the importance of factoring in porosity when

using or interpreting cross-property bounds/relations. Finally, we demonstrate the use of the empirically constrained cross-bounds in estimating the Archie cementation factor of a rock when presented with large-scale elastic (e.g., seismic) and electrical (e.g., CSEM) surveys.

4.2 Background and motivation

Effective properties of a random heterogeneous medium depend on and hence reflect some of its morphological characteristics. Therefore, knowing one effective property of the medium (e.g. electrical conductivity) can help us extract useful information about another effective property of the medium (e.g. bulk modulus) even though the two properties may be governed by very different constitutive relations (Torquato, 2002 [43]). Understanding how two different physical properties of the same random heterogeneous medium (e.g. porous rocks) are correlated is an interesting scientific problem with important practical uses. As an example, if one physical property is more easily/frequently measured than another, understanding cross property relations can help us use the more frequently measured property to obtain some estimate/range of its less frequent counterpart. In geophysics, this routinely happens in well logging, where formation resistivity/conductivity is typically measured as part of the basic logging suite, while formation sonic velocities (and hence elastic moduli) are far less frequent. Even if both physical properties are available, understanding their correlation can help us interpret the properties jointly for better formation evaluation.

In seismic geophysics, one popular and convenient workflow for obtaining elastic-electrical cross-property relations has been to choose a specific elasticity-porosity relation (empirical/theoretical) and a specific conductivity-porosity relation and eliminate porosity between the two to obtain an elasticity-conductivity relation. This workflow

has been extensively used by Carcione et. al. (2007, [107]) to explore many possible combinations of constitutive relations in rocks to obtain multiple elastic-electrical cross-property relations. Some of these cross-relations between the electrical conductivity and bulk modulus of a quartz-brine composite are shown in Figure 4.1. Since these relations are heuristic, they are often limited to very specific lithology types where the parent constitutive relations are valid, and are not always realizable.

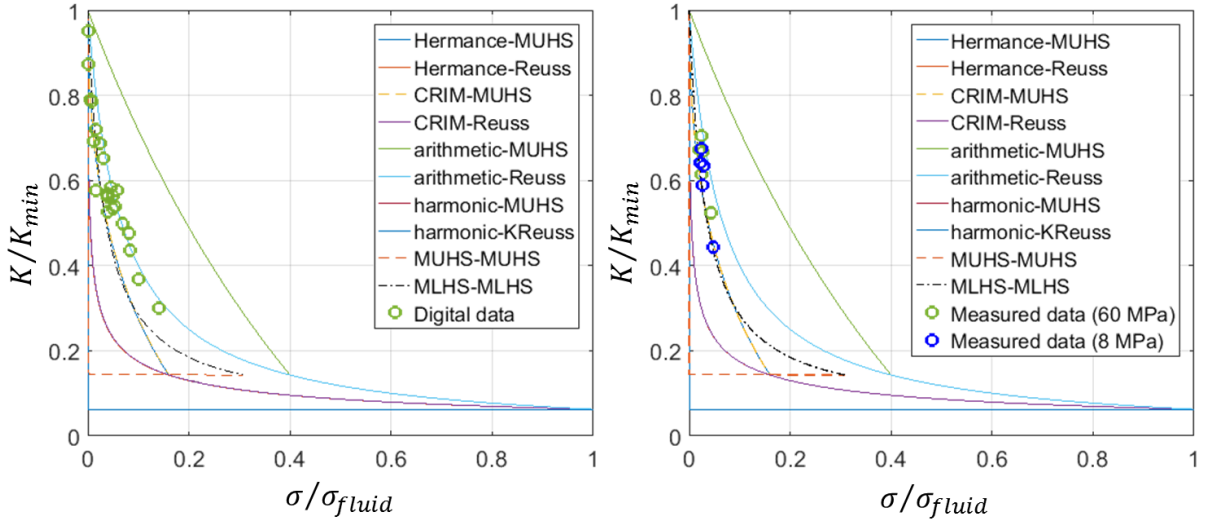


Figure 4.1: Cross-property relations by Carcione et. al. (2007) for [left] digital bulk modulus-conductivity computations on brine filled sandstone samples, and [right] laboratory measurements on brine filled clean sandstone samples.

In Figure 4.1, the x and y axes have been normalized to have a maximum value of one, with K & σ representing the effective bulk modulus and effective electrical conductivity of the composite, and K_m & S_{fluid} representing the bulk modulus of quartz and conductivity of brine respectively. The left sub-figure is overlain with digitally computed (FEM) bulk modulus-conductivity data points for CT scan samples of brine filled sandstone (Saxena and Mavko, 2016 [108]). The right sub-figure is overlain with laboratory measurements on another set of brine filled sandstone samples at two different confining pressures of 8 and 60 MPa (Han, 2010, [109]).

It is evident that despite considering only sandstone samples, there is no one cross-relation that is optimum for all the data points. The data points have a spread in the cross-property space. This is expected, as even with known phase properties, a given value of conductivity can be associated with multiple values of porosity, making multiple values of bulk modulus plausible. In fact, as we shall see later in the chapter, even with a specific value of porosity, a given value of conductivity does not map on to a unique value of bulk modulus for a composite with known phase properties. This inherent non-uniqueness in cross-property relations captures the uncertainty due to the unknown exact micro-geometry of a composite.

This brings us to the primary motivation for the research presented in this chapter. Since the exact microgeometry of a naturally occurring composite is rarely characterized in its entirety, we will explore cross-property bounds as an alternative to unique but often inaccurate cross-property relations. With this approach, for a given value of composite porosity and effective conductivity along with known phase end-properties (bulk modulus, shear modulus and conductivity) we will be able to predict a range of values for the effective bulk modulus, accounting for all possible micro-geometries of the composite. We will compare the bounds against data (both digital and laboratory) and use effective medium models as tools to understand how phase shapes can move us between cross-property bounds. Finally we will explore how empirically constrained cross-bounds can be used to estimate the Archie cementation factor (necessary for saturation computations) of a rock when presented with large scale elastic (e.g.: seismic) and electrical (e.g.:CSEM) surveys.

4.3 Hashin-Shtrikman cross-plot lines in the σ^* - K^* plane

One of the simplest attempts at cross-property bounds consists of combining Hashin-Shtrikman's (HS) separate bounds for effective elastic moduli (Hashin and Shtrikman, 1963 [8]) and effective conductivity (Hashin and Shtrikman, 1962 [7]) for two-phase three dimensional composites (Carcione et al., 2007 [107], Sevostianov and Kachanov, 2009 [110], Han, 2010 [109]).

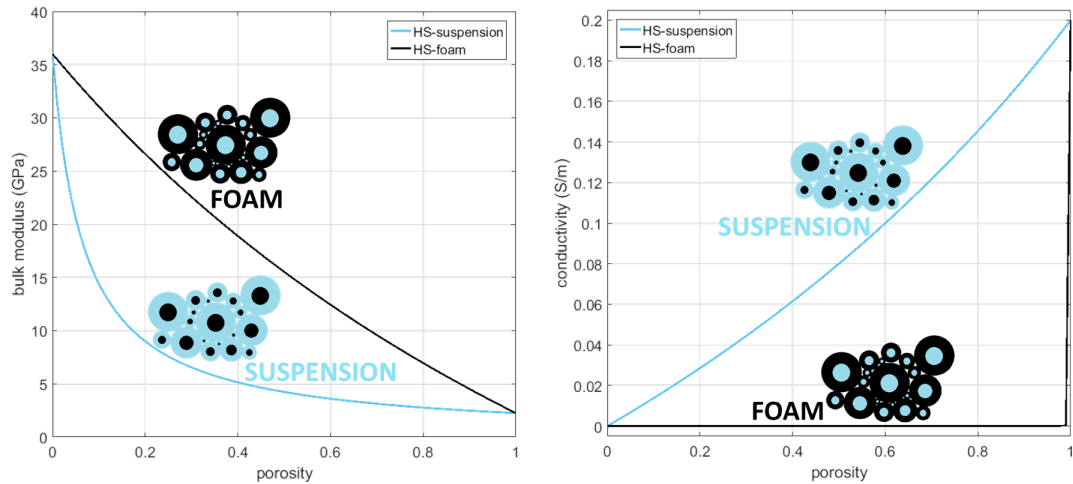


Figure 4.2: Foam and suspension micro-geometries and their mapping to Hashin-Shtrikman (HS) bounds. Foams correspond to upper HS bounds for bulk modulus and lower HS bounds for conductivity. Suspensions correspond to the opposite HS bound combination.

Let us consider a composite of quartz ($K_1 = 36$ GPa, $G_1 = 45$ GPa, $\sigma_1 = 10^{-5}$ S/m) and brine ($K_2 = 2.5$ GPa, $G_2 = 0$ GPa, $\sigma_2 = 0.2$ S/m). Figure 4.2 shows the separate HS bounds for bulk modulus (left) and conductivity (right). We know that for both bulk modulus and conductivity, a common micro-structure corresponding to the HS bounds is the coated-spheres, as shown in figure 4.2. Based on the phase properties considered in this exercise, when the coated spheres have quartz (black

color) as the outer shell and brine (blue color) as the inner core (referred to as ‘foam’ in this chapter) the bulk modulus attains the upper HS bound while the conductivity attains the lower HS bound. Similarly, when the coated spheres have brine as the outer shell and quartz as the inner core (referred to as ‘suspension’ in this chapter) the bulk modulus attains the lower HS bound while the conductivity attains the lower HS bound. Accordingly, the first set of HS bounds are referred to and labeled as ‘HS-foam’ while the second set of HS bounds are referred to and labeled as ‘HS-suspension’ respectively.

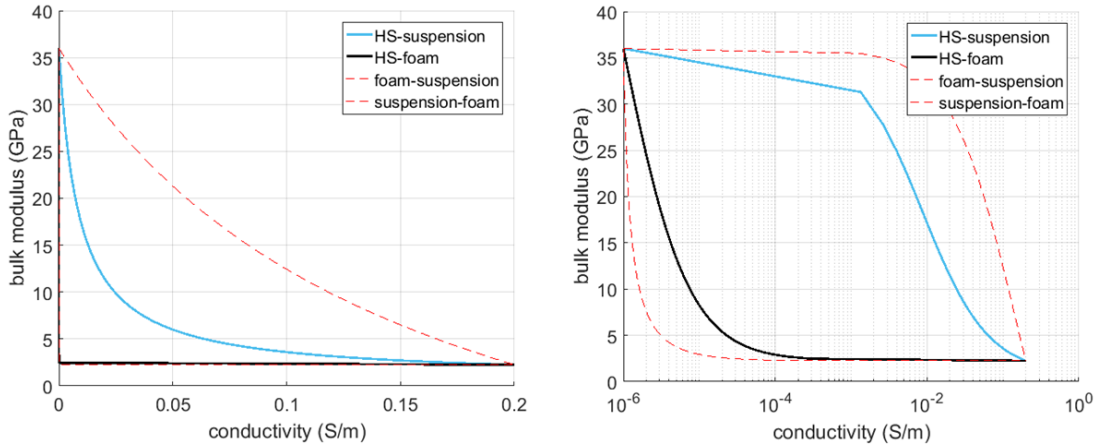


Figure 4.3: The mapping of HS-foam (black line) and HS-suspension (blue line) micro-geometries in the σ^* - K^* plane. Micro-geometry inconsistent and physically non-realizable ‘foam-suspension’ and ‘suspension-foam’ lines are also plotted as dashed red lines. The sub-figure on the right plots conductivity on a log scale, the kink in the ‘HS-suspension’ line is an artifact of sampling, accentuated by the large conductivity contrast between the constituent phases.

When we combine the separate conductivity and modulus bounds in the σ^* - K^* plane, for the sake of micro-geometric consistency, it makes sense to combine the two HS-suspension curves to form a cross-property ‘HS-suspension’ line (blue) and the two HS-foam curves to form a cross-property ‘HS-foam’ line, as demonstrated in Figure 4.3, also noted by Carcione (Carcione et al., 2007 [107]). The geometrically

inconsistent ‘foam-suspension’ and ‘suspension-foam’ lines (red) are, as apparent, are generated by combining the ‘HS-suspension’ in conductivity with the ‘HS-foam’ in bulk modulus and vice-versa. Sevostianov and Kachanov (2009 [110]) note that the geometry-inconsistent bounds are too wide to be useful, while Gibiansky and Torquato (1996, [9]) show that they are physically non-realizable. Both the left and right sub-figures in 4.3 show the combined HS-bounds in the σ^* - K^* plane, with the right sub-figure plotting conductivity on a log scale, to show the separation between the curves better, especially at low values of conductivity. Note that the kink in the ‘HS-suspension’ line in the right sub-figure is an artifact of sampling, accentuated by the large conductivity contrast between the constituent phases in this example.

A word of caution: while every suspension or foam micro-geometry lies on one of the HS lines in the σ^* - K^* plane, not every point on the cross-plot HS lines corresponds to a suspension or foam micro-geometry. We will illustrate this using Figure 4.4. In this figure, the point ‘ X_1 ’ has a suspension micro-geometry, with effective bulk modulus ‘ K_1 ’, conductivity ‘ σ_1 ’ and porosity ‘ ϕ_1 ’. Points ‘ X_2 ’ and ‘ X_3 ’ do not correspond to a suspension micro-geometry, but they have the same bulk modulus ‘ K_1 ’ and conductivity ‘ σ_1 ’ at porosities ‘ ϕ_2 ’ and ‘ ϕ_3 ’. In the σ^* - K^* plane depicted by Figure 4.3, all of these points would coincide on the ‘HS-suspension’ line, though only X_1 is a true suspension. Obviously, the same phenomenon is true for the HS-foam line as well. The only way to determine if a point that falls on the σ^* - K^* suspension line is truly a suspension/foam is by considering the corresponding porosity. While there is a large body of cross-property work that connects elastic and electrical properties by eliminating porosity between pairs of equations, as discussed in section 4.2, this is an important example of the significance of including porosity to better understand elastic-electrical cross-properties in composites. As we move forward in the chapter, we will encounter more instances where including porosity becomes significant in understanding cross-property relations.

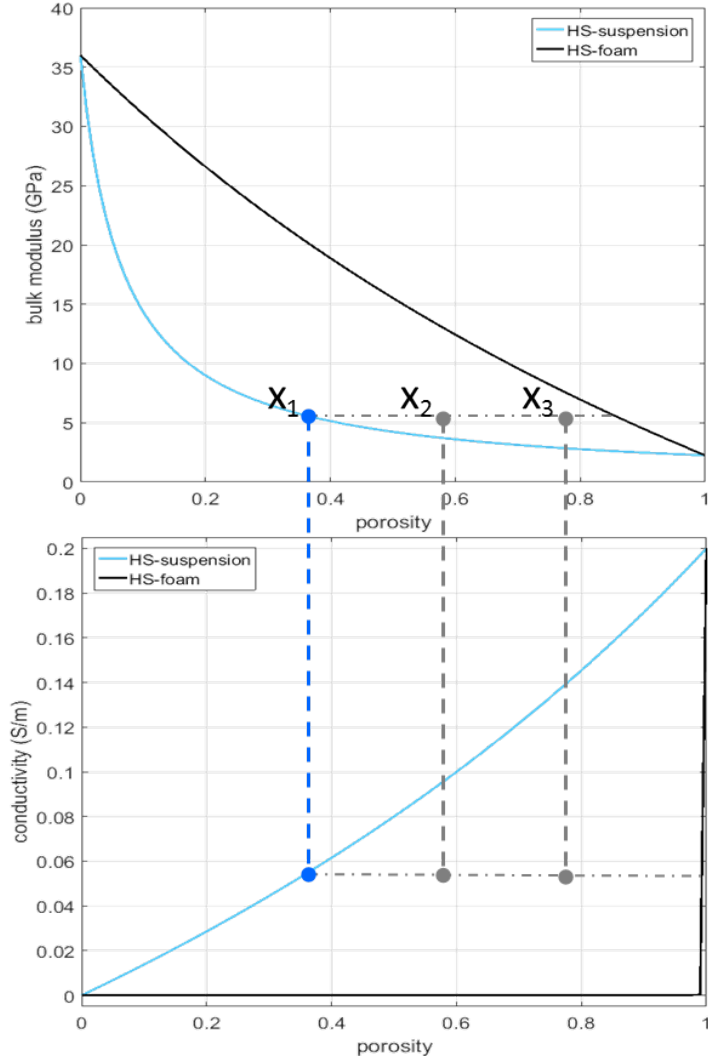


Figure 4.4: The importance of porosity in cross-property relations: points X_1 , X_2 and X_3 have the same values of bulk modulus and conductivity but at different values of porosity. Only X_1 is a true suspension, but in the σ^*-K^* plane all three points plot on the HS-suspension cross-plot line, and can potentially cause misinterpretations.

HS-foam and suspension cross-plot lines do not bound data in the σ^*-K^* plane. Figure 4.5 shows the individual HS bounds and the combined geometry-consistent HS lines against cross-property digital data on brine-saturated quartz rocks (Saxena and Mavko, 2016 [108]). Details about this dataset can be found in Section 4.6 of the

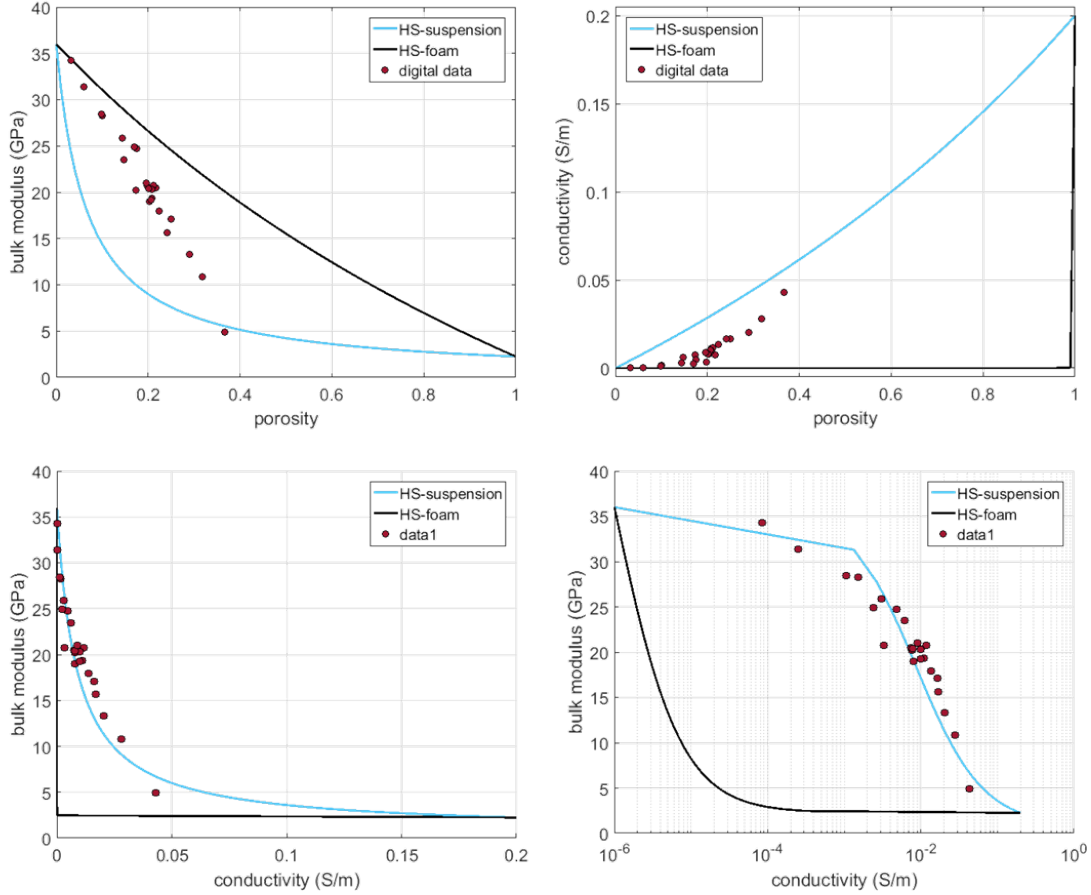


Figure 4.5: Data-points that lie well within the individual HS bounds for bulk modulus or conductivity don't necessarily lie within the micro-geometry consistent HS-lines in the σ^* - K^* plane.

chapter. The top panel of the figure shows individual HS-bounds for bulk modulus and conductivity, with all of the digital data (except one bulk modulus point) lying within the bounds. The bottom panel shows the geometry consistent HS lines in the σ^* - K^* plane, with conductivity in linear (left) and logarithmic (right) scales, along with the digital data. It is apparent from this figure that data-points that lie well within the HS bounds for bulk modulus or conductivity don't necessarily lie within the envelope defined by micro-geometry consistent HS cross-plot lines in the σ^* - K^* plane.

Hence this recipe for elastic-electrical cross-bounds, though easy to implement, is scientifically inaccurate. To remedy this, in the next section of the chapter we will focus on the rigorously derived Gibiansky and Torquato crossbounds (1996, [9], 1998 [10]), which are also the tightest bounds in the absence of any information about composite micro-structure.

4.4 Gibiansky and Torquato cross-bounds

In this section we look at rigorous bulk modulus-electrical conductivity cross bounds in materials of isotropic and by extension, cubic symmetry, since cubic symmetry is indistinguishable from isotropy in the σ^* - K^* domain. This topic has been widely researched over several decades and some seminal works are due to Milton (1984 [111]), Berryman and Milton (1988 [1]) and Gibiansky and Torquato (1996 [9], 1998 [10]). Gibiansky and Torquato (GT) obtained the sharpest known bounds on σ^* - K^* pairs for 2-phase, 3-dimensional isotropic (and cubic) composites of all possible micro-geometries using the translational method. These bounds enclose lens-shaped regions in the σ^* - K^* space.

4.4.1 GT bounds for known phase volume fractions

The GT cross-bounds on the set of (σ^*, K^*) pairs for a 2-phase, 3D, isotropic composite with phase volume fractions f_1 and $f_2 (= 1 - f_1)$, are determined from 5 hyperbola segments, the outermost pair of these curves define the bounds. The 5 hyperbola segments of interest are mathematically expressed by Equations 4.1 - 4.5.

$$GT_1 = HYP [(\sigma_{1*}, K_{1*}), (\sigma_{2*}, K_{2*}), (\sigma_a, K_a)] \quad (4.1)$$

$$GT_2 = HYP [(\sigma_{1*}, K_{1*}), (\sigma_{2*}, K_{2*}), (\sigma_1, K_1)] \quad (4.2)$$

$$GT_3 = HYP [(\sigma_{1*}, K_{1*}), (\sigma_{2*}, K_{2*}), (\sigma_2, K_2)] \quad (4.3)$$

$$GT_4 = HYP [(\sigma_{1*}, K_{1*}), (\sigma_{2*}, K_{2*}), (\sigma_{1**}, K_h)] \quad (4.4)$$

$$GT_5 = HYP [(\sigma_{1*}, K_{1*}), (\sigma_{2*}, K_{2*}), (\sigma_{2**}, K_h)] \quad (4.5)$$

In equations 4.1 - 4.5, $HYP[(x_1, y_1), (x_2, y_2), (x_3, y_3)]$ represents the segment of a hyperbola that passes through points (x_1, y_1) , (x_2, y_2) and (x_3, y_3) and may be parameterized by Equation 4.6.

$$\begin{aligned} x &= \gamma_1 x_1 + \gamma_2 x_2 - \frac{\gamma_1 \gamma_2 (x_1 - x_2)^2}{\gamma_2 x_1 + \gamma_1 x_2 - x_3} \\ y &= \gamma_1 y_1 + \gamma_2 y_2 - \frac{\gamma_1 \gamma_2 (y_1 - y_2)^2}{\gamma_2 y_1 + \gamma_1 y_2 - y_3} \end{aligned} \quad (4.6)$$

where $\gamma_1 = 1 - \gamma_2 \in [0, 1]$. Further explanation of quantities used in Equations 4.1 - 4.5 are as follows:

$$\sigma_{1*} = F_\sigma(2\sigma_1); \quad \sigma_{2*} = F_\sigma(2\sigma_2) \quad (4.7)$$

$$\sigma_{1**} = F_\sigma(-2\sigma_1); \quad \sigma_{2**} = F_\sigma(-2\sigma_2) \quad (4.8)$$

$$K_{1*} = F_K\left(\frac{4}{3}\mu_1\right); \quad K_{2*} = F_K\left(\frac{4}{3}\mu_2\right) \quad (4.9)$$

$$\sigma_a = f_1\sigma_1 + f_2\sigma_2 = F_\sigma(\infty); \quad \sigma_b = \left(\frac{f_1}{\sigma_1} + \frac{f_2}{\sigma_2} \right)^{-1} = F_\sigma(0) \quad (4.10)$$

$$K_a = f_1K_1 + f_2K_2 = F_K(\infty); \quad K_b = \left(\frac{f_1}{K_1} + \frac{f_2}{K_2} \right)^{-1} = F_K(0) \quad (4.11)$$

$$F_d(y) = f_1d_1 + f_2d_2 - \frac{f_1f_2(d_1 - d_2)^2}{f_1d_2 + f_2d_1 + y} \quad (4.12)$$

Equations 4.7 and 4.9 represent the upper and lower Hashin-Shtrikman (HS) bounds on effective conductivity (Hashin and Shtrikman, 1962 [7]) and effective bulk modulus (Hashin and Shtrikman, 1963 [8]) for isotropic composites, respectively. Equations 4.10 and 4.11 represent the Voigt-Reuss bounds on effective conductivity and effective bulk modulus respectively. So far, Equation 4.8 has no known physical meaning.

Figure 4.6 shows the GT cross-bounds for a solid-brine isotropic composite with a porosity of 0.35. The solid has properties close to quartz with bulk modulus (K_1) = 36GPa, shear modulus (μ_1) = 45GPa, and conductivity (σ_1) = 0.0005 S/m. The brine has bulk modulus (K_2) = 2.5GPa, shear modulus (μ_2) = 0GPa, and conductivity (σ_2) = 4.7 S/m. The 5 hyperbola segments are labeled GT1, GT2, GT3, GT4 and GT5, as indicated by the figure's legend.

For the choice of parameters in this particular example, GT4 and GT5 (Equations 4.4 and 4.5) are co-incident. They are also very close to GT2 (Equation 4.2) except at very low values of conductivity and of bulk modulus. The upper left corner of the figure, marked by a black star, corresponds to HS-foam (coated spheres micro-structure with quartz outside and brine inside) while the lower right corner, marked by a blue star, corresponds to HS-suspension (coated spheres micro-structure with brine outside and quartz inside). σ^* - K^* pairs that lie outside of the GT bounds, shaded in gray, cannot exist (including the two corners marked by red crosses) even

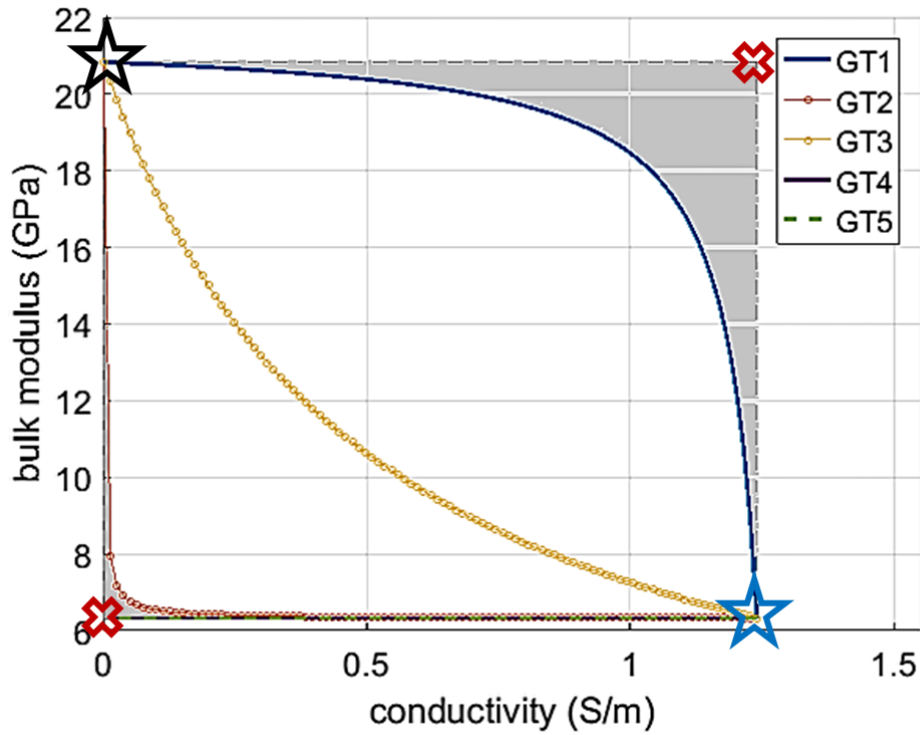


Figure 4.6: GT cross-bounds (given by outermost pair of 5 hyperbolae segments GT1, GT2, GT3, GT4, GT5) for a solid-brine isotropic composite with a porosity of 0.35.

though they lie inside their individual Hashin-Shtrikman bounds at specific porosities.

The recipe for estimating the 5 GT points for bulk modulus for a given value of porosity and effective conductivity (and vice versa) (Gibiansky and Torquato, 1998 [10]) is slightly more involved and is discussed in the Appendix for this chapter.

4.4.2 Realizability of the GT bounds

A realizable bound is one for which a micro-geometry exists. The hyperbola segment ‘GT1’ is realizable at three specific points that correspond to very special and rare (in terms of natural occurrence) micro-geometries (Milton, 1981 [112], Gibiansky and Milton, 1993 [113], Vinogradov and Milton, 2005 [70]). GT2 and GT3 are realizable at all points, and correspond to doubly-coated spheres. In fact, they are the same as

the mineral and fluid coated embedded bounds respectively, originally developed by Mavko and Saxena (2013 [11], 2014 [114]) for elastic solid substitution, and discussed in details in the conductivity substitution chapter of this thesis. It is interesting to note that for the solid substitution problem, digital computations and measurements on real rock geometries rarely violate the embedded bounds. Also noteworthy is the fact that envelopes of stacked (for different porosities) GT2 and GT3, essentially the embedded bounds, in the σ^* - K^* plane coincide exactly with the HS-foam and HS-suspension lines, as demonstrated in the next section. GT4 and GT5 are of unknown realizability.

4.4.3 GT bounds for arbitrary phase volume fractions

For arbitrary phase volume fractions, GT cross-bounds can be formed by taking the envelopes of the GT curves at many porosities stacked together, as shown by Figure 4.7. The top sub-figure plots conductivity in a linear scale while the bottom one plots conductivity in a log scale to show the low conductivity/porosity features better. In both plots, each rectangle (drawn in gray dashed lines) correlates to a single porosity and encloses the 5 corresponding GT hyperbolae given by equations 4.1 - 4.5 (considering the quartz-brine composite described in the previous section). The largest and rightmost rectangle corresponds to a porosity of 0.4 and the smallest and leftmost rectangle corresponds to a porosity of 0.02. It is interesting to note that in the σ^* - K^* plane, the envelopes of GT2 and GT3, corresponding to the embedded bounds (realized by a micro-geometry of doubly coated spheres) are the HS-foam and HS-suspension lines respectively.

When we know nothing about the porosity of a quartz-brine composite, our best estimate of the effective bulk modulus of the composite is anywhere between the mineral (36 GPa) and suspension (5.5 GPa, assuming 0.4 critical porosity) modulus. Adding a conductivity measurement of the composite, say at 0.5 S/m, can significantly

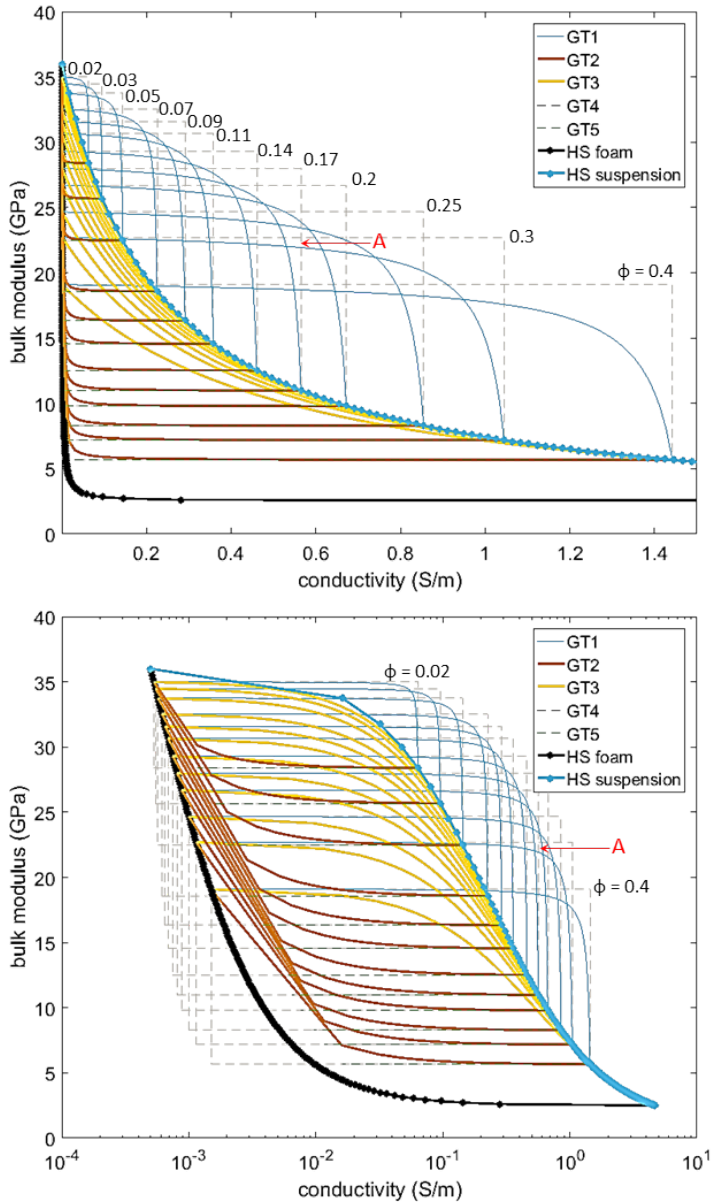


Figure 4.7: GT bounds at multiple porosities, stacked in the conductivity-bulk modulus space (σ^* - K^* plane). Porosity decreases as we move up and left. The top sub-figure plots conductivity in a linear scale while the bottom one plots conductivity in a log scale to show the low conductivity/porosity features better.

reduce the upper limit of the previous estimate to 26 GPa, as evident from figure 4.7. Supplementing this with information about porosity will further reduce the bulk modulus range; in our case specifying a porosity of 0.3 in addition to a conductivity of 0.5 S/m, further constricts our bulk modulus range to 7- 22.5 GPa.

The GT bounds are rigorous and may be used to test the validity of cross-property measurements on/estimates of isotropic composites. However we need to be careful when using the GT envelopes in the σ^* - K^* plane for such tests. Consider the point ‘A’ in figure 4.7. The fact that the (σ, K) pair corresponding to ‘A’ lies well within the GT envelopes in the σ^* - K^* plane, might mislead us into believing that for an isotropic quartz-brine composite, (σ, K) represents a valid cross-property pair. However, this validity strictly depends on the associated composite porosity. Hence, while (σ, K) would indeed represent a valid cross-property pair for a porosity of 0.2 or 0.25, it would not be valid for a porosity of 0.3 (or higher) or 0.17 (or lower). Therefore, cross-property bounds are best used in conjunction with porosity/ phase volume fraction information, both for predicting the range of one property when the other is known and also for testing the validity of a given (σ, K) pair.

4.5 GT cross-bounds vs. effective medium modeling: Oblate and prolate pore-spaces

Effective medium models are often used to understand how variation in phase shapes (generally idealized as ellipsoids, and in this chapter as spheroids of varying aspect ratios) can move us between bounds on composite properties. In this section of the chapter we look at estimates of the bulk modulus and conductivity from a couple of effective medium models: self-consistent approximation, abbreviated as ‘SCA’ (Berryman, 1980 [115], 1995 [12]) and differential effective medium, abbreviated as

‘DEM’(Bruggeman, 1935 [116], Sen et al., 1980 [117], Berryman, 1992 [118]). We use these models to understand how various phase shapes span the space between the GT bounds in the σ^* - K^* plane.

Figure 4.8 shows estimates of effective medium models against the GT cross-bounds for a sandstone-brine composite with 10% porosity. The sandstone matrix has a bulk modulus of 36GPa , shear modulus of 45GPa and electrical conductivity of 10^{-5}S/m . The brine that saturates the pore space has a bulk modulus of 2.5GPa , shear modulus of 0GPa and electrical conductivity of 0.2S/m .

The top panel of the figure shows results of self-consistent modeling on the left and DEM modeling with two critical porosity values (1 and 0.4) on the right. The bottom panel shows the same plots with conductivity on a log-scale instead of linear, to better examine the low-conductivity features. For each effective medium model, distinct implementations are used to separately compute the bulk modulus and electrical conductivity values at a specific porosity for a wide range of pore aspect ratios ($\exp(-5) = 0.0067$ to $\exp(5) = 148.4132$) and the results (for the same aspect ratio) are cross-plotted in the σ^* - K^* plane. The effective medium points are color coded by the natural log of pore/brine-phase aspect ratios, with the cooler (bluish) colors representing oblate/disk-like pore spaces and the warmer (reddish) colors representing prolate/tube-like pore spaces. For the SCA models, the mineral phase is assumed to have spherical shape (aspect ratio = 1). For the DEM model, the mineral phase is considered to be the ‘host matrix’ with inclusions in the form of brine-filled pores.

It becomes immediately evident that in the σ^* - K^* cross-property space oblate pores look significantly different from their prolate counter-parts. Irrespective of the effective medium model considered, at a given porosity spherical pore shapes result in the stiffest and least conductive composite. As we move away from spherical pores to more oblate/crack-like pore shapes, composite bulk modulus falls rapidly, approaching/reaching the lower Hashin-Shtrikman limit; composite electrical conductivity also

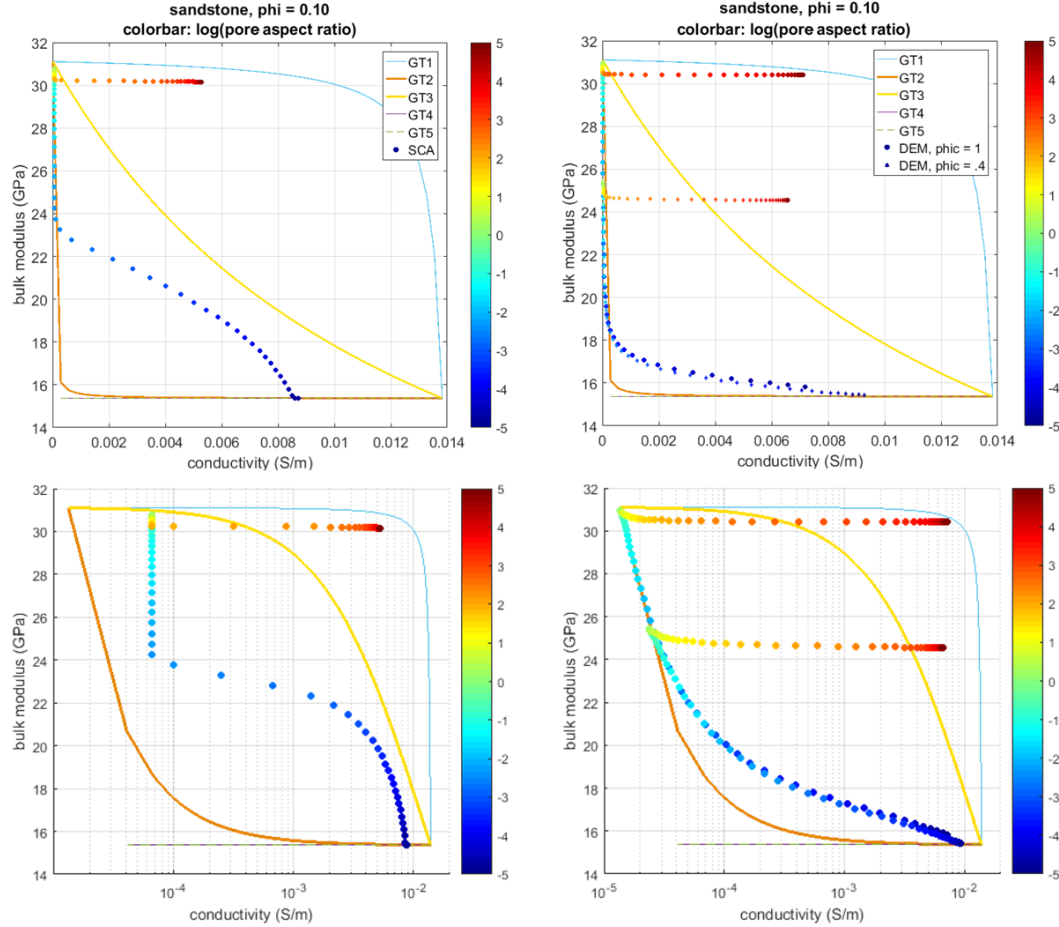


Figure 4.8: Estimates of effective medium models against the GT cross-bounds for a sandstone-brine composite with 10% porosity. Top panel of the figure shows results of self-consistent modeling (labeled ‘SCA’ on the left and DEM modeling (labeled ‘DEM’) with two critical porosity (PHIC) values (1 and 0.4) on the right. The bottom panel shows the same plots with conductivity on a log-scale instead of linear.

undergoes substantial increase, approaching the upper Hashin-Shtrikman limit, but even for the large range of aspect ratios considered, never quite reaching it. On the other hand, moving from spherical to prolate/needle-like pore shapes causes some reduction in composite bulk modulus, but even for the large range of aspect ratios considered, the modulus remains closer to the upper Hashin-Shtrikman limit; composite conductivity increases substantially, approaching, but never quite reaching the

upper Hashin-Shtrikman limit.

The DEM model with a critical porosity of 0.4, as expected, is substantially softer than its counterpart with critical porosity 1, though the conductivity difference between the models is not as strong. The bottom panel plots conductivity on a logarithmic scale.

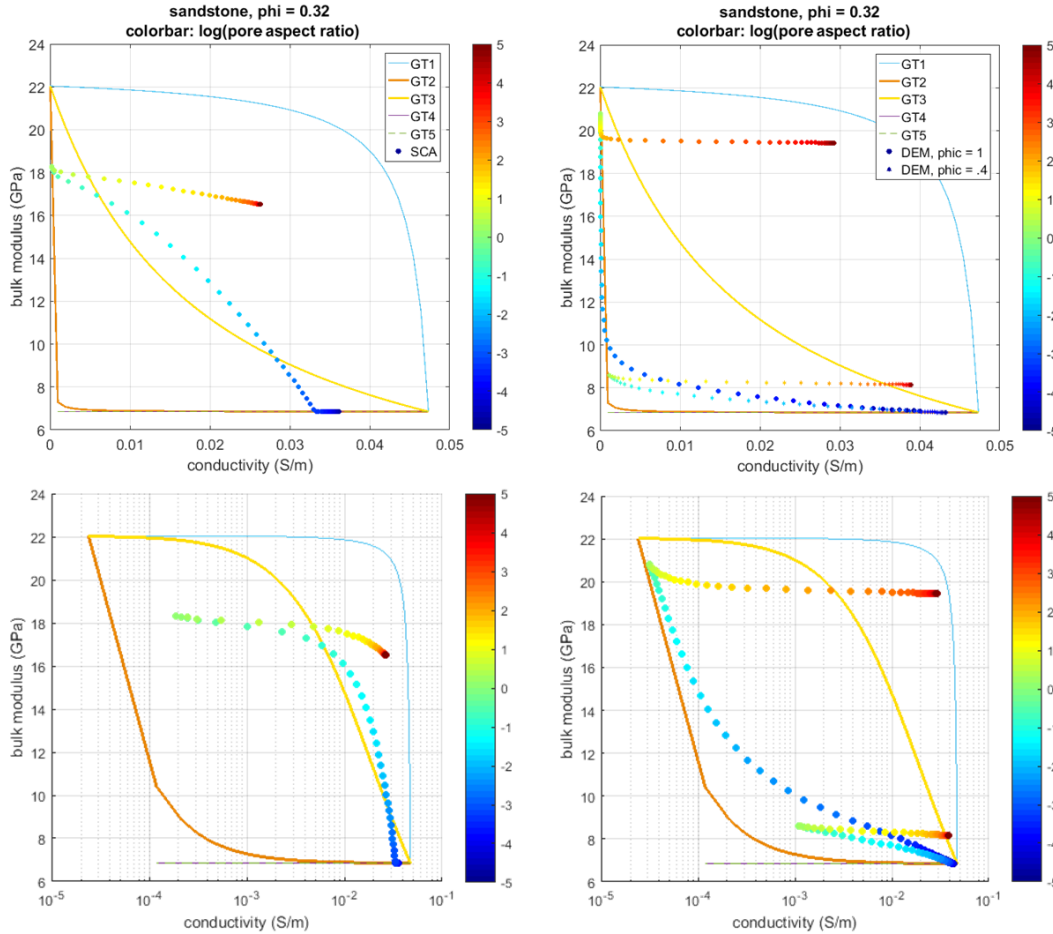


Figure 4.9: Estimates of effective medium models against the GT cross-bounds for a sandstone-brine composite with 10% porosity. Top panel of the figure shows results of self-consistent modeling (labeled ‘SCA’ on the left and DEM modeling (labeled ‘DEM’) with two critical porosity (PHIC) values (1 and 0.4) on the right. The bottom panel shows the same plots with conductivity on a log-scale instead of linear.

Figure 4.9 shows estimates of effective medium models against the GT cross-bounds for the same sandstone-brine composite with 32% porosity. Once again, oblate pores look different from their prolate counter-parts in the σ^* - K^* cross-property space, though the difference is not as pronounced as in case of the lower porosity case, especially for the self-consistent points. oblate pores cause the composite bulk modulus to fall rapidly, approaching/reaching the lower Hashin-Shtrikman limit, while the composite electrical conductivity increases to approach but never quite reach the upper Hashin-Shtrikman limit. Prolate pore shapes, on the other hand, cause some reduction in composite bulk modulus, larger than in the previous example, but still much smaller than oblate pores; conductivity approaches the upper Hashin-Shtrikman limit without reaching it, while being slightly lower than for oblate pores.

It is interesting to note from figures 4.8 and 4.9 that overall, a large fraction of the modeled cross-property points with oblate/plate-like pore shapes fall with the ‘embedded’ cross-property bounds ‘GT2’ and ‘GT3’, except for some in the self-consistent model with 32% porosity. The space between ‘GT3’ and the partially realizable bounds ‘GT1’ is primarily spanned by prolate/needle-like pores. Also, even with the wide range of pore aspect ratios modeled in this section, some regions of the GT cross-bounds space in the σ^* - K^* plane remain poorly spanned, most notably regions of high conductivity (approaching the HS upper limit), and regions of low conductivity coupled with low bulk modulus.

4.6 GT bounds vs. cross-property data

4.6.1 Comparison with digital data

4.6.1.1 Sandstone data

Bulk modulus and conductivity were simultaneously computed on 24 3D digital brine-saturated sandstone samples using FEM in NIST codes (Saxena and Mavko, 2016 [108]), sample properties (porosity, digitally estimated bulk modulus and conductivity) given in Table 4.1.

Table 4.1: Properties of digital sandstone samples, sorted by porosity. The computed bulk modulus of the last sample, marked by ‘**’, violates the HS bounds (Saxena & Mavko, 2016).

index	phi	K (GPa)	C (S/m)	index	phi	K (GPa)	C (S/m)
1	0.032	34.251	8.44E-05	13	0.203	18.97	0.00793
2	0.061	31.391	0.00025	14	0.206	19.214	0.01001
3	0.098	28.458	0.00107	15	0.208	19.373	0.01095
4	0.1	28.239	0.00153	16	0.209	20.298	0.00991
5	0.144	25.879	0.00309	17	0.212	20.747	0.01174
6	0.148	23.487	0.00623	18	0.217	20.503	0.00749
7	0.17	24.899	0.00241	19	0.224	17.953	0.01363
8	0.173	20.185	0.0077	20	0.242	15.661	0.01677
9	0.175	24.74	0.00481	21	0.25	17.105	0.01637
10	0.196	21.024	0.00899	22	0.29	13.286	0.02028
11	0.197	20.768	0.00328	23	0.317	10.823	0.0281
12	0.201	20.38	0.00791	24**	0.366	4.9349	0.04314

Figure 4.10 shows 4 of these samples, spanning the overall porosity range, along with the 5 GT curves (labeled ‘GT1’,‘GT2’,‘GT3’,‘GT4’ & ‘GT5’) and modeled self-consistent points for a range of aspect ratios (labeled ‘SCA’) corresponding to each sample. The self-consistent points are color coded by the aspect ratio of the brine-filled pore-space, the quartz phase modeled as spherical grains with aspect ratio 1. Obviously the end-members used for the GT and SCA computations are quartz and

brine (bulk modulus = 36.6 GPa & 2.29 GPa, shear modulus = 45 GPa & 0 GPa, electrical conductivity = 10^{-5} & 0.2 S/m respectively).

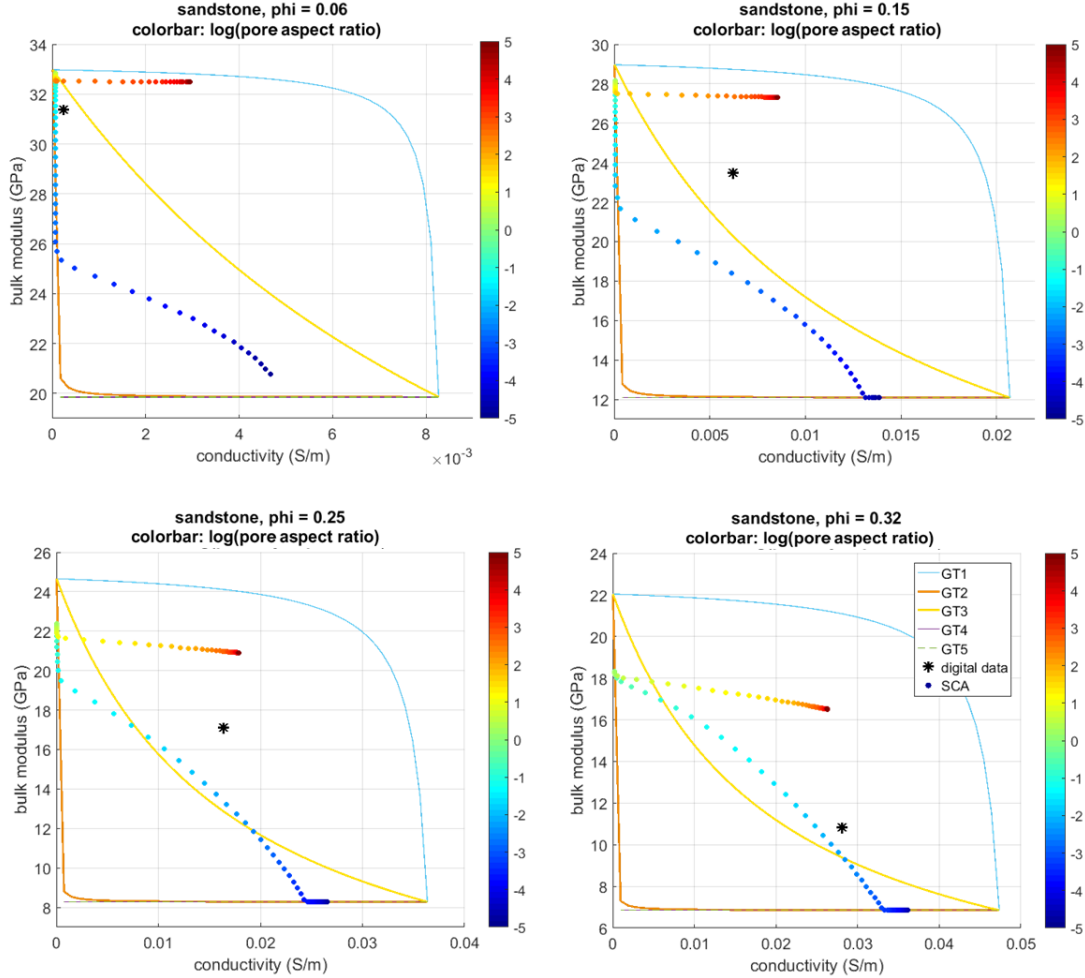


Figure 4.10: Digitally computed bulk modulus and conductivity (black stars) for four brine filled sandstone samples with different porosities, along with the 5 GT curves (labeled ‘GT1’,‘GT2’,‘GT3’,‘GT4’ & ‘GT5’) and modeled self-consistent points for a range of aspect ratios (labeled ‘SCA’) corresponding to each sample. The self-consistent points are color coded by the aspect ratio of the brine-filled pore-space, the quartz phase modeled as spherical grains with aspect ratio 1.

It is evident from Figure 4.10 that all of the digitally computed data-points fall within the GT cross-bounds. The data-point corresponding to a porosity of 0.06 falls

between the embedded bounds ‘GT2’ and ‘GT3’ while the other three data points fall between one of the embedded curves ‘GT3’ and the partially realizable three-point bound ‘GT1’. As pointed out in the previous section, the difference between oblate and prolate pore shapes modeled using the self-consistent approximation is greatest at lower porosities and progressively less significant with increasing porosity. The placement of the digitally estimated data-points with respect to the corresponding self-consistent arcs in the σ^* - K^* plane suggests a mix of oblate and prolate pore-spaces. This is important as it suggests that while a vast majority of single property effective medium modeling in rock physics is done assuming only oblate/disk-like pore-spaces, cross-property modeling suggests that to jointly satisfy both bulk-modulus and electrical conductivity data, we might also need to add prolate or tube-like pores to the mix.

This is in line with the recent observation made by Han et al. (2016, [119]) when attempting to jointly model elastic velocity and electrical conductivity of reservoir sandstones using self-consistent models. The authors of the paper attempt to use only oblate pores in the modeling exercise, and observe that the pore aspect ratios corresponding to the conductivity data are typically smaller than the pore aspect ratios corresponding to elastic velocity data. In Figure 4.10, if compare the digital data points to the oblate arm of the self-consistent model only, it becomes apparent that pore aspect ratios corresponding to the conductivity are typically smaller than those corresponding to bulk modulus in our examples too. Han et al. (2016, [119]) interpret this observation as systematic discrepancy in the estimated pore structure predicted by the self-consistent model, suggesting the need for a new model to link the elastic and electrical properties to a unified pore aspect ratio in reservoir rocks. An alternate interpretation based on our cross-property study is simply the need for a mix of oblate and prolate pore shapes in the self-consistent model to link the elastic and electrical properties to a unified pore aspect ratio.

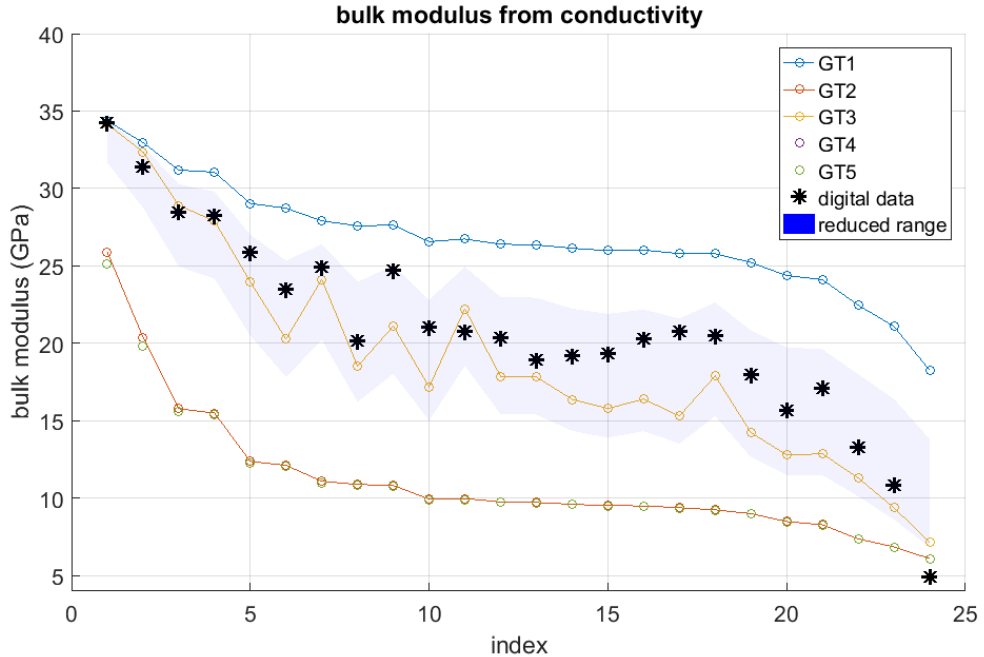


Figure 4.11: Digital data points against the corresponding GT bounds for all 24 sandstone samples, plotted in order of increasing sample porosity. The GT curves are estimated using the digital estimate of electrical conductivity combined with information on porosity and phase property end-points. The digital sandstone samples, spanning a wide range of porosity values, lie within a narrow bulk modulus band around the embedded curve ‘GT3’, shaded and labeled as ‘reduced range’.

In Figure 4.11 we plot digital data points against the corresponding GT bounds for all 24 sandstone samples, plotted in order of increasing sample porosity. For each sample (plotted as sample ‘index’ along the x-axis, index corresponding to Table 4.1), we consider the digital estimate of electrical conductivity and combine it with the porosity and phase property end-points to obtain 5 GT estimates of bulk modulus (labeled ‘GT1’-‘GT5’). The black stars are the FEM computed digital bulk modulus for each sample. It is apparent that most of the digital bulk modulus estimates lie between one of the embedded bounds ‘GT3’ and the partially realizable 3-point bound ‘GT1’, on an average lying closer to ‘GT3’ than any other GT estimate. 3 of the 24 samples lie within the embedded bounds ‘GT2’ and ‘GT3’. The one sample

that falls outside the GT cross-bounds, also violates the HS bounds on bulk modulus, indicating error in estimation.

While the most general case for bounds on bulk modulus for a specific electrical conductivity is given by the outermost GT bounds, the digital sandstone samples, spanning a wide range of porosity values, actually lie within a much narrower bulk modulus band around the embedded curve ‘GT3’. ‘GT3’ corresponds to the fluid-coated embedded bound, discussed in details in the chapter on conductivity substitution, and it represents micro-structures with optimally connected pore-space. The narrow band around ‘GT3’ has been shaded and labeled in Figure 4.11 as ‘reduced range’. Empirically the upper and lower ends of the ‘reduced range’ are given by linear combinations of ‘GT3’ & ‘GT1’ (Equation 4.13) and ‘GT3’ & ‘GT2’ (Equation 4.14) respectively.

$$range_{upper} = 0.4GT3 + 0.6GT1 \quad (4.13)$$

$$range_{lower} = 0.7GT3 + 0.3GT2 \quad (4.14)$$

Figure 4.12 is very similar to 4.11, except that we start with bulk modulus and attempt to predict conductivity instead of going the other way. In the figure we plot digital estimates of electrical conductivity (black stars) against their 5 GT estimates (labeled ‘GT1’-‘GT5’) obtained using the corresponding digital bulk modulus values combined with porosity and phase property end-points for the 24 sandstone samples, plotted in order of increasing sample porosity. Once again, it is apparent that most of the digital electrical conductivity estimates lie between one of the embedded bounds ‘GT3’ and the partially realizable 3-point bound ‘GT1’, while 3 of the 24 samples lie within the embedded bounds ‘GT2’ and ‘GT3’. The one sample that falls outside the GT cross-bounds, also violates the HS bounds on bulk modulus, indicating error in

estimation.

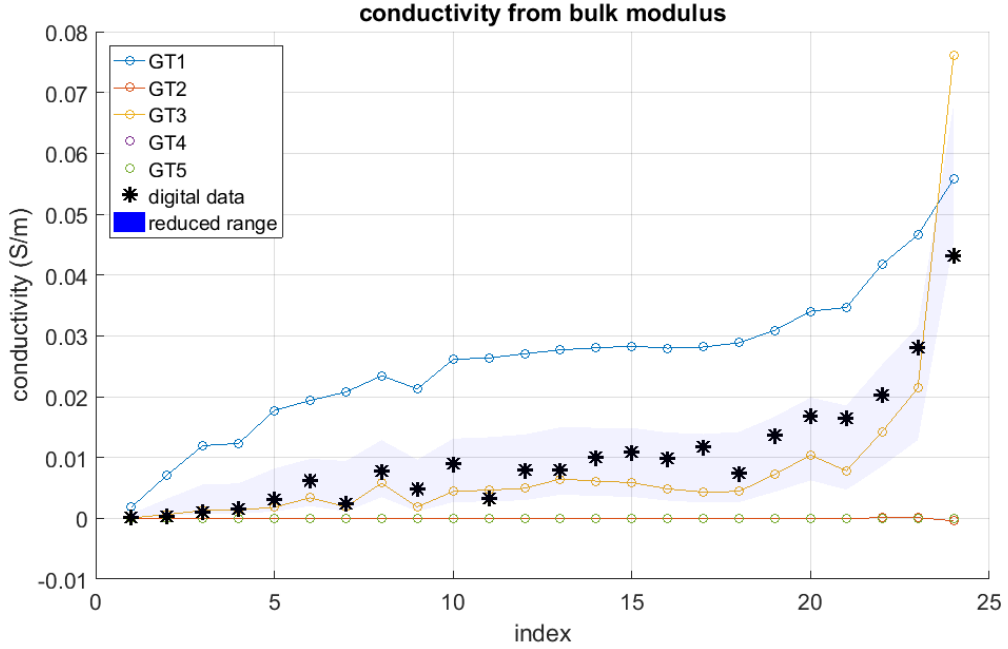


Figure 4.12: Digital data points against the corresponding GT bounds for all 24 sandstone samples, plotted in order of increasing sample porosity. The GT curves are estimated using the digital estimate of bulk modulus combined with information on porosity and phase property end-points. The digital sandstone samples, spanning a wide range of porosity values, lie within a narrow conductivity band around the embedded curve ‘GT3’, shaded and labeled as ‘reduced range’.

As before, the electrical conductivity of the digital sandstone samples, spanning a wide range of porosity values, lie within a narrow conductivity band approximately centered around the embedded curve ‘GT3’. This relatively narrow band is shaded and labeled in Figure 4.11 as ‘reduced range’, the upper and lower ends of which are empirically given by linear combinations of ‘GT3’ & ‘GT1’ (Equation 4.15) and ‘GT3’ & ‘GT2’ (Equation 4.16) respectively.

$$range_{upper} = 0.6GT3 + 0.4GT1 \quad (4.15)$$

$$range_{lower} = 0.6GT3 + 0.4GT2 \quad (4.16)$$

4.6.1.2 Carbonate data

Bulk modulus and conductivity were simultaneously computed on 5 3D digital brine-saturated carbonate samples using FEM in COMSOL (Saxena and Mavko, 2016 [108]), sample properties (porosity, digitally estimated bulk modulus and conductivity) given in Table 4.2.

Table 4.2: Properties of digital carbonate samples, sorted by porosity (Saxena and Mavko, 2016).

index	porosity	K (GPa)	C (S/m)
1	0.126522	38.75334	0.005689
2	0.126755	45.15817	0.001133
3	0.168434	38.34353	0.001593
4	0.204617	34.92427	0.008048
5	0.232471	25.98273	0.007688

Figure 4.13 shows 2 of these samples, spanning the overall porosity range, along with the 5 GT curves (labeled ‘GT1’,‘GT2’,‘GT3’,‘GT4’ & ‘GT5’) and modeled self-consistent points for a range of aspect ratios (labeled ‘SCA’) corresponding to each sample. The self-consistent points are color coded by the aspect ratio of the brine-filled pore-space, the calcite phase modeled as spherical grains with aspect ratio 1. The end-members used for the GT and SCA computations are calcite and brine (bulk modulus = 77 GPa & 2.29 GPa, shear modulus = 32 GPa & 0 GPa, electrical conductivity = 10^{-5} & 0.2 S/m respectively).

As with the digital sandstone samples, it is evident from Figure 4.13 that the digitally computed data-points fall within the GT cross-bounds, one lying between the embedded bounds ‘GT2’ and ‘GT3’ ($\phi = 0.13$) and the other between one of the embedded curves ‘GT3’ and the partially realizable three-point bound ‘GT1’

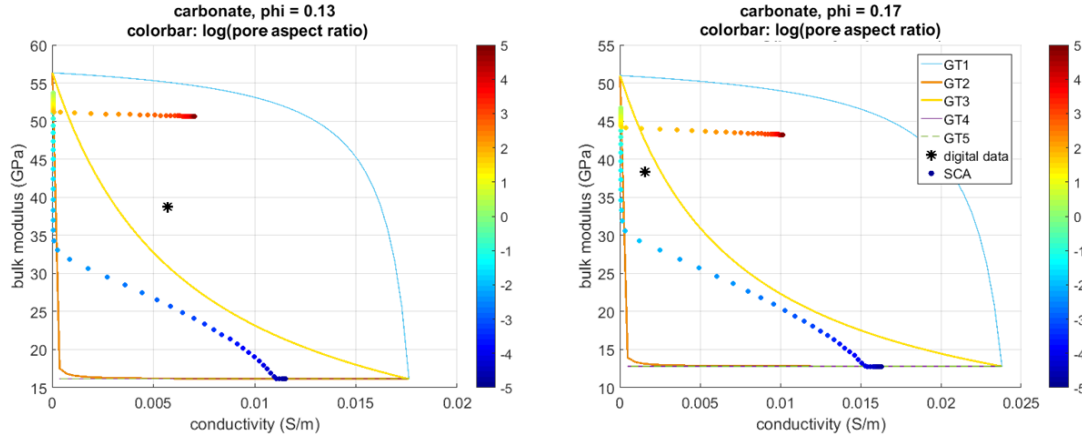


Figure 4.13: Digitally computed bulk modulus and conductivity (black stars) for two brine filled carbonate samples with different porosities, along with the 5 GT curves (labeled ‘GT1’, ‘GT2’, ‘GT3’, ‘GT4’ & ‘GT5’) and modeled self-consistent points for a range of aspect ratios (labeled ‘SCA’) corresponding to each sample. The self-consistent points are color coded by the aspect ratio of the brine-filled pore-space, the calcite phase modeled as spherical grains with aspect ratio 1.

($\phi = 0.17$). While a vast majority of single property effective medium modeling in rock physics is done assuming only oblate/disk-like pore-spaces, the placement of the digitally estimated data-points with respect to the corresponding self-consistent arcs in the σ^*-K^* cross-property space suggests the need for a mix of oblate and prolate pore-spaces.

Figure 4.14 is the exactly analogous to Figure 4.11, plotting carbonate data points instead of sandstone, and showing that most of the digital bulk modulus estimates lie within a narrow band approximately centered around the embedded curve ‘GT3’. This relatively narrow band is shaded and labeled in figure as ‘reduced range’, the upper and lower ends of which are empirically given by linear combinations of ‘GT3’ & ‘GT1’ (Equation 4.17) and ‘GT3’ & ‘GT2’ (Equation 4.18) respectively.

$$carb-range_{upper} = 0.4GT3 + 0.6GT1 \quad (4.17)$$

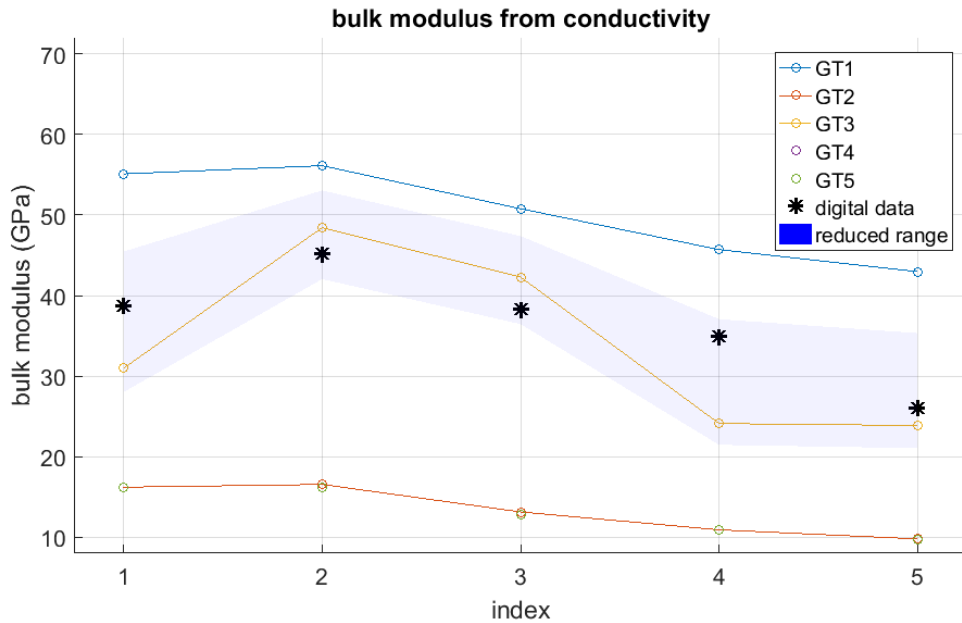


Figure 4.14: Digital data points against the corresponding GT bounds for all 5 carbonate samples, plotted in order of increasing sample porosity. The GT curves are estimated using the digital estimate of conductivity combined with information on porosity and phase property end-points. The digital carbonate samples, spanning a wide range of porosity values, lie within a narrow bulk modulus band around the embedded curve ‘GT3’, shaded and labeled as ‘reduced range’.

$$\text{carb} - \text{range}_{\text{lower}} = 0.8\text{GT3} + 0.2\text{GT2} \quad (4.18)$$

Figure 4.15 is the exactly analogous to Figure 4.12, plotting carbonate data points instead of sandstone, and showing that most of the digital electrical conductivity estimates lie within a narrow band approximately centered around the embedded curve ‘GT3’. This band is shaded and labeled in the figure as ‘reduced range’, the upper and lower ends of which are empirically given by Equations 4.19 and 4.20 respectively.

$$\text{carb} - \text{range}_{\text{upper}} = 0.7\text{GT3} + 0.3\text{GT1} \quad (4.19)$$

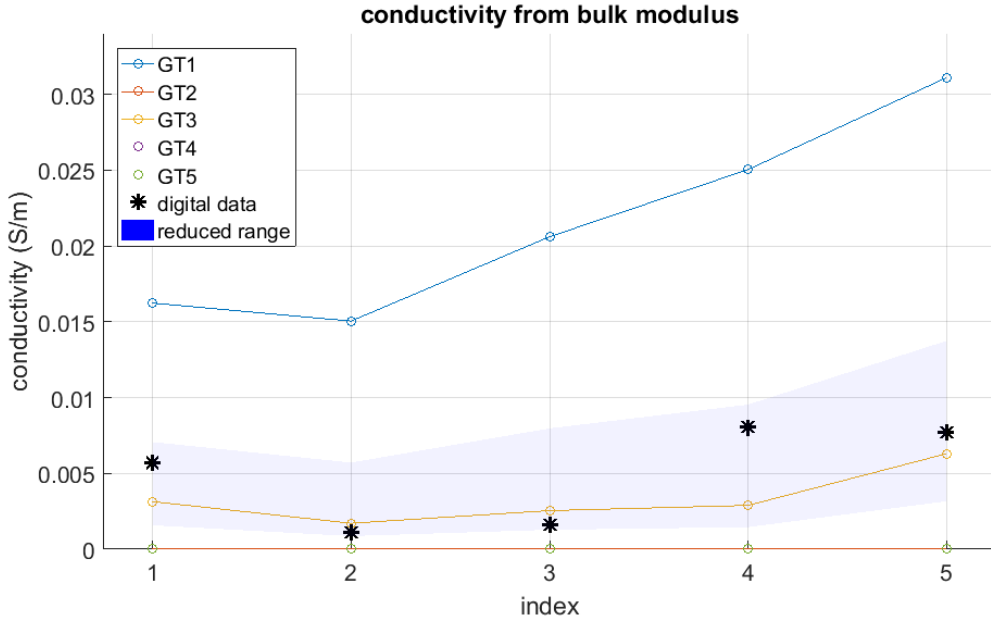


Figure 4.15: Digital data points against the corresponding GT bounds for all 5 carbonate samples, plotted in order of increasing sample porosity. The GT curves are estimated using the digital estimate of bulk modulus combined with information on porosity and phase property end-points. The digital carbonate samples, spanning a wide range of porosity values, lie within a narrow conductivity band around the embedded curve ‘GT3’, shaded and labeled as ‘reduced range’.

$$\text{carb} - \text{range}_{\text{lower}} = 0.5\text{GT3} + 0.5\text{GT2} \quad (4.20)$$

4.6.2 Comparison with laboratory data

We further test the GT cross-bounds using a rich lab-measured dataset by T. Han (2010 [109]). The dataset has 67 reservoir sandstone samples of various mineralogical compositions, specified using X-ray diffraction (XRD) tests and scanning electron microscope (SEM) analyses of thin sections. Also available for each rock sample are measurements of Vp (P-wave velocity), Vs (S-wave velocity), Qp (P-wave attenuation factor), Qs (P-wave attenuation factor), and resistivity/complex impedance

(measured at 2Hz and 440Hz) at multiple confining pressures (8, 15, 20, 26, 40, 60 MPa).

Of the 67 samples, we choose a subset of 17 samples with clay volume fraction $< 5\%$, to minimize the phase-property uncertainty associated with clays. Table 4.3 lists the sample properties of the selected subset relevant to our current exercise. Table 4.4 lists the porosity and mineralogy of the selected sub-samples. Table 4.5 lists the physical properties of the end-member components used in modeling this dataset. Properties of quartz, clay and brine are taken from T. Han's work (2010, [109]) while calcite and feldspar properties are from the handbook (Mavko et al., 2009 [19]).

Table 4.3: Laboratory measurements on selected low clay samples (Han et al., 2010).

Sample	Vp_60	Vs_60	R_2Hz_60	Vp_8	Vs_8	R_2Hz_8
E3	4660	3060	8.59	4548	2975	8.17
E5	4800	3119	10.39	4687	3044	10.01
E6	4745	2995	9.15	4609	2890	8.63
E4	4775	3085	7.88	4643	2996	7.55
STONERAISE	4896	3070	25.12	4626	2822	21.16
COVERED	4168	2476	5.07	3747	2137	4.61
1VSF	3845	2227	5.03	3476	1966	4.55
BEESTONE	4123	2449	5.92	3802	2179	5.31
PEAKMOOR	4233	2559	11.1	3925	2324	9.64
DUKES	4318	2569	13.8	3981	2279	11.31
CZ13	4223	2274	4.4	3839	1954	4.1
RES1	4575	2841	21.01	4196	2524	16.77
4SU	4449	2717	31.9	3982	2300	21.67
WATTSCLIFFE	4116	2507	8.23	3814	2268	7.27
W165.7H	4285	2670	6.37	4036	2479	6.08
W165.7	4096	2646	6.45	3896	2513	6.01
CZ5	3233	1736	1.91	2753	1381	1.74

Figure 4.16 shows 4 of these 17 samples in the σ^*-K^* cross-property space along with the GT bounds and modeled self-consistent points for a range of pore aspect ratios (labeled 'SCA', color-coded by aspect ratio) corresponding to each sample. For

Table 4.4: Porosity and mineralogy of selected low clay samples (Han et al., 2010).

Sample	Porosity	Quartz	Calcite	Clay	Feldspar
E3	13.4	81.96	0.36	0	4.27
E5	12.86	81.91	0.34	0	4.89
E6	12.75	80.57	0.54	0	6.14
E4	14.12	80.06	0.45	0	5.36
STONERAISE	10.34	77.35	0.36	0	11.95
COVERED	17.44	58.66	4.63	0	19.27
1VSF	18.81	74.47	5.39	0.29	1.05
BEESTONE	18.88	64.03	0.04	0.54	16.52
PEAKMOOR	13.74	64.18	5.88	1.23	14.97
DUKES	14.39	62.09	9.87	1.23	12.43
CZ13	16.52	30.73	13.89	1.85	37.01
RES1	10.65	69.91	3.7	2.92	12.81
4SU	9.22	61.6	8.05	3.08	18.04
WATTSCLIFFE	16	59.43	5.7	3.4	15.48
W165.7H	17.55	76.91	1.05	3.89	0.6
W165.7	16.87	77.58	1.03	3.92	0.6
CZ5	28.99	32.08	1.15	3.93	33.86

Table 4.5: Physical properties of components used in modeling Han's (2010) data.

Component	Bulk Modulus (GPa)	Shear Modulus (GPa)	Conductivity (S/m)	Density (g/cc)
Quartz	36.6	45	1e-5	2.65
Clay	20.9	6.85	0.02	2.58
Calcite	77	32	1e-5	2.71
Feldspar	74.5	33.7	1e-5	2.63
Brine	2.29	0	4.69	1.025

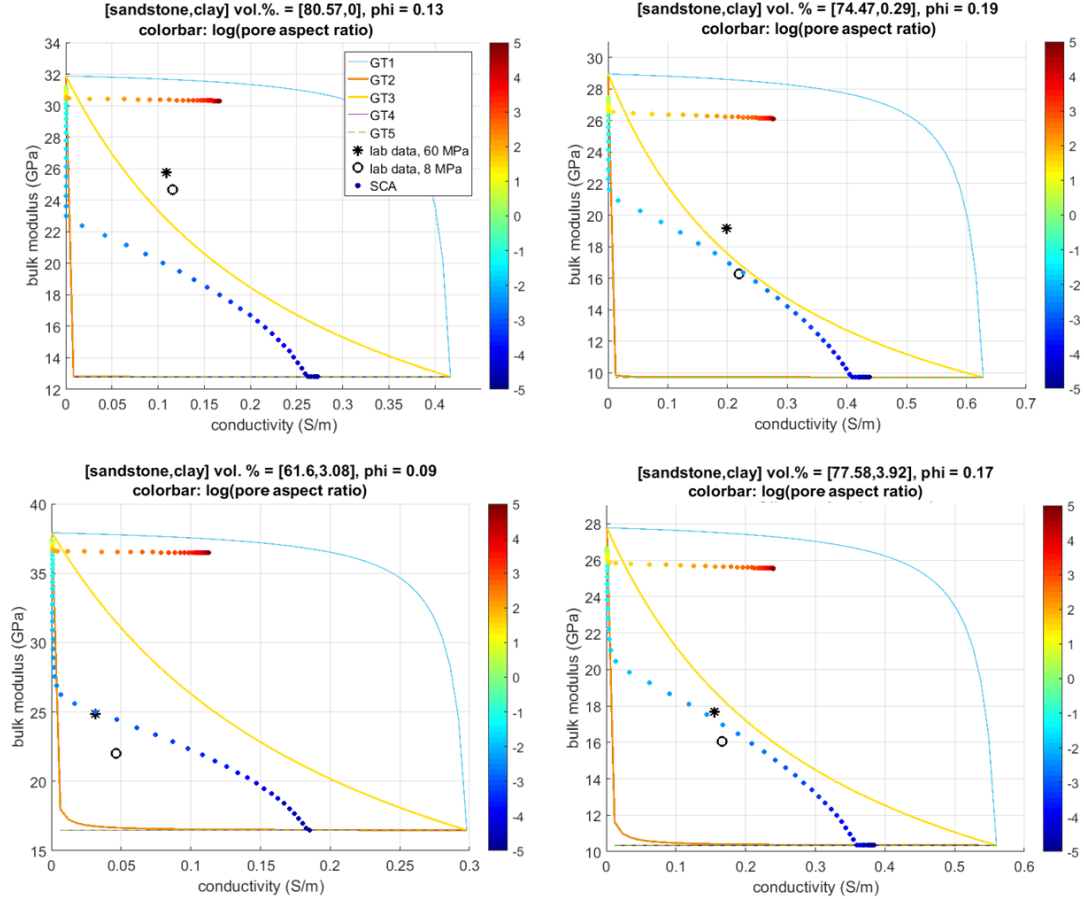


Figure 4.16: Laboratory measured conductivity and bulk modulus estimates (black stars [60 MPa] and circles [8MPa]) for four brine filled sandstone samples with different porosities, along with the 5 GT curves (labeled ‘GT1’, ‘GT2’, ‘GT3’, ‘GT4’ & ‘GT5’, for bulk modulus computed from 60 MPa conductivity) and modeled self-consistent points for a range of aspect ratios (labeled ‘SCA’) corresponding to each sample. The self-consistent points are color coded by the aspect ratio of the brine-filled pore-space, the quartz phase modeled as spherical grains with aspect ratio 1.

each sample, measured σ^*-K^* pairs for confining pressures of 60 MPa and 8 MPa are plotted. All of the measured data-points fall within the GT cross-bounds, two samples with low clay volume fraction ($< 0.3\%$) lying between one of the embedded curves ‘GT3’ and the partially realizable three-point bound ‘GT1’ and the other two, with relatively high clay volume fraction ($> 3\%$) lying between embedded bounds

'GT2' and 'GT3'.

The placement of the low-clay data-points with respect to the corresponding self-consistent arcs in the σ^*-K^* cross-property space suggests the need for a mix of oblate and prolate pore-spaces in effective medium modeling. In general, going from the 8 MPa to the 60 MPa data points in the cross-property space moves us further away from oblate and towards prolate pore shapes, which intuitively makes sense, since a primary effect of increasing confining pressure is the closing of compliant crack-like/oblate pores.

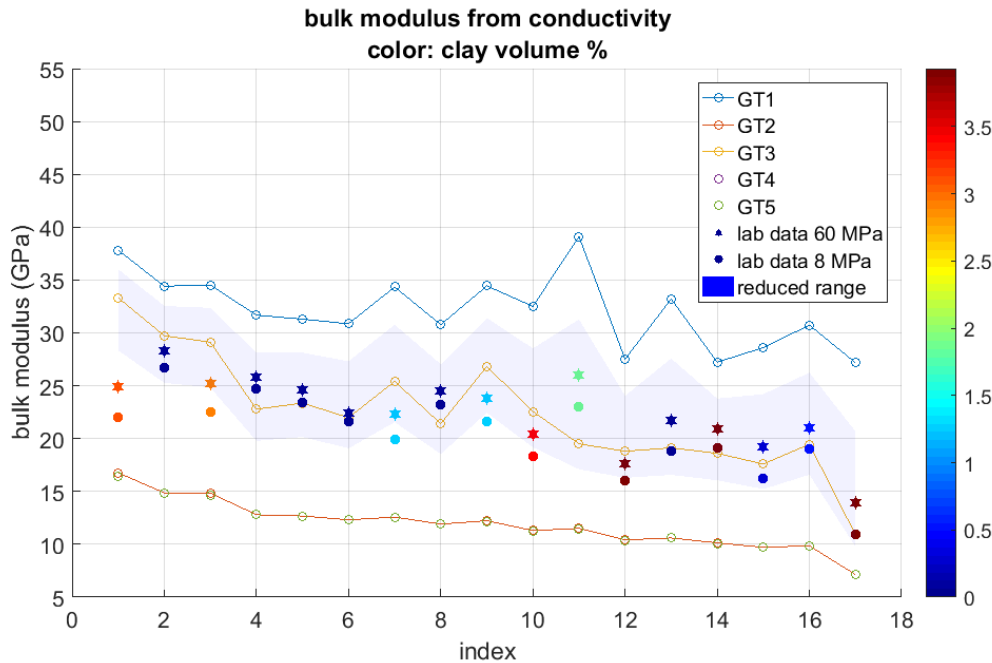


Figure 4.17: Laboratory measured data points against the corresponding GT bounds for the 17 selected sandstone samples (clay component < 5%) from Han's (2010) dataset, plotted in order of increasing sample porosity. The GT curves are estimated using the laboratory measurement of sample conductivities combined with information on porosity and phase property end-points. The sandstone samples, spanning a wide range of porosity values, lie within a narrow conductivity band around the embedded curve 'GT3', shaded and labeled as 'reduced range'.

Figure 4.17 is analogous to Figures 4.11 and 4.14, plotting laboratory measured

data points instead of digital, and showing that despite differences in the mineralogical composition of the samples, a large fraction of the measured bulk modulus estimates lie within a narrow band approximately centered around the embedded curve ‘GT3’, given by Equations 4.13 and 4.14, derived in the previous section for digital sandstone samples. For each sample, the GT bounds on bulk modulus are derived using conductivity measured at 60 MPa, and measured bulk modulus values plotted correspond to confining pressures of both 8 & 60 MPa. Barring one sample with relatively high clay volume fraction (3%), all of the 60 MPa points fall within the reduced range. The few 8 MPa points that lie outside the reduced range, typically have high clay fractions, and are all softer than predicted by the range.

Figure 4.18 is analogous to Figures 4.12 and 4.15, plotting laboratory measured data points instead of digital, showing the prediction of conductivity from bulk modulus. Once again, the figure shows that despite differences in the mineralogical composition of the samples, a large fraction of the measured electrical conductivity estimates lie within a narrow band approximately centered around the embedded curve ‘GT3’, given by Equations 4.15 and 4.16, derived in the previous section for digital sandstone samples. For each sample, the GT bounds on conductivity are derived using bulk modulus measured at 60 MPa, and measured conductivity values plotted correspond to confining pressures of both 8 & 60 MPa. Barring one sample with relatively high clay volume fraction (3%), all of the 60 MPa points fall within the reduced range. The two 8 MPa points that lie outside the reduced range, typically have high clay fractions, and are less conductive than predicted by the range.

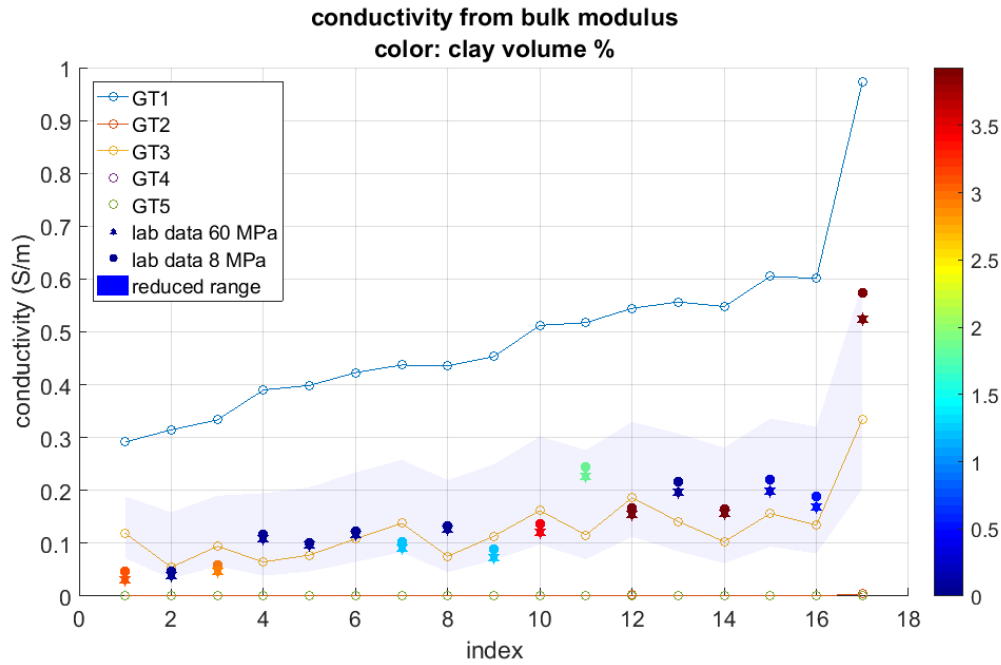


Figure 4.18: Laboratory measured data points against the corresponding GT bounds for the 17 selected sandstone samples (clay component < 5%) from Han's (2010) dataset, plotted in order of increasing sample porosity. The GT curves are estimated using estimates of sample bulk moduli from laboratory measurements, combined with information on porosity and phase property end-points. The sandstone samples, spanning a wide range of porosity values, lie within a narrow conductivity band around the embedded curve 'GT3', shaded and labeled as 'reduced range'.

4.7 GT bounds for determining Archie cementation factor

So far, we have spoken about practical/empirical constraints that can be added to the GT bounds to make them more useful in real-life geophysical applications. In this section we discuss the second key contribution of this chapter, the joint interpretation of conductivity-bulk modulus cross-property data for better formation evaluation. We will demonstrate how bulk modulus and conductivity data can be jointly used for formation evaluation, which in this specific case helps us estimate the Archie

cementation factor ‘m’ (Archie, 1942 [16]).

Archie (1942) proposed the following empirical relationship between the effective conductivity of clean sandstone fully saturated with conductive brine and the brine conductivity:

$$S_{eff} = S_{fluid}F^{-1} \quad \text{where} \quad F = \phi^{-m} \quad (4.21)$$

In equation 5.1 S_{eff} is the effective conductivity of the fully saturated clean sandstone, S_{fluid} is the brine conductivity, F is the ‘formation factor’ assumed to be independent of the fluid, ϕ is the formation porosity and ‘m’ is the ‘cementation factor’. Obviously, determining ‘m’ is important for any rock physics analysis involving computation of fluid saturations in a formation. Rearranging the terms in equation 5.1, we can derive an expression for ‘m’ as given by Equation 4.22.

$$m = \frac{\log(S_{eff}/S_{fluid})}{\log(\phi)} \quad (4.22)$$

Equation 4.22 clearly shows that for a given brine conductivity, ‘m’ is simply a function of the effective conductivity and porosity of the formation. This demonstrated in Figure 4.19, showing the variation of ‘m’ in the σ^* - K^* cross-property space for a brine saturated sandstone of porosity 0.3, brine and sandstone properties as discussed in the previous section. The figure shows that for a constant value of formation conductivity, we get a range of possible values of formation bulk modulus (computed as per the ‘reduced range’ GT bounds, given by Equations 4.13 and 4.14) and a constant value of ‘m’. At the HS ‘suspension point’ (lower right corner of the sub-figures), ‘m’ encounters its lowest value (=1.25) and changes slowly with changing formation conductivity while at the HS ‘foam point’ (upper left corner of the sub-figures), ‘m’ encounters its highest value (=5.7) and changes rapidly with changing conductivity. The color bar on left sub-figure shows the entire range of ‘m’ for this example, while

on the right sub-figure the color bar has a maximum of ' m ' = 2.5, to better reveal the variation of ' m ' at higher values of formation conductivity.

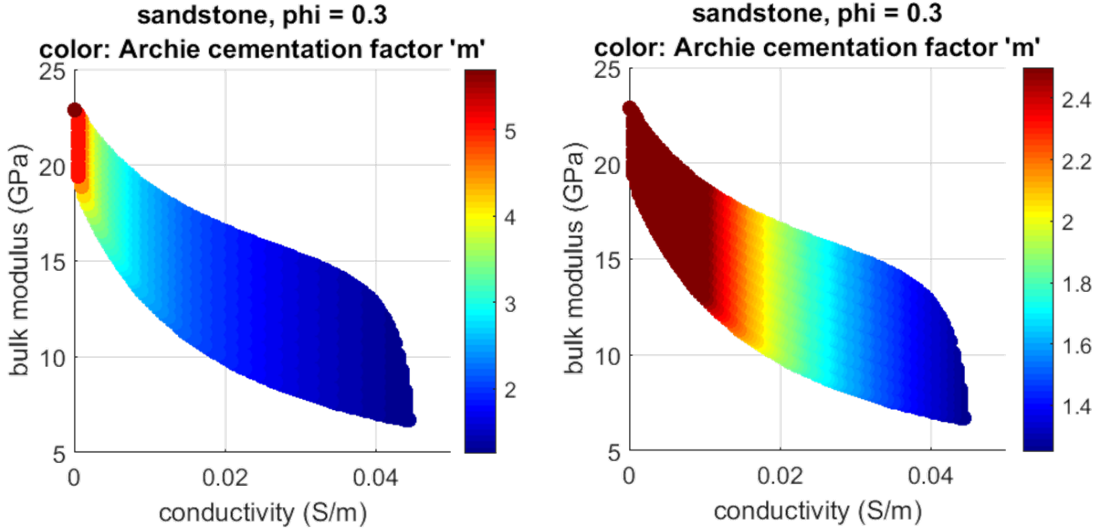


Figure 4.19: Variation of ' m ' in the σ^* - K^* cross-property space for a brine saturated sandstone of porosity 0.3. For a constant value of formation conductivity, we get a range of possible values of formation bulk modulus (computed as per the 'reduced range' GT bounds) and a constant value of ' m '. The color-bar on left sub-figure shows the entire range of ' m ' for this example, while on the right sub-figure the color-bar has a maximum of ' m ' = 2.5, to better reveal the variation of ' m ' at higher values of formation conductivity.

Now suppose we want to predict ' m ', given large scale measurements of formation bulk modulus (as from a seismic survey) and electrical conductivity (as from a CSEM survey), without knowing the formation porosity. Since in the absence of complete micro-geometry characterization formation bulk modulus and conductivity are not uniquely related with porosity, the best we can do in this scenario is predict a reasonable range of ' m ' values. Based on our discussion in the previous sections of the chapter, any given pair of σ^* - K^* values is potentially associated with a range of porosities, resulting in a range of ' m ' values. The most rigorous bounds/range on

'm' can be determined by using the GT cross-bounds. This range can be substantially reduced based on empirical evidence, as discussed in the previous section. For sandstones, the relevant 'reduced range' GT bounds is given by Equations 4.13 and 4.14).

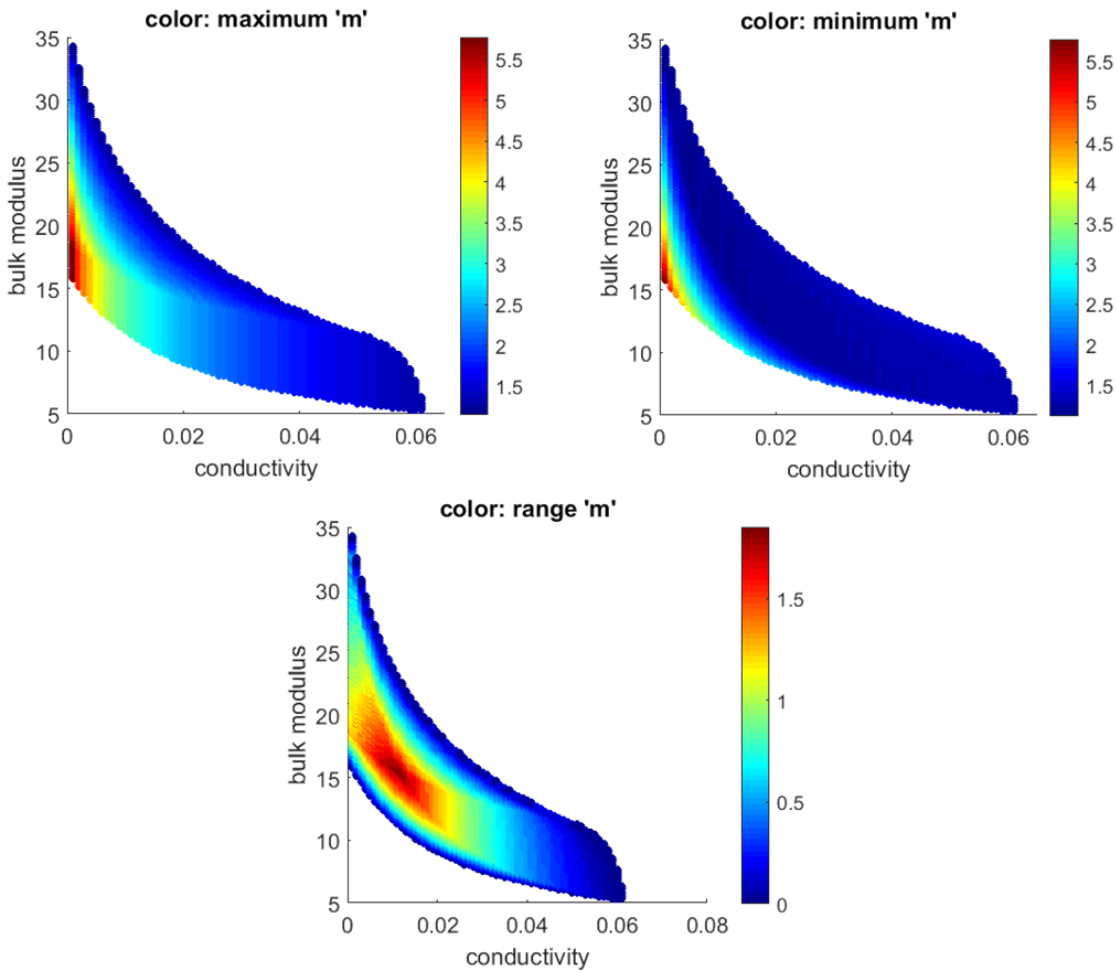


Figure 4.20: Variation in 'm' in the σ^* - K^* plane, using the 'reduced range' GT bounds. The top left sub-figure shows the variation in the maximum possible value of 'm', the top right sub-figure shows variations in the minimum values of 'm'. The bottom panel shows the variation in the range of 'm' (= the difference between the maximum and minimum values of 'm' for any given σ^* - K^* pair). While the theoretical maximum value of 'm' can be as high as 5.5, the range of 'm' for any allowable σ^* - K^* pair is only about 1.75.

For a brine-filled sandstone formation with porosity anywhere between 0 and 0.4, Figure 4.20 shows the variation in ‘m’ in the σ^* - K^* plane, using the ‘reduced range’ GT bounds given by Equations 4.13 and 4.14). Since any specific σ^* - K^* pair is potentially associated with a range of porosities, any point in the σ^* - K^* space is potentially associated with a range of ‘m’ values, given by equation 4.22. For all allowable σ^* - K^* pairs, the top left sub-figure shows the variation in the maximum possible value of ‘m’: the highest values (= 5.77) occur in the low conductivity-low bulk modulus region while the lowest values (=1.15) occur in the high conductivity-low modulus region. For a given conductivity, the lowest values of maximum ‘m’ occur for the highest values of corresponding bulk modulus and vice versa. Similarly, the right sub-figure shows variations in the minimum values of ‘m’, once again the highest (=5.77) and lowest (=1.11) values occur in the low conductivity-low bulk modulus and high conductivity-low modulus regions respectively.

The bottom panel of figure 4.20 shows the variation in the range of ‘m’ (= the difference between the maximum and minimum values of ‘m’ for any given σ^* - K^* pair). The range is the lowest along the top, bottom and high-conductivity edges of the allowable σ^* - K^* cloud, while it is highest (≈ 1.75) in the middle of the cloud, biased slightly towards low conductivity-low bulk modulus values. The plot shows us that while the theoretical maximum value of ‘m’ can be as high as ≈ 5.5 , the range for any allowable σ^* - K^* pair is only about 1.75. It is interesting to note that the maximum values of ‘m’ from this exercise are higher than the values usually reported in published literature and these values correspond to the low conductivity-low bulk modulus region of the σ^* - K^* plane. This region is not spanned by the digital/laboratory data we studied, indicating that while theoretically it is possible to have micro-structures that correspond to this region of the σ^* - K^* plane, such micro-structures are generally not prevalent among naturally occurring rocks.

4.8 Conclusions

In this chapter, we propose the use of Gibiansky and Torquato's (GT) rigorous cross-property bounds between the electrical conductivity and bulk modulus of a rock. The bounds help in predicting the range of effective bulk modulus for a known effective conductivity (and vice-versa) and known constituent phase properties, for three dimensional, isotropic, 2-phase composites. The inherent non-uniqueness in cross-property relations captured by the bounds correspond to the uncertainty due to the unknown exact micro-geometry of a composite.

Gibiansky and Torquato gave us equations for five hyperbolae in the σ^* - K^* space, with the widest of the five forming the cross-bounds for a given set of constituent phase properties. Two of these hyperbolae are the embedded bounds discussed by Mavko & Saxena in addressing elastic solid substitution, realizable by doubly coated spheres. Using digital and laboratory data, we established empirical constraints on the rigorous GT cross-bounds to make them narrower and therefore more useful when dealing with some common reservoir rocks, specifically brine filled sandstones and carbonates. Despite having very different sources of errors/uncertainties, both digital and laboratory measured rock properties show that in the σ^* - K^* space real rocks lie close to the fluid-coated embedded bound ('GT3'), representative of optimally connected pore-space. Effective medium theories helped us demonstrate the need for considering a mix of oblate and prolate pore spaces when jointly modeling the elastic and electrical properties of a rock.

We also demonstrated the importance of factoring in porosity when using or interpreting cross-property bounds/relations. Finally, we showed the use of the empirically constrained cross-bounds in estimating the Archie cementation factor 'm' of a rock when presented with large-scale elastic (e.g., seismic) and electrical (e.g., CSEM) surveys. We found that while the theoretical maximum value of 'm' can be as high as 6

in brine-filled sandstones, the maximum range of ‘m’ for any allowable σ^* - K^* pair is only about 1.75.

4.9 Appendix

The recipe for estimating the 5 GT points for bulk modulus for a given value of porosity and effective conductivity (and vice versa) (Gibiansky and Torquato, 1998 [10]) is given as follows. For a specific value of composite effective conductivity σ^* , the possible values of the composite effective bulk modulus K^* are restricted by Equation 4.23.

$$K^* \in [F(\alpha_{min}, \sigma^*), F(\alpha_{max}, \sigma^*)] \quad (4.23)$$

In Equation 4.23 $F(\alpha, \sigma^*)$ is given by function 4.24.

$$F(\alpha, \sigma^*) = \frac{\alpha K_1^*(\sigma_2^* - \sigma^*)(\sigma_1^* - \sigma_2^*) - K_2^*(\sigma_2^* - \sigma^*)(K_1^* - K_2^*)}{\alpha(\sigma_2^* - \sigma^*)(\sigma_1^* - \sigma_2^*) - (\sigma_2^* - \sigma^*)(K_1^* - K_2^*)} \quad (4.24)$$

$$\alpha_{max} = max(\alpha_1, \alpha_2, \alpha_3, \alpha_4, \alpha_5), \alpha_{min} = min(\alpha_1, \alpha_2, \alpha_3, \alpha_4, \alpha_5)$$

$$\alpha_1 = \frac{6(\mu_1 - \mu_2)(f_1\sigma_2 + f_2\sigma_1 + 2\sigma_2)^2(K_1 - K_2)^2}{(\sigma_1 - \sigma_2)^3(3f_1K_2 + 3f_2K_1 + 4\mu_2)^2} \quad (4.25)$$

$$\begin{aligned} \alpha_2 &= \alpha_1 \frac{3\sigma_1(3K_1 + 4\mu_2)}{(\sigma_1 + 2\sigma_2)(3K_1 + 4\mu_1)} \\ \alpha_3 &= \alpha_1 \frac{(2\sigma_1 + \sigma_2)(3K_2 + 4\mu_2)}{3\sigma_2(3K_1 + 4\mu_1)} \end{aligned} \quad (4.26)$$

$$\begin{aligned}\alpha_4 &= \alpha_1 \frac{2\sigma_1\mu_2}{(\sigma_1 + \sigma_2)\mu_1} \\ \alpha_5 &= \alpha_1 \frac{(\sigma_1 + \sigma_2)\mu_2}{2\sigma_2\mu_1}\end{aligned}\quad (4.27)$$

...

Chapter 5

Conductivity substitution

5.1 Abstract

This chapter discusses the problem of electrical fluid substitution - predicting the change in effective conductivity or dielectric constant of a three dimensional, two-phase, isotropic composite that occurs when one conducting phase is substituted with another while the microgeometry remains fixed. The substitution problem is non-unique. For a given composite, knowing the initial effective conductivity, the phase conductivities, and the porosity permits prediction of only the range of effective conductivity upon a change of the phase (fluid or solid) conductivity. The precise change of effective electrical properties depends on details of the composite microstructure, which are seldom completely known. Extending the concept of the embedded bounds from elastic to conductivity substitution, rigorous equations for substitution bounds for two-phase isotropic composites are discussed. When the conductivity contrast between the composite phases is high, predictions from Archie's law correspond approximately to the upper bound on the change of conductivity upon substitution. Inclusion modeling suggests that vuggy or poorly-connected pore space could account for conductivity changes smaller than predicted by Archie's law.

Comparison of the conductivity substitution bounds with brine-saturated sandstone data of varying clay content reveals that the position of measured data with respect to the conductivity substitution bounds can be indicative of the effective clay content in shaly sand samples.

5.2 Introduction

In rock physics, the term fluid substitution is usually reserved for predicting how the effective elastic properties of rocks change when one pore fluid is replaced with another. In this chapter we explore a very similar problem, investigating how the effective electrical conductivity and/or effective dielectric constant of a three dimensional, two-phase, isotropic composite changes when one pore fluid is replaced with another or when one solid is replaced with another.

Gassmann's (1951 [66]) equations allow us to make unique predictions of the change in the effective elastic moduli of two-phase media (mixtures of mineral and fluid), for composites that are macroscopically either isotropic or anisotropic. The uniqueness of Gassmann's prediction results from the assumption that the pore fluid pressure remains uniform and equilibrated everywhere under any externally applied load. Deviation from pressure equilibration can occur when the pore space is poorly connected, the fluid viscosity is high, or the measurement frequency is large. Gibiansky and Torquato (1998 [10]) showed rigorously that, in fact, elastic fluid substitution is intrinsically non-unique and that Gassmann's prediction is merely the lower bound on the possible change in elastic moduli upon substitution.

An interesting parallel can be found in describing the effective electrical conductivity of a two-phase rock. Archie (1942 [16]) proposed an empirical relationship between the effective conductivity ' σ_{eff} ' of a fully brine saturated clean sandstone (with brine conductivity ' σ_{fluid} ') and formation factor ' F ', given by Equation 5.1.

$$\sigma_{eff} = \sigma_{fluid} F^{-1} \quad (5.1)$$

In Equation 5.1 formation factor ‘ F ’ is assumed to be independent of the saturating fluid/brine. Obviously, if this equation is always correct, then fluid substitution for conductivity is trivial and unique. It can be shown, however, that Archie’s equation only gives an upper bound on the change of conductivity upon substitution of the pore fluid, when the conductivity contrast between the rock matrix and pore-fluid is high. In this paper, we discuss theoretical bounds on fluid substitution for effective conductivity of mono-mineralic rocks with a single fluid phase. All of the formulations apply equally well to effective dielectric constant, thermal conductivity, and magnetic permeability (Torquato, 2002 [43]).

5.3 Theory

5.3.1 Previous work

The Hashin-Shtrikman (HS) variational bounds (1962 [7]) were originally formulated for magnetic permeability but also apply to electrical conductivity, dielectric constant, thermal conductivity, and elastic moduli. For electrical conductivity, the HS bounds on an isotropic, three-dimensional, two-phase composite can be expressed as Equation 5.2

$$\frac{1}{\sigma_{HS+/-} + 2\sigma_{+/-}} = \frac{1 - \phi}{\sigma_{min} + 2\sigma_{+/-}} + \frac{\phi}{\sigma_{fluid} + 2\sigma_{+/-}} \quad (5.2)$$

In Equation 5.2, ϕ is the porosity, σ_{min} is the mineral phase conductivity, and σ_{fluid} is the fluid phase conductivity. Setting the parameter $\sigma_{+/-} = \sigma_+ = \text{maximum}(\sigma_{min}, \sigma_{fluid})$ yields the upper bound , and setting $\sigma_{+/-} = \sigma_- = \text{minimum}(\sigma_{min}, \sigma_{fluid})$ yields the lower bound on the effective

composite conductivity respectively. Using the HS bounds, a very general, but not particularly useful, statement that can be made about fluid substitution is that the effective conductivity $\sigma_{eff}^{(1)}$ of a rock with initial fluid $\sigma_{fluid}^{(1)}$ and the effective conductivity $\sigma_{eff}^{(2)}$ of the same rock saturated with a different fluid with conductivity $\sigma_{fluid}^{(2)}$ must satisfy the (obvious) constraints:

$$\sigma_{HS-}^{(1)} \leq \sigma_{eff}^{(1)} \leq \sigma_{HS+}^{(1)} \quad (5.3)$$

$$\sigma_{HS-}^{(2)} \leq \sigma_{eff}^{(2)} \leq \sigma_{HS+}^{(2)} \quad (5.4)$$

In Equations 5.3 and 5.4 superscripts (1) and (2) everywhere refer to the initial and final compositions, respectively. Note that the constraints on $\sigma_{eff}^{(1)}$ and $\sigma_{eff}^{(2)}$ are independent of each other, so that one is not used to predict the other.

Prager (1969 [120]) introduced improvements to the variational bounds by using a known value of $\sigma_{eff}^{(1)}$ as a constraint on $\sigma_{eff}^{(2)}$ when one or both of the phase properties change. His equations for the bounds are given by 5.5 and 5.6.

$$\begin{aligned} \sigma_{eff}^{(2)} &< \sigma_a^{(2)} - (\sigma_a^{(1)} - \sigma_{eff}^{(1)}) \\ &\left(\frac{\sigma_{min}^{(1)} \phi (\sigma_{min}^{(2)} - \sigma_{fluid}^{(2)})^2}{\sigma_{min}^{(1)} \phi (\sigma_{min}^{(2)} - \sigma_{fluid}^{(2)}) (\sigma_{min}^{(1)} - \sigma_{fluid}^{(1)}) + (\sigma_{eff}^{(1)} - \sigma_{min}^{(1)}) (\sigma_{fluid}^{(1)} \sigma_{min}^{(2)} - \sigma_{min}^{(1)} \sigma_{fluid}^{(2)})} \right) \end{aligned} \quad (5.5)$$

$$\sigma_{eff}^{(2)} > \left\{ \sigma_h^{(2)} - \frac{\left(\frac{1}{\sigma_h^{(1)}} - \frac{1}{\sigma_{eff}^{(1)}} \right) \left(\frac{1}{\sigma_{min}^{(2)}} - \frac{1}{\sigma_{fluid}^{(2)}} \right)^2 \left(\frac{1-\phi}{\sigma_{fluid}^{(1)}} \right)}{\left(\frac{1-\phi}{\sigma_{fluid}^{(1)}} \right) \left(\frac{1}{\sigma_{min}^{(2)}} - \frac{1}{\sigma_{fluid}^{(2)}} \right) \left(\frac{1}{\sigma_{min}^{(1)}} - \frac{1}{\sigma_{fluid}^{(1)}} \right) + \left(\frac{1}{\sigma_{eff}^{(1)}} - \frac{1}{\sigma_{fluid}^{(1)}} \right) \left(\frac{1}{\sigma_{min}^{(1)} \sigma_{fluid}^{(2)}} - \frac{1}{\sigma_{fluid}^{(1)} \sigma_{min}^{(2)}} \right)} \right\}^{-1} \quad (5.6)$$

In Eqns. 5.5 and 5.6, $\sigma_a^{(i)} = (\sigma_{min}^{(i)} + \sigma_{fluid}^{(i)})/2$ is the arithmetic average of the phase conductivities, and $\sigma_h^{(i)} = 2(1/\sigma_{min}^{(i)} + 1/\sigma_{fluid}^{(i)})^{-1}$ is the harmonic average of the phase conductivities. Prager's bounds on are narrower than the simple HS bounds.

5.3.2 The embedded bounds

A further improvement on prediction of $\sigma_{eff}^{(2)}$ from $\sigma_{eff}^{(1)}$ can be found by extending the concept of the embedded bounds developed by Mavko and Saxena (2013 [11]) for elastic phase (solid/fluid) substitution to the case of electrical conductivity substitution. To understand how the embedded bounds bounds are derived we will start with the Hashin-Shtrikman (HS) bounds on the effective conductivity of a 2-phase, three dimensional isotropic composite. Figure 5.1 shows the HS bounds for an isotropic mineral-fluid composite with mineral conductivity $\sigma_{min} = 0.01S/m$, and fluid conductivity $\sigma_{fluid} = 10S/m$. In the absence of any micro-geometric information, our best prediction of the effective conductivity σ_{eff} of this composite can lie anywhere between the upper and lower HS bounds.

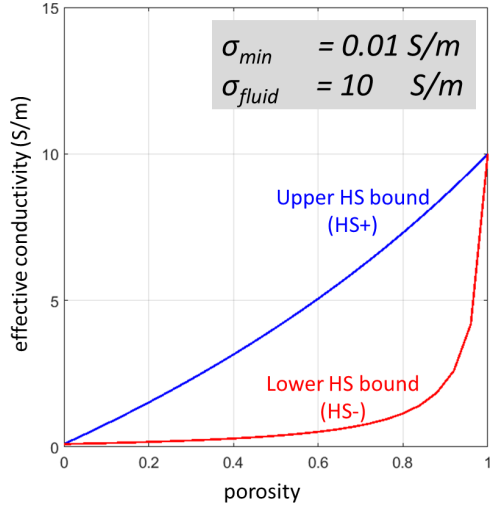


Figure 5.1: HS bounds for a 2-phase, 3-dimensional, isotropic mineral-fluid composite with mineral conductivity $\sigma_{min} = 0.01 \text{ S/m}$, and fluid conductivity $\sigma_{fluid} = 10 \text{ S/m}$.

5.3.2.1 Derivation of the embedded bounds

To derive the embedded bounds we will first use the fact that points on the HS bounds of the initial composite also fall on the corresponding HS bounds of the final/substituted composite (Milton, 2002 [121]). This is demonstrated by Figure 5.2 where points P1 and Q1 on the lower and upper HS bounds of the initial composite ($\sigma_{min} = 0.01 \text{ S/m}$, $\sigma_{fluid}^{(1)} = 10 \text{ S/m}$, shown as solid HS lines) map exactly and uniquely to points P2 and Q2, respectively on the lower and upper bounds of the final/substituted composite ($\sigma_{min} = 0.01 \text{ S/m}$, $\sigma_{fluid}^{(2)} = 15 \text{ S/m}$, shown as dashed HS lines).

Next we use the fact that any point within but not on the HS bounds of the initial composite can be connected by HS constructs between intermediate end points. To understand this let us consider the point R1 in the initial composite, lying about mid-way between the HS bounds, as shown in Figure 5.3. We can find points P1 and Q1 such that an upper (or lower) HS line connecting points P1 and Q1 also passes through the point R1. This is an HS construct between intermediate end-points.

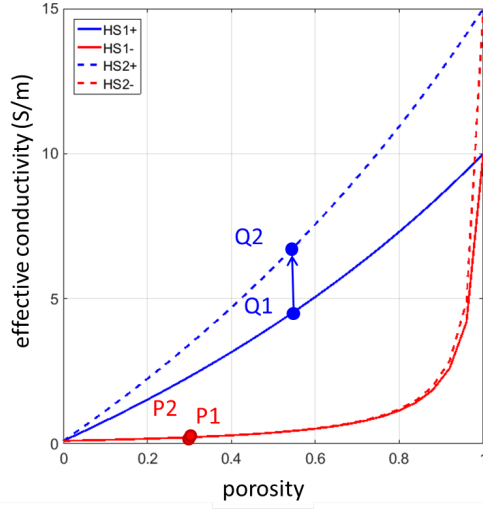


Figure 5.2: Points P1 and Q1 on the lower and upper HS bounds of the initial composite (shown as solid HS lines) map exactly and uniquely to points P2 and Q2, respectively on the lower and upper bounds of the final/substituted composite (shown as dashed HS lines).

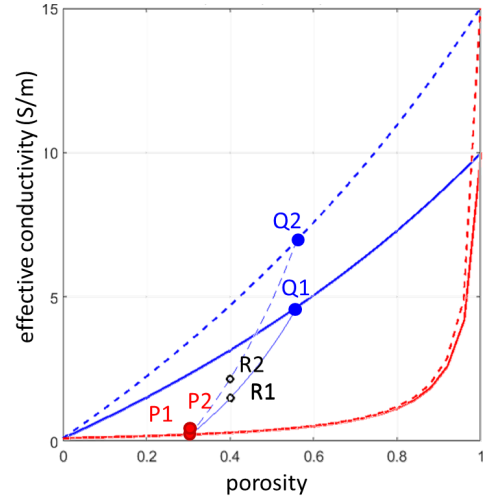


Figure 5.3: For a point R1 in between the HS bounds of the initial composite (solid lines), we can find points P1 and Q1 such that an upper (or lower) HS line connecting points P1 and Q1 also passes through R1. With this construct, points P1, Q1 and R1 in the initial composite map exactly and uniquely to the points P2, Q2, and R2 in the final/substituted composite.

Now, by virtue of this construct, we know the exact and unique mapping of each of the points P1, Q1 and R1 in the initial composite to the points P2, Q2, and R2 in the final/substituted composite, as shown in Figure 5.3.

Finally we use the fact that there are an infinite number of possible HS constructs between intermediate end-points that pass through the point R1 (lying within the HS bounds) in the initial composite, as shown by the solid gray lines in Figure 5.4. Each of these constructs through R1 represents a slightly different micro-geometry, even though they have the same effective conductivity with the initial phase properties.

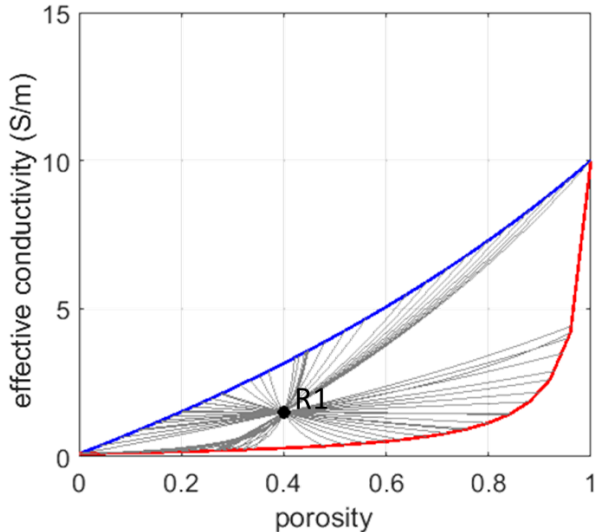


Figure 5.4: Infinite number of possible HS constructs between intermediate end-points that pass through the point R1 (lying within the HS bounds) in the initial composite, shown by gray lines.

For every HS construct through R1 in the initial composite, we can find the exact and unique position of R2 in the final/substituted composite, as discussed earlier in this section. All of the mapped R2 points are shown together in Figure 5.5. We see that the R2 points are not co-incident, instead they map over a range of values in the final composite. This shows that micro-geometries that yield the same effective conductivity with the initial composition (as represented by a single point R1) no

longer yield the same effective conductivity with the final/substituted composition (as represented by a range of values of R2).

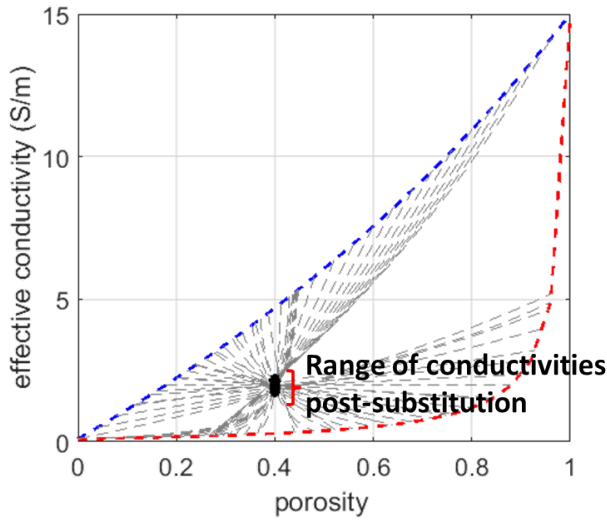


Figure 5.5: The single point R1 in the initial composite maps over a range of conductivity values in the final/substituted composite, showing that the problem of conductivity substitution is inherently non-unique due to the unknown exact micro-geometry of a composite.

In other words, this shows that the conductivity substitution problem is inherently non-unique due to the unknown exact micro-geometry of a composite. The effect of non-uniqueness in conductivity substitution becomes even more apparent when the contrast between conductivities of the initial ($\sigma_{fluid}^{(1)} = 5\text{S}/\text{m}$) and final/substituting fluids ($\sigma_{fluid}^{(2)} = 15\text{S}/\text{m}$) in the composite is made larger, as demonstrated by Figure 5.6.

The limits of the conductivity substitution range shown in Figures 5.5 and 5.6 are the ‘embedded bounds’, so named because they are derived by embedding one set of HS bounds inside of another. The embedded bounds correspond to the outermost of four possible Hashin-Shtrikman constructs: HS_{min+} , HS_{min-} , HS_{fluid+} and HS_{fluid-} , as shown in Figure 5.7. HS_{min+} and HS_{min-} are respectively, the upper

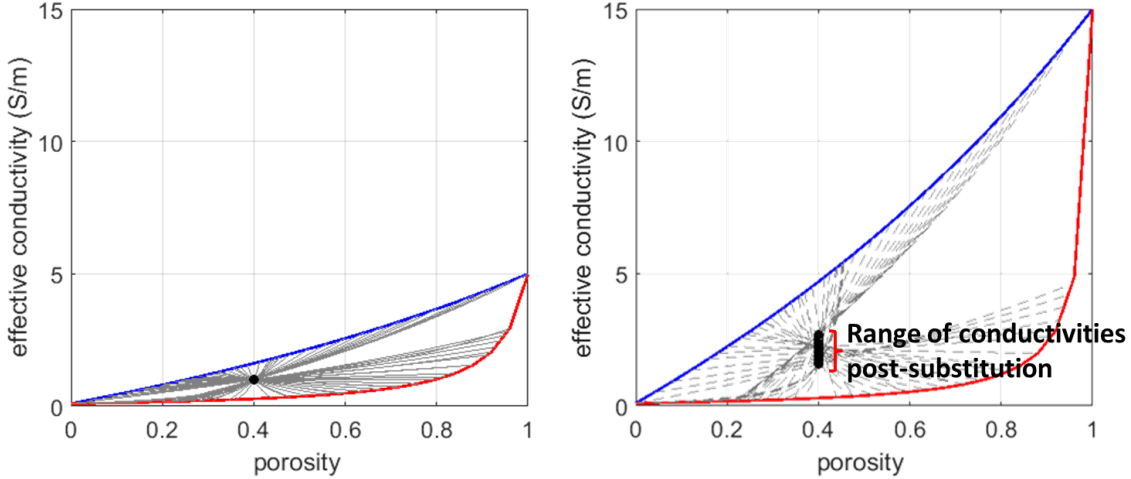


Figure 5.6: Micro-geometry induced non-uniqueness in conductivity substitution enhanced for larger contrast between conductivity of the initial ($\sigma_{fluid}^{(1)} = 5\text{ S}/\text{m}$) and final fluids ($\sigma_{fluid}^{(2)} = 15\text{ S}/\text{m}$).

and lower HS bounds through the mineral point, also passing through R1, the data point of interest in the initial composite. Similarly, HS_{fluid+} and HS_{fluid-} are the upper and lower HS bounds through the fluid point, also passing through R1. We find computationally that the substituted conductivities corresponding to construct pairs HS_{min+} & HS_{min-} are very close, being $< 1\%$ for a wide array of tested mineral and fluid conductivities. We also find that the substituted conductivities predicted by constructions HS_{fluid+} & HS_{fluid-} are within 1%. It is important to note that the embedded bounds span the range of constructs represented schematically by Figures 5.5 and 5.6, and there may exist some very special micro-geometries (such as the laminar aggregates discussed in the chapter on isotropic poly-crystals) that fall outside the embedded bounds.

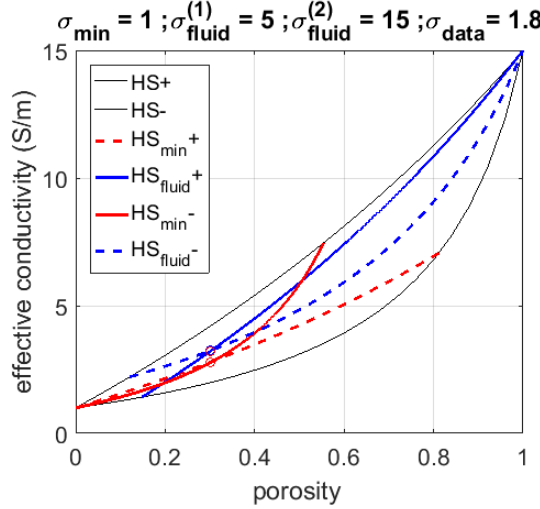


Figure 5.7: Embedded constructs corresponding to conductivity substitution limits in the final/substituted composite: HS_{min}^+ , HS_{min}^- , HS_{fluid}^+ and HS_{fluid}^- .

5.3.2.2 Equations describing the embedded bounds

The HS_{min}^- and HS_{fluid}^+ constructs are realizable as doubly-coated spheres and are two of the curves developed by Vinogradov and Milton (2005 [70]) for viscoelastic substitution, and by Gibiansky and Torquato (1998 [10]) for elastic-electrical cross-bounds. In the initial-final conductivity space $(\sigma_{eff}^{(1)} - \sigma_{eff}^{(2)})$, these constructs are given by equations 5.7 and 5.8.

$$HS_{min}^- = HYP_1 = HYP \left[(\sigma_{HS-}^{(1)}, \sigma_{HS-}^{(2)}), (\sigma_{HS+}^{(1)}, \sigma_{HS+}^{(2)}), (\sigma_{min}^{(1)}, \sigma_{min}^{(2)}) \right] \quad (5.7)$$

$$HS_{fluid}^+ = HYP_2 = HYP \left[(\sigma_{HS-}^{(1)}, \sigma_{HS-}^{(2)}), (\sigma_{HS+}^{(1)}, \sigma_{HS+}^{(2)}), (\sigma_{fluid}^{(1)}, \sigma_{fluid}^{(2)}) \right] \quad (5.8)$$

In Equations 5.7 and 5.8, HYP_1 is a hyperbola in the $\sigma_{eff}^{(1)} - \sigma_{eff}^{(2)}$ plane that

passes through the two HS points $(\sigma_{HS-}^{(1)}, \sigma_{HS-}^{(2)})$, $(\sigma_{HS+}^{(1)}, \sigma_{HS+}^{(2)})$, and the mineral point $(\sigma_{min}^{(1)}, \sigma_{min}^{(2)})$, while HYP_2 is a hyperbola that passes through the two HS points and the fluid point $(\sigma_{fluid}^{(1)}, \sigma_{fluid}^{(2)})$. The $HYP[(x_1, y_1), (x_2, y_2), (x_3, y_3)]$ function can be parameterized by Equations 5.9 and 5.10.

$$x = \gamma_1 x_1 + \gamma_2 x_2 - \frac{\gamma_1 \gamma_2 (x_1 - x_2)^2}{\gamma_2 x_1 + \gamma_1 x_2 - x_3} \quad (5.9)$$

$$y = \gamma_1 y_1 + \gamma_2 y_2 - \frac{\gamma_1 \gamma_2 (y_1 - y_2)^2}{\gamma_2 y_1 + \gamma_1 y_2 - y_3} \quad (5.10)$$

In Equations 5.9 and 5.10, $\gamma_1 = 1 - \gamma_2 \in [0, 1]$. Equations 5.7 and 5.8 form a lens in the $\sigma_{eff}^{(1)} - \sigma_{eff}^{(2)}$ plane that defines the allowable pairs of effective conductivity values before and after substitution. The mathematical expressions of the other two limiting constructs HS_{min+} and HS_{fluid-} are considerably more complicated. Due to the very small difference in conductivity construct pairs HS_{min+} and HS_{min-} , and HS_{fluid+} and HS_{fluid-} for a wide variety of cases of practical interest, going forward, for ease of application, the term embedded bounds will refer to constructs HS_{min-} (mineral-coated embedded bound) and HS_{fluid+} (fluid-coated embedded bound).

The embedded bounds, given by Equations 5.7 and 5.8, allow for substitution of the fluid conductivity or the solid conductivity, or both. By contrast, the popularly used Archie's law, works primarily for substitution of the fluid conductivity only. Figure 5.8 demonstrates examples of substitution of both fluid and solid conductivities: the top sub-figure shows the effect of increasing the fluid conductivity by a factor of ten, while holding the solid phase constant, while bottom sub-figure shows the effect of increasing the solid conductivity by a factor of ten while keeping the fluid conductivity constant. In both cases, the porosity is 0.3.

The equations and theory presented in this paper are intended for a strictly 2-phase material. There is no explicit treatment of surface conductivity, and the theory

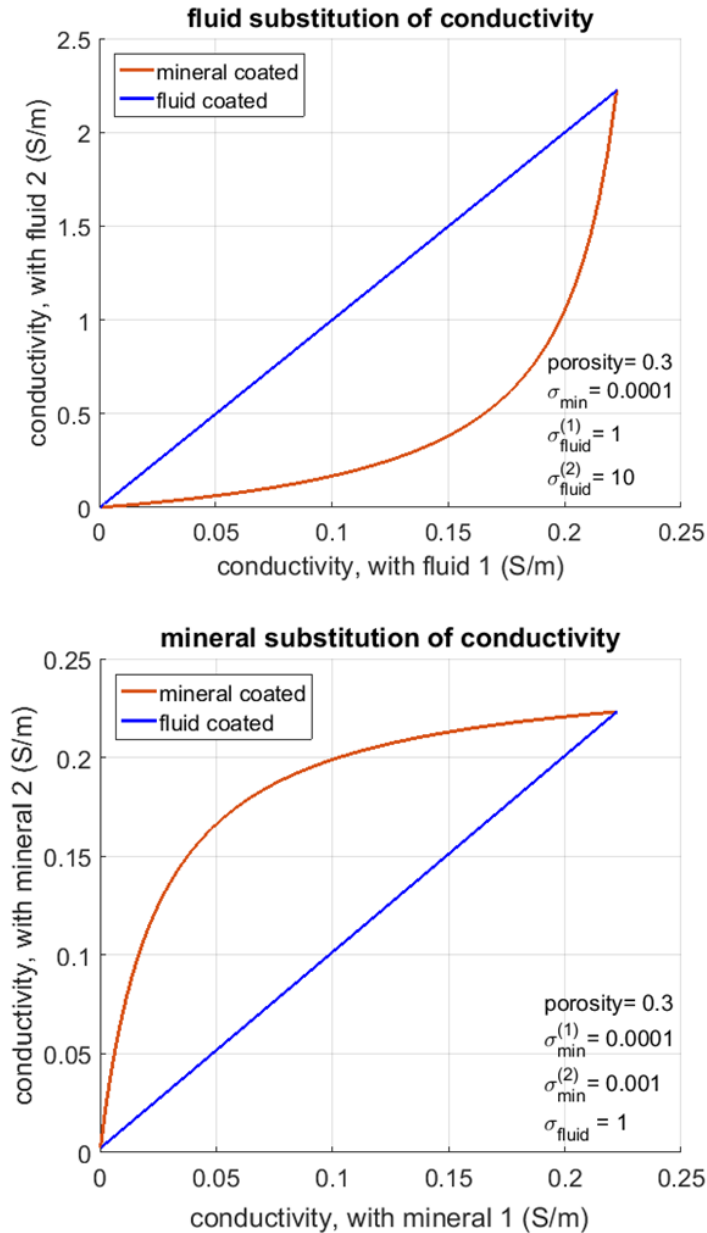


Figure 5.8: Embedded bound curves for electrical conductivity substitution. Top: Fluid substitution, increase of fluid conductivity by a factor of 10; mineral conductivity constant. Bottom: Mineral substitution, increase of mineral conductivity by a factor of 10; fluid conductivity constant. Porosity = 0.3.

does not account for a transition between ionic and electronic current flow. All of the changes that we discuss are the result of the phase properties and the microgeometry. Having said that, some authors (Bussian 1983 [122]; Glover, et al., 2010 [123]) have suggested that the conductivity of the solid phase can be used to approximate surface-enhanced conductivity.

5.4 Geometric interpretation of the embedded bounds

5.4.1 Mineral and fluid coated embedded bounds

The $HS_{min}-$ and the $HS_{fluid}+$ embedded substitution bounds correspond to a micro-geometry of doubly coated spheres and are labeled the ‘mineral coated embedded bound’ and the ‘fluid coated embedded bound’ respectively. Figure 5.9 schematically shows the doubly-coated sphere geometries that realize the embedded bounds. Constituent spheres in the fluid coated bound have a fluid (shown in blue) outer shell, that can be interpreted as optimally connected pore space. On the other hand, constituent spheres in the mineral coated bound have a mineral (shown in yellow) outer shell, interpretable as poorly connected pore-space. This geometric interpretation of the embedded substitution bounds in terms of pore space connectivity is also borne out by effective medium modeling, as discussed in the following sub-section.

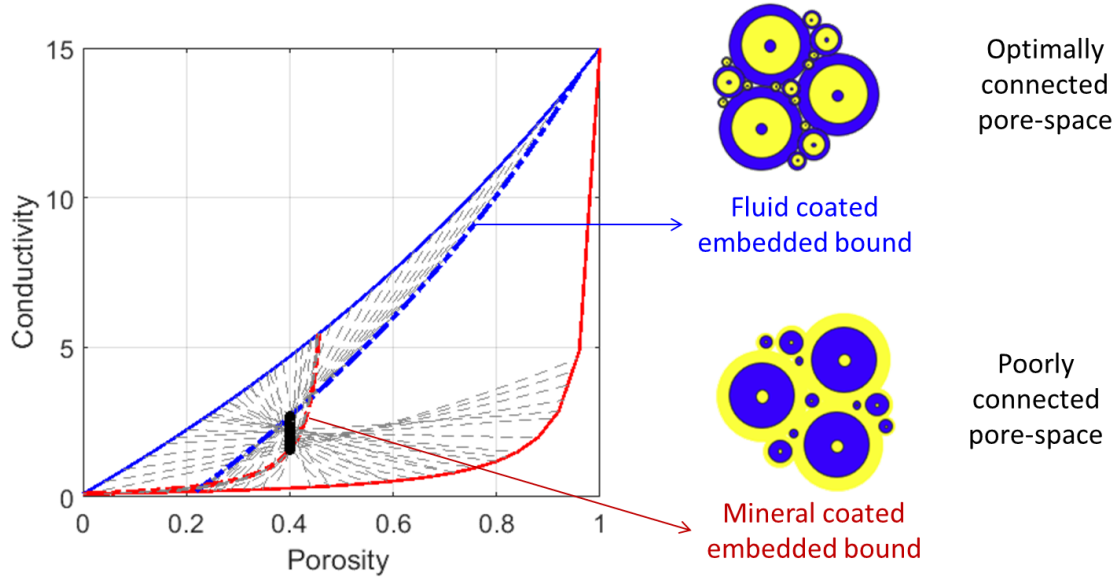


Figure 5.9: Schematic representation of the doubly-coated sphere geometries that realize the embedded bounds for conductivity substitution.

5.4.2 Interpretation using effective medium theories

We explore the geometric interpretation of non-unique conductivity substitution using the Self-Consistent approximation (SC) model and the Differential Effective Medium (DEM) model, both of which represent rock heterogeneity with ellipsoidal inclusions. While the SC and DEM models only approximate heterogeneous media, they are known to always give realizable predictions (i.e., the predicted effective conductivities lie within the HS bounds). This implies that there always exists a micro-geometrical arrangement of the two phases that will have the effective conductivity of the model prediction.

The SC model for conductivity used in this study is equivalent to the model introduced by Berryman (1995 [12]). Figure 5.10 compares embedded bounds predictions (red and blue curves) with SC model predictions (black filled circles) for

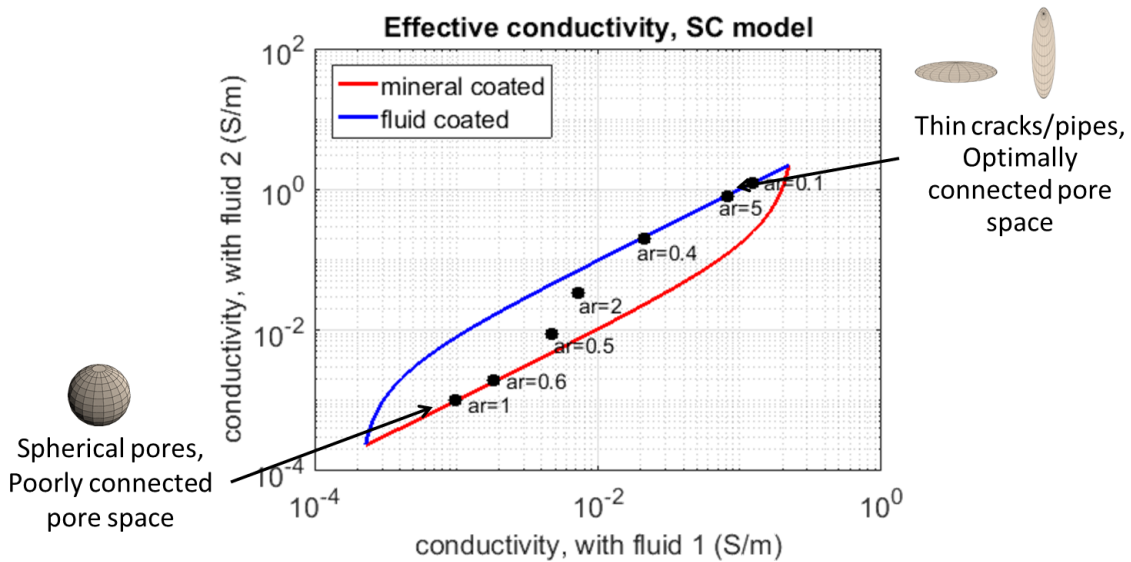


Figure 5.10: SC model predictions (black dots) compared with embedded bound predictions (red and blue curves) for conductivity substitution. Porosity=0.3. The fluid conductivity increases by a factor of 10; mineral conductivity remains constant. Aspect ratios (labeled ‘ar’ in the figure) close to 1 represent shapes that are spherical, less than 1 are oblate/crack-like and greater than 1 are prolate/tube-like.

different pore aspect ratios; the solid is represented in the Sc model as spherical inclusions. The conductivities of the phase end members (units: S/m) are as follows: $\sigma_{min} = 0.0001$, $\sigma_{fluid}^{(1)} = 1$, $\sigma_{fluid}^{(2)} = 10$. The entire plot corresponds to a constant porosity of 0.3. When the water-saturated pores are spherical ($ar=1$), the SC model predicts relatively low conductivity with the point falling on the red mineral-coated embedded bound curve, close to the lower HS bounds. This would represent poorly connected pore space. As the pore aspect ratio decreases, the pores become more crack-like, pore connectivity increases, and the effective conductivity increases as we assume the pores to be saturated with conductive brine. We observe a transition from the red curve to the blue curve over the aspect ratio range of about 0.6-0.4. The blue fluid-coated embedded bound curve represents an optimally connected pore space, as demonstrated by Figure 5.9.

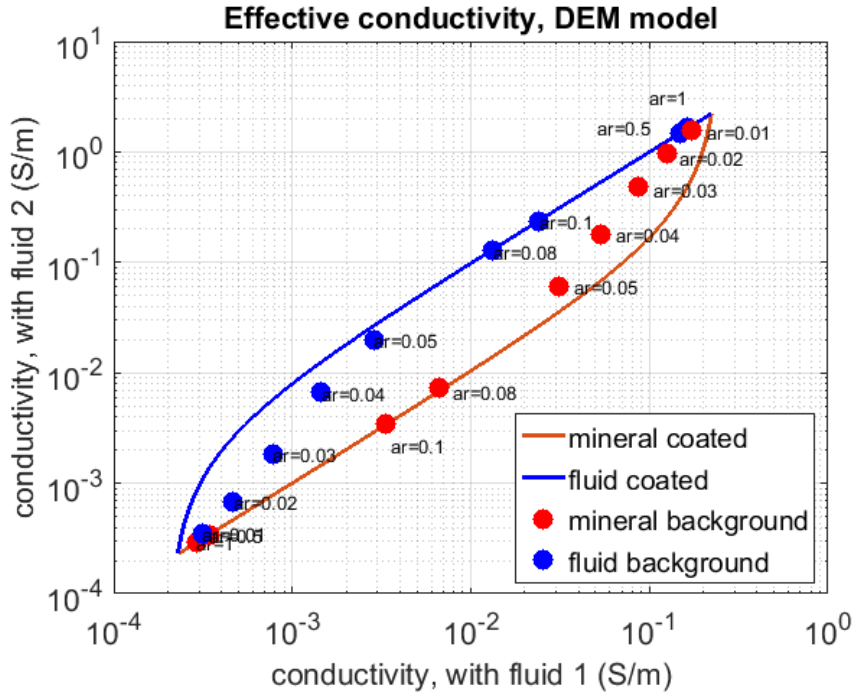


Figure 5.11: DEM predictions compared with embedded bound predictions (red and blue curves) for conductivity substitution. Porosity=0.3. The fluid conductivity increases by a factor of 10; mineral conductivity remains constant. Blue dots show low conductivity grains added to a high conductivity background. Red dots show high conductivity pores added to a low conductivity background.

Figure 5.11 compares the embedded bound predictions (red and blue curves) with predictions of the DEM model (red and blue dots). Again, the entire plot corresponds to a constant porosity 0.3. The blue dots correspond to ellipsoidal inclusions of a low-conductivity solid added to an initial background of high conductivity pore fluid. We can think of the low-conductivity grains as blocking the high current in the fluid. DEM predicts that spherical grains cause the least decrease of conductivity. As the grain aspect ratio decreases, the grains become more disk-like, and effective conductivity drops. A transition in the DEM predictions is observed from the blue fluid coated embedded bound to the red mineral coated embedded bound for grains with aspect ratio less than 0.08. On the other hand, the red dots in Figure 5.11 correspond to

ellipsoidal inclusions of high conductivity fluid added to an initial background of low conductivity solid/mineral. Spherical pores give a low effective conductivity, while thin, crack-like pores cause larger conductivity. A transition from the red curve to the blue curve is observed for pore aspect ratios less than 0.1.

The DEM model for conductivity used here is equivalent to the model introduced by Bruggeman (1935 [116]) and Hanai (1960 [124], 1961 [125], 1962 [126]) for a fluid background with suspended particles. Sen (1980 [117], 1981 [127]) and Sen et al. (1981 [128]) showed that this model with a well-connected fluid could lead to Archie's law. The Bruggemann-Hanai model can be expressed by Equation 5.11.

$$\left(\frac{\sigma_{eff} - \sigma_{min}}{\sigma_{fluid} - \sigma_{min}} \right) \left(\frac{\sigma_{min}}{\sigma_{eff}} \right)^d = \phi \quad (5.11)$$

In Equation 5.11 each of the conductivities can also be complex. The exponent in the equation can be written as $d = 1/(a - m)$, where m is Archie's cementation constant. Equation 5.11 was separately derived by Pal (2002 [129]) for the effective complex moduli of a viscoelastic background with suspended particles with contrasting viscoelasticity. Parameters d and m are determined by the particle shape, but d and m do not uniquely determine the shape.

5.5 Comparison of the embedded bounds with Archie's Law

An example of the embedded bound curves relating the initial and final effective conductivities is shown in Figure 5.12, where the horizontal axis is the effective conductivity with the initial fluid and the vertical axis is the effective conductivity with the final/substituted fluid. In this example, the porosity is 0.05, $\sigma_{min} = 0.0001S/m$,

$\sigma_{fluid}^{(1)} = 1S/m$ and $\sigma_{fluid}^{(2)} = 5S/m$. The top sub-figure plots the conductivities in a linear scale while bottom one plots the conductivities in a logarithmic scale, to better reveal lower conductivity features.

The lenses defined by the red and blue curves (corresponding to the mineral and fluid coated embedded bounds) in Figure 5.12 define the combinations of initial and final effective conductivity that are possible for this porosity and this composition. In the next sub-section, we mathematically show that except at very low values of conductivity, the blue fluid-coated embedded curve is approximately equal to Archie's law predictions (plotted as black stars), given by Equation 5.1, and corresponds to an optimally connected fluid phase. The dashed lines show the Hashin-Shtrikman limits.

It is important to note that the approximate equivalence between Archie's Law predictions and the fluid coated embedded bound (representing the highest possible change in conductivity due to substitution), is valid only for a large contrast between the mineral and fluid conductivities, as in case of the example in Figure 5.12. For smaller contrasts, Archie's Law predicts a change larger than that predicted by the embedded bounds. This is demonstrated in Figure 5.13, where the contrast between the initial mineral and fluid phase is reduced to 10.

5.5.1 Conditional equivalence between Archie's Law and the fluid-coated embedded bound

Here we present the mathematical proof of equivalence between Archie's Law and the fluid-coated embedded bound at high phase conductivity contrast. Consider a two phase quartz-brine isotropic composite. σ_{min} represents the quartz conductivity and $\sigma_{fluid}^{(1)}$ represents the brine conductivity in the initial/unsubstituted state with effective conductivity $\sigma_{eff}^{(1)}$. In the final/substituted state, the quartz conductivity remains unchanged at σ_{min} , but the brine conductivity changes to $\sigma_{fluid}^{(2)}$, with effective

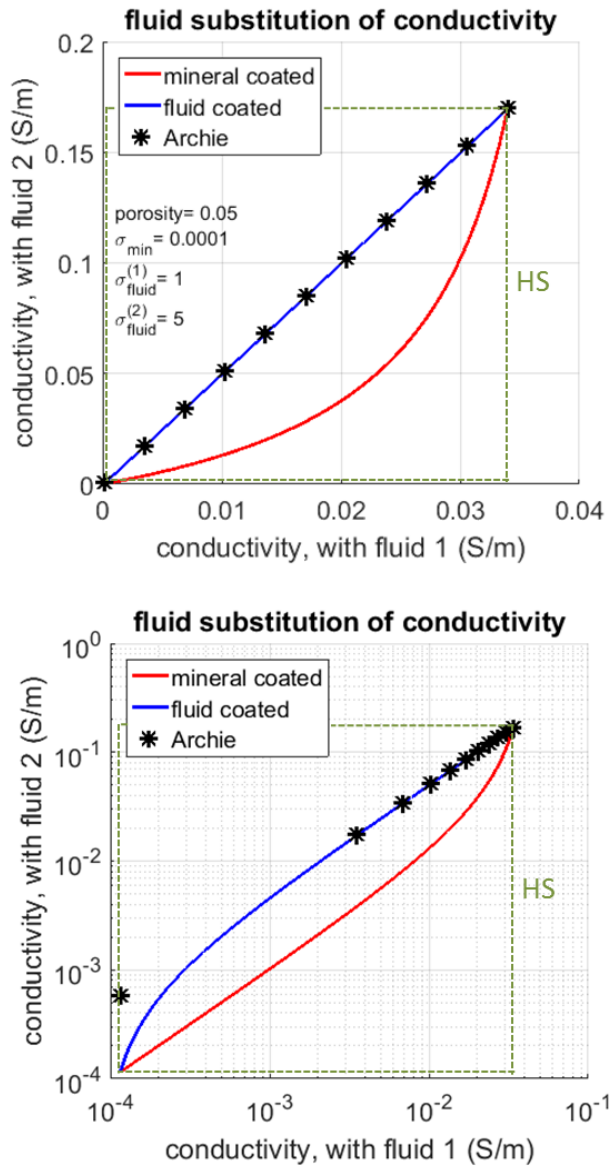


Figure 5.12: Embedded bound curves for fluid substitution of conductivity, labeled ‘mineral coated’ and ‘fluid coated’. Fluid conductivity increases by factor of 5; porosity = 0.05; initial fluid conductivity is 10,000 times larger than the mineral conductivity. The blue curve shows the embedded bound which is almost equal to Archie’s law (black stars) predictions except at very low conductivities. Dashed lines show the HS bounds for initial and final compositions.

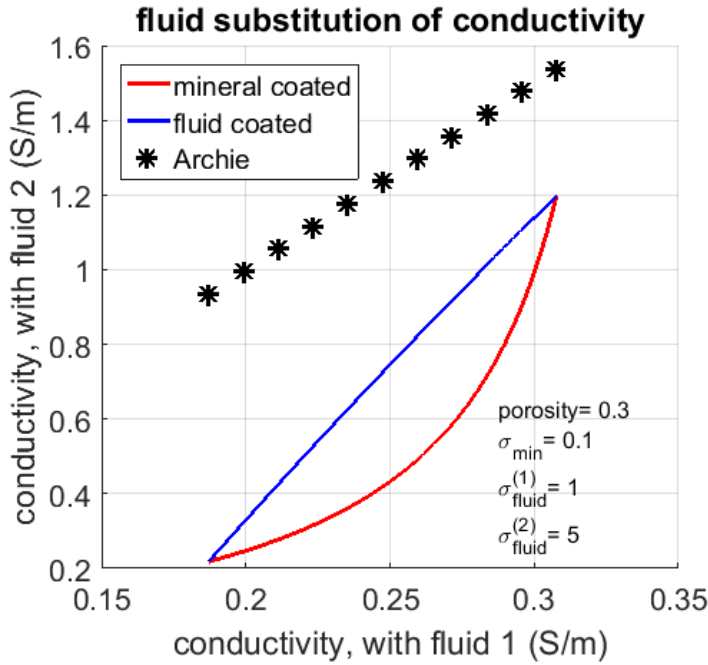


Figure 5.13: Embedded bound curves for fluid substitution of conductivity, labeled ‘mineral coated’ and ‘fluid coated’. Fluid conductivity increased by factor of 5; porosity = 0.3; initial fluid conductivity is only 10 times larger than the mineral conductivity. Archie’s law (black stars) significantly over predicts the change due to substitution for this reduced conductivity contrast between the constituent phases.

conductivity $\sigma_{eff}^{(2)}$. We will consider the case when the conductivity contrast between the quartz phase and both the initial and final brine phases is very high, i.e., $\sigma_{min} \ll \sigma_{fluid}^{(1)}$ and $\sigma_{min} \ll \sigma_{fluid}^{(2)}$. The volume fraction of quartz in the composite is f_1 , and the volume fraction of brine is f_2 .

If $HS_+^{(1)}$ and $HS_-^{(1)}$ represent the upper and lower HS bounds for the unsubstituted composite, then, except at very low values of f_2 , $HS_-^{(1)} \ll HS_+^{(1)}$ if $\sigma_{min} \ll \sigma_{fluid}^{(1)}$. Similarly, if $HS_+^{(2)}$ and $HS_-^{(2)}$ represent the upper and lower HS bounds for the unsubstituted composite, then, except at very low values of f_2 , $HS_-^{(2)} \ll HS_+^{(2)}$ if $\sigma_{min} \ll \sigma_{fluid}^{(2)}$.

In the $\sigma_{eff}^{(1)} - \sigma_{eff}^{(2)}$ plane, representing the unsubstituted composite on the x-axis

and the substituted composite on the y-axis, any point on the fluid coated embedded bound lies on the hyperbola $HYP_2 = HYP \left[(HS_-^{(1)}, HS_-^{(2)}), (HS_+^{(1)}, HS_+^{(2)}), (\sigma_{fluid}^{(1)}, \sigma_{fluid}^{(2)}) \right]$, parameterized as per Equations 5.12 and 5.13.

$$x = \sigma_{eff}^{(1)} = \gamma_1 HS_-^{(1)} + \gamma_2 HS_+^{(1)} - \frac{\gamma_1 \gamma_2 (HS_-^{(1)} - HS_+^{(1)})^2}{\gamma_2 HS_-^{(1)} + \gamma_1 HS_+^{(1)} - \sigma_{fluid}^{(1)}} \quad (5.12)$$

$$y = \sigma_{eff}^{(2)} = \gamma_1 HS_-^{(2)} + \gamma_2 HS_+^{(2)} - \frac{\gamma_1 \gamma_2 (HS_-^{(2)} - HS_+^{(2)})^2}{\gamma_2 HS_-^{(2)} + \gamma_1 HS_+^{(2)} - \sigma_{fluid}^{(2)}} \quad (5.13)$$

In Equations 5.12 and 5.13, $\gamma_2 = 1 - \gamma_1 \in [0, 1]$. Since $HS_-^{(1)} \ll HS_+^{(1)}$, we can say that $HS_+^{(1)} \pm HS_-^{(1)} \approx HS_+^{(1)}$. Further, $HS_-^{(1)} \ll \sigma_{fluid}^{(1)}$, implying that $\sigma_{fluid}^{(1)} \pm HS_-^{(1)} \approx \sigma_{fluid}^{(1)}$. Using this Equation 5.12 can be rewritten as:

$$x = \sigma_{eff}^{(1)} = \gamma_1 HS_-^{(1)} + (1 - \gamma_1) HS_+^{(1)} - \frac{\gamma_1 (1 - \gamma_1) (HS_-^{(1)} - HS_+^{(1)})^2}{(1 - \gamma_1) HS_-^{(1)} + \gamma_1 HS_+^{(1)} - \sigma_{fluid}^{(1)}} \quad (5.14)$$

$$= HS_+^{(1)} - \gamma_1 (HS_+^{(1)} - HS_-^{(1)}) - \frac{\gamma_1 (1 - \gamma_1) (HS_-^{(1)} - HS_+^{(1)})^2}{\gamma_1 (HS_+^{(1)} - HS_-^{(1)}) - (\sigma_{fluid}^{(1)} - HS_-^{(1)})} \quad (5.15)$$

$$= HS_+^{(1)} - \gamma_1 (HS_+^{(1)}) - \frac{\gamma_1 (1 - \gamma_1) (HS_+^{(1)})^2}{\gamma_1 (HS_+^{(1)}) - \sigma_{fluid}^{(1)}} = \frac{\sigma_{fluid}^{(1)} (1 - \gamma_1) HS_+^{(1)}}{\sigma_{fluid}^{(1)} - \gamma_1 HS_+^{(1)}} \quad (5.16)$$

Similarly, Equation 5.13 can be reduced to Equation 5.17.

$$y = \sigma_{eff}^{(2)} = \frac{\sigma_{fluid}^{(2)}(1 - \gamma_1)HS_+^{(2)}}{\sigma_{fluid}^{(2)} - \gamma_1 HS_+^{(2)}} \quad (5.17)$$

Using Equations 5.16 and 5.17 the ratio of the effective conductivity values of initial and final/substituted composites can be expressed by Equation 5.19.

$$\frac{\sigma_{eff}^{(1)}}{\sigma_{eff}^{(2)}} = \frac{\sigma_{fluid}^{(1)}}{\sigma_{fluid}^{(2)}} \frac{HS_+^{(1)}(1 - \gamma)(\sigma_{fluid}^{(2)} - \gamma_1 HS_+^{(2)})}{HS_+^{(2)}(1 - \gamma)(\sigma_{fluid}^{(1)} - \gamma_1 HS_+^{(1)})} \quad (5.18)$$

$$= \frac{\sigma_{fluid}^{(1)}}{\sigma_{fluid}^{(2)}} \frac{\sigma_{fluid}^{(2)}HS_+^{(1)} - \gamma_1 HS_+^{(2)}HS_+^{(1)}}{\sigma_{fluid}^{(1)}HS_+^{(2)} - \gamma_1 HS_+^{(2)}HS_+^{(1)}} \quad (5.19)$$

Using the expression for Hashin Shtrikman bounds for electrical conductivity, and using the high conductivity contrast condition ($\sigma_{min} << \sigma_{fluid}^{(1)}$) can show that:

$$\frac{HS_+^{(1)}}{\sigma_{fluid}^{(1)}} = \frac{1}{\sigma_{fluid}^{(1)}} \left(\frac{1}{\frac{f_1}{\sigma_{min} + 2\sigma_{fluid}^{(1)}} + \frac{(1 - f_1)}{\sigma_{fluid}^{(1)} + 2\sigma_{fluid}^{(1)}}} - 2\sigma_{fluid}^{(1)} \right) \quad (5.20)$$

$$= \frac{1}{\sigma_{fluid}^{(1)}} \left(\frac{1}{\frac{f_1}{2\sigma_{fluid}^{(1)}} + \frac{(1 - f_1)}{3\sigma_{fluid}^{(1)}}} - 2\sigma_{fluid}^{(1)} \right) = \frac{6}{2 + f_1} - 2 \quad (5.21)$$

Similarly, we can show that:

$$\frac{HS_+^{(2)}}{\sigma_{fluid}^{(2)}} = \frac{6}{2 + f_1} - 2 \quad (5.22)$$

Comparing Equations 5.21 and 5.22, we can say that:

$$\frac{HS_+^{(1)}}{\sigma_{fluid}^{(1)}} = \frac{HS_+^{(2)}}{\sigma_{fluid}^{(2)}} \Rightarrow \sigma_{fluid}^{(2)} HS_+^{(1)} = \sigma_{fluid}^{(1)} HS_+^{(2)} \quad (5.23)$$

Using the result obtained in Equation 5.23, we can simplify Equation 5.19 further to:

$$\frac{\sigma_{eff}^{(1)}}{\sigma_{eff}^{(2)}} = \frac{\sigma_{fluid}^{(1)}}{\sigma_{fluid}^{(2)}} \quad \frac{\sigma_{fluid}^{(2)} HS_+^{(1)} - \gamma_1 HS_+^{(2)} HS_+^{(1)}}{\sigma_{fluid}^{(1)} HS_+^{(2)} - \gamma_1 HS_+^{(2)} HS_+^{(1)}} = \frac{\sigma_{fluid}^{(1)}}{\sigma_{fluid}^{(2)}} \quad (5.24)$$

Equation 5.24 shows that for high contrast between the mineral and fluid phases of a composite, except at very low values of porosity, the effective composite conductivity is proportional to the fluid conductivity, which is equivalent to Archie's empirical law.

5.6 Comparison of the embedded bounds with measured data

5.6.1 The Waxman-Smits dataset

Waxman and Smits (1968 [130]) published laboratory measurements of electrical conductivity and petrophysical parameters on 55 core samples ranging from clean sandstones to very shaly sandstones. The electrical conductivities of the samples were reported for 4 different values of the saturating brine conductivity: 228, 81.9, 37.3 and 21.3 mS/cm. Bussian (1983 [122]) applied a slight modification of the Bruggeman-Hanai model (Equation 5.11) to the Waxman-Smits dataset to back-calculate effective matrix conductivity and cementation factor for all the samples as per Equation 5.25. We use Waxman and Smits' (WS) original dataset and Bussian's estimates of matrix conductivity for our current exercise.

$$\begin{aligned}\sigma_{eff} &= \sigma_{fluid}\phi^m \left(\frac{1 - \sigma_{min}/\sigma_{fluid}}{1 - \sigma_{min}/\sigma_{eff}} \right)^m \\ &= \sigma_{fluid}\phi^{m/(1-m)} \left(\frac{1 - \sigma_{fluid}/\sigma_{min}}{1 - \sigma_{eff}/\sigma_{min}} \right)^{m/(1-m)}\end{aligned}\quad (5.25)$$

5.6.2 Comparison using constant and variable mineral conductivity

In Figure 5.14 we start with the measured WS sample conductivities corresponding to a brine conductivity (C_{brine}) of 228 mS/cm, use the embedded substitution bounds and the Archie's Law to predict sample conductivities at a brine conductivity of 21.3 mS/cm, and compare the predictions against the measured WS sample conductivities at $C_{brine} = 21.3$ mS/cm. The top panel shows results assuming a constant matrix conductivity of 0.0001 mS/cm (corresponding approximately to wet sandstones), while the bottom panel shows results for variable matrix conductivity using Bussian's estimates. The Archie points are color coded by the corresponding sample ' Q_v ', the ratio of cation exchange capacity and pore-volume, approximately equal to the samples' effective clay content (Waxman and Smits, 1968, [130]).

In the top sub-figure of 5.14, in going from a brine conductivity of 228 to 21.3 mS/cm, the embedded substitution bounds enclose all of the measured data-points at the final brine conductivity, despite the fact that assuming a constant matrix/grain conductivity of 0.0001 mS/cm (corresponding to wet sandstone) is not strictly correct because of the varying amount of clay in the samples. The conductivity contrast between the matrix and the fluid is quite high in this instance, causing the Archie predictions to coincide with the fluid coated embedded bound, representing an optimally connected fluid-phase and the greatest possible change due to substitution.

In the bottom sub-figure of 5.14, in going from a brine conductivity of 228 to 21.3

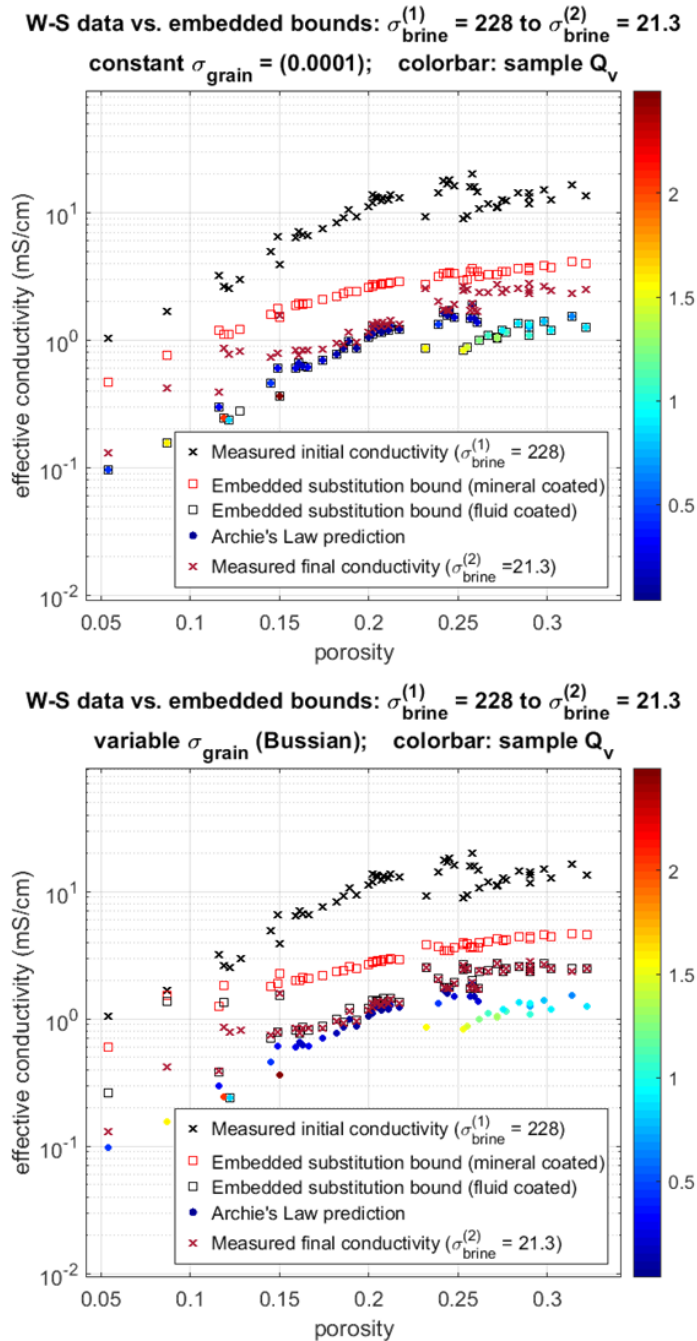


Figure 5.14: Embedded bounds, Archie's Law predictions and measured data for fluid substitution in sandstones with variable clay content, going from an initial brine conductivity of 228 to a final of 21.3 mS/cm using (top) a constant matrix conductivity of 0.0001 mS/cm, and (bottom) Bussian's inverted grain conductivity, accounting for the variable clay content.

mS/cm, the embedded substitution bounds enclose most of the measured data-points at the final brine conductivity, except at low porosities. In fact, most of the measured data points coincide with the fluid-coated embedded bound. We use Bussian's estimates of the matrix/grain conductivity, which ensures that the varying levels of clay in the samples are better accounted for than in the top sub-figure. Bussian's estimates of the matrix/grain conductivity vary between 0-1.23 mS/cm (histogram in Figure 5.15), in many cases greatly reducing the conductivity contrast between the matrix and the fluid as compared to the case of constant matrix conductivity.

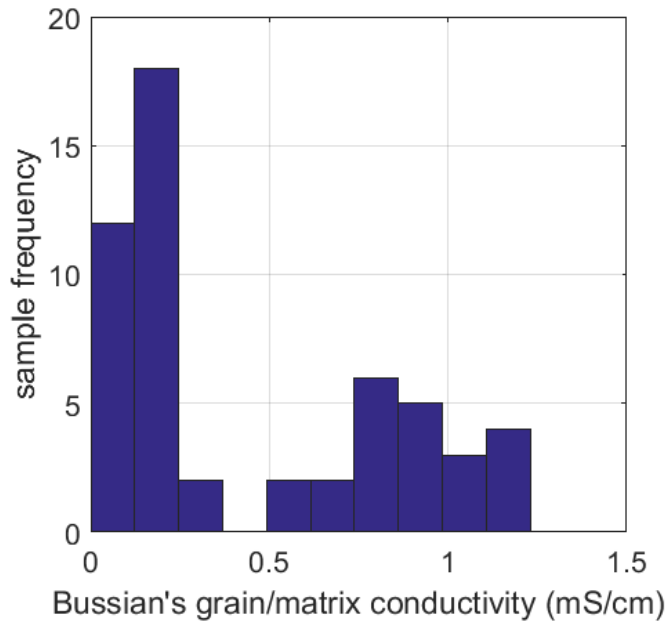


Figure 5.15: Histogram of Bussian's estimates of the matrix/grain conductivity, varying between 0-1.23 mS/cm.

In general, larger the sample clay content, larger the Bussian estimate of matrix conductivity and smaller the conductivity contrast between matrix and fluid. Accordingly, the Archie predictions, especially those with high values of ' Q_v ' deviate from the fluid coated embedded bound, registering a larger change due to substitution. A general trend becomes apparent from Figure 5.14, except at very low porosities:

when matrix conductivity accounts for presence of clay, on average, the deviation of the Archie predictions from the fluid-coated embedded bound is proportional to ' Q_v ', and hence representative of the effective clay content of shaly sand samples. On the other hand, when matrix conductivity does not account for presence of clay, on average, the deviation of measured conductivity from the fluid-coated embedded bound is proportional to ' Q_v ', and hence representative of the effective clay content of shaly sand samples.

The observations and discussions in changing brine conductivity from 228 to 21.3 mS/cm in the WS dataset are also valid for changing brine conductivity from 228 to 37.3 and 81.9 mS/cm, demonstrated by Figures 5.16 and 5.17 respectively.

Both figures show that in general, when using a constant, low value (0.0001 mS/cm) of matrix conductivity (without accounting for the presence of clays) the embedded substitution bounds enclose all of the measured data-points at the final brine conductivity. The Archie predictions coincide with the fluid coated embedded bound in this high conductivity contrast case (between matrix and fluid), representing the largest possible change due to substitution. On average, except at low porosities, the deviation of measured conductivity from the fluid-coated embedded bound is proportional to ' Q_v ', and representative of the sample clay content.

When using Bussian's inverted values for matrix conductivity (accounting for the presence of clays), except at low porosities, the embedded substitution bounds enclose most of the measured data-points at the final brine conductivity, with the majority of measured data points coinciding with the fluid-coated embedded bound. Except at low porosities, on average, the deviation of the Archie predictions from the fluid-coated embedded bound is proportional to ' Q_v ', and hence representative of the effective clay content in these shaly sand samples.

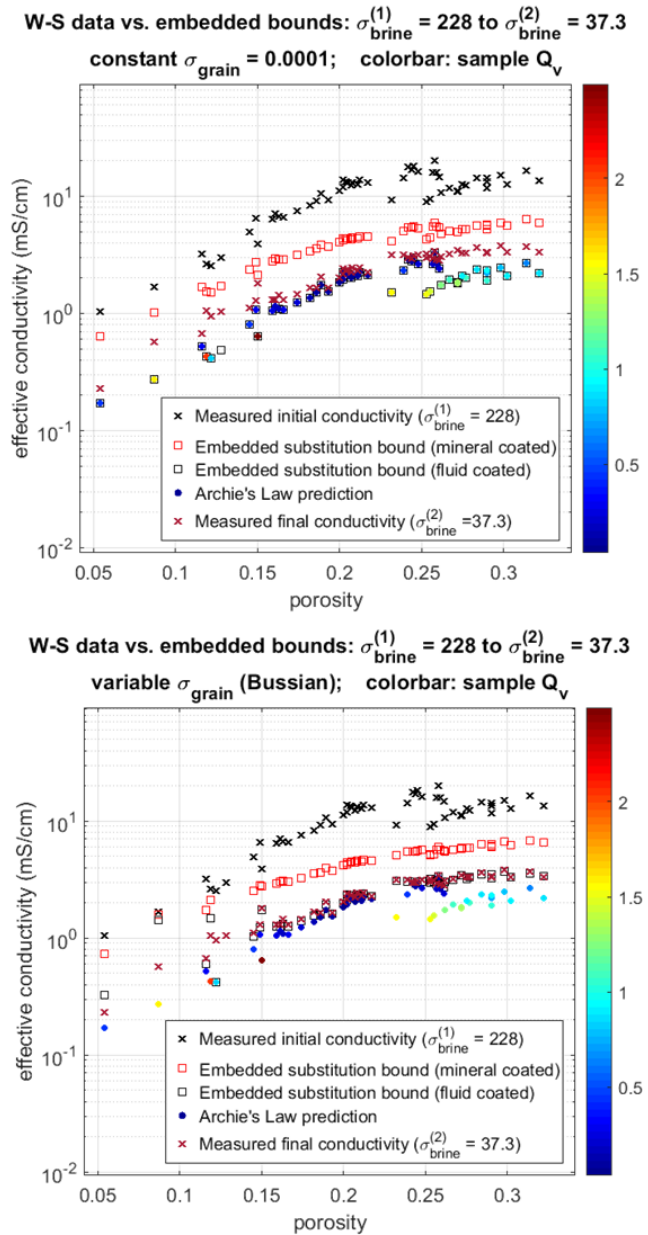


Figure 5.16: Embedded bounds, Archie's Law predictions and measured data for fluid substitution in sandstones with variable clay content, going from an initial brine conductivity of 228 to a final of 37.3 mS/cm using (top) a constant matrix conductivity of 0.0001 mS/cm, and (bottom) Bussian's inverted grain conductivity, accounting for the variable clay content.

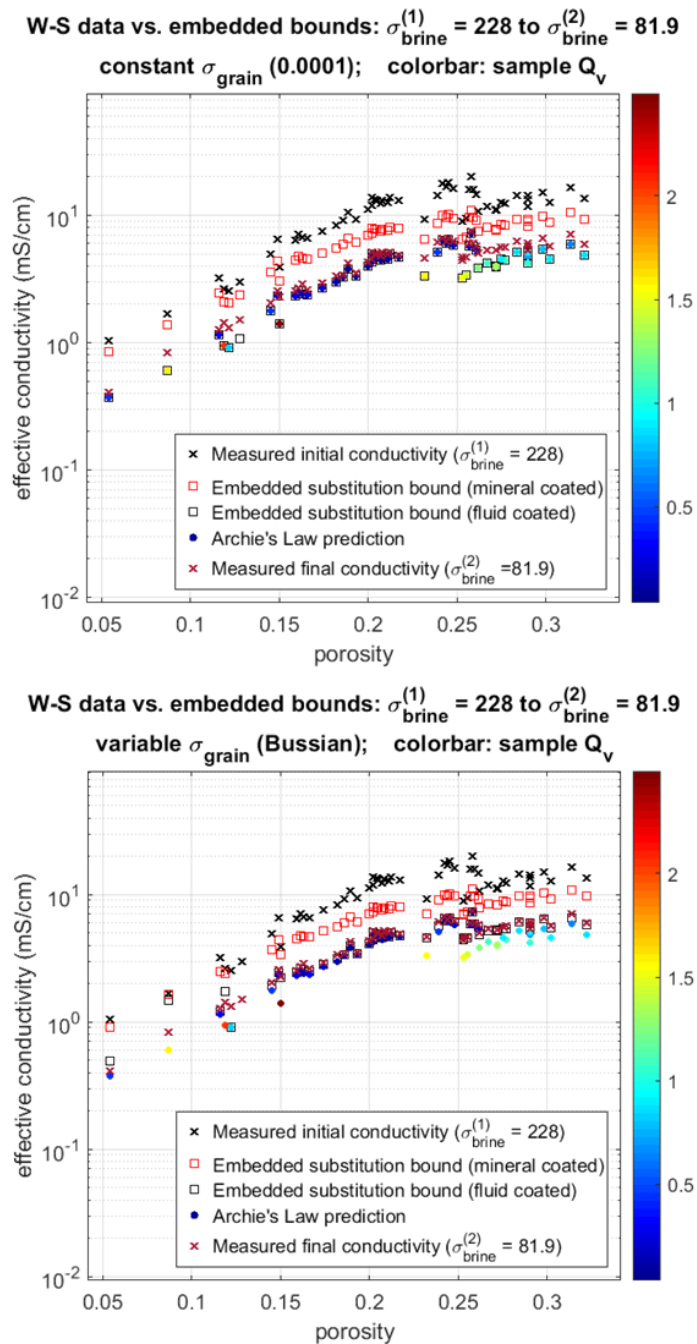


Figure 5.17: Embedded bounds, Archie's Law predictions and measured data for fluid substitution in sandstones with variable clay content, going from an initial brine conductivity of 228 to a final of 81.9 mS/cm using (top) a constant matrix conductivity of 0.0001 mS/cm, and (bottom) Bussian's inverted grain conductivity, accounting for the variable clay content.

5.7 Conclusions

Rigorous theory and numerical models show that fluid substitution prediction for electrical properties is non-unique. The uncertainty is entirely due to variations in pore space micro-structure. The embedded bounds, realizable by doubly coated sphere assemblages, provide upper and lower bounds on the change of effective conductivity and dielectric constant for both fluid and mineral substitution in three dimensional, isotropic, 2-phase composites.

For composites with a large conductivity contrast between phases, the commonly used Archie's Law coincides with one of the embedded bounds for fluid substitution, representing an optimally connected fluid phase and the largest possible change in conductivity due to substitution. When the conductivity contrast between the phases is small, the change predicted by Archie's Law is too large.

Realizable effective medium models like SC and DEM lie within the embedded bounds and show that fluid substitution in composites with spherical pores (assuming that the matrix has low conductivity and the pore-saturating fluid has high conductivity), representing poorly connected pore space, fall on the mineral coated embedded bound, representing the smallest possible change in effective conductivity due to substitution. On the other hand, oblate/crack-like and prolate/tube-like pores, representing optimally connected pore space, fall on the fluid coated embedded bound, representing the largest possible change in effective conductivity due to substitution.

Comparing the embedded substitution bounds to Waxman-Smits measurements on sandstones with varying clay content reveals some interesting trends, except at low porosities (< 10%). When using a constant, low value (0.0001 mS/cm) of matrix conductivity (without accounting for the presence of clays) the embedded substitution bounds enclose all of the measured data-points at the final brine conductivity. The Archie predictions coincide with the fluid coated embedded bound, representing the

largest possible change due to substitution. clean samples with low effective clay content, given by low values of ' Q_v ', the ratio of cation exchange capacity and pore-volume, lie close to the fluid-coated embedded bound, which makes sense as clean porous sandstones are expected to have well-connected pores. On average, deviation of measured conductivity from the fluid-coated embedded bound is proportional to ' Q_v ', and indicative of the effective clay content of samples.

When using Bussian's inverted values for matrix conductivity (accounting for the presence of clays), the embedded substitution bounds enclose most of the measured data-points at the final brine conductivity, and the majority of measured data-points coincide with the fluid-coated embedded bound. It is interesting to note that even in our work on cross-bounds, a vast majority of both measured and digitally estimated data points plotted close to the fluid-coated embedded bound. On average, in this case, deviation of the Archie predictions from the fluid-coated embedded bound is proportional to ' Q_v ', and may be used as an indicator of effective clay content in these shaly sand samples.

...

Bibliography

- [1] James G Berryman and Graeme W Milton. Microgeometry of random composites and porous media. *Journal of Physics D: Applied Physics*, 21(1):87, 1988.
- [2] Stephen C Blair, Patricia A Berge, and James G Berryman. Using two-point correlation functions to characterize microgeometry and estimate permeabilities of sandstones and porous glass. *Journal of Geophysical Research: Solid Earth*, 101(B9):20359–20375, 1996.

- [3] M Schild, S Siegesmund, A Vollbrecht, and Martin Mazurek. Characterization of granite matrix porosity and pore-space geometry by in situ and laboratory methods. *Geophysical Journal International*, 146(1):111–125, 2001.
- [4] AP Radlinski, MA Ioannidis, AL Hinde, M Hainbuchner, M Baron, H Rauch, and SR Kline. Multiscale characterization of reservoir rock microstructure: Combining small angle neutron scattering and image analysis. In *SCA2002-35, Proceedings of 2002 International Symposium of the Society of Core Analysts*, pages 22–25, 2002.
- [5] S Youssef, E Rosenberg, N Gland, S Bekri, and O Vizika. Quantitative 3d characterisation of the pore space of real rocks: improved μ -ct resolution and pore extraction methodology. *Int. Sym. of the Society of Core Analysts*, 2007.
- [6] Lawrence M Anovitz and David R Cole. Characterization and analysis of porosity and pore structures. *Reviews in Mineralogy and geochemistry*, 80(1):61–164, 2015.
- [7] Z Hashin and S Shtrikman. A variational approach to the theory of the elastic behaviour of polycrystals. *Journal of the Mechanics and Physics of Solids*, 10(4):343–352, 1962.
- [8] Zvi Hashin and Shmuel Shtrikman. A variational approach to the theory of the elastic behaviour of multiphase materials. *Journal of the Mechanics and Physics of Solids*, 11(2):127–140, 1963.
- [9] LV Gibiansky and S Torquato. Connection between the conductivity and bulk modulus of isotropic composite materials. In *Proc. R. Soc. Lond. A*, volume 452, pages 253–283. The Royal Society, 1996.

- [10] Leonid Gibiansky and Salvatore Torquato. Rigorous connection between physical properties of porous rocks. *Journal of Geophysical Research: Solid Earth*, 103(B10):23911–23923, 1998.
- [11] Gary Mavko and Nishank Saxena. Embedded-bound method for estimating the change in bulk modulus under either fluid or solid substitution. *Geophysics*, 78(5):L87–L99, 2013.
- [12] James G Berryman. Mixture theories for rock properties. *Rock physics & phase relations: A handbook of physical constants*, pages 205–228, 1995.
- [13] W Voigt. Lehrbuch der kristallphysik (teubner, leipzig, 1928). *Google Scholar*, page 962, 1908.
- [14] A Reuss. A. reuss, z. angew. math. mech. 9, 49 (1929). *Z. Angew. Math. Mech.*, 9:49, 1929.
- [15] Leon Thomsen. Weak elastic anisotropy. *Geophysics*, 51(10):1954–1966, 1986.
- [16] Gustave E Archie et al. The electrical resistivity log as an aid in determining some reservoir characteristics. *Transactions of the AIME*, 146(01):54–62, 1942.
- [17] Brian E Hornby, Larry M Schwartz, and John A Hudson. Anisotropic effective-medium modeling of the elastic properties of shales. *Geophysics*, 59(10):1570–1583, 1994.
- [18] Kaushik Bandyopadhyay. *Seismic anisotropy: Geological causes and its implications to reservoir geophysics*. Stanford University, 2009.
- [19] Gary Mavko, Tapan Mukerji, and Jack Dvorkin. *The rock physics handbook: Tools for seismic analysis of porous media*. Cambridge university press, 2009.

- [20] Warren P Mason. Chapter i: Quartz crystal applications. *Bell Labs Technical Journal*, 22(2):178–223, 1943.
- [21] Issac Koga, Masanao Aruga, and Yōichirō Yoshinaka. Theory of plane elastic waves in a piezoelectric crystalline medium and determination of elastic and piezoelectric constants of quartz. *Physical Review*, 109(5):1467, 1958.
- [22] HJ McSkimin, P Andreatch Jr, and RNl Thurston. Elastic moduli of quartz versus hydrostatic pressure at 25 and- 195.8 c. *Journal of Applied Physics*, 36(5):1624–1632, 1965.
- [23] Orson L Anderson and Robert C Liebermann. Sound velocities in rocks and minerals [by] orson l. anderson [and] robert c. liebermann. 1966.
- [24] De-hua Han, A Nur, and Dale Morgan. Effects of porosity and clay content on wave velocities in sandstones. *Geophysics*, 51(11):2093–2107, 1986.
- [25] Jean-Pierre Dominique Blangy. *Integrated seismic lithologic interpretation: The petrophysical basis*, volume 51. Department of Geophysics, School of Earth Sciences, 1992.
- [26] BC Hendrix and LG Yu. Self-consistent elastic properties for transversely isotropic polycrystals. *Acta materialia*, 46(1):127–135, 1998.
- [27] Christopher M Kube and Andrea P Arguelles. Bounds and self-consistent estimates of the elastic constants of polycrystals. *Computers & Geosciences*, 95:118–122, 2016.
- [28] Richard Hill. The elastic behaviour of a crystalline aggregate. *Proceedings of the Physical Society. Section A*, 65(5):349, 1952.

- [29] Dae-Hyun Chung. Elastic moduli of single crystal and polycrystalline mgo. *Philosophical Magazine*, 8(89):833–841, 1963.
- [30] J Peter Watt. Hashin-shtrikman bounds on the effective elastic moduli of polycrystals with orthorhombic symmetry. *Journal of Applied Physics*, 50(10):6290–6295, 1979.
- [31] Z Hashin and S Shtrikman. On some variational principles in anisotropic and nonhomogeneous elasticity. *Journal of the Mechanics and Physics of Solids*, 10(4):335–342, 1962.
- [32] J Michael Brown. Determination of hashin–shtrikman bounds on the isotropic effective elastic moduli of polycrystals of any symmetry. *Computers & Geosciences*, 80:95–99, 2015.
- [33] J Peter Watt, Geoffrey F Davies, and Richard J O’Connell. The elastic properties of composite materials. *Reviews of Geophysics*, 14(4):541–563, 1976.
- [34] J Michael Brown, Ross J Angel, and Nancy L Ross. Elasticity of plagioclase feldspars. *Journal of Geophysical Research: Solid Earth*, 121(2):663–675, 2016.
- [35] J Peter Watt. Hashin-shtrikman bounds on the effective elastic moduli of polycrystals with monoclinic symmetry. *Journal of Applied Physics*, 51(3):1520–1524, 1980.
- [36] FI Fedorov. Theory of elastic waves in crystals (translated by j, 1968).
- [37] Klaus Helbig. Running title:jj approximation of elastic tensors. *Seismic Anisotropy*, page 37, 1996.
- [38] Jules Thomas Browaeys and Sébastien Chevrot. Decomposition of the elastic tensor and geophysical applications. *Geophysical Journal International*, 159(2):667–678, 2004.

- [39] Joe Dellinger. Computing the optimal transversely isotropic approximation of a general elastic tensor. *Geophysics*, 70(5):I1–I10, 2005.
- [40] Maher Moakher and Andrew N Norris. The closest elastic tensor of arbitrary symmetry to an elasticity tensor of lower symmetry. *Journal of Elasticity*, 85(3):215–263, 2006.
- [41] Andrew N Norris. Elastic moduli approximation of higher symmetry for the acoustical properties of an anisotropic material. *The Journal of the Acoustical Society of America*, 119(4):2114–2121, 2006.
- [42] Miguel A Caro. Extended scheme for the projection of material tensors of arbitrary symmetry onto a higher symmetry tensor. *arXiv preprint arXiv:1408.1219*, 2014.
- [43] Salvatore Torquato. Random heterogeneous materials. interdisciplinary applied mathematics. *Springer-Verlag, New York. doi*, 10:978–1, 2002.
- [44] Ilya Tsvankin. Anisotropic parameters and p-wave velocity for orthorhombic media. *Geophysics*, 62(4):1292–1309, 1997.
- [45] DH Chung and WR Buessem. The elastic anisotropy of crystals. *Journal of Applied Physics*, 38(5):2010–2012, 1967.
- [46] Shivakumar I Ranganathan and Martin Ostoja-Starzewski. Universal elastic anisotropy index. *Physical Review Letters*, 101(5):055504, 2008.
- [47] Sanjeev Rajput and Naresh Kumar Thakur. *Geological Controls for Gas Hydrates and Unconventionals*. Elsevier, 2016.
- [48] J Alberto Ortega, Franz-Josef Ulm, and Younane Abousleiman. The effect of the nanogranular nature of shale on their poroelastic behavior. *Acta Geotechnica*, 2(3):155–182, 2007.

- [49] Leo Breiman. Arcing the edge. Technical report, Technical Report 486, Statistics Department, University of California at Berkeley, 1997.
- [50] Jerome H Friedman. Greedy function approximation: a gradient boosting machine. *Annals of statistics*, pages 1189–1232, 2001.
- [51] Jerome H Friedman. Stochastic gradient boosting. *Computational Statistics & Data Analysis*, 38(4):367–378, 2002.
- [52] Llew Mason, Jonathan Baxter, Peter L Bartlett, and Marcus R Frean. Boosting algorithms as gradient descent. In *Advances in neural information processing systems*, pages 512–518, 2000.
- [53] Jerome Friedman, Trevor Hastie, and Robert Tibshirani. *The elements of statistical learning*, volume 1. Springer series in statistics New York, 2001.
- [54] Leo Breiman, Jerome Friedman, Charles J Stone, and Richard A Olshen. *Classification and regression trees*. CRC press, 1984.
- [55] Ekkehart Kröner. Berechnung der elastischen konstanten des vielkristalls aus den konstanten des einkristalls. *Zeitschrift für Physik*, 151(4):504–518, 1958.
- [56] John D Eshelby. The determination of the elastic field of an ellipsoidal inclusion, and related problems. In *Proc. R. Soc. Lond. A*, volume 241, pages 376–396. The Royal Society, 1957.
- [57] Morteza M Mehrabadi and Stephen C Cowin. Eigentensors of linear anisotropic elastic materials. *The Quarterly Journal of Mechanics and Applied Mathematics*, 43(1):15–41, 1990.
- [58] Maarten Moesen, Luis Cardoso, and Stephen C Cowin. A symmetry invariant formulation of the relationship between the elasticity tensor and the fabric tensor. *Mechanics of Materials*, 54:70–83, 2012.

- [59] Bertram Alexander Auld. *Acoustic fields and waves in solids.* , 1973.
- [60] Keith W Katahara et al. Clay mineral elastic properties. In *1996 SEG Annual Meeting*. Society of Exploration Geophysicists, 1996.
- [61] RFS Hearmon. The elastic constants of crystals and other anisotropic materials. *Landolt-Börnstein Tables*, 3(18):559, 1984.
- [62] Michael T Vaughan and Stephen Guggenheim. Elasticity of muscovite and its relationship to crystal structure. *Journal of Geophysical Research: Solid Earth*, 91(B5):4657–4664, 1986.
- [63] James G Berryman. Bounds and self-consistent estimates for elastic constants of random polycrystals with hexagonal, trigonal, and tetragonal symmetries. *Journal of the Mechanics and Physics of Solids*, 53(10):2141–2173, 2005.
- [64] James G Berryman. Bounds and self-consistent estimates for elastic constants of polycrystals composed of orthorhombics or crystals with higher symmetries. *Physical Review E*, 83(4):046130, 2011.
- [65] YP Qiu and GJ Weng. Elastic constants of a polycrystal with transversely isotropic grains, and the influence of precipitates. *Mechanics of materials*, 12(1):1–15, 1991.
- [66] Fritz Gassmann. Elasticity of porous media. *Vierteljahrsschrder Naturforschenden Gessellschaft*, 96:1–23, 1951.
- [67] Robert JS Brown and Jan Korringa. On the dependence of the elastic properties of a porous rock on the compressibility of the pore fluid. *Geophysics*, 40(4):608–616, 1975.

- [68] Radim Ciz and Serge A Shapiro. Generalization of gassmann equations for porous media saturated with a solid material. *Geophysics*, 72(6):A75–A79, 2007.
- [69] George E Backus. Long-wave elastic anisotropy produced by horizontal layering. *Journal of Geophysical Research*, 67(11):4427–4440, 1962.
- [70] V Vinogradov and GW Milton. The total creep of viscoelastic composites under hydrostatic or antiplane loading. *Journal of the Mechanics and Physics of Solids*, 53(6):1248–1279, 2005.
- [71] Carol Tosaya and Amos Nur. Effects of diagenesis and clays on compressional velocities in rocks. *Geophysical Research Letters*, 9(1):5–8, 1982.
- [72] Ryong-Joon Roe. Description of crystallite orientation in polycrystalline materials. iii. general solution to pole figure inversion. *Journal of Applied Physics*, 36(6):2024–2031, 1965.
- [73] CM Sayers. Elastic wave anisotropy in the upper mantle. *Geophysical Journal International*, 88(2):417–424, 1987.
- [74] Tor Arne Johansen, Bent Ole Ruud, and Morten Jakobsen. Effect of grain scale alignment on seismic anisotropy and reflectivity of shales. *Geophysical Prospecting*, 52(2):133–149, 2004.
- [75] Peter R Morris. Averaging fourth-rank tensors with weight functions. *Journal of Applied Physics*, 40(2):447–448, 1969.
- [76] CM Sayers. Anisotropic velocity analysis. *Geophysical Prospecting*, 43(4):541–568, 1995.

- [77] CM Sayers and M Kachanov. Microcrack-induced elastic wave anisotropy of brittle rocks. *Journal of Geophysical Research: Solid Earth*, 100(B3):4149–4156, 1995.
- [78] CM Sayers. The elastic anisotropy of shales. *Journal of Geophysical Research: Solid Earth*, 99(B1):767–774, 1994.
- [79] CM Sayers. The elastic anisotropy of polycrystalline aggregates of zirconium and its alloys. *Journal of Nuclear Materials*, 144(3):211–213, 1987.
- [80] LIANG Zuo, MICHEL Humbert, and CLAUDE Esling. Elastic properties of polycrystals in the voigt-reuss-hill approximation. *Journal of applied crystallography*, 25(6):751–755, 1992.
- [81] Chi-Sing Man and Mojia Huang. A simple explicit formula for the voigt-reuss-hill average of elastic polycrystals with arbitrary crystal and texture symmetries. *Journal of Elasticity*, 105(1-2):29–48, 2011.
- [82] Hsun Hu. Elastic properties of cold-rolled and annealed sheets of phosphorus steel having high normal plastic anisotropy. *Texture, Stress, and Microstructure*, 4(2):111–127, 1980.
- [83] M Hirao, K Aoki, and H Fukuoka. Texture of polycrystalline metals characterized by ultrasonic velocity measurements. *The Journal of the Acoustical Society of America*, 81(5):1434–1440, 1987.
- [84] S Hirsekorn. Elastic properties of polycrystals: a review. *Texture, Stress, and Microstructure*, 12(1-3):1–14, 1990.
- [85] CM Sayers. Seismic anisotropy of shales. *Geophysical prospecting*, 53(5):667–676, 2005.

- [86] Richard H Bennett, Neal R OBrien, and Matthew H Hulbert. Determinants of clay and shale microfabric signatures: processes and mechanisms. In *Microstructure of Fine-Grained Sediments*, pages 5–32. Springer, 1991.
- [87] TJ Katsebe and MA Williamson. Effects of diagenesis on shale nano-pore structure and implications for sealing capacity. *Clay minerals*, 29(4):451–472, 1994.
- [88] WH Owens. Strain modification of angular density distributions. *Tectonophysics*, 16(3-4):249–261, 1973.
- [89] David W Baker, Kanwarjit S Chawla, and Raymond J Krizek. Compaction fabrics of pelites: experimental consolidation of kaolinite and implications for analysis of strain in slate. *Journal of Structural Geology*, 15(9-10):1123–1137, 1993.
- [90] Geoffrey S Watson. The statistics of orientation data. *The Journal of Geology*, 74(5, Part 2):786–797, 1966.
- [91] Tariq Alkhailah and Ilya Tsvankin. Velocity analysis for transversely isotropic media. *Geophysics*, 60(5):1550–1566, 1995.
- [92] KS Aleksandrov. The elastic properties of rock forming minerals ii: Layered silicates. *Bull. Acad. Sci. USSR, Geophys. Ser.*, 9:1165–1168, 1961.
- [93] Leonie EA Jones and Herbert F Wang. Ultrasonic velocities in cretaceous shales from the williston basin. *Geophysics*, 46(3):288–297, 1981.
- [94] Lev Vernik and Amos Nur. Ultrasonic velocity and anisotropy of hydrocarbon source rocks. *Geophysics*, 57(5):727–735, 1992.

- [95] Joel E Johnston and Nikolas I Christensen. Seismic anisotropy of shales. *Journal of Geophysical Research: Solid Earth*, 100(B4):5991–6003, 1995.
- [96] Zhijing Wang. Seismic anisotropy in sedimentary rocks, part 2: Laboratory data. *Geophysics*, 67(5):1423–1440, 2002.
- [97] George R Pickett et al. Acoustic character logs and their applications in formation evaluation. *Journal of Petroleum technology*, 15(06):659–667, 1963.
- [98] GHF Gardner, MH Harris, et al. Velocity and attenuation of elastic waves in sands. In *SPWLA 9th Annual Logging Symposium*. Society of Petrophysicists and Well-Log Analysts, 1968.
- [99] AR Gregory. Fluid saturation effects on dynamic elastic properties of sedimentary rocks. *Geophysics*, 41(5):895–921, 1976.
- [100] Robert H Tatham. V p/v s and lithology. *Geophysics*, 47(3):336–344, 1982.
- [101] Brian E Hornby and William F Murphy III. V p/v s in unconsolidated oil sands: Shear from stoneley. *Geophysics*, 52(4):502–513, 1987.
- [102] John P Castagna, Michael L Batzle, and Raymond L Eastwood. Relationships between compressional-wave and shear-wave velocities in clastic silicate rocks. *Geophysics*, 50(4):571–581, 1985.
- [103] Myung W Lee. *Velocity ratio and its application to predicting velocities*.
- [104] Emmanuel C David, Jérôme Fortin, Alexandre Schubnel, Yves Guéguen, and Robert W Zimmerman. Laboratory measurements of low-and high-frequency elastic moduli in fontainebleau sandstone. *Geophysics*, 78(5):D369–D379, 2013.

- [105] Leon Thomsen, JP Castagna, and M Backus. Weak anisotropic reflections. *Offset-dependent reflectivity Theory and practice of AVO analysis: Soc. Expl. Geophys*, pages 103–111, 1993.
- [106] Andreas Rüger. P-wave reflection coefficients for transversely isotropic models with vertical and horizontal axis of symmetry. *Geophysics*, 62(3):713–722, 1997.
- [107] José M Carcione, Bjørn Ursin, and Janniche I Nordskag. Cross-property relations between electrical conductivity and the seismic velocity of rocks. *Geophysics*, 72(5):E193–E204, 2007.
- [108] Nishank Saxena and Gary Mavko. Estimating elastic moduli of rocks from thin sections: digital rock study of 3d properties from 2d images. *Computers & Geosciences*, 88:9–21, 2016.
- [109] Tongcheng Han. *Joint elastic-electrical properties of reservoir sandstones*. PhD thesis, University of Southampton, 2010.
- [110] Igor Sevostianov and Mark Kachanov. Connections between elastic and conductive properties of heterogeneous materials. In *Advances in applied mechanics*, volume 42, pages 69–252. Elsevier, 2009.
- [111] GW Milton. Correlation of the electromagnetic and elastic properties of composites and microgeometries corresponding with effective medium approximations. In *AIP Conference Proceedings*, volume 107, pages 66–77. AIP, 1984.
- [112] GW Milton. Bounds on the transport and optical properties of a two-component composite material. *Journal of Applied Physics*, 52(8):5294–5304, 1981.
- [113] LV Gibiansky and GW Milton. On the effective viscoelastic moduli of two-phase media. i. rigorous bounds on the complex bulk modulus. In *Proc. R. Soc. Lond. A*, volume 440, pages 163–188. The Royal Society, 1993.

- [114] Nishank Saxena and Gary Mavko. Exact equations for fluid and solid substitution. *Geophysics*, 79(3):L21–L32, 2014.
- [115] James G Berryman. Long-wavelength propagation in composite elastic media ii. ellipsoidal inclusions. *The Journal of the Acoustical Society of America*, 68(6):1820–1831, 1980.
- [116] Von DAG Bruggeman. Berechnung verschiedener physikalischer konstanten von heterogenen substanzen. i. dielektrizitätskonstanten und leitfähigkeiten der mischkörper aus isotropen substanzen. *Annalen der physik*, 416(7):636–664, 1935.
- [117] Pabitra N Sen et al. The dielectric and conductivity response of sedimentary rocks. In *SPE Annual Technical Conference and Exhibition*. Society of Petroleum Engineers, 1980.
- [118] James G Berryman, Steven R Pride, and Herbert F Wang. A differential scheme for elastic properties of rocks with dry or saturated cracks. *Geophysical Journal International*, 151(2):597–611, 2002.
- [119] Tongcheng Han, Michael Ben Clennell, Arthur CH Cheng, and Marina Peruvukhina. Are self-consistent models capable of jointly modeling elastic velocity and electrical conductivity of reservoir sandstones? *Geophysics*, 81(4):D377–D382, 2016.
- [120] Stephen Prager. Improved variational bounds on some bulk properties of a two-phase random medium. *The Journal of Chemical Physics*, 50(10):4305–4312, 1969.
- [121] Graeme W Milton. The theory of composites. *The Theory of Composites, by Graeme W. Milton, pp. 748. ISBN 0521781256. Cambridge, UK: Cambridge University Press, May 2002.*, page 748, 2002.

- [122] AE Bussian. Electrical conductance in a porous medium. *Geophysics*, 48(9):1258–1268, 1983.
- [123] Paul WJ Glover. A generalized archies law for n phases. *Geophysics*, 75(6):E247–E265, 2010.
- [124] Tetsuya Hanai. Theory of the dielectric dispersion due to the interfacial polarization and its application to emulsions. *Kolloid-Zeitschrift*, 171(1):23–31, 1960.
- [125] Tetsuya Hanai. A remark on the theory of the dielectric dispersion due to the interfacial polarization. *Colloid & Polymer Science*, 175(1):61–62, 1961.
- [126] Tetsuya Hanai. Dielectric theory on the interfacial polarization for two-phase mixtures. 1962.
- [127] PN Sen. Relation of certain geometrical features to the dielectric anomaly of rocks. *Geophysics*, 46(12):1714–1720, 1981.
- [128] PN Sen, C Scala, and MH Cohen. A self-similar model for sedimentary rocks with application to the dielectric constant of fused glass beads. *Geophysics*, 46(5):781–795, 1981.
- [129] Rajinder Pal. Complex shear modulus of concentrated suspensions of solid spherical particles. *Journal of colloid and interface science*, 245(1):171–177, 2002.
- [130] Monroe H Waxman, LJM Smits, et al. Electrical conductivities in oil-bearing shaly sands. *Society of Petroleum Engineers Journal*, 8(02):107–122, 1968.